A THEORETICAL ANALYSIS OF THE CURRENT-VOLTAGE
CHARACTERISTICS OF SOLAR CELLS

Final Report on

NASA Grant NGR 34-002-195

NASA Lewis Research Center

January 1979

R. C. Y. Fang and J. R. Hauser

Solid State Electronics Laboratory
Department of Electrical Engineering
North Carolina State University
Raleigh, North Carolina 27650

A THEORETICAL ANALYSIS OF THE CURRENT-VOLTAGE CHARACTERISTICS OF SOLAR CELLS

Final Report on

NASA Grant NGR 34-002-195

NASA Lewis Research Center

January 1979

R. C. Y. Fang and J. R. Hauser

Solid State Electronics Laboratory
Department of Electrical Engineering
North Carolina State University
Raleigh, North Carolina 27650

TABLE OF CONTENTS

TABLE OF CONTENTS (continued)

TABLE OF CONTENTS (continued)

TABLE OF CONTENTS (continued)

LIST OF TABLES (continued)

LIST OF FIGURES

LIST OF FIGURES (continued)

1. INTRODUCTION

1.1 The Need for a General Analysis

Silicon solar cells have been used for 22 years and have been a major space power source from the very beginning. During the last two decades there has been a great deal of improvement in the basic design and technology of solar cells and this has resulted in the latest 15% AMO cell [1] as compared to the 6% cell of 1954 [2]. Despite recent theoretical analyses, which point to a practical 19-20% AMO efficiency, there is still a technological "gap" in achieving this high efficiency [3,4]. The lack of agreement between theory and actual conversion efficiency has been the basic motivating factor in the development of a complete solar cell numerical analysis program.

Silicon technology has reached a very high degree of development allowing meaningful comparisons between theory and experiments. Hence the present work emphasizes the correlation of theoretical and experimental data in addition to the development of a complete solar cell analysis. It is believed that through a detailed comparison, it may be possible to reveal the problem area which could evenually lead to performance improvements and high conversion efficiency.

1.2 A Brief Review of the Development of Silicon Solar Cells

Although the discovery of the photovoltaic effects in an electrolytic cell was made by Becquerd in 1839, the first practical solar cell was not made until 1954 by Chapin, Fuller and Pearson [2]. In the following years there was progress in the understanding of

solar cell theory such as the spectral response theory, the p-n junction theory, the series resistance effect and the determination of the optimum bandgap for materials, etc. At the same time, solar cell efficiency was steadily increased to about 10 percent. However the major technological and theoretical breakthroughs have only been achieved in this decade. These accomplishments should be attributed to the extensive financial support of photovoltaic research activities throughout the world since 1972. This section reviews the progress of the silicon solar cell during the past seven years. The earlier development of the silicon solar cell has been summarized elsewhere.

Considerable efforts have been given to raise the efficiency of silicon solar cells in the past few years. The average cell efficiency is about 15 percent under AMO solar intensity. Practical high efficiency cells of 19 to 20 percent are expected to be achieved in the near future.

1.2.1 High Efficiency and Short Circuit Current

The high efficiency of silicon solar cells has been partly achieved by increasing the output current density in the last few years. This has been due to novel technologies for increasing the surface collecting efficiency and improving violet photon response. In 1973, a new generation of silicon solar cells was produced which utilized Ta_2O_5 oxide, shallow junctions and a fine grid pattern to enhance the collection efficiency. The metal coverage area has also been reduced from .10 percent to about 6 percent and the number of collecting fingers has been

increased from 3/cm to 30/cm. In 1975 a textured cell was also fabricated and the surface reflectivity was reduced to the lowest limit of about 3 percent. Figure 1.1 shows the chronological progress of the average short circuit current density of cells produced during the past seven years.

1.2.2 High Efficiency and Open Circuit Voltage

Efforts to improve cell output voltage has been steadily going on during the past few years. These include the trends of using a low resistivity substrate of 1∿3 Ω-cm instead of the conventional 10 Ω-cm substrate and the fabrication of a high low back surface junction for a high resistivity cell. In 1973, the development of this back surface field or BSF cell produced about a 50 mV increase in open circuit voltage for a thin 10 Ω-cm solar cell. However, the highest voltage achieved from low resistivity cells is much less than that obtained from simple theoretical predictions. Hence, there is recently a great interest in the physical explanations of this discrepancy between theory and experiment.

1.2.3 High Efficiency and Curve Factor

The conventional 10 Ω-cm silicon solar cell has a low curve factor of 0.72. This value is much less than the theoretically predicted value of 0.82. The discrepancy has been identified as due to high space charge current density and high series resistance of a high resistivity cell. However, the curve factor of a recent 1∿3 Ω-cm cell has been raised to about 0.80 since 1972. The high curve factor has been achieved
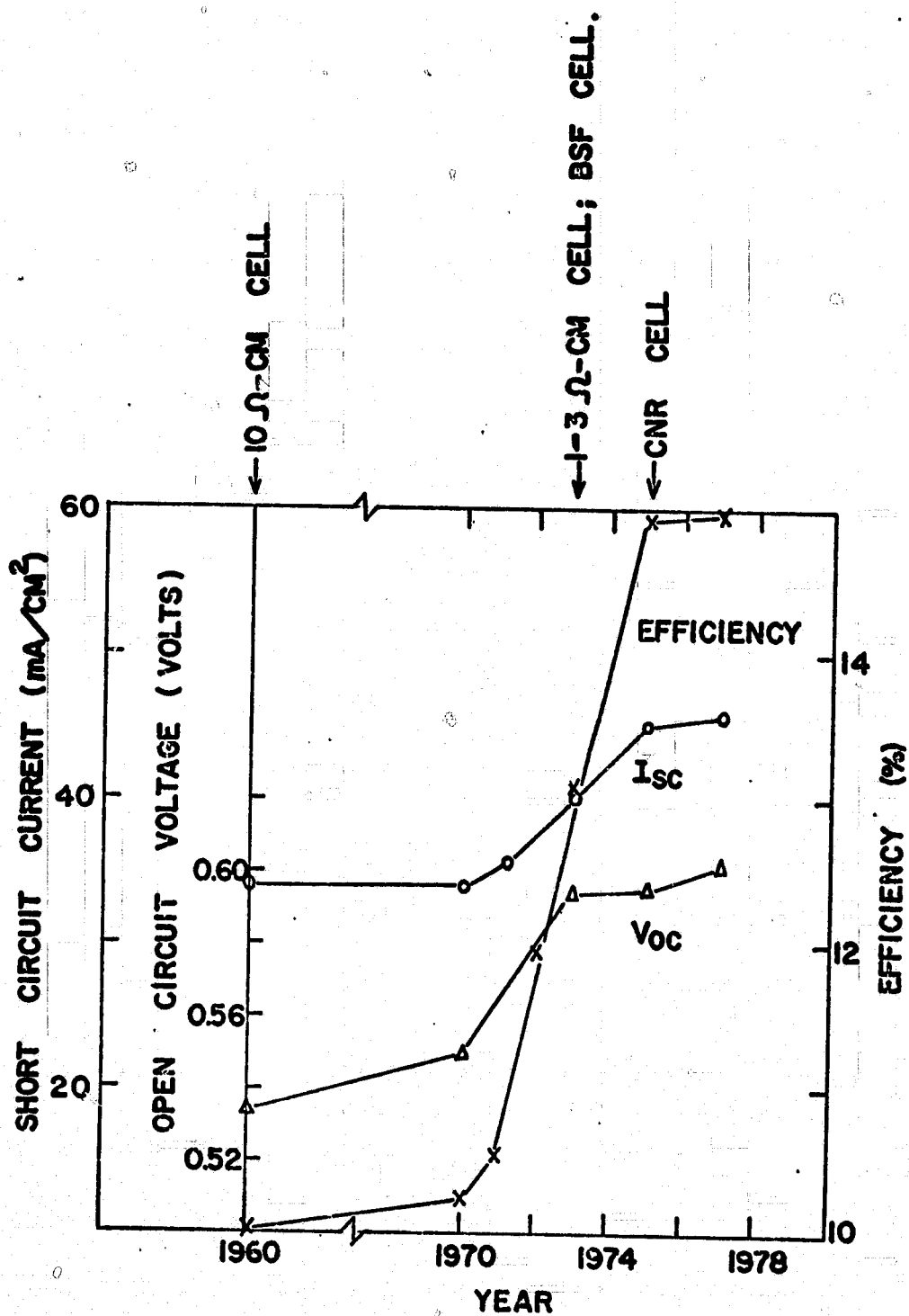
Figure 1.1. The historical development of silicon solar cells.

by a lower series resistance and lower saturation current density of a
low resistivity cell. Further improvements of the curve factor can
be obtained by using a low resistivity substrate and an improved design
of the collection junction and grid pattern.

1.3 The Major Characteristics of the Analytical Technique

The approach taken by the present analysis of solar cell operation
is a complete numerical solution of the semiconductor device equations.
This system of equations is quite well known, although it has been only
recently that solutions have been possible due to the advent of high
speed computers and computer oriented numerical techniques. These
equations include Poisson's equation, the hole and electron current
density equations, and the hole and electron continuity equations. Much
information regarding these equations is presented in the following
chapters of this report; however, some general remarks can be made as
to the generality and completeness of the operation which they describe.
It is known that the presence and interplay of both drift
and diffusion current components must be present in the
solution to allow for the appearance of such effects as high
injection and bulk resistance. This is possible through the use of the
general current density equations. The continuity equations include an
internal net recombination rate which plays a significant role in solar
cell operation. This phenomena is readily included through a selection
of a recombination model with empirical models for lifetime parameters
based on available experimental data. In a solar cell there is the
additional factor of an external generation rate due to the full spectrum
solar irradiance. This highly variable spatial factor is calculated

separately and then included point by point in the continuity equation through the external generation term. Thus the analysis does not start with an assumed optically generated short circuit current, but begins with the generation rate itself at each point within the device. This term has been calculated using the most current information available on spectral irradiance for various air mass conditions, antireflection films, and the relevant material properties for silicon. The inclusion of this term directly into the continuity equation avoids any a priori assumptions with respect to the collection efficiency in various regions of the device.

The surface region of contemporary solar cells is analytically quite complex. These regions are typically very heavily doped, diffused regions. The analysis includes an erfc or Gaussian impurity profile and the attendant electric fields due to this type of profile are thus included in the analysis through a spatially dependent impurity concentration in Poisson's equation. The doping of the surface region is usually high enough to cause significant heavy doping effects. Thus various models postulated for heavy doping effects are included within the solution.

Within the device equations themselves, there are several parameters such as mobility, lifetime, and diffusion coefficients which in a real device are not constant but vary with doping level and/or electrostatic potential variation. These variations must be included in an accurate analysis. Although not derived analytically, these variations are taken as empirical data from currently available measurements.

In general the analysis presented is quite free from the normal simplifying approximations made in semiconductor device analysis. A summary of the major features of the analysis include the following:

(a) Optical generation is calculated directly from available empirical measurements of a specific irradiance spectrum, including the effects of antireflection films and wavelength dependent absorption and index of refraction coefficients.

(b) The optically generated current is calculated directly from the interplay of the above generation rate and the device operation i.e. there are no assumptions pertaining to collection efficiency.

(c) Recombination is included within the analysis, not only for the bulk regions, but also for surface and depletion regions.

(d) Both drift and diffusion components of current flow are included. This allows the appearance of high injection effects, resistive loading, and the effects of any Dember type potentials.

(e) A diffused impurity profile is included in the surface region through an erfc or more complex impurity distribution.

(f) Band gap shrinkage due to heavy doping effects is included in the diffused surface region.

(g) A non-ohmic contact is included at the irradiated surface through a finite surface recombination velocity.

1.4 General Device Equations

The fundamental physical mechanisms in semiconductor device analysis such as the existence of space charge regions, drift and diffusion currents, and carrier recombination are contained in the general device equations. In one dimension, neglecting any magnetic or thermal gradients, these can be expressed as:

$$\frac{\partial E}{\partial x} = \frac{q}{\varepsilon} [p - n + N(x)], \tag{1.1}$$

$$E = -\frac{\partial \psi}{\partial x}, \tag{1.2}$$

$$J_n = q\mu_n nE + qD_n \frac{\partial n}{\partial x}, \tag{1.3}$$

$$J_p = q\mu_p pE - qD_p \frac{\partial p}{\partial x}, \tag{1.4}$$

$$\frac{\partial n}{\partial t} = U + G_e + \frac{1}{q}\frac{\partial J_n}{\partial x}, \tag{1.5}$$

$$\frac{\partial p}{\partial t} = U + G_e - \frac{1}{q}\frac{\partial J_p}{\partial x}. \tag{1.6}$$

These equations have general three dimensional forms; however, in this work only the one dimensional case has been considered. In the above equations, U is the internal net recombination-generation rate, G_e is any generation rate due to external physical processes, and the other terms take on their conventional meanings. The net ionized impurity doping is represented by $N(x)$ and can be a complicated function of x in that it can represent the doping profile in a diffused region plus the changeover from donor to acceptor doping as an n-p interface is crossed. Equations (1.1) and (1.2) are Poisson's equation and the

defining relationship between electrostatic potential ψ and electric field E. The current densities are expressed by Equations (1.3) and (1.4) and include both drift and diffusion terms for both species of carriers. Equations (1.5) and (1.6) are the continuity equations for holes and electrons. The internal net recombination rate of electron-hole pairs due to thermal processes as represented by U, is treated in greater detail in the following sections. Chapter 3 discusses the extensive analysis behind the development of the electron-hole pair generation due to external sources such as incident light as represented by the term G_e.

In addition to the above equations, several connecting expressions can be noted. For one, the Einstein relations can be used in relating the diffusion coefficient to mobility. For non-degenerate doping these can be expressed as:

$$D_{n,p} = \frac{kT}{q} \mu_{n,p}. \tag{1.7}$$

Another set of useful relationships can be obtained through a definition of quasi-Fermi potentials. In equilibrium the Fermi energy, E_f, can be defined from Boltzman statistics as follows:

$$n = n_i \exp\left[\frac{E_f - E_i}{kT}\right],$$

$$\tag{1.8}$$

$$p = n_i \exp\left[\frac{E_i - E_f}{kT}\right],$$

where E_i is the energy level corresponding to the center of the band gap. The electrostatic potential may be expressed as $\psi = -E_i/q$ and the Fermi potential as $\phi = -E_f/q$. In terms of these potentials, Equation (1.8) may be expressed as

$$n = n_i \exp\left[\frac{(\psi-\phi)}{kT}\right],$$

$$p = p_i \exp\left[\frac{q(\phi-\psi)}{kT}\right]. \tag{1.9}$$

In non-equilibrium conditions, the quasi-Fermi potentials, ϕ_n and ϕ_p, may then be defined from

$$n = n_i \exp\left[\frac{q(\psi-\phi_n)}{kT}\right],$$

$$p = n_i \exp\left[\frac{q(\phi_p-\psi)}{kT}\right]. \tag{1.10}$$

Note that under these conditions the np product is no longer necessarily equal to n_i^2; in fact,

$$np = n_i^2 \exp\left[\frac{q(\phi_p-\phi_n)}{kT}\right]. \tag{1.11}$$

This defines a quasi-equilibrium as that condition in which the np product remains constant although differing from its equilibrium value. Thus the difference in quasi-Fermi levels can be viewed as a measure of the amount of displacement from equilibrium.

The general set of six equations and six unknowns as expressed by Equations (1.1) thru (1.6) then represent all necessary phenomena for

solar cell analysis excluding of course variations in mobility, choice of recombination model, and external generation rate. For the complete analysis however this set of six equations can be reduced to a set of three coupled equations through the quasi-Fermi level and electric field definitions.

1.5 Organization of the Report

This report is divided into several major chapters. The first chapter is a simple introduction of a silicon solar cell and its current status of technology. The particular semiconductor transport equations which are of fundamental importance in solar cell type devices are also discussed. Chapter 2 presents the results of the detailed correlation between theory and experiment. The detailed comparisons have included the most important measurements such as photovoltaic I-V characteristics, dark I-V characteristics and spectral responses, etc. The simulations of violet and CNR cells are presented in Chapter 3. Chapter 4 discusses the temperature dependence of the short circuit current density. It is emphasized in this chapter that the temperature dependence of the absorption coefficient cannot be neglected in the calculation of short circuit current. Chapter 5 discusses the heavy doping effects and Keldysh-Franz effects in order to explain the low open circuit voltage in a highly doped cell. The characteristics of a thin silicon solar cell are presented in Chapter 6. The effects of the series resistance on concentrating solar cells are shown in Chapter 7. Due to the distortions of the input spectral intensities of a concentrator, the effects of non-uniform illumination

in limiting solar cell conversion efficiency are discussed in Chapter 8.
Chapter 9 presents calculations for a recently proposed high-low
junction emitter solar cell. Finally, appendices 10 is divided into
five sections. Appendix 10.1 discusses the detailed comparison of
theoretical and experimental solar cell performance. Appendix 10.2
presents a two dimensional analysis of sheet resistance and contact
resistance effects in solar cells. Appendix 10.3 discusses impurity
gradients and high efficiency solar cells. A detailed two-dimensional
model of a solar cell is presented in Appendix 10.4. Finally,
Appendix 10.5 discusses the fill factor and diode factor of a solar cell.

1. R. A. Ardt, J. F. Allison, J. G. Haynos and A. Meulenberg. 1975.
    Optical properties of the COMSAT non-reflection cell. Eleventh
    Photovoltaic Specialists Conference, Scottsdale, AZ. 40-43.

2. G. L. Pearson, etc. The Bell solar battery. 1954. Bell Lab.
    Record 32(6): 232-233.

3. P. M. Dunbar and J. R. Hauser. 1975. Efficiency of silicon solar
    cells as a function of a base layer resistivity. Proc. Eleventh
    IEEE Photovoltaic Spec. Conf., Scottsdale, AZ. 13-18.

4. J. G. Fossum. 1976. Computer-aided numerical analysis of silicon
    solar cells. Solid State Electronics 19: 269-278.

2. BASIC SOLAR CELL CHARACTERISTICS AND DEVICE PARAMETERS

Since the discovery of metal-semiconductor non-ohmic behavior the rectifying effects between metal-semiconductor and semiconductor-semiconductor contacts have received a great deal of attention. In 1949 Shockley proposed the modern p-n junction theory which established the important role of minority carrier density and its exponential behavior across the junction barrier [1]. The transport equations for minority carriers are particularly simple for low injection and uniform doped semiconductor regions. The minority carrier current density can be expressed as

$$J = J_s[\exp(qV/nkT)-1],$$ (2.1)

$$J_s = q[\frac{n_{po}}{\tau_n} L_n + \frac{p_{no}}{\tau_p} L_p],$$

where the saturation current density J_s is a function of semiconductor parameters on both sides of the junction, and $n = 1$. Departures from Shockley's simple I-V characteristic are usually observed in silicon at room temperature and further evolutions of the p-n junction theory have modified and extended Shockley's theory [2-5].

In all silicon p-n junctions, several current transport mechanisms may exist simultaneously. The diffusion current density which is due to the injection of minority carrier over the junction barrier is, of course, the most important. Other mechanisms include recombination current within the depletion region [2], tunneling through the band-gap for highly doped semiconductors [5] and high injection effects for high resistivity semiconductors at large forward bias voltages [3,4].

In addition to these fundamental limitations there are several other current mechanisms which are due to improper fabrication processes and/or material imperfections. Especially important are the series resistance and any shunting resistance. Fortunately these can be minimized by using good contact metals, grid patterns and proper sintering treatments.

In general, the departures from the simple diffusion theory always lead to poor rectification in diodes and poor curve factors and low open circuit voltages in solar cell application. Figure 2.1 shows the ideal I-V characteristics and some of the modifications at forward bias voltages. As can be seen in the figure, the simple Shockley diffusion current has a diode n factor of 1 for all bias voltages. The space charge recombination current has an n factor of 2. Such an n factor may also be found at high currents caused by high injection. An abnormally large n value may be found in some devices at small voltages which is caused by small shunting resistances. An n factor of 2 may also be present at high voltages and caused by a high sheet resistance. Curves (c) and (e) of Figure 2.1 show examples of these effects.

The dark I-V characteristics of a solar cell are as important as the short circuit photocurrent in determining the efficiency and power output. The components of the dark I-V characteristics described above are discussed in detail in the following sections.

a. Simple diffusion current
b. Space charge current
c. Shunting leakage current
d. Modified by contact resistance
e. High injection or modified surface sheet resistance
f. Modified by combined contact and sheet resistance.
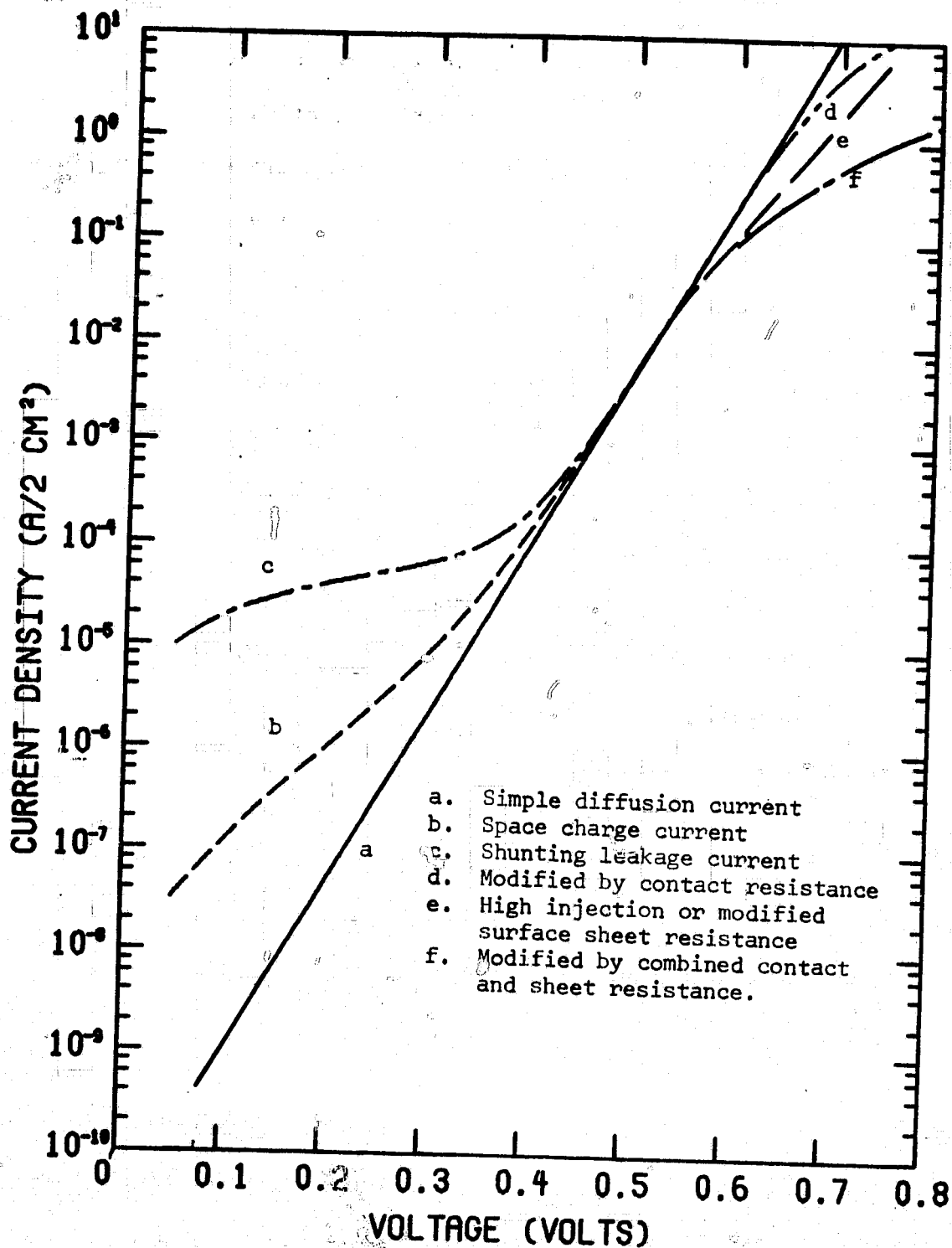
Figure 2.1. Prototype of the dark I-V characteristics of a solar cell.

2.1 Simple Diffusion Current

The current density for minority carriers in Shockley's model is

$$J = J_s[\exp(qV/kT)-1], \tag{2.2}$$

where the saturation current density J_s is a function of semiconductor parameters and the appropriate boundary conditions. First order analytical expressions for J_s have been compiled in Hovel's book [6] for several models with different boundary conditions.

2.2 Space Charge Recombination Current

The generation-recombination current of the Sah-Noyce-Shockley model is given by Equation 2.3 which assumes that the recombination is through a center located in the vicinity of the center of the bandgap.

$$J_\gamma = q_o \int^{W_d} \frac{pn-n_i^2}{\tau_{po}(n+n_1)+\tau_{no}(p+p_1)} dx$$

$$\simeq \frac{qn_i^2 W_d[\exp(qV/kT)-1]}{(\tau_{po}n_1+\tau_{no}p_1)+(\tau_{po}+\tau_{no})n_i\exp(qV/2kT)}, \tag{2.3}$$

$$\simeq \frac{qn_iW_d}{\tau_{po}+\tau_{no}} \exp(qV/2kT) \text{ for medium voltages.}$$

It is clear that for a silicon p-n junction the space charge recombination current has a diode n factor of two at medium voltages and at room temperature.

2.3 High Injection Current

High injection occurs when the minority carrier density on one side of the junction becomes comparable with the majority carrier density. The calculation of the high injection current indicates an $\exp(qV/2kT)$

behavior [7]. High injection is likely to occur for low base doping densities near the junction or for silicon solar cells operating in multi-sun environments. For normal silicon solar cells with resistivities in the range of 10 $\Omega \cdot$ cm to 0.1 $\Omega \cdot$ cm which operate under one sun power intensity, high injection is unlikely to occur.

2.4 Tunneling Current

A tunneling current may exist in heavily doped junctions with a resistivity of less than 0.01 $\Omega \cdot$ cm. The tunneling current takes the form [8]

$$J_T = KN_T \exp(\beta V) \qquad (2.4)$$

where N_T is the density of energy states available for an electron or hole to tunnel into, and K and β are functions of semiconductor parameters. The n factor for tunneling currents lies between 1.3 and 2 at room temperature [8].

2.5 Leakage Current

Since a solar cell is a relatively large area device, there is a great chance of a leakage channel existing through the imperfect junction, especially under the metal contact [9]. The leakage current can be modeled by a shunting resistor R_{ST} across the junction and the current form is quite simple

$$I_{ST} = \frac{V_1}{R_{ST}} . \qquad (2.5)$$

Where V_j is the junction voltage at the imperfection location. As a result of this leaky current, the diode n factor may be very high with values of 3 to 5 usually being observed at voltages of less than 0.4 volts.

2.6 Current Voltage Characteristics Modified by Series Resistance

Series resistance becomes important as the current density increases and/or junction depth decreases. The series resistance comes from two sources: the surface sheet resistance and the metal-semiconductor contact resistance. For the contact resistance R_c which appears in series with the cell, the exponential dependence of current on voltage can be modified by replacing V in the exponential with $V-R_c I$. For the sheet resistance, however, the two dimensional distributed nature of the current flow does not allow one to define a purely lumped resistance. In this case at large currents the equation becomes,[+]

$$I = \sqrt{AJ_s I_T} \exp(qV/2kT),$$ (2.6)

$$I_T = \frac{2kT}{q} \frac{h^2}{\rho_{ST}} \cdot \frac{1}{A},$$ (2.7)

where A is the total area of the solar cell, J_s is the saturation current density of the simple diffusion theory, ρ_{ST} is the surface sheet resistance and h is the total perimeter of the contact grid pattern.

The parameter I_T has the physical significance that it is the current level at which the characteristic makes a transition from an $\exp(qV/kT)$ dependence to an $\exp(qV/2kT)$ dependence. In a practical

[+] This effect is very similar to current crowding which occurs in bipolar transistors. A discussion is contained in Appendix 10.2.

silicon solar cell both sheet resistance and contact resistance may exist simultaneously and the diode n factor may be as high as 5 at voltages greater than 0.5 volts. In this combined case one cannot model the cell correctly by a lumped constant resistance.

2.7 Parameters for Device Model

2.7.1 Diffusion Length and Lifetime

The lifetimes of electrons and holes are of great importance in understanding the electrical and optical behavior of a semiconductor device. For indirect bandgap semiconductors such as silicon, the carrier lifetime is generally high and basically determined by recombination through intermediate centers within the bandgap instead of direct band-to-band recombination. The minority carrier lifetime has been developed by assuming a single Shockley-Read center as [10]

$$\tau_p = \frac{1}{\sigma_p V_{th} N_R} [(1 + \frac{N_C}{n_{no}} \exp[-(E_C - E_R)/kT]) + \frac{\sigma_p}{\sigma_n} \frac{N_V}{n_{no}} \exp[-(E_R - E_V)kT]],$$

$$(2.8)$$

where τ_p = hole lifetime in an n-type semiconductor with doping density N_{no}, N_R = density of recombination centers, σ_p, σ_n = hole and electron capture coefficients. A similar form can be written for electrons in p-type material. Equation 2.8 indicates that the minority carrier lifetime is lower in general for a higher doping density. This behavior of minority carrier lifetime with doping density has been experimentally observed [11,12].

Some representative curves of measured diffusion lengths as a function of doping density are shown in Figure 2.2 [11]. Comparisons
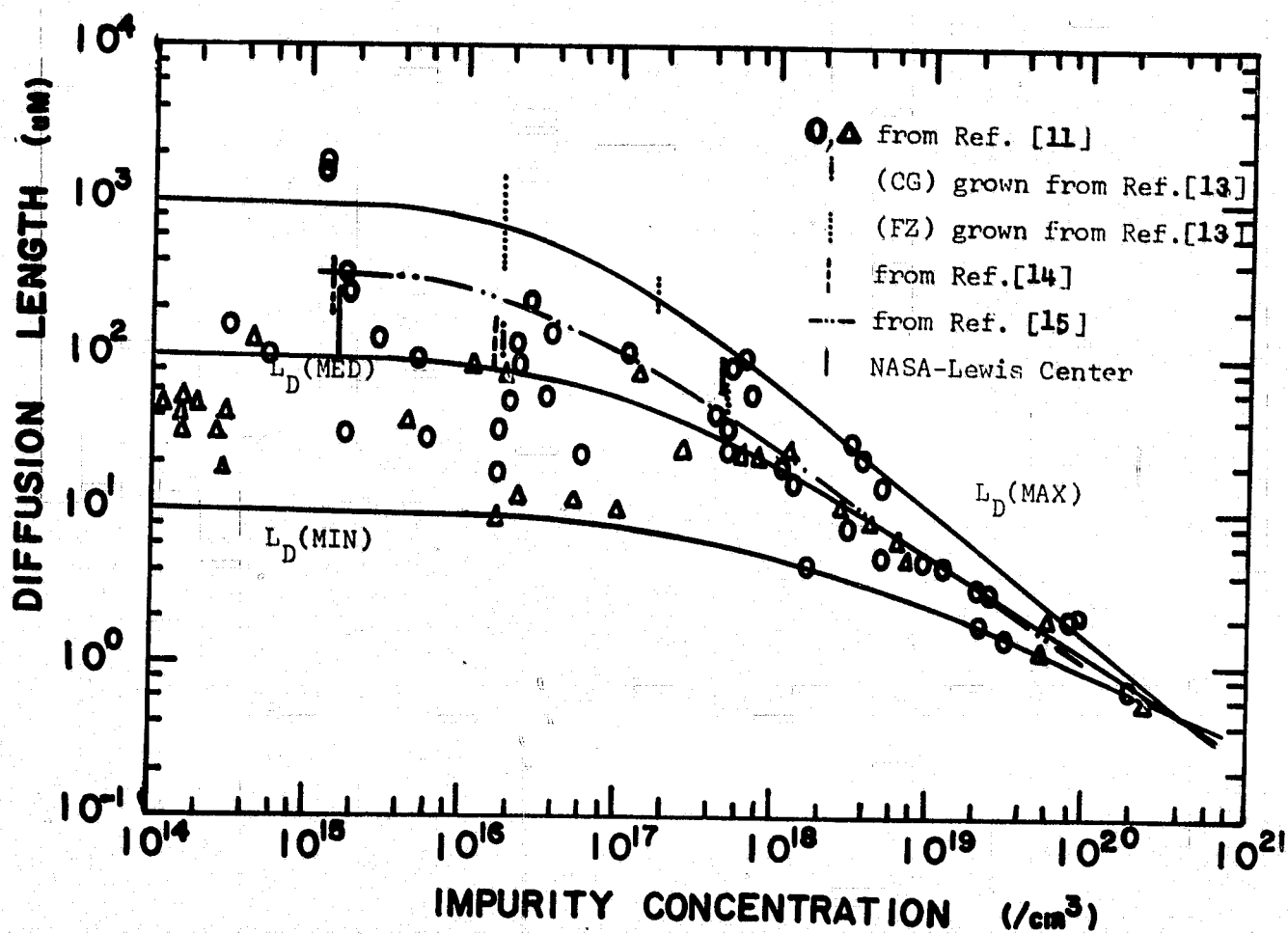
Figure 2.2. Model of the diffusion length and comparison to the experimental data. All experimental data are for p-type material except those marked by the triangle.

to other experimental data are also shown on the same graph [11-15].
At high doping densities band-to-band Auger recombination may become
the dominant recombination process. This gives a decreasing life-
time which is inversely proportional to the square of the doping
density. The experimental curve of L_D(MAX) in Figure 2.2 has a life-
time dependence on doping density with an exponent of -1.7 at doping
densities greater than $10^{17}/cm^3$. This value is close to the
theoretical band-to-band Auger lifetime model which has an exponent
of -2.

Hence it is a fairly good approximation to define L_D(MAX) and
L_D(MED) of Figure 2.2 as the upper and lower bounds for electron
diffusion length in p-type silicon. Similarly L_D(MED) and L_D(MIN)
of Figure 3.1 could be considered as upper and lower bounds for hole
diffusion length in n-type silicon because of the lower hole mobility.
In a practical silicon solar cell, the actual diffusion length may
vary between some upper and lower bound depending on the material
perfection and the fabrication processes. In a solar cell the density
of recombination centers is generally much smaller than the doping
density; hence, the majority carrier lifetime equals that of the
minority carriers [16].

Although the diffusion length data of Figure 2.2 was measured in
bulk material, it is assumed valid for the shallow diffused layer of
solar cells. If the lifetime is a function of total doping density
only, such as in the Auger process, this will be a good approximation.
However, this may not be valid if lifetime is dominated by deep level
impurity recombination.

2.7.2 Surface Recombination Velocity

In addition to bulk recombination, surface recombination is
another loss mechanism which is modeled by a surface recombination
velocity S. The minority carrier current flow toward the surface is
given as

$$J_s = q\Delta p_s S, \tag{2.9}$$

where Δp_s is the surface excess minority carrier density.

The value of S is basically determined by surface conditions such
as the density of interface states, any anti-reflection oxide layer and
surface treatments. Very low S values of 10^2 cm/sec can probably be
achieved only through the use of high temperature oxidation processes
which may cause a drive-in of the surface diffused layer and may not
be compatible with solar cell technology [17]. Hence, a value of
10^3 cm/sec may be a lower limit for SRV of typical oxide coated solar
cells [18,19].

2.7.3 Diffusion Doping Profile

It has been found that shallow diffusions (≤ 1 µm) of phosphorous
in silicon result in considerable deviations from the simple diffusion
theory of an erfc function [20,21]. For short diffusion times
(≤ 1 hr) and temperature below 1100°C, it has been found that a constant
concentration layer exists near the surface of about 1/3 ∿ 1/4 of the
junction depth and the electrical active phosphorous concentration in
this layer is about half of the solid solubility limit at the particular
diffusion temperature. Beyond the constant concentration region, the
diffusion profile can be reasonably well represented by a complementary

error function. One of the typical diffusion profiles is reproduced here in Figure 2.3 [21]. The parameters which characterize this particular diffusion profile are the surface doping density C_s, width of the constant doping layer X_c and the doping density C_B at the boundary of the constant doping and the erfc doping profile.

2.7.4 Mobility

Two major contributions to mobility are phonon scattering and impurity scattering. These effects make mobilities a function of doping density, temperature and internal electric field intensity. The general empirical equation developed by Gummel [22] was used in this work.

$$(\frac{\mu_o}{\mu})^2 = 1 + \frac{N_D}{\frac{N_D}{S} + N} + \frac{(E/A)^2}{E/A + F} + (\frac{E}{B})^2 \qquad (2.10)$$

This equation has been confirmed by measuring the relations between drift velocity and electric field [23].

2.7.5 Heavy Doping Effects

Heavy doping phenomena occurs in silicon for total doping densities above about $10^{19}/cm^3$. The high doping effect on minority carriers can be represented by a bandgap reduction where the empirical expression of Equation 2.11 has been used in this work.

$$\Delta E_G = -0.45\sqrt{N/(10^{21}cm^{-3})} \quad (eV), \qquad (2.11)$$

In this expression, N is the net doping density.
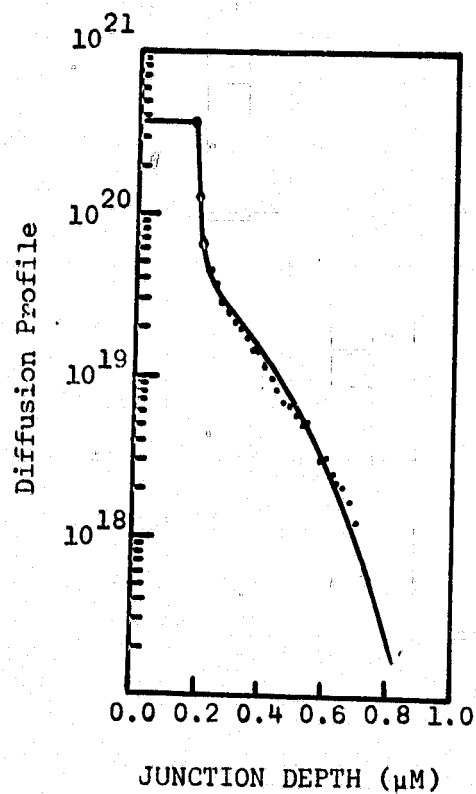
Figure 2.3. One sample of the shallow phosphorous diffused profile at 900°C. Ref. [21]

2.7.6 Absorption Coefficient

The ability of a semiconductor to absorb light of a given wave-
length is characterized by the absorption coefficient α. Values of the
absorption constant α were taken from Dash and Newman [24] up to about
0.95 μm wavelength. At wavelengths above 0.95 μm there is considerable
variation in the reported absorption coefficient values. Several
reported values at 0.95 μm, 1.0 μm and 1.1 μm are shown in Table 2.1
[24-29]. The data of Dash and Newman is seen to be larger than most
of the reported data at 0.95 μm and 1.0 μm. Good agreement in the long
wavelength spectral response of solar cells could not be obtained by
using the data of Dash and Newman. Best results have been obtained
by using the values of the last line which are intermediate between the
largest and smallest reported experimental values. Thus the absorption
data which has been used is that of Dash and Newman with the data at
0.95 μm, 1.0 μm and 1.1 μm modified to the values of Table 2.1. The
index of refraction as a function of incident wavelength was taken from
Phillip (1972) [30].

Table 2.1 Comparison of reported absorption coefficient values at long
wavelengths

		1.1 μm	1.0 μm	0.95 μm
		Absorption Coefficient (cm^{-1})		
[24]	Dash & Newman	7	100	220
[25]	Vedam	-	-	270
[26]	Runyan	-	67	170
[27]	Vol'fson & Subashiev	-	64	150
[28]	Macfarlon	3.9	61	-
This work		3.9	74	204

2.7.7 Spectral Response

The spectral sensitivity of a solar cell to incident photons is measured by the spectral response or the quantum yield. For a practical solar cell the quantum yield is always less than unity because of surface reflection losses and internal recombination losses.

Internal quantum yield can be defined as the ratio of the collected short circuit current density to the input current density which is generated by the incident photons assuming 100 percent transmission through the surface, i.e.

$$QY(\lambda) = \frac{I_{SC}(\lambda)}{qF(\lambda)(1-R(\lambda)-A(\lambda))(1-e^{-W_d\alpha(\lambda)})}, \qquad (2.12)$$

where $F(\lambda)$ = incident photon flux (proportional to input power density),

$R(\lambda)$ = reflection at surface,

$A(\lambda)$ = absorption in AR layer if any,

W_d = device thickness.

Another practical parameter is the external quantum yield $QY_{ext}(\lambda)$ which includes losses due to surface reflection and antireflecting layer absorption:

$$QY_{ext}(\lambda) = \frac{I_{sc}(\lambda)}{qF(\lambda)(1-e^{-W_d\alpha(\lambda)})} \qquad (2.13)$$

The spectral response is represented by the ratio of collected current to input power density as:

$$SR_{ext}(\lambda) = \frac{I_{SC}(\lambda)}{P_{input}}. \qquad (2.14)$$

The spectral response theory of Prince and Wolf [31] shows that the overall spectral responses can be considered as made up of somewhat independent responses from the surface and base layers. Hence it is sometimes useful to specify the spectral response from the surface region, depletion region and base region respectively as

$$SR_{ext}(\lambda) = SR_{ext}(\lambda, \text{surface}) + SR_{ext}(\lambda, \text{depletion}) + SR_{ext}(\lambda, \text{base}). \quad (2.15)$$

Some of the parameters and results of the spectral response analysis are shown in Table 2.2.

The calculated reflectance R in Table 2.2 is in direct agreement with Phillips data of oxide free silicon [30], although it is well known that a thin layer of oxide of about 20 $\sim$ 35Å in thickness may be grown on an exposed bare silicon surface. The correction on R due to such a layer is less than 1 percent for photon wavelengths of 0.4 to 1.0 micrometer (This also agrees with Ref. [30].).

For Tantalum oxide calculations, a reflection index of 2.20 was used which is based upon ellipsometry measurements performed at a wavelength of 5461Å [32]. This value of reflection index is in general agreement with reported literature values [33].

The calculated transmission and reflection coefficients for Ta_2O_5 are shown in Figure 2.4. The data indicates a much better surface efficiency at short wavelengths as compared to a bare Si, SiO or SiO_2 coated surface. Since the AM0 power spectrum peaks between 0.4 μm and 0.6 μm, Ta_2O_5 is superior to the other oxides studied.

Table 2.2. Parameters for spectral response calculation at various wavelengths.

λ	0.4	0.45	0.5	0.6	0.7	0.8	0.9	0.95	1.0
Absorption Coeff. (cm^{-1})	8.70E4	2.62E4	1.23E4	4.56E3	2.10E3	9.64E2	3.67E2	2.04E2	7.42E1
Photon Energy (eV)	3.09	2.75	2.47	2.06	1.77	1.54	1.37	1.30	1.24
Transmission for Bare Si	0.521	0.583	0.615	0.647	0.663	0.672	0.679	0.681	0.683
Reflection for Bare Si	0.478	0.416	0.384	0.352	0.336	0.327	0.318	0.318	0.316
INPUT POWER (mW)	10	10	10	10	10	10	10	10	10
Surface Rate $(\#/cm^2)$	9.15E20	3.47E20	1.91E20	8.91E19	4.91E19	2.61E19	1.13E19	6.65E18	2.55E18
INCIDENT CURRENT (mA/cm^2)	3.226	3.629	4.032	4.839	5.646	6.452	7.259	7.662	8.065
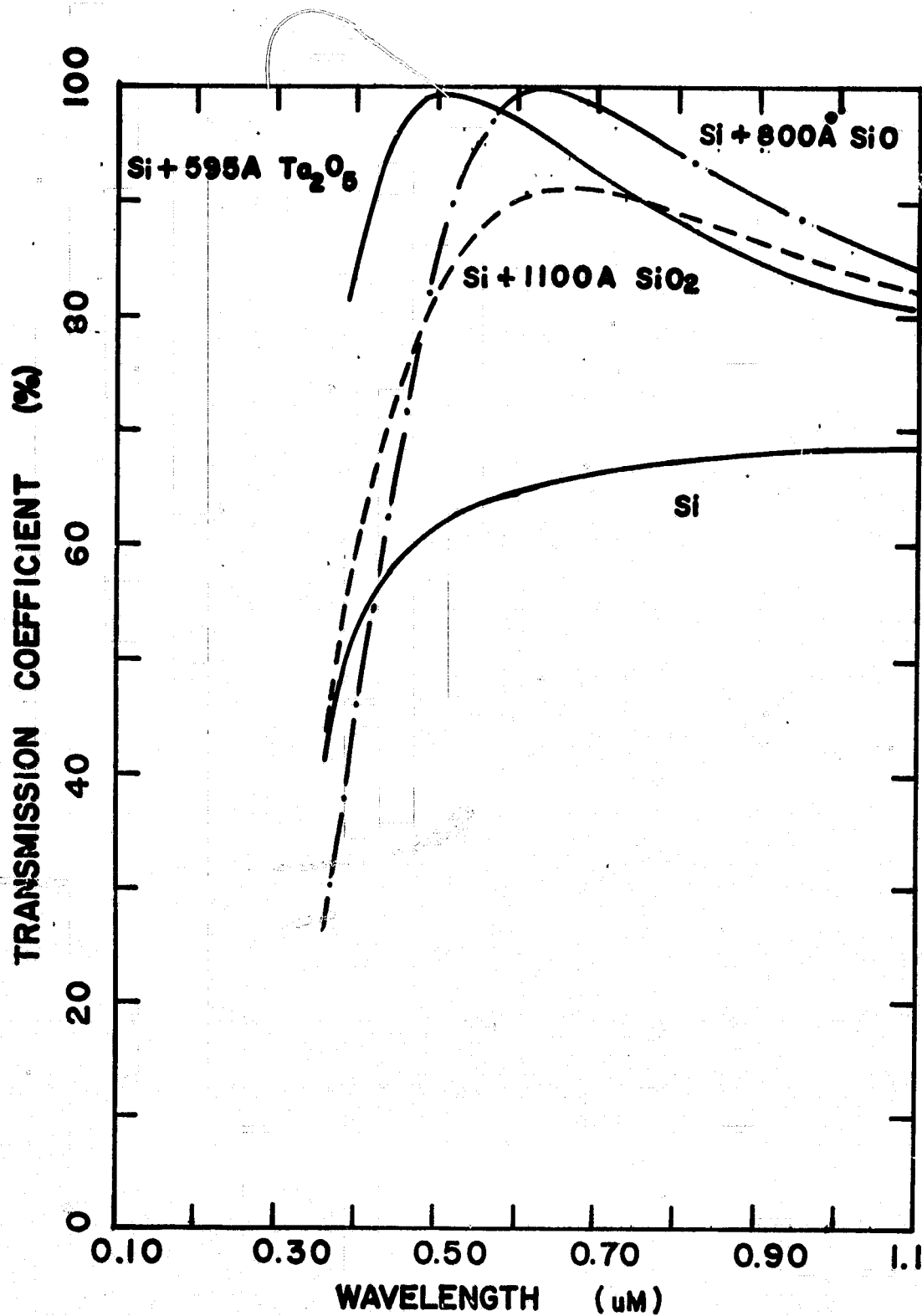
Figure 2.4.   Transmission coefficients for bare and anti-reflection film
           coated silicon surfaces at wavelength 0.35 μm to 1.1 μm.

2.7.8 General Comparison of Theoretical and Experimental Results

The solar cells which have been studied can be broadly divided into three categories based upon the origin of the bulk material and the cell design. The first category consists of n^+p cells on 0.1 $\Omega \cdot$ cm base layers with a finished thickness of about 6 mils. The second category consists of n^+p cells on 10 $\Omega \cdot$ cm base layers with thicknesses of about 10.5 mils. Both types of cells were made in a standard 2 cm^2 area and use a NASA Lewis Research Center 10-finger grid. No anti-reflection layers were present on the silicon surface.

The third type of cell is the Aluminum BSF cell on 16 $\Omega \cdot$ cm substrates with a finished cell thickness of about 6.5 mils. These cells have a Ta_2O_5 coating about 595Å in thickness and a 5 mil "Teflon" FEP cover on the Tantalum Pentoxide. On these the nine finger grid pattern of Spectro Lab was present.

The n-type surface layers were phosphorous diffusion, using $POCl_3$ at the NASA Lewis Research Center. The temperature and the duration of the diffusion process are described for each type of cell in the following sections. The top and bottom contacts were made using metal masks and by evaporating a thin layer of Aluminum (200∿500Å) followed by the evaporation of about 3 to 5 micrometers of silver on the surface. The contacts were then sintered at temperatures of 550 to 650°C in H_2.

Al-Ag contacts have been found to have less degradation in the cell electrical characteristics than that which occurs for sintered Ag-Ti contacts, although Ti makes a better ohmic contact than Al. For BSF

cells the Aluminum was alloyed at about 800°C for one hour or less and

this produced a high-low junction of 0.5 to 1.0 μm in depth [34].

The detailed comparison of the theoretical and experimental results are

shown as Appendix 10.1 and 10.2.

1. W. Shockley. 1949. The theory of p-n junctions in Semiconductors and p-n junction transistor. Bell Syst. Tech. J. 28: 435.

2. C. T. Sah, R. N. Noyce and W. Shockley. 1957. Carrier generation and recombination in p-n junctions and p-n junction characteristics. Proc. IRE 45: 1228.

3. W. M. Webster. 1954. On the variation of junction-transistor current-amplification factor with emitter current. Proc. IRE 42: 914-920.

4. E. S. Rittner. 1954. Extension of the theory of the junction transistor. Phys. Rev. 94: 1161-1171.

5. L. Esaki. 1958. New phenomenon in narrow germanium p-n junction. Phys. Rev. 109: 603.

6. H. J. Hovel. 1975. Solar Cells. Semiconductor and Semimetals 11. Academic Press, New York.

7. J. R. Hauser. 1968. Fundamentals of Silicon Integrated Device Technology II, Prentice Hall, New Jersey.

8. A. G. Milnes and D. L. Feucht. 1972. Heterojunctions and Metal-Semiconductor Junctions. Academic Press, New York.

9. R. J. Stirn. 1972. Junction characteristics of silicon solar cells. Ninth Photovoltaic Specialists Conference, Silver Spring, Maryland: 72-82.

10. A. S. Grove. 1967. Physics and Technology of Semiconductor Devices. John Wiley, New York.

11. P. A. Iles and S. I. Soclof. 1973. Effect of impurity doping concentration on solar cell output. Tenth Photovoltaic Specialists Conference, Palo Alto, CA: 19-24.

12. D. Kendall. 1969. Conf. Physics and Application of Lithium Diffused Silicon. NASA-Goddard Space Flight Center.

13. H. Fisher and W. Pschunder. 1973. Impact of material and junction properties on silicon solar cell efficiency. Tenth Photovoltaic Specialists Conference, Palo Alto, CA: 404.

14. M. Wolf. 1971. A new look at silicon solar cell performance. Energy Conv. 11: 63-73.

15. E. S. Rittner. 1977. Improved theory of the silicon p-n junction solar cell. Journal of Energy 1(1): 9-17.

16. A. Rose. 1957. Lifetimes of free electrons and holes in solids.[34] Progress in Semiconductor, John Wiley: 109.

17. C. A. T. Salama and F. Holmes. 1970. On the determination of surface recombination velocity from the transient response of MIS structure. Solid State Electronics 13: 1204-1206.

18. H. W. Brandhorst, Jr. 1975. Current status of silicon solar cell technology. NASA Technical memorandum, NASA TM X-71828.

19. M. Wolf. 1972. Solar cell - outlook for improved efficiency. National Academy of Sciences, Washington, DC.

20. E. Tannenbaum. 1961. Detailed analysis of thin phosphorous diffused layers in p-type silicon. Solid State Electronics 2: 123.

21. J. C. C. Tsai. 1969. Shallow phosphorus diffusion profiles in silicon. Proc. IEEE 57(9): 1499-1506.

22. D. L. Scharfetter and H. K. Gummel. 1969. Large signal analysis of a silicon Read diode oscillator. IEEE Trans. on ED-16: 64.

23. M. Sze. 1969. Physics of Semiconductor Device. John Wiley and Sons, Inc., New York.

24. W. C. Dash and R. Newman. 1955. Intrinsic optical absorption single crystal germanium and silicon at 77°K and 300°K. Phys. Rev. 99 (4): 1151.

25. K. Vedam. 1969. JPL Contract No. 952385. (Unpublished)

26. W. R. Runyan. 1969. Final Report, NASA-Grant No. NGR 44-007-016. (Unpublished)

27. A. A. Vol'fson and V. K. Subashiev. 1967. Sov. Phys.-Semicond. 1: 327.

28. G. G. MacFarlon, T. P. McLean, J. E. Quarrington and V. Roberts. 1958. Fine structure in the absorption-edge spectrum of silicon. Phys. Rev. 111: 1245-1254.

29. J. H. Reynolds and A. Meulenberg, Jr. 1974. Measurement of diffusion length in solar cell. Journal of Applied Physics 45: 2582-2592.

30. H. R. Phillip. 1972. Influence of oxide layers on the determination of the optical properties of silicon. Journal of Applied Physics 43(6): 2835-2839.

31. M. B. Prince and M. Wolf. 1958. New developments in silicon photovoltaic devices. Journal of British IRE 18: 583-593.

32. A. G. Reversz, J. H. Reynolds and J. F. Allison. 1976. Optical properties of tantalum oxide films on silicon. J. Electrochem. Soc. 123(6): 889-894.

33. W. H. Knausenberger and R. N. Tauber. 1973. Selected properties of pyrolytic Ta_2O_5 films. Journal of Electrochem. Society 120(7): 927.

34. J. Mandelkorn, T. H. Lamneck and L. R. Scudder. 1973. Design, fabrication and characteristics of new types of back surface field cells. Tenth Photovoltaic Specialists Conference, Palo Alto, CA.

3. HIGH EFFICIENCY SILICON SOLAR CELLS

3.1 Introduction

Although silicon solar cells were first made during the mid-fifties, several important technological breakthroughs were not achieved until recent years. During this time, improvements in solar cell technology have lead to the production of high efficiency silicon solar cells. Higher efficiency of a silicon solar cell has been mainly achieved by increasing the output voltage and/or short circuit current density.

The discovery of the back surface field concept raised the output voltage of a lightly doped solar cell in 1973 [1]. Then the violet cell, which utilizes a very shallow junction, fine grid and improved anti-reflection film to enhance the optical responses of short wavelength photons, was introduced to produce higher short circuit current density [2]. Later this cell was further improved by preferentially etching to give a serrated surface and higher surface efficiency was achieved. This novel cell was named a CNR (COMSAT non-reflective) cell due to the non-reflecting properties of the serrated surface [3]. Calculations of a CNR cell are difficult because the incident light is not in a normal direction to the cell surface and several reflections and refractions usually occur on the serrated surface.

It is the purpose of this section to model these high efficiency solar cells including the violet and CNR cells. It is also shown that the limitation to cell efficiency due to the surface optical efficiency can be predicted from the calculations.

3.2 Optical Reflection and Transmission

Traditional solar cells have a flat polished surface and normal illumination can be assumed. In this case the surface reflection and transmission can be straightforwardly calculated. However, the calculation for oblique illumination is far more difficult. A brief review is outlined in Appendix (A).

In a CNR cell, light illuminates normally at the serrated surface where it strikes the face of a pyramid at an angle of 54.75°. The reflected rays then strike the face of an adjacent pyramid at a smaller angle of 15.75° as shown in Figure 3.1. It is known that the reflected light will be elliptically polarized whenever the incident angle is other than the normal direction. Also, the Fresnel reflection coefficient is different for TE or TM polarized light. Therefore, the total surface reflection and transmission coefficient must be deduced by the superpositions of the decomposed TE and TM components of the incident light which is assumed here to be uniformly polarized.

Figure 3.2 shows the surface transmission coefficients of the incident light with angles of 54.75° and 15.75° for TE and TM modes respectively. The refractive index of silicon is taken from reference [4] and is shown in Figure 3.3. The calculated surface transmission coefficients of the violet and CNR cell with and without anti-reflection films are shown in Figure 3.4 and Figure 3.5 along with reported experimental values. The comparison to the reported values is very good which substantiates the above calculations [3,5]. Although the comparisons are not satisfactory for wavelengths greater than 1.0 μm, there

are several other reported values which do follow the calculations in
these wavelength ranges [6-8]. Several calculated surface optical
properties are shown in Table 3.1 and Table 3.2.
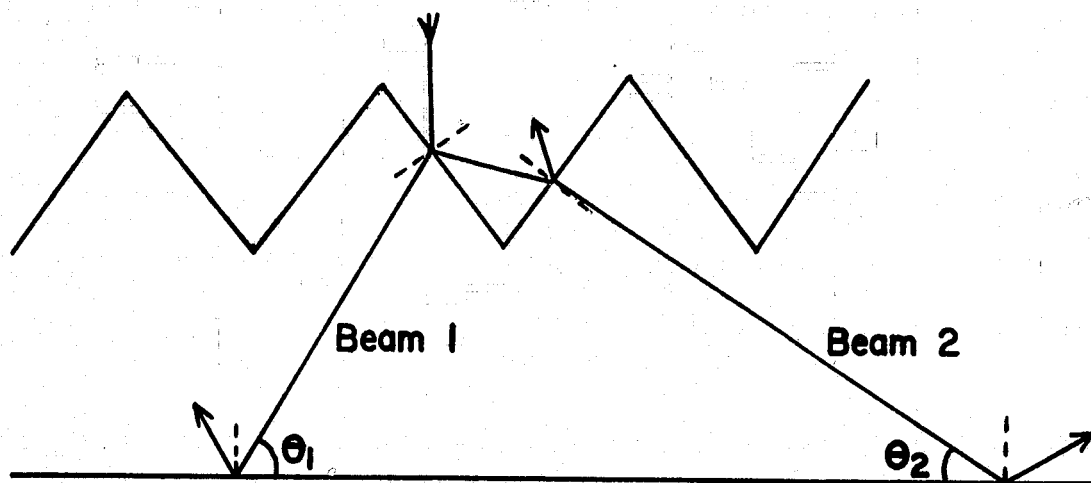
Figure 3.1. The serrated surface of a CNR cell.

The optimum thicknesses of Ta_2O_5 are found to be about 600Å and
700Å for a solar cell under AMO and AM2 solar spectrums respectively.
A solar cell under an AM2 solar spectrum has a higher optimum thickness
of anti-reflection films. This is because the AM2 spectral intensity
peaks at higher wavelengths. The average surface reflection losses
weighted to the AMO spectral density are about 3.5 percent for a 600Å
thickness of Ta_2O_5. This value is very close to the reported value of
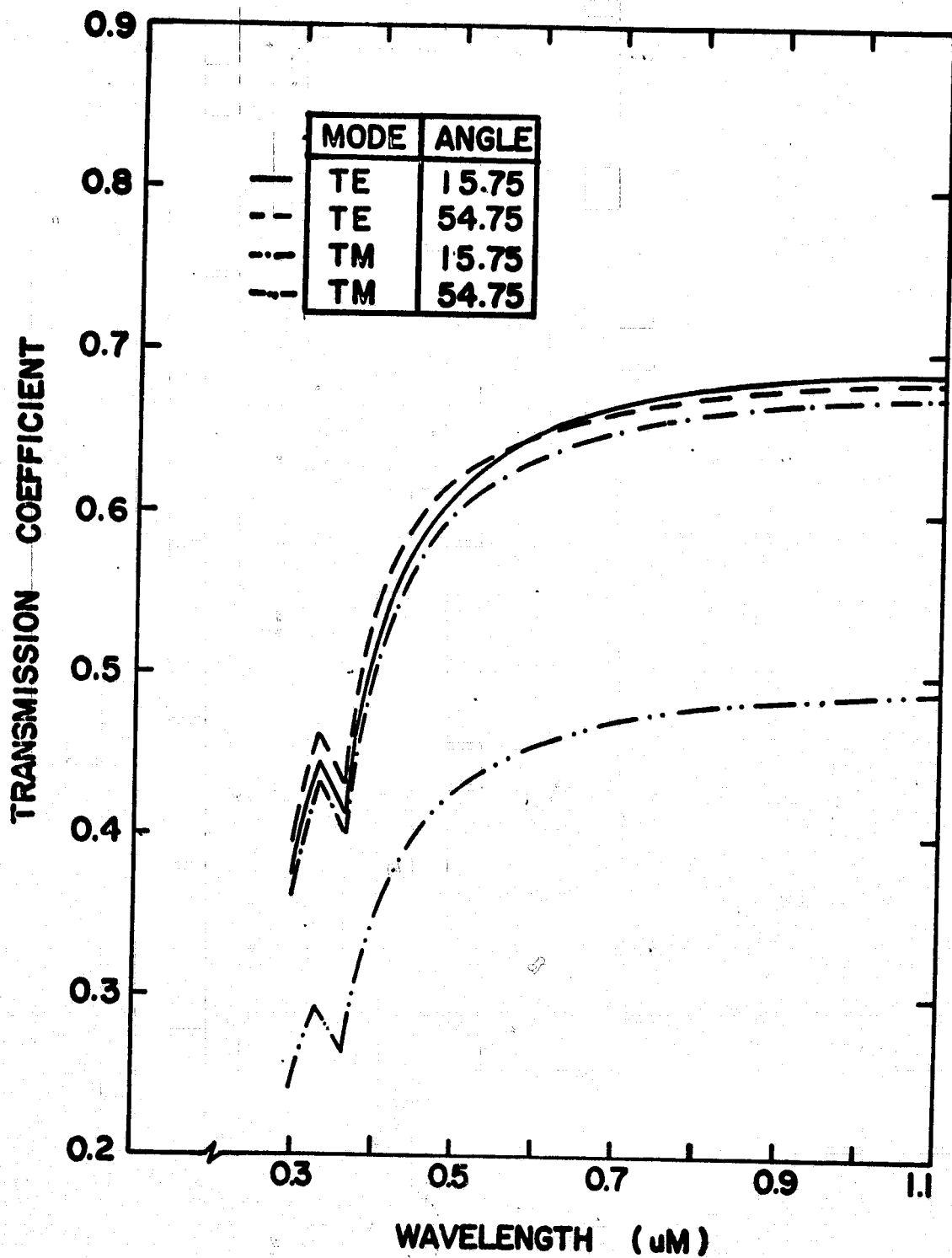
Figure 3.2. The Oblique Surface Transmission Coefficient at a Bare Silicon Surface.
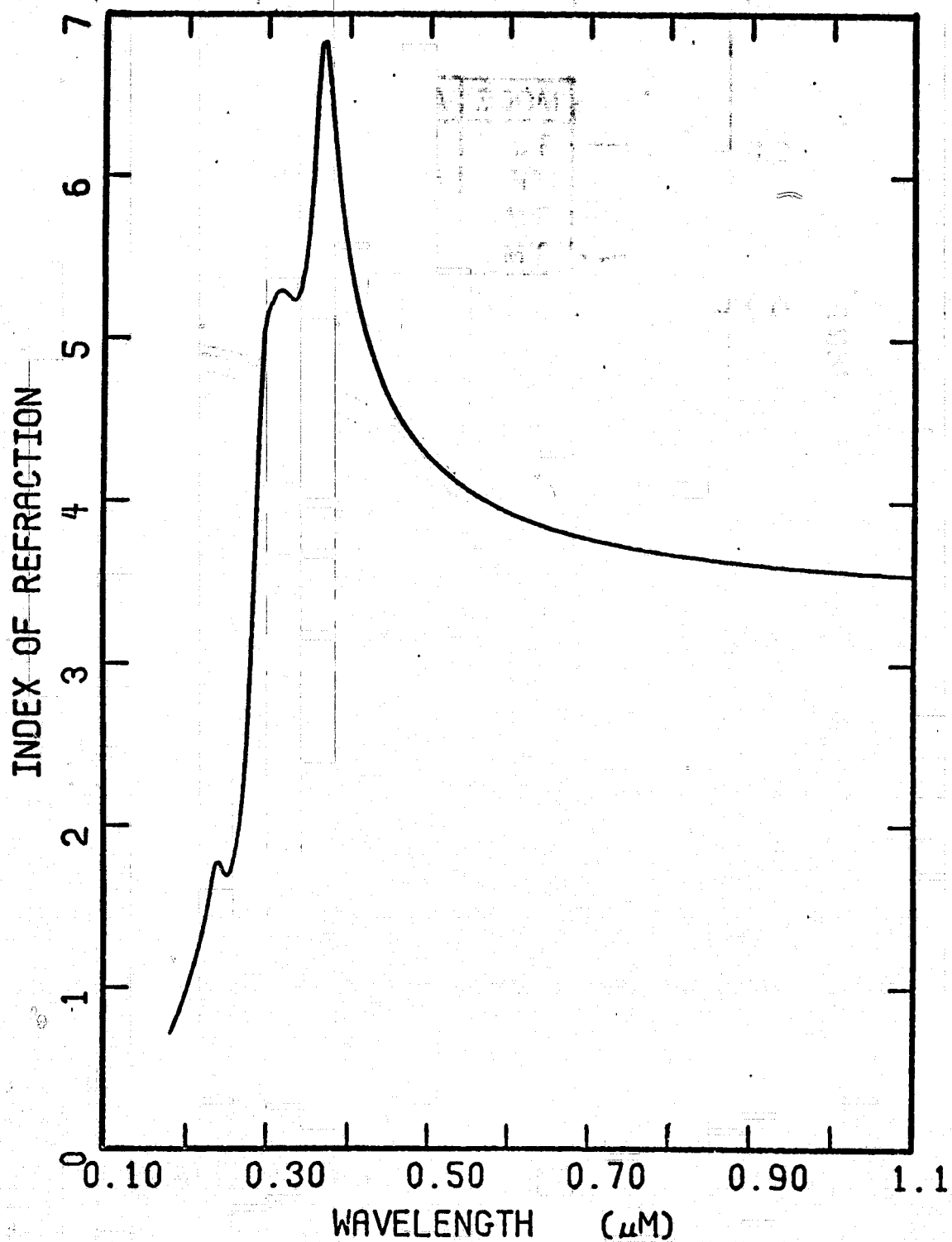
Figure 3.3. Variation of the index of refraction of silicon as a function of wavelength (Phillip, 1972)
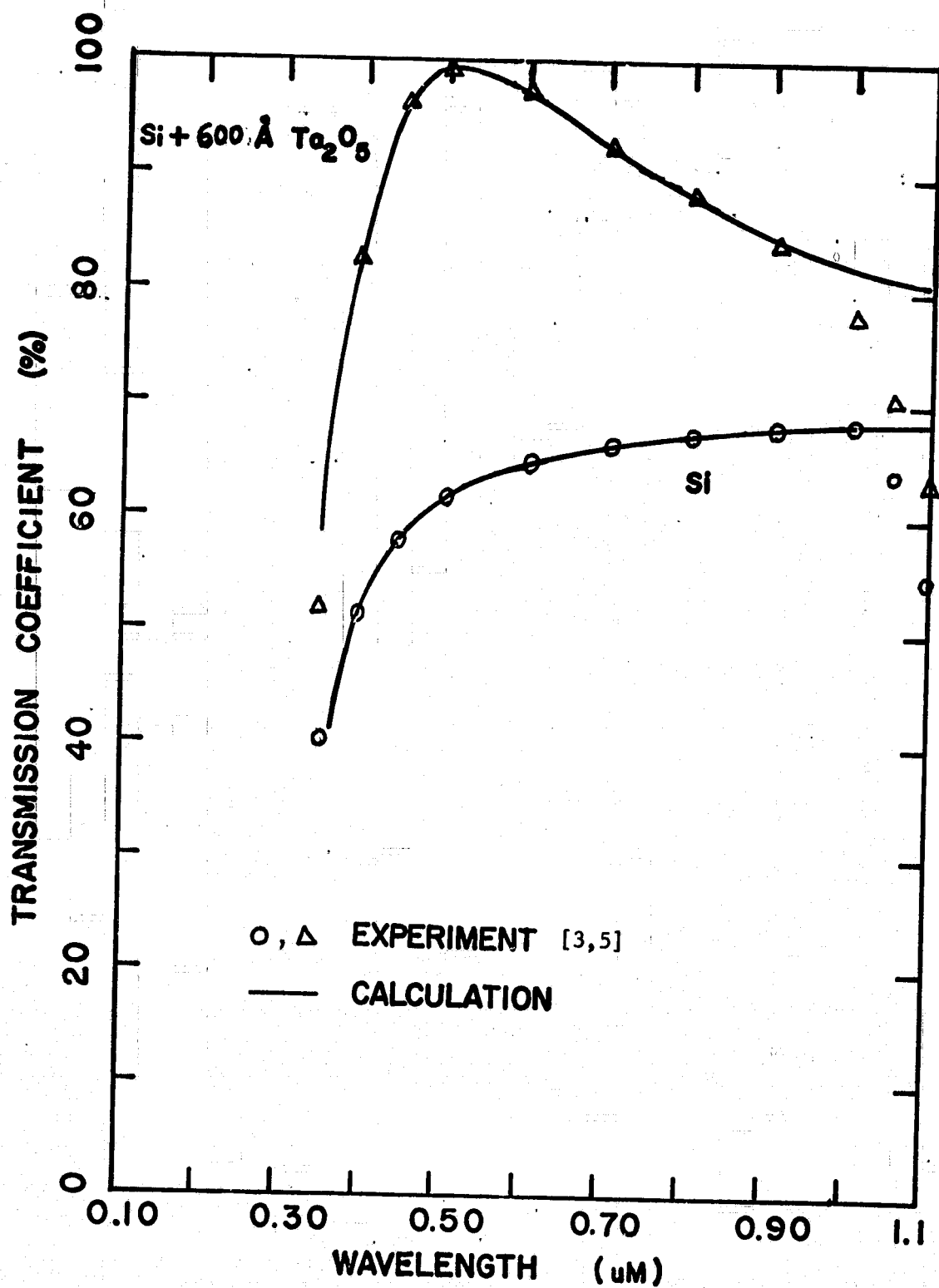
Figure 3.4. Transmission coefficient for a plane silicon surface at wavelength 0.3 μm to 1.1 um.
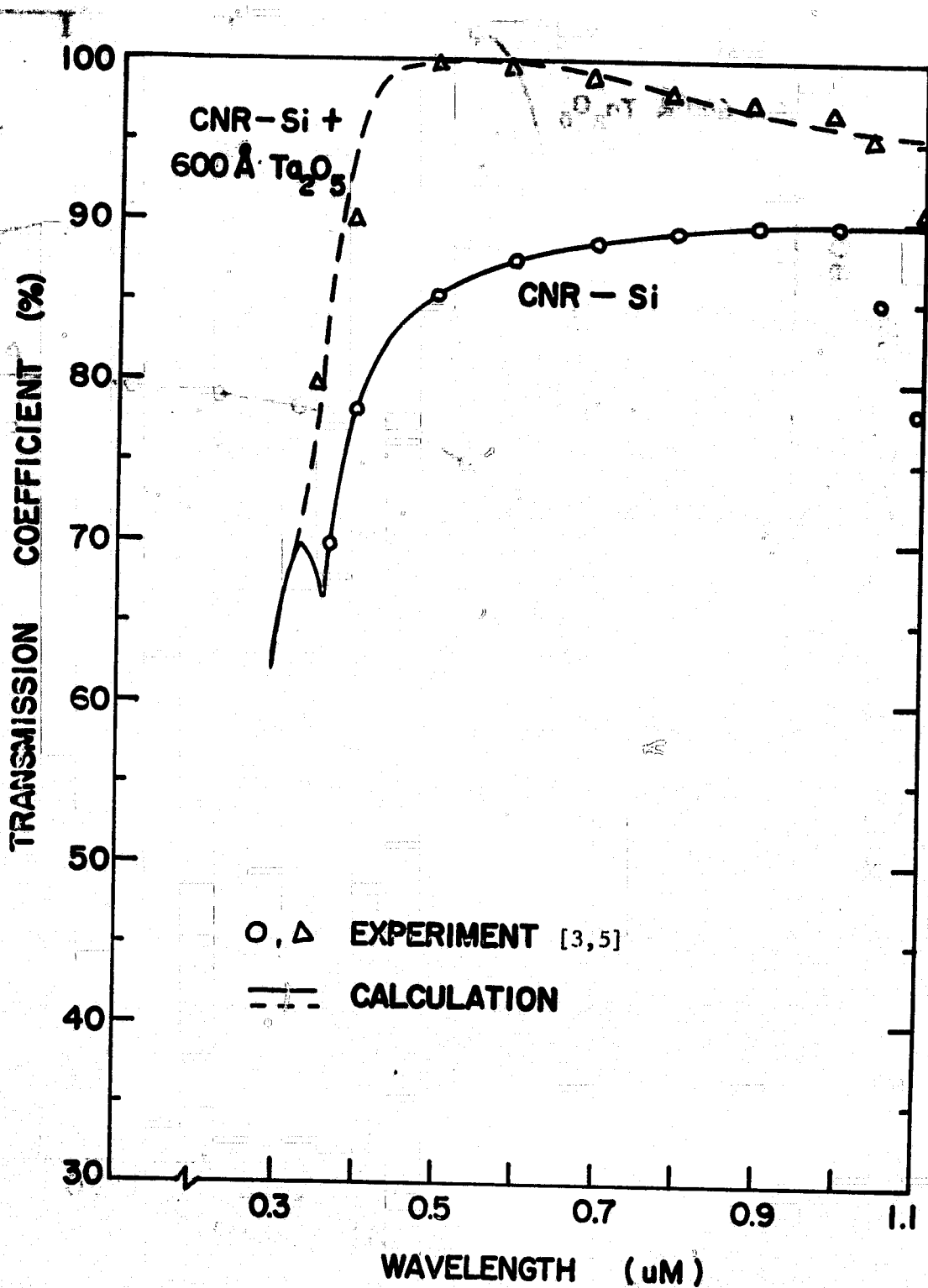
Figure 3.5. Transmission coefficient for a serrated silicon surface at wavelength 0.3 μm to 1.1 μm.

8

3

Table 3.1 Optical properties of a silicon solar cell.

	Spectral Condition	Optimum Anti-ref. (Å)	Surface Loss (%)	Available Optical Current (mA/cm^2)	Surface Generation
Si	AMO	No	36.4	34.2	1.15E22
	AM2	No	34.7	22.4	1.62E21
Si (CNR)	AMO	No	13.6	46.4	2.93E22
	AM2	No	12.2	30.1	3.85E21
Si+SiO	AMO	800	15.6	45.4	5.96E21
	AM2	800	10.4	30.7	1.39E21
$Si+SiO_2$	AMO	1100	17.6	44.3	1.25E22
	AM2	1100	14.5	29.3	1.83E21
$Si+Ta_2O_5$	AMO	600	13.0	46.8	1.33E22
	AM2	700	9.5	31.0	1.89E21
$Si+Ta_2O_5$ (CNR)	AMO	600	3.5	51.8	3.29E22
	AM2	700	1.8	33.7	4.28E21

2.5 to 3 percent [3]. It should be noted that the above optimum thickness of anti-reflection oxide refers to the perfect collection of the input light intensity.

Table 3.2. Optical properties of CNR cell with an anti-reflection film of Ta_2O_5.

	Spectral Condition	Thickness of Ta_2O_5 (Å)	Surface Efficiency (%)	Available Optical Current (mA/cm^2)	Surface Generation	Wavelength of peak Transmission (μm)
S1	AMO	0	86.35	46.40	2.93E22	1.05
	AMO	500	96.18	51.68	3.62E22	0.45
	AMO	600	96.48	51.84	3.29E22	0.53
	AMO	650	96.46	51.83	3.24E22	0.57
	AMO	700	96.36	51.78	3.26E22	0.61
S1	AM2	0	87.84	30.13	3.84E21	1.05
	AM2	500	96.98	33.26	5.00E21	0.45
	AM2	600	97.93	33.59	4.58E21	0.53
	AM2	700	98.16	33.67	4.27E21	0.61
	AM2	800	97.80	33.54	4.20E21	0.71
	AM2	900	97.05	33.29	4.40E21	0.80

3.3 Optical Generation

In a solar cell, the number of absorbed photons can be represented as

$$N_{pha}(x) = N_{phi}(\lambda)[1 - \exp(-\alpha(\lambda)x)] \tag{3.1}$$

where $N_{phi}(\lambda)$ is the input photon density at wavelength λ within the wavelength interval $\Delta\lambda$ and $\alpha(\lambda)$ is the absorption coefficient at wavelength λ. If it is assumed that each absorbed photon creates $n_\lambda(\lambda)$ electron-hole pairs, then the resulting current density is

$$J_G(x,\lambda) = q \cdot T(\lambda) \cdot N_{phi}(\lambda) \cdot n(\lambda) \cdot [1-\exp(-\alpha(\lambda)x)], \tag{3.2}$$

where $T(\lambda)$ is the surface transmission coefficient at wavelength λ. The actual generation rate is

$$G_e(x,) = -\frac{1}{q}\frac{\partial J_G(x,\lambda)}{\partial x}, \tag{3.3}$$

or

$$G_e(x,\lambda) = T(\lambda) \cdot n_\lambda(\lambda) \cdot N_{phi}(\lambda)\alpha(\lambda)\exp(-\alpha(\lambda)x). \tag{3.4}$$

For a full spectral irradiance, the generation rate at each spectral point must be added over the incident wavelengths to give

$$G_e(x) = \sum_{\lambda=0.18}^{1.1} T(\lambda)n_\lambda(\lambda)N_{phi}(\lambda)\alpha(\lambda)\exp(-\alpha(\lambda)x). \tag{3.5}$$

If the incident light is in other than the normal direction, the actual traversed path is lengthened by a factor of $1/\sin\theta_1$ and $1/\sin\theta_2$ of the device width for the first and second refracted light rays respectively. These factors are shown in Figure 3.6 as a function of
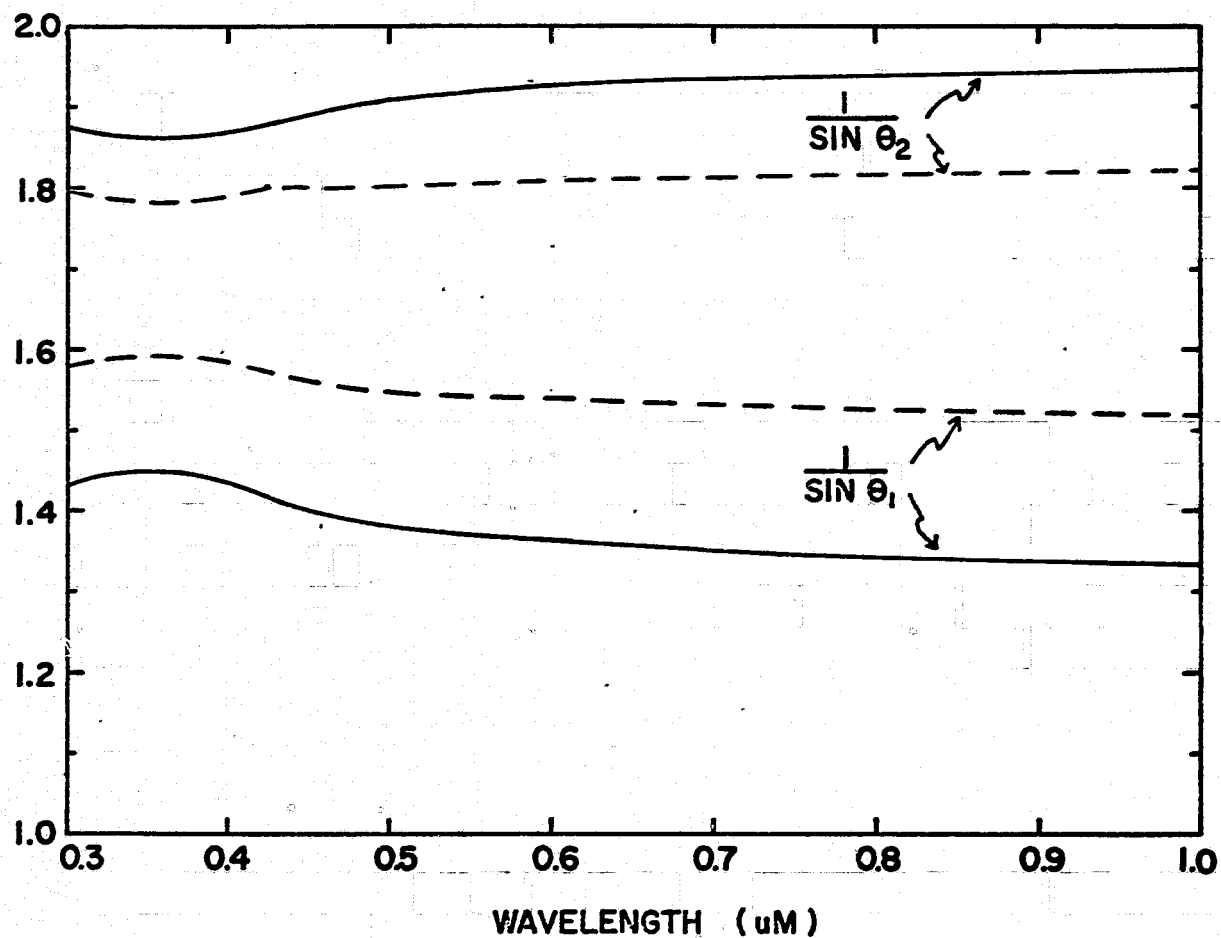
Figure 3.6. Factors of $1/\sin\theta_1$, and $1/\sin\theta_2$ as a function of wavelength. Bare silicon surface (solid lines), 600Å Ta_2O_5 anti-reflection film (dashed lines).

photon wavelength. Therefore the absorbed photon density becomes

$$N_{pha}(x) = N_{phi}(\lambda)[1-\exp(-\alpha(\lambda)x/\sin\theta_1)]+N_{phi}(x)R_1(\lambda)[1-\exp(-\alpha(\lambda)x/\sin\theta_2)]$$

(3.6)

and the resultant generation rate becomes

$$G_e(x)= \sum_{\lambda=0.18}^{1.1} [T_1(\lambda)n_\lambda(\lambda)N_{phi}(\lambda)\alpha(\lambda)\exp(-\alpha(\lambda)x/\sin\theta_1)/\sin\theta_1+R_1(\lambda)T_2(\lambda)$$

$$n_\lambda(\lambda)N_{phi}(\lambda)\alpha(\lambda)\exp(-\alpha(\lambda)x/\sin\theta_2)/\sin\theta_2],$$

(3.7)

where T_1, R_1 are the coefficients of transmission and reflection with respect to the i-th refracted light.

The calculated generation rates are shown in Figure 3.7 and 3.8. It is seen that a CNR cell has a higher generation rate near the illuminated surface within about 20 μm, and has a lower generation rate at distances deeper than about 20 μm. This is because more carriers can be generated near the surface from the oblique transmission of the incident light. The comparison of the generation rates for the plane and serrated surfaces is presented in Figure 3.9 at one particular wavelength of 0.9 μm and 100 mW power density without any anti-reflection film. The crossing point of the generation rates for both cases occurs around 40 μm from the illuminated surface.

The maximum possible collection efficiency of a solar cell is plotted against the cell depth in Figure 3.10. The CNR cell has a steeper slope of the collection efficiency vs. width curve. This implies that more carriers are generated near the irradiated surface. Therefore
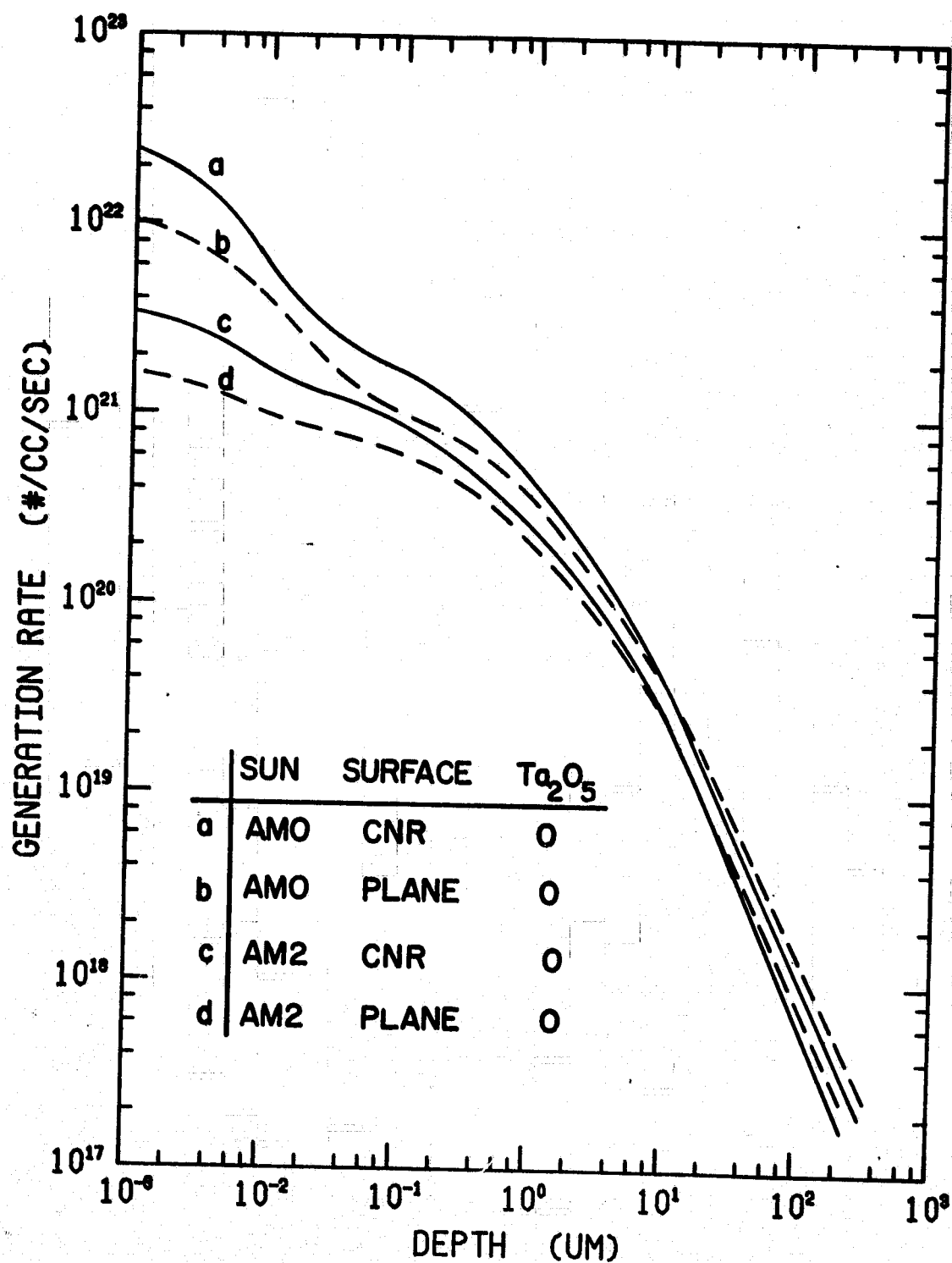
Figure 3.7. Generation rates of AMO and AM2 solar spectrums for a plane
surface cell or a CNR cell.
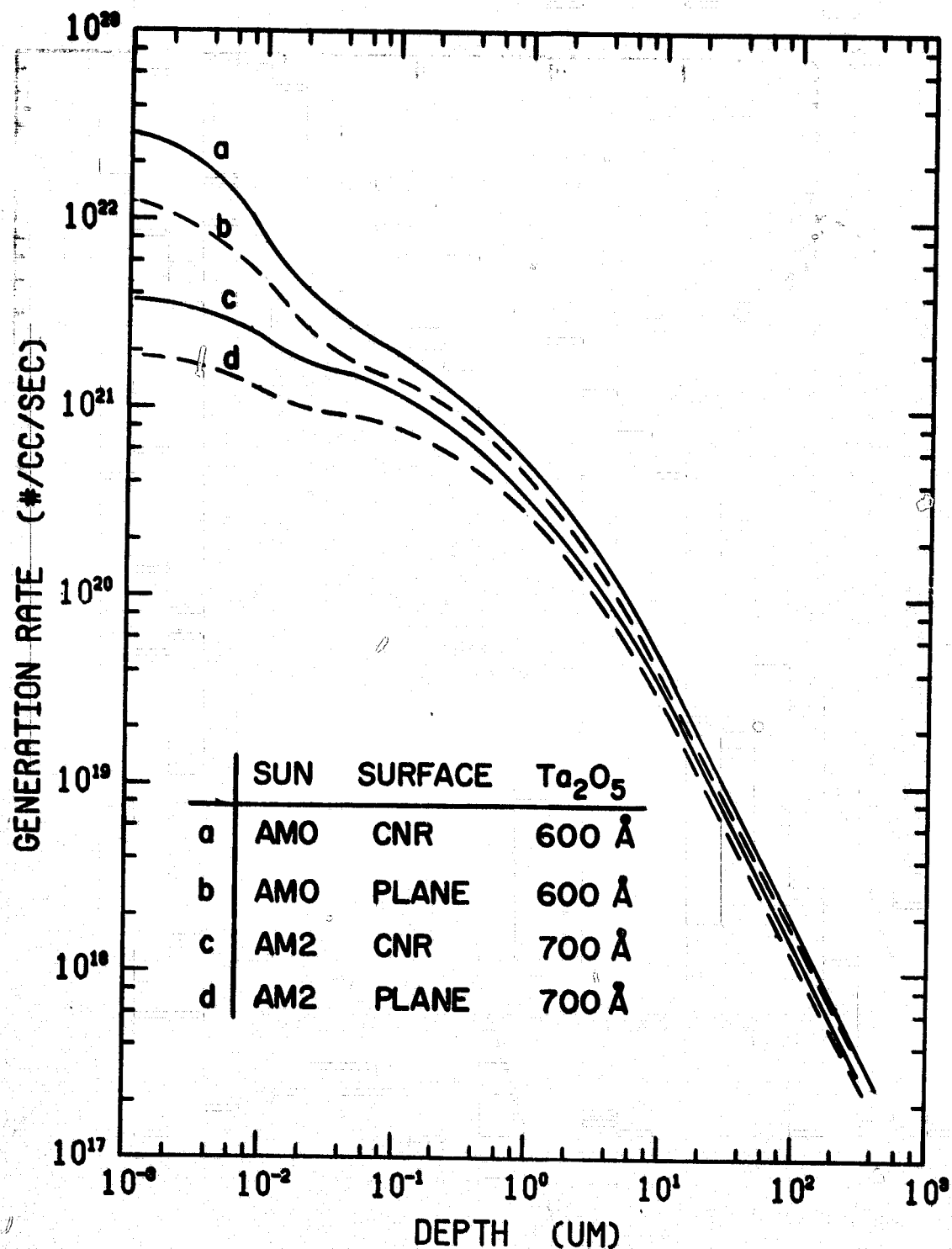
Figure 3.8. Generation rates of AMO and AM2 solar spectrums for a plane surface cell or a CNR cell.
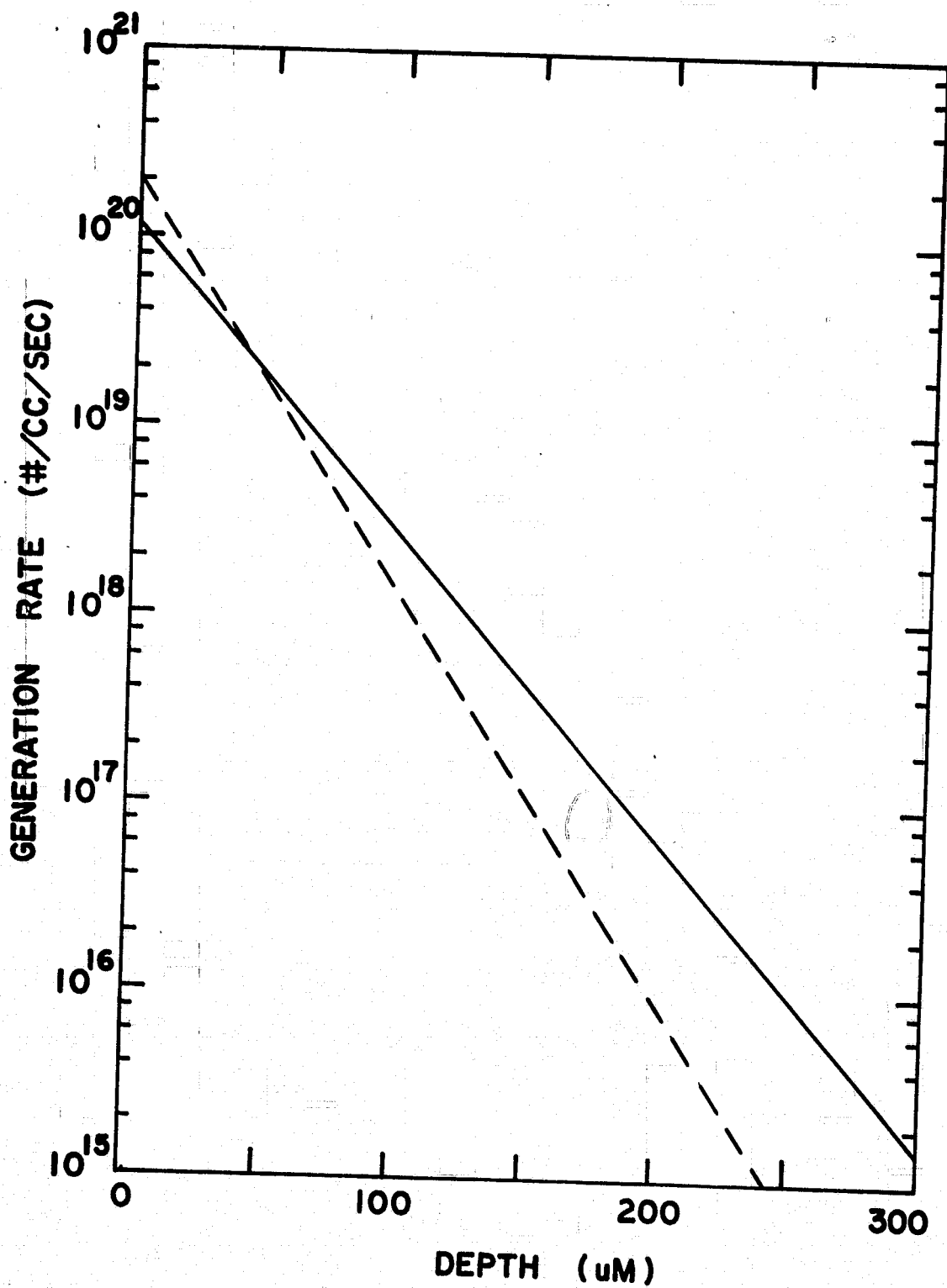
Figure 3.9. Comparison of the generation rates of plane and serrated surfaces at a wavelength of 0.9 μm. Plane surface (solid), serrated surface (dashed).
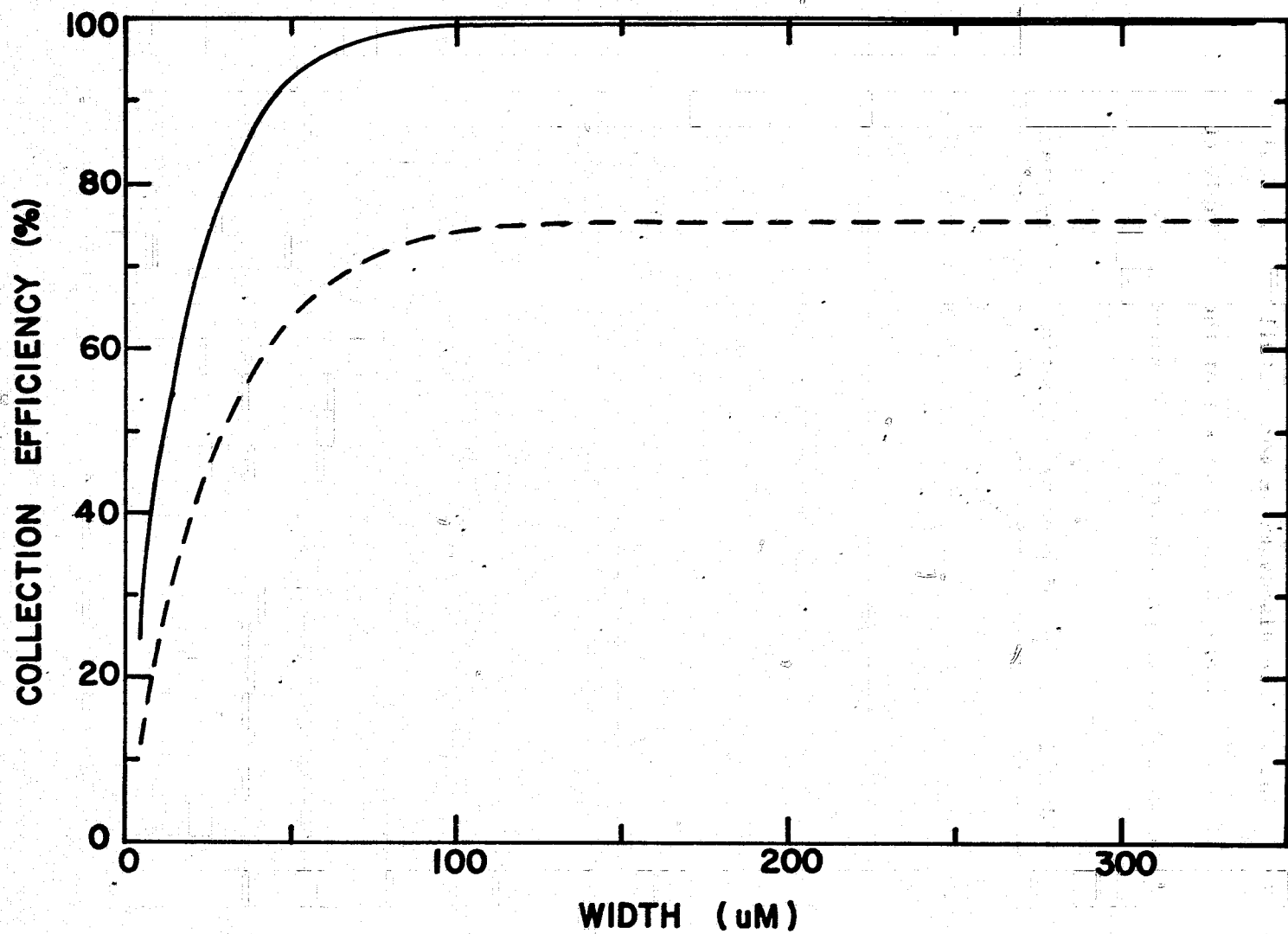
Figure 3.10. Collection efficiency as a function of cell depth for CNR cell (solid) and plane surface cell (dashed) at a wavelength of 0.9 μm.

a CNR cell is more radiation resistant as compared to a conventional cell. This point will be discussed in more detail later. Table 3.3 shows the cell widths where 90 or 95 percent of the available current densities can be potentially collected for both type cells.

Table 3.3. Widths for 90 and 95 percent collection efficiencies.

Width (μm) Collection Efficiency (%)	(μm) Bare Plane S_i	(μm) CNR No Anti-Ref.	(μm) CNR 600A Ta_2O_5	(μm) Bare Plane Si λ=0.9 μm	(μm) CNR λ=0.9μm
90	90	80	60	65	45
95	250	240	210	80	60
Available Current Density	34.2	46.40	51.8	-	-

3.4 Violet and CNR Cells

The parameters of the violet and CNR cells used in the present calculations are listed in Table 3.4. The parameters of this table are reasonable when compared to reference [2]. A CNR cell differs from a violet cell mainly in the surface transmission efficiency as a result of its specific surface texture. Also, a CNR cell has a larger surface diffusion current density and space charge recombination current density due to the enlarged surface area of 2.83 times that of the original flat surface area.

Table 3.4. Models of the violet and CNR cell.

Structure	n^+p (Cell A)	; n^+pp^+ (Cell B)
Base resistivity	2 $\Omega \cdot$ cm	; 1.3 $\Omega \cdot$ cm
Surface junction	0.13 μm	
Surface doping density	$10^{20}/cm^3$, erfc	
Device width	250 μm	
Device area	4 cm^2	
SRV	10^3 cm/sec	
Two-way reflection	Yes	
Anti-reflection film	Ta_2O_5, 600Å	
Sheet resistance	550 $\Omega/\square$	
Contact resistance	10^{-4} $\Omega \cdot cm^2$	
Sun power density	AMO, (135.3 mA/cm^2)	
Temperature	27°C	
Surface diffusion length	$\dfrac{L_D(MED)+L_D(MIN)}{2}$	
Base diffusion length	$\dfrac{L_D(MAX)+L_D(MED)}{2}$	; 210 μm
Grid pattern	Two tapered bus bar	20 μm to 200 μm)
Number of fingers	60	
Width of fingers	20 μm	
Thickness of fingers	1.9 μm	

The predicted results of the computer analysis are listed in Table 3.5. Here the one-dimensional analysis refers to the solution of the fundamental device equations in a one-dimensional model. However, it is more realistic to simulate a practical solar cell by the general two-dimensional program of Appendix 10.4. The calculated efficiency values can be compared to reported values of 13 and 15 percent for violet and CNR cells respectively. The predicted spectral responses of violet and CNR cells are shown in Figure 3.11. The experimental data

Table 3.5. The predicted results of the violet and CNR cells.

Model	Violet-A		CNR-A		Violet-B
	1-DIM	2-DIM	1-DIM	2-DIM	2-DIM
I_{sc} (mA/4cm^2)	164.4	151.5	185.6	171.1	154.0
V_{oc} (volts)	0.582	0.582	0.585	0.582	0.590
CFF	0.821	0.802	0.821	0.779	0.803
I_M (mA/4cm^2)	153.9	143.7	177.2	161.4	146.1
V_M (volts)	0.510	0.492	0.504	0.481	0.500
P_M (mW)	78.5	70.6	89.3	77.6	73.0
EFF (%)	14.5	13.1	16.5	14.4	13.5
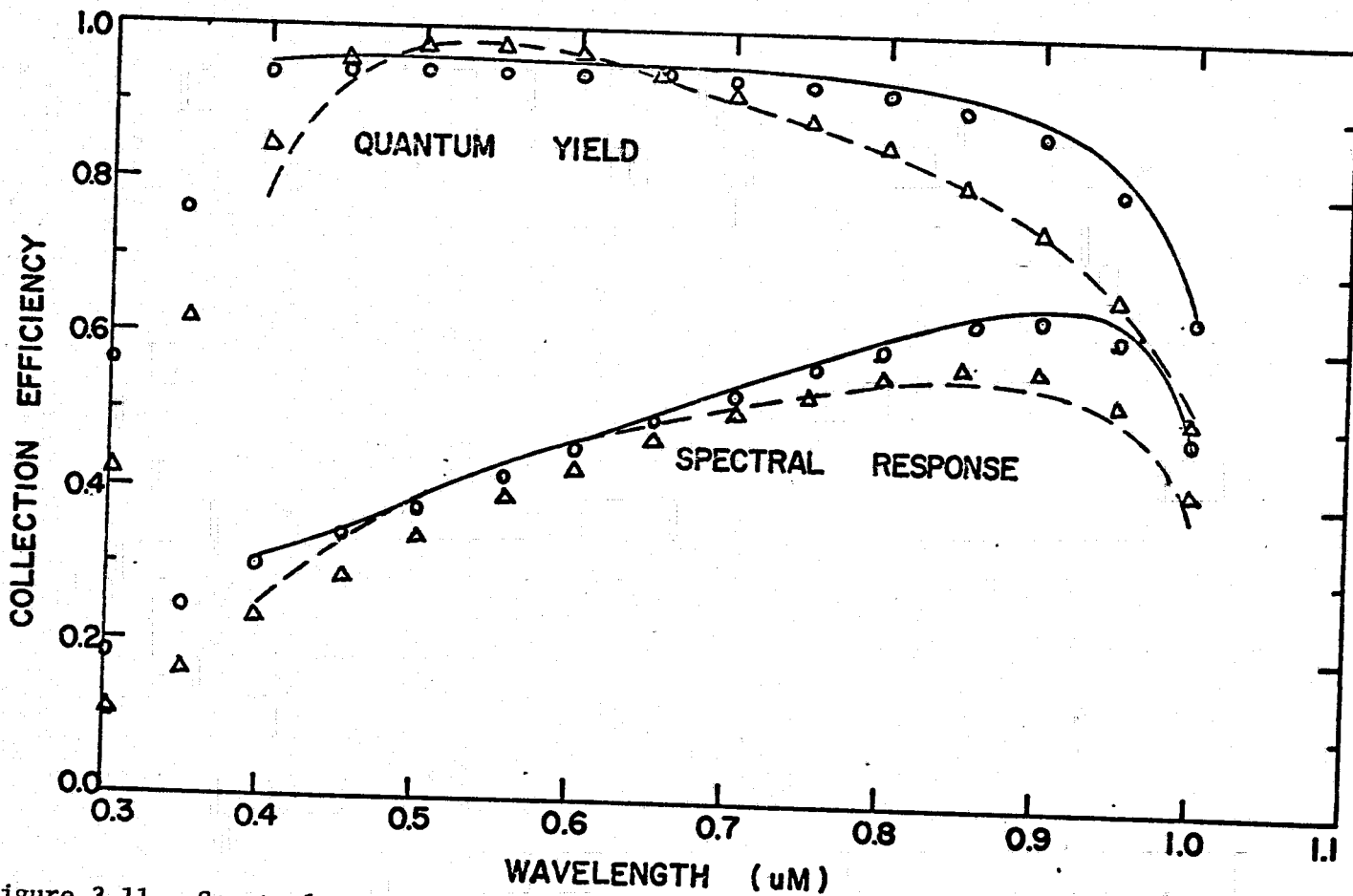
Figure 3.11. Spectral responses of violet and CNR cells. Violet cell (dashed lines), CNR cell (solid lines). o,Δ are the reported values from reference 11.

of the spectral response are taken from reference 11. The quantum yield

is then deduced from Equations 2.12 and 2.14. It is clear from

Figure 3.11 that there is a general agreement between the calculation

and the experiment.

It has been pointed out that there are three different forces

acting on the charged particles in the diffused surface region [9].

They are the electrostatic force, an additional force due to the

position-dependent band structure and the diffusion force from the

optically generated carriers. In a solar cell, the short wavelength

photons can generate large carrier densities near the surface and the

diffusion force is quite large in this region. Our calculation shows

that the minority current is in the direction of the collecting junction

despite the large retrogate field force from the position-dependent

band structure in the heavily doped surface layer. This suggests that

the diffusion force can counteract the internal retrogate field force.

Therefore, most of the carriers generated in the surface region can be

collected instead of being lost by recombination at the surface.

Within the base region, the calculation shows a much shorter

collection width than the device width. Collection widths of 85 μm

and 95 μm are calculated for type A violet and CNR cells respectively.

This is because the back surface ohmic contact is in competition with

the p-n junction for the collection of the light generated carriers.

The available device short circuit current density over the above

collection width can be readily calculated. These calculated results

are 42.3 and 47.6 mA/cm^2 respectively, which are about 90.5 and 92 percent

of the total available current density for violet and CNR cells respectively. These values are close to the predicted short circuit current densities of Table 3.5 indicating only a small percentage of the available current density within the collection width is lost through bulk and depletion region recombination.

3.5 Models of the New Generation Violet and CNR Cells

Since 1977 violet and CNR cells have been made by combining the technologies of the back surface field and the early violet cell of 1973. The difficult back diffusion process can then be controlled and the back contact has also been made highly reflective in order to improve the long wavelength response [10].

Typical parameters for such cells are listed in Table 3.4 as cell B. The base resistivity of a violet cell is nominally between 1 to 3 $\Omega \cdot$ cm. However, measurements indicate that the majority of cells have a resistivity around 1.3 $\Omega \cdot$ cm. The base diffusion length is taken from the measurement of reference [11] where a typical value of 210 μm is given for the preradiated cell. The radiation damage coefficient K_L for the diffusion length is assumed to be 2.5×10^{-10} at a doping density of $10^{16}/\text{cm}^3$.

The short circuit current density under radiation has been calculated and compared to the reported measurements for a typical violet and CNR cell. These are the type B cells of Table 3.4. The results are shown in Table 3.6.

Tables 3.6. Comparison of the short circuit current density for
typical violet and CNR cells. The experimental data are
taken from reference [10].

	Radiation Dose	0	10^{13}	10^{14}	10^{15}	5×10^{15}
Violet Cell	Experiment (mA/cm^2)	39.11	38.31	36.45	31.8	28.3
	Calculation (mA/cm^2)	40.62	39.56	36.46	31.57	27.28
	Agreement (%)	+2	+3.2	+0.02	-0.7	-3.7
CNR Cell	Experiment (mA/cm^2)	46.98	44.43	41.9	37.27	33.83
	Calculation (mA/cm^2)	45.85	44.81	41.81	37.08	32.92
	Agreement (%)	-2.4	+0.8	-0.2	-0.5	-2.8

The calculated short circuit current density has been corrected for the 6 percent metal coverage and the magnitude of the simulated AMO power density of 140 mW/cm^2. The small discrepancy at low radiation dose is perhaps due to the unknown base diffusion length for the particular cell measured. The discrepancy for heavily radiated cells may be due to an annealing effect before taking the measurement. However, it has been found from a comparison of baloon-flown cells and ground measurement that solar cell response is a few percent less in the space measurement [12]. This is consistent with our calculation and may suggest that there are problems in the simulated solar spectrum in the short wavelength region.

The calculation of spectral response under radiation is shown in Figure 3.12 for a typical violet and CNR cell. This is in very good agreement with Figure 8 of reference [11].

3.6 Conclusions

The following conclusions can be drawn based upon the work in this section.

(1) High efficiency silicon solar cells can be made by increasing the surface optical transmission efficiency through a textured silicon surface. Such textured surfaces have been found to produce the highest surface transmission efficiency, and it has also been found that the thickness of the anti-reflection film is not very critical for near optimum surface transmission.
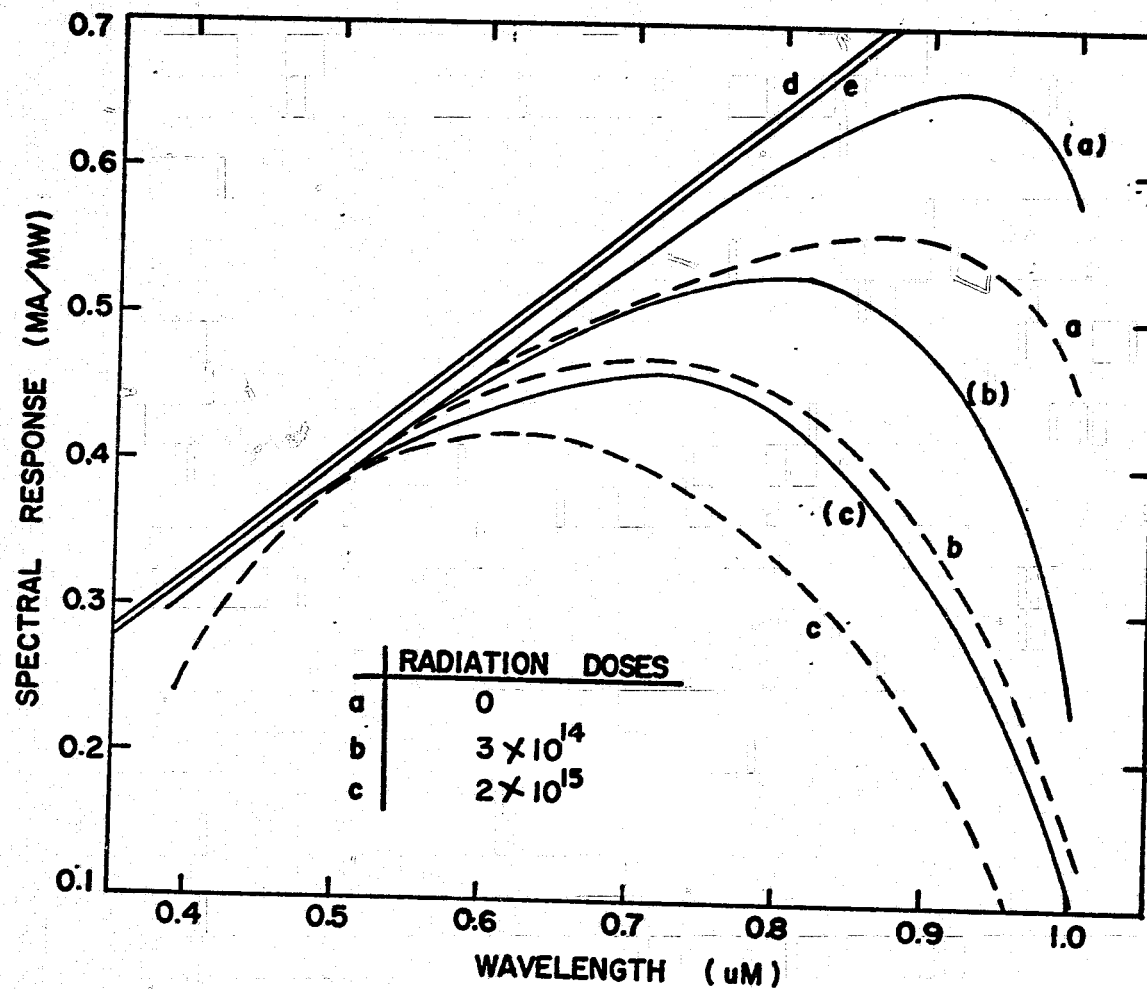
Figure 3.12. The calculated spectral responses for violet (dashed lines) and CNR (solid lines) cells under one Mev electron radiation doses. d - ideal spectral response for infinite cell depth, e - ideal spectral response for actual cell depth.

(2) It has been found that a high efficiency silicon solar cell can be made by combining the technology of the BSF structure and the shallow surface doping density. Good collection efficiency can be obtained with a practical base region diffusion length which has a value in the range of the device depth.

(3) CNR cells are found to be more radiation resistant than a standard planar surface cell. This is due to the fact that more carriers are generated near the collecting junction in a textured surface cell. Hence it degrades slowly with high energy particle irradiation.

3.7 Appendix A

The oblique optical reflection and transmission coefficients from an anti-reflection film on a silicon surface [13].

a) Reflection at the boundary of an absorbing medium
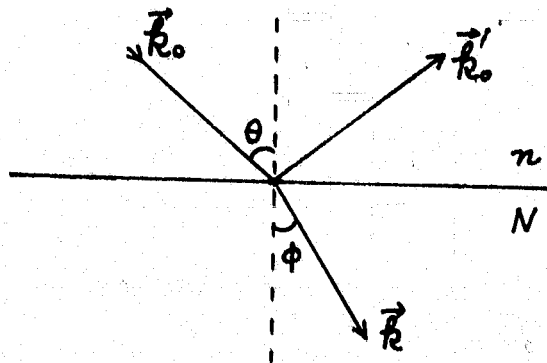
Figure A.1 The oblique optical reflection and transmission on a silicon surface.

Let the medium have the complex index of refraction $N=n+ik$ and the complex propagation vector of the refracted wave be $K = k + i\alpha$. At the reflection boundary

$$\vec{k}_o \cdot \vec{\gamma} = \vec{k}_o' \cdot \vec{\gamma} \tag{3.8}$$

$$\vec{k}_o \cdot \vec{\gamma} = \vec{K} \cdot \vec{\gamma} = (\vec{k}+i\vec{\alpha}) \cdot \vec{\gamma}, \tag{3.9}$$

$$k_o \sin\theta = k\sin\phi. \tag{3.10}$$

The wave equation can be written as

$$\nabla^2 E = \frac{N^2}{c^2} \frac{\partial^2 E}{\partial t^2}. \tag{3.11}$$

For plane harmonic waves we have $\nabla = -iK$, $\frac{\partial E}{\partial t} \to -i\omega$, so

$$\vec{K} \cdot \vec{K} = \frac{N^2 \omega^2}{c^2} = N^2 k_o^2.$$

By equating the real and imaginary parts, we have

$$k^2 - \alpha^2 = (n^2 - K^2)k_o^2, \tag{3.12}$$

$$\vec{k} \cdot \vec{\alpha} = k\alpha\cos\phi = nKk_o^2. \tag{3.13}$$

After some algebraic manipulation of Equations (3.12) and (3.13), it is found that

$$k\cos\phi + i\alpha = k_o\sqrt{N^2 - \sin^2\theta}. \tag{3.14}$$

Snell law of refraction can be written as

$$n_1 \sin\theta = N\sin\phi. \tag{3.15}$$

Now ϕ is a complex number and has no direct correlation to the angle ϕ. By Equations (3.14) and (3.15)

$$N = \frac{k\cos\phi + i\alpha}{k\cos\phi} \tag{3.16}$$

The boundary condition of continuity of the tangential components of electric and magnetic fields leads to Fresnel's equation for TE and TM polarization.

$$\gamma_{TE} = \frac{n_1\cos\theta - N\cos\phi}{n_1\cos\theta + N\cos\phi} , \tag{3.17}$$

$$\gamma_{TM} = \frac{-N\cos\theta + n_1\cos\phi}{N\cos\theta + n_1\cos\phi}. \tag{3.18}$$

If there is an antireflection film, the transmitted and reflection amplitudes need to be added as Fig. A2 shows. In this figure,
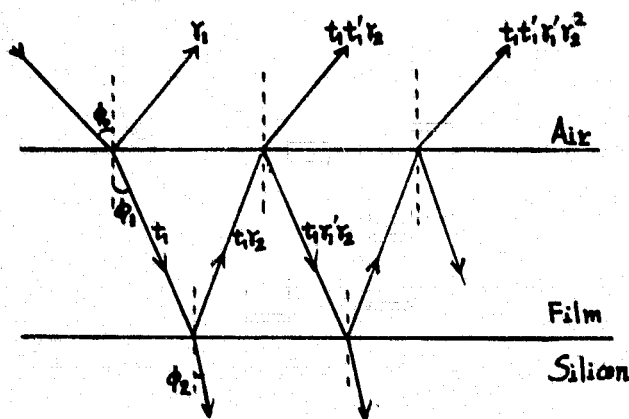
Figure A.2 The multiple reflection and transmission across an anti-reflection film on a silicon surface.

Where $\gamma'=-\gamma$ and $t'=-t$ from the Fresnel coefficients of Equations (3.17) and (3.18). Hence the total reflected amplitude is given by

$$R = \gamma_1 + t_1 t_1' \gamma_2 e^{-2i\delta_1} + t_1 t_1' \gamma_1' \gamma_2^2 e^{-4i\delta_1} + \cdots = \frac{\gamma_1 + \gamma_2 e^{-2i\delta_1}}{1 + \gamma_1 \gamma_2 e^{-2i\delta_1}} , \quad (3.19)$$

where λ_1 is the change in phase of the beam on transversing the films and

$$\delta_1 = \frac{2\rho}{\lambda} n_1 d_1 \cos\phi_1 .$$

Finally, it is the energy instead of amplitude which is needed and the resultant total reflection and transmission coefficients are

$$R = RR* \quad\quad\quad (3.20)$$

$$T = \text{Real} \left(\frac{n_2}{n_1}\right) TT* \quad\quad\quad (3.21)$$

The exact coefficients of reflection R and transmission T could be solved from Equations (3.10), (3.12), (3.13) and (3.16)-(3.19) using the appropriate complex refractive index of n_2 and n_3 for TE or TM modes. The complete equation, however, is cumbersome and hopelessly complicated. The desired values of R and T however can be calculated numerically using complex algebra.

3.8. REFERENCES

1. J. Mandelkorn and J. H. Jr. Lamneck. 1972. Ninth Photovoltaic Specialists Conference, Silver Spring, MD.

2. J. Lindmayer and J. F. Allison. 1972. Ninth Photovoltaic Specialists Conference, Silver Spring, MD: 83. Also Comsat Tech. Rev. 3, 1972.

3. R. A. Arndt, J. F. Allison, J. G. Haynos and A. Meulenberg, Jr. 1975. Optical Properties of the COMSAT Non-Reflective Cell. Tenth Photovoltaic Specialists Conference, Palo Alto, CA: 40-43.

4. H. R. Phillip. 1972. Influence of oxide layers on the determination of the optical properties of silicon. Journal of Applied Physics 43(6): 2835-2839.

5. C. R. Baraona and H. W. Brandhorst. 1975. V-Grooved Silicon Solar Cells. Tenth Photovoltaic Specialists Conference, Palo Alto, CA: 44-48.

6. E. Y. Wang, F. T. S. Yu and V. L. Simms, etc. 1974. Optimum Design of Antireflection Coating for Silicon Solar Cells. Ninth Photovoltaic Specialists Conference, Silver Spring, MD: 168-173.

7. M. G. Coleman, W. L. Bailey and R. A. Pryor. 1976. Processing Ramifications of Textured Surfaces. Twelfth Photovoltaic Specialists Conference, Baton Rouge, LA: 313-316.

8. F. Restrepo and C. E. Backus. 1976. On Black Solar Cells or the Tetrahedral Texturing of a Silicon Surface. IEEE Trans. on ED-23: 1195-1196.

9. R. J. VAN Overstraeten, H. J. DeMAN and R. P. Mertens. 1973. Transport Equations in Heavily Doped Silicon. IEEE Trans. on Electron Devices ED-20(3): 290-298.

10. A. Meulenberg, D. J. Curtin and R. W. Cool. 1977. Comparative Testing of High Efficiency Silicon Solar Cells. Twelfth Photovoltaic Specialists Conference, Baton Rouge, LA: 238-246.

11. A. Meulenberg, Jr., J. F. Allison, R. A. Arndt, and J. G. Haynos. 1975. Radiation Damage to the COMSAT Non-Reflective Cell. Eleventh Photovoltaic Specialists Conference, Scottsdale, AZ: 204-208.

12. N. L. Thomas and F. W. Sarles, Jr. 1977. High Altitude Calibration of Thirty-Three Silicon and Gallium Arsenide Solar Cells on a Sounding Rocket. Twelfth Photovoltaic Specialists Conference, Baton Rouge, LA: 560-568.

13. O. S. Heavens. 1955. Optical Properties of Thin Solid Films. Butterworths Scientific Publications, London, UK.

4. SHORT CIRCUIT CURRENT DENSITY AS A FUNCTION OF TEMPERATURE AND RADIATION INTENSITY

4.1 Introduction

Although solar cells were conventionally measured at room temperature, the operation of solar cells is usually under varied temperature and solar intensities. The cell temperature may vary from 60°C to 90°C in the earth's synchronous orbit, and there are extreme temperatures of -120°C and +140°C near Jupiter and Mercury respectively. In the terrestrial operation of solar cells, the consideration of temperature is also important because of the large temperature variations with respect to locations and seasons. Especially in a multi-sun concentrated system, a high working temperature is usually inevitable from the higher input solar intensity.

The subject of the temperature dependence of short circuit current density is the main topic in this section. The material parameters as a function of temperature will be discussed, and a comparison between theory and experiment will also be presented.

4.2 Material Parameters as a Function of Temperature

Several important material parameters, which determine solar cell operation as a function of temperature, are (a) intrinsic carrier density (b) diffusion length and lifetime (c) absorption coefficient and refractive index (d) mobility and diffusion coefficient.

(a) Intrinsic carrier density n_i.

The intrinsic carrier density n_i is a function of temperature and bandgap energy. The general form is [1]

$$n_i = \sqrt{N_c N_v} \; e^{-E_g(T)/2kT} \qquad (4.1)$$

$$= 4.9 \cdot 10^{15} \cdot \left(\frac{m_{de} m_{dh}}{m_o^2}\right)^{3/4} \cdot T^{3/2} \cdot e^{-E_g(T)/2kT} , \qquad (4.2)$$

where m_{de} and m_{dh} are the density-of-state effective mass of electron and hole and $E_g(T)$ is the bandgap energy at temperature T. The empirical form of the temperature dependent intrinsic carrier density, which satisfies the above function of temperature, is used in this work [2]

$$n_i = 3.73 \cdot 10^{16} \cdot T^{3/2} \cdot e^{-7014/T} . \qquad (4.3)$$

The open circuit voltage of a solar cell is found to decrease with temperature. This is due to the strong temperature dependence of the intrinsic carrier density. In the first order model the open circuit voltage can be defined by

$$V_{oc}(T) = n \cdot \frac{kT}{q} \ln \left[\frac{I_{sc}(T)}{I_s(T)}\right] \qquad (4.4)$$

where $I_s(T)$ is the saturation current density which is proportional to n_i^2 and n_i in Shockley's diffusion current model or Sah's recombination current model respectively. The diode factor n is 1 or 2 for the above models respectively. Hence, the reduction of open circuit voltage as a function of temperature can be derived from Equations 4.3 and 4.4 with the same result for both cases.

$$\Delta V_{oc}(T_1, T_2) = V_{oc}(T_2) - V_{oc}(T_1) = \frac{3k}{q} [T_1 \log T_1 - T_2 \log T_2] \qquad (4.5)$$

or

$$\Delta V_{oc}(273°K, T) \simeq -1.9 \text{ mV/K°} \qquad (4.6)$$

However, both current mechanisms may exist simultaneously in a practical silicon solar cell. In this case $\Delta V_{OC}(T)$ can be derived assuming an abnormal diode factor A and the dominance of diffusion current near $V_{OC}(T)$.

$$\Delta V_{OC}(T_1,T_2) = V_{OC}(T_2)-V_{OC}(T_1) = A \cdot \frac{3k}{q} [T_1 \log T_1 - T_2 \log T_2] \qquad (4.7)$$

where A is between 1 and 2. Therefore the $\Delta V_{OC}(T)$ value is usually lower than -1.9 mV/K° depending on the A value of a practical solar cell. The experimental measurements always show a negative temperature coefficient of $V_{OC}(T)$ with a value of -2.2 to -2.3 mV/K° for 10 Ω-cm and 2 Ω-cm silicon cell respectively [3]. These values are in agreement with other reports. Luft reported a value of -2.13 to -2.29 mV/°K for 10 Ω-cm cells [4]. A value of about -2.2 mV/K° was reported by Yasi [5] for a 2 Ω-cm cell. For GaAs, the reported data is between -1.9 and -2.2 mV/°K [6,7].

The negative temperature coefficient of the open circuit voltage can partly be compensated by the small positive temperature coefficient of short circuit current. However, this compensating effect is small due to the very small temperature coefficient of the short circuit current density.

(b) Diffusion length

The magnitude of the diffusion length is determined by the carrier lifetime and the diffusion coefficient as,

$$L_n = \sqrt{D_n \tau_n} . \qquad (4.8)$$

A similar formula can be written for holes by substituting sub-index p for n. The diffusion coefficient is calculated from Einstein relation for non-degenerate semiconductors as

$$D_n = \frac{kT}{q}\mu_n,$$ (4.9)

where the mobility μ_n is generally determined for silicon by the acoustical phonon scattering mechanism and the impurity scattering mechanism. The component of lattice scattering has the theoretical temperature dependence of $T^{-3/2}$, while a temperature dependence of $T^{-2.5}$ and $T^{-2.7}$ is experimentally observed for electrons and holes in a lightly doped material [8]. The component of impurity scattering has a temperature dependence of $T^{+3/2}$.

In this work total mobility is calculated from lattice scattering mobility μ_L and impurity scattering mobility μ_I, as

$$\frac{1}{\mu} = \frac{1}{\mu_L} + \frac{1}{\mu_I},$$ (4.10)

where

$$\mu_I = 4.7 \times 10^{17} \left(\frac{m_o}{m_{eff}}\right)^{1/2} \frac{T^{3/2}}{N_D \ln(1+4.5 \times 10^8 T^2/N_D^{2/3})}$$ (4.11)

and

$$\mu_{Ln} = 2.1 \times 10^9 T^{-2.5} cm^2/V\cdot sec \text{ (electrons)},$$ (4.12)

$$\mu_{Lp} = 2.3 \times 10^9 T^{-2.7} cm^2/v\text{-}sec \text{ (holes)}.$$ (4.13)

For an indirect bandgap material such as silicon, lifetime is primarily controlled by defect levels located in the forbidden bandgap. If the single defect level of Shockley and Read's model is assumed, the lifetime of the minority carriers can be shown to be

$$\tau_p = \tau_{po}[1 + \exp(E_t - E_{fn})/kT]$$ (4.14)

in the n-type region and similarly

$$\tau_n = \tau_{no}[1+\exp(E_t+E_{fp}-2E_i)/kT] \tag{4.15}$$

in the p-type region, where τ_{po} and τ_{no} are equal to $1/\sigma_p v_{th} N_t$ and $1/\sigma_n v_{th} N_t$ respectively. Hence the carrier lifetime depends on the relative location of the trap level with respect to the quasi-Fermi level and the intrinsic energy level. In early reports, the lifetime was found to increase exponentially with temperature as Equation 4.14 and 4.15 for a shallow trap level [9]. However, more recent measurements indicate the dominance of a deep recombination level near the intrinsic energy level and this implies that the above exponential terms of Equations 4.14 and 4.15 can be neglected [10]. The lifetime will then be approximately constant for operation near room temperature. These considerations suggest a relatively constant diffusion length as a function of temperature for the deep recombination level model of a silicon solar cell. The published results of the measured diffusion length as a function of temperature demonstrate the almost constant diffusion length except at very low temperature [11].

(c) Absorption coefficient and refractive index

The temperature dependence of the absorption band edge in a silicon material is a well established physical phenomenon. The temperature dependence of the absorption coefficient can, in general, be obtained by the appropriate displacement along the horizontal and vertical axes in the absorption-wavelength curve. The horizontal displacement is basically due to the bandgap shrinkage as temperature increases. The empirical value of the bandgap temperature coefficient for silicon is about -2.4×10^{-4} eV/°K at temperatures above 150K° [1].

Since silicon is an indirect bandgap material, the photon excitation of the absorption mechanism requires phonon participation for the conservation of momentum and energy. Therefore the temperature functional dependence of the vertical shift can be deduced from the phonon statistics assuming McLean's model of two phonon interaction with energies at temperatures of 212°K and 670°K respectively [12].

The absorption coefficient will then increase or decrease with temperature beyond the 300°K curve by a factor f in the vertical direction of [13]

$$f = \frac{1 + \dfrac{1}{e^{212/T}-1} + \dfrac{1}{e^{670/T}-1}}{1 + \dfrac{1}{e^{212/300}-1} + \dfrac{1}{e^{670/300}-1}}. \qquad (4.16)$$

Since the absorption coefficient is determined by the direct bandgap for photon energy greater than the direct bandgap energy, vertical movement of the α-λ curves is negligible for these high energy photons. Several absorption-wavelength curves at different temperature can then be obtained by the appropriate horizontal and vertical movement with respect to that at room temperature. These are shown in Figure 4.1.

Measured data of Dash and Newman [14] on the photon absorption of silicon are replotted in Figure 4.2 as $\alpha^{1/2}$ versus $(\hbar\nu - E_g)$ at temperatures of 300°K and 77°K [15]. The straight line matching of the $\alpha^{1/2}$-$(\hbar\nu - E_g)$ relation is a well known characteristic of the indirect optical transition. Our analysis predicts a good fitting to the experimental data except in the short wavelength range, where the direct bandgap photon transition becomes dominant over the indirect-bandgap photon transition.
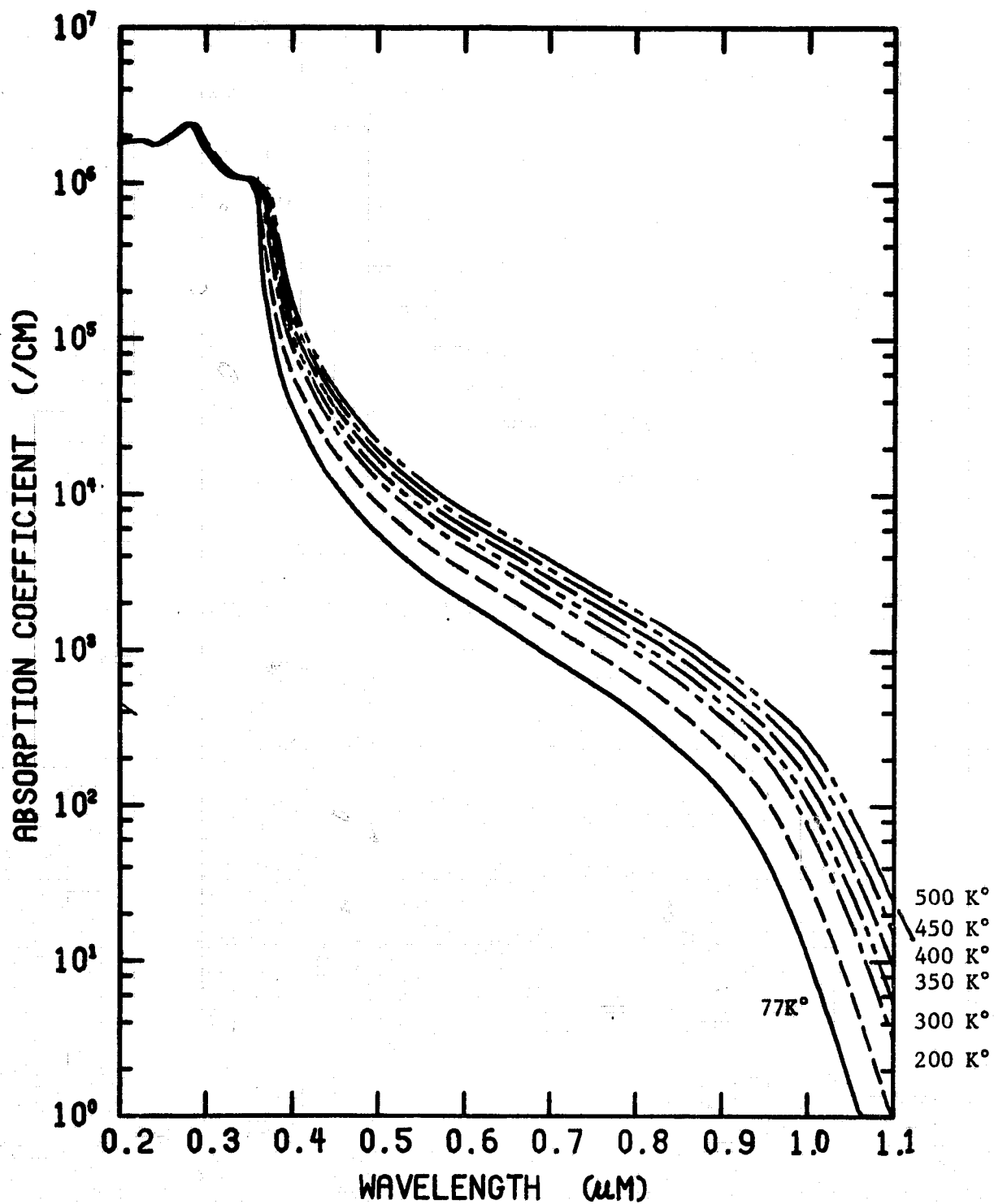
Figure 4.1. Absorption coefficient as a function of temperature by
the proper horizontal and vertical movements in the
α-λ plot.
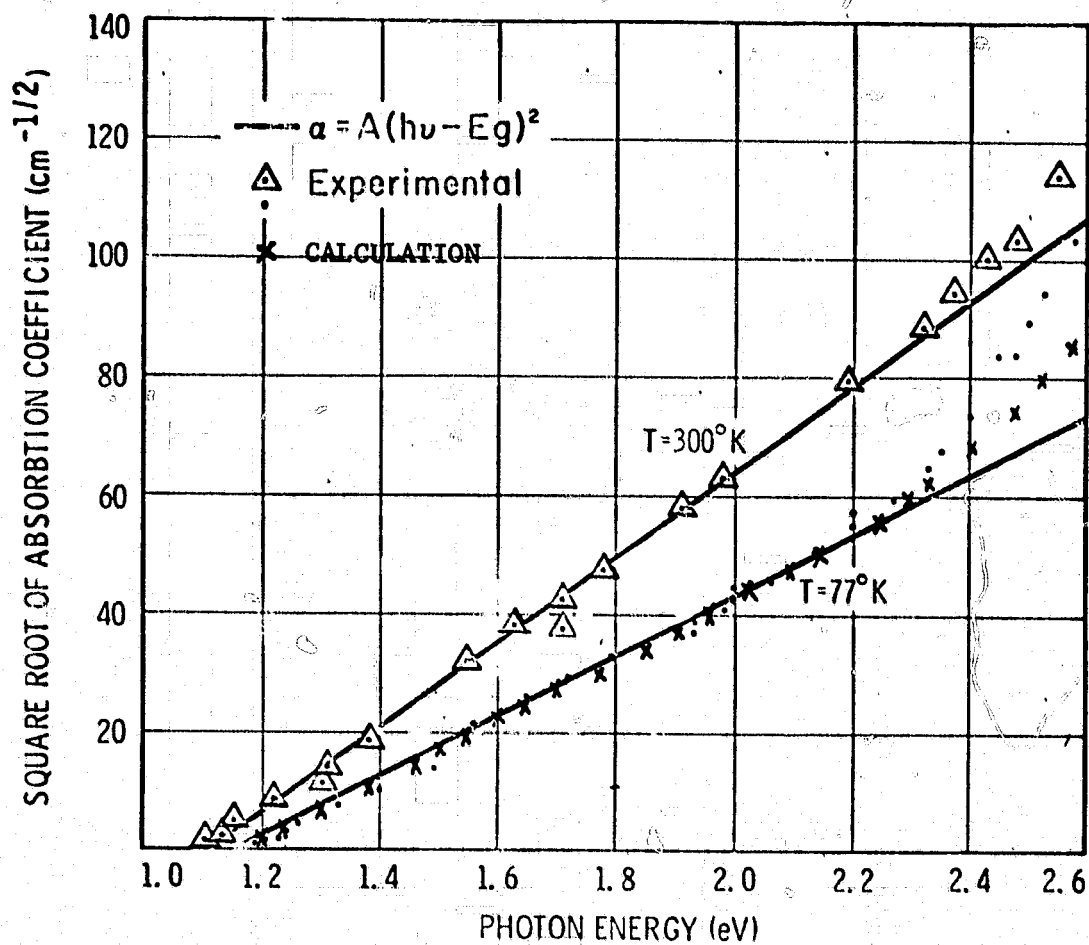
Figure 4.2. Comparison of the calculated absorption coefficient and experimental measurement at 77°K.

The general correlation between calculation and experiment shows the ability to determine the absorption coefficient as a function of temperature by suitable horizontal and vertical translations of the $\alpha-\lambda$ curves. Since the major portion of the solar spectral intensity is located at photon energy below about 2.5 eV, the deviation of the predicted absorption coefficient for higher energy photons has only small effects on the predicted short circuit current density.

The temperature dependence of the refractive index is taken from reference [16] for the wavelength range from 0.18 μm to 1.1 μm. However, the temperature coefficient of the refractive index has a very small value of 5×10^{-3} %/K°.

4.3 The Temperature Dependence of Short Circuit Current as a Function of Base Doping Density and Radiation Dose

The variation of the short circuit current as a function of temperature can be conveniently defined by the normalized temperature coefficient K_I of the short circuit current

$$K_I = \frac{1}{I_{SC}(T_o)} \cdot \frac{dI_{SC}(T_o)}{dT}, \tag{4.17}$$

where T_o is a convenient reference of temperature such as 0°C or 27°C. Several reported experimental results for conventional silicon solar cells have been compiled in Tables 4.1 and 4.2 [3,4,17,18].

Theoretical calculations were made to compare with this experimental data. The diffusion length was kept constant with respect to the temperature variation in the calculation. (A few calculations using constant lifetime are also attempted. However they have given identical results.) A modified generation rate, which is calculated from the linearly horizontally and vertically shifted absorption coefficient, was used.

A violet-cell model has been assumed to be a typical structure of 250 μm thickness, 0.12 μm junction depth, and 0.5 μm high-low junction with a 600 Å thickness of Ta_2O_5 for an anti-reflection film. The base layer has been assumed to have a doping density of $10^{16}/cm^3$ and the surface layer has a doping density of $10^{20}/cm^3$ with a profile of a complementary error function. The model of the conventional cell has been assumed to have a structure of 300 μm thickness and 0.25 μm junction depth with an 800 Å thickness of SiO. The base and surface doping density are assumed to have values of $1.3 \times 10^{15}/cm^3$ and $2 \times 10^{20}/cm^3$, respectively. The one MeV electron radiation damage coefficient K_L is assumed to be 9×10^{-11} e/cm^4 and 2.5×10^{-10} e/cm^4 for 10 Ω-cm and 1.3 Ω-cm p-type silicon substrates respectively.

Several characteristics of the calculated normalized temperature coefficient of short circuit current are found to be in agreement with experimental measurement. The I_{sc}-T curves were found generally not to be a linear function of temperature. The nonlinear behavior intensified at larger radiation doses. This characteristic has been reported previously [19]. Also it was found that the normalized temperature coefficient of short circuit current has a larger value at a heavier radiation dose. This is due to more photon-generated carriers available near the surface through the absorption coefficient change with temperature. Hence the rate of increase of short circuit current with temperature is higher for the solar cells with a shorter diffusion length after radiation bombardment.

The compiled data are shown in Figure 4.3 along with the calculated results. In Tables 4.1 and 4.2, the temperature coefficient of short

Table 4.1. Normalized temperature coefficient of short circuit current density for 10 Ω-cm conventional silicon solar cell.

		TEMPERATURE (C°)			1Mev Electron Radiation Dose (e^-/cm^2)				
		T_o	ΔT	0	10^{13}	10^{14}	10^{15}	5×10^{15}	10^{16}
a.	Faith [3]	0	0–200	–	7.0	11.0	16.0	22.0	25.0
b.	Luft [4]	28	10–80	5.93	–	10.2	13.1	–	20.7
c.	Luft [4]	28	10–80	7.2	–	12.0	16.5	–	31.3
d.	Curtin [17]	25	15–55	5.3	–	–	10.0	13.0	–
e.	RCA [17]	–	–	5.0	5.0	10.0	15.0	–	20.0
f.	Martin [18]	23	13–54	6.2	–	–	–	14.6	–
	Mean Value			5.9	6.0	10.8	14.1	16.5	24.2
	Standard Deviation			0.77	1.0	0.72	2.2	3.9	2.7

Table 4.2. Normalized temperature coefficient of short circuit current for 1~3 Ω-cm, n^+p silicon solar cell.

	TEMPERATURE (°C)		1 MeV Electron Radiation Dose (e^-/cm^2)					
	T_o	ΔT	0	10^{13}	10^{14}	10^{15}	5×10^{15}	10^{16}
a. Faith [3]	0	0-200	–	7.2	7.6	10.5	20.0	25.0
b. Curtin [17]	25	15-55	4.5	5.6	9.5	13.0	18.0	–
c. Martin [18]	28	13-54	6.2	–	–	–	13.9	–
Mean value			5.4	6.4	8.6	11.8	17.3	25
Standard Deviation			0.85	0.8	0.9	1.3	1.9	–

10^3

10^2

$\frac{1}{I_{SC}} \cdot \frac{\Delta I_{SC}}{\Delta T}$ (10^{-4}/K°)

10

10^0

CELL (Ω-CM)	10	1-3
EXPERIMENT	o	x
CALCULATION	Δ	□

10^0 10^{13} 10^{14} 10^{15} 10^{16}

RADIATION   DOSES   (e/CM^2)
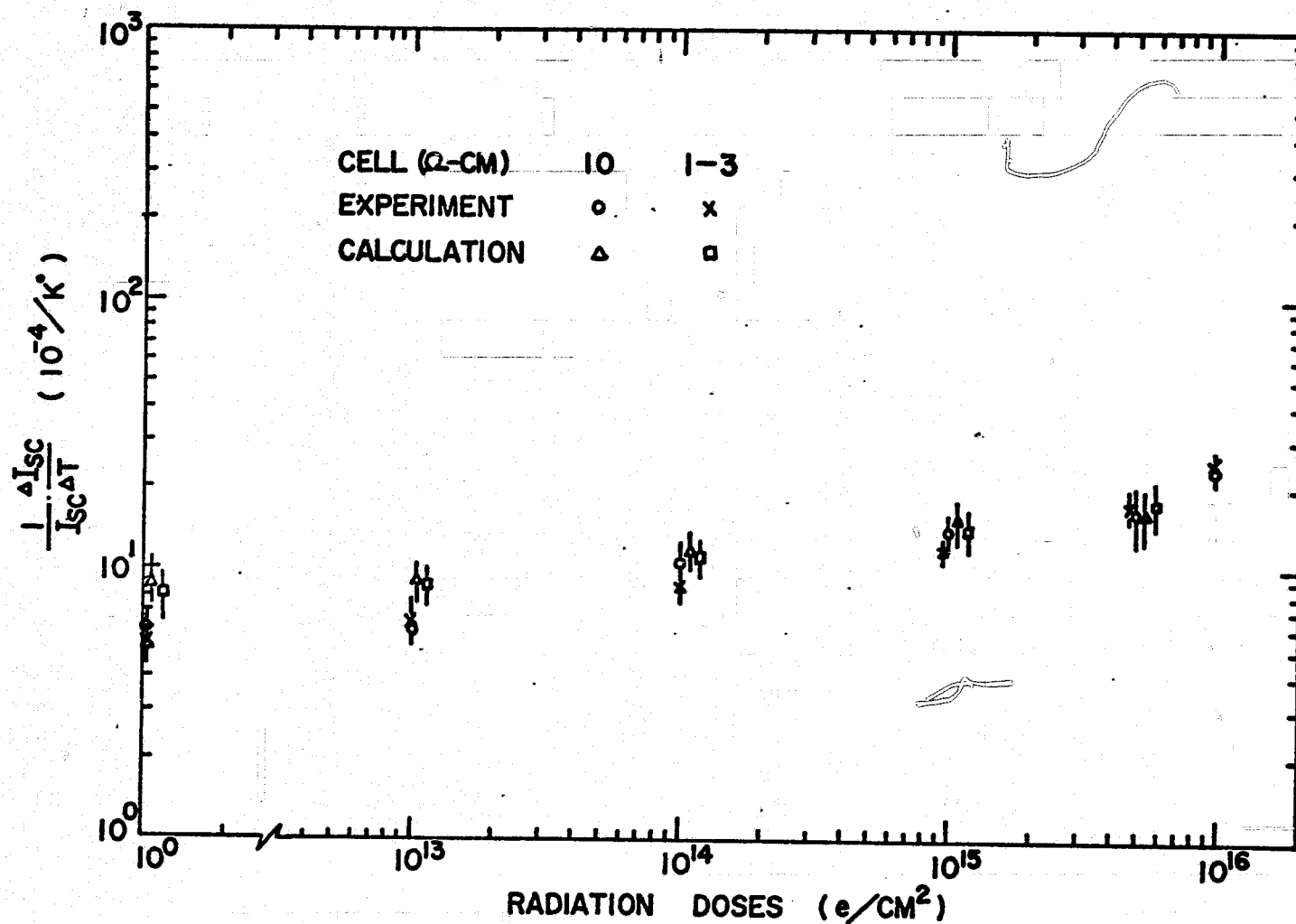
Figure 4.3. Normalized temperature coefficient of short circuit current density as a function of one MeV electron radiation.

circuit current was measured within the temperature range ΔT and normalized to $I_{SC}(T_o)$. Despite the minor differences of these measurements, the mean value and standard deviation of the normalized temperature coefficient K_T were calculated and shown in Figure 4.3. On the other hand, the numerical calculation was performed in two temperature ranges of 27°C to 77°C and 27°C to 127°C respectively. The normalized temperature coefficient K_I was then calculated within these temperature ranges and normalized to I_{SC} (27°C). Therefore, a mean value and standard deviation of K_I can be calculated with respect to the above temperature ranges.

The predicted value of K_I is higher than the measured value at the pre-irradiation condition. This discrepancy could be due to an improper initial diffusion length used in the calculation. However the comparison between measured and calculated values is pretty good at high radiation dose density where the diffusion length is primarily determined by the radiation damage coefficient K_L irrespective of the initial value assumed.

4.4 Discussions and Conclusions

Although the small positive temperature coefficient of short circuit current has been a well known experimental result, the physical explanation has been unsatisfactory. Wysocki and Rappaport discussed the dependence of diffusion length on temperature [20]. Luft suggests that it is the increase in the minority carrier lifetime with temperature which improves the red response of the long wavelength photons.

He also surmised that the higher normalized temperature coefficient
after heavy radiation bombardment is due to the stronger tempera-
ture dependence of the carrier lifetime for the heavily radiated cells
than for the lightly radiated cells. However, the temperature dependent
absorption coefficient and generation rate were found to have the
dominant influence in this work and these were not considered by
these previous authors.

One factor, which may affect the temperature coefficient of short
circuit current, is the reduction of the forbidden bandgap and
consequently its effect on long wavelength response. However, the
chances of collecting these long wavelength photons are very small due
to the low absorption coefficient of 10/cm or less. The short circuit
current contributed from this spectral range can be calculated by the
Equation [21] as

$$J_{SC}(\lambda) = \frac{qN_{phi}\alpha L_D}{1 + \alpha L_D} \left[1 - \frac{e^{-W/L_D} - \alpha L_D e^{-\alpha/L_D}}{(1-\alpha L_D)\cosh W/L_D}\right]. \qquad (4.18)$$

The calculation shows a negligible effect because of the small solar
spectrum density and small absorption coefficient in this long wave-
length range. Another factor, which has been suggested as responsible
for the temperature dependence of short circuit current, is the high
temperature annealing effect of the minority carriers [55]. However,
the above cited experiments except reference [3] were carefully performed
near room temperature to avoid any annealing effects.

1. S. M. Sze. 1969. Physics of Semiconductor Devices. John Wiley Co., New York, New York.

2. F. J. Morin and J. P. Maita. 1954. Phy. Rev. 96: 28.

3. T. J. Faith and A. F. Obenschain. 1973. Temperature, Illumination, and Fluence Dependence of Current and Voltage in Electron Irradiated Solar Cells. Tenth Photovoltaic Specialists Conference, Palo Alto, CA: 384-392.

4. W. Luft. 1965. Effects of Electron Irradiation on N or P Silicon Solar Cells. Advanced Energy Conversion 5: 21-41.

5. R. K. Yasui and L. W. Schmidt. 1970. Eighth Photovoltaic Specialists Conference, Seattle, WA: 110.

6. A. R. Gobat, M. F. Lamorte and G. W. McIver. 1962. IRE Trans. Military Electron 6: 20.

7. H. J. Hovel and J. M. Woodall. 1973. J. Electrochem Soc. 120: 1246.

8. E. M. Conwell. 1952. Proc. IRE 40: 1327. Also RTI Report ASD-TDR-63-316 V, 1964.

9. B. Ross and J. R. Madigan. 1957. Thermal Generation of Recombination Centers in Silicon. Phy. Rev. 108: 1428-1433.

10. M. Wolf, G. T. Noel and R. J. Stirn. 1977. Investigation of the double exponential in the Current-Voltage Characteristics of Silicon Solar Cells. IEEE Trans. on Elect. Dev. ED-24(4): 419-428.

11. J. Mandelkorn, C. R. Baraona and J. H. Jr. Lamneck. 1972. Ninth Photovoltaic Specialists Conference, Siver Spring, MD: 15.

12. T. P. McLean. 1960. The Abosrption Edge Spectrum of Semiconductors. Progress in Semiconductor 5, John Wiley, New York, New York: 53-102.

13. D. W. Spaderna and D. Navon. 1977. Solar Cell Operation Under Concentrated Illumination. Private Communication.

14. W. C. Dash and R. Newman. 1955. Intrinsic Optical Absorption in Single-Crystal Germanium and Silicon at 77°K and 300°K. Phy. Rev. 99: 1151.

15. A. Shumka. 1970. Temperature Effects of Silicon Solar-Cell Short-Circuit Currents. Eighth Photovoltaic Specialists Conference, Seattle, WA: 96-101.

16. W. Paul and H. Brooks. 1963. Progress in Semiconductors 7, John Wiley and Sons, New York, New York: 135.

17. D. J. Curtin and R. W. Cool. 1973. Qualification Testing of Laboratory Produced Violet Solar Cells. Tenth Photovoltaic Specialists Conference, Palo Alto, CA: 139-152.

18. J. H. Martin, R. L. Statler and R. L. Ralph. 1967. Radiation Damage to Thin Silicon Solar Cells. Proc. of Intersociety Energy Conversion Engineering Conference: 289-296.

19. L. J. Goldhammer and L. W. Slifer, Jr. 1977. ATS-6 Solar Cell Flight Experiment Through Two Years in Orbit. Twelfth Photovoltaic Specialists Conference: 199-207.

20. J. J. Wysocki and P. Rappaport. 1961. Effect of Temperature on Photovoltaic Solar Energy Conversion. Journal of Applied Physics 31: 571-578.

21. A. Meulenberg, Jr., J. F. Allison, R. A. Arndt and J. G. Haynos. 1975. Radiation Damage to the COMSAT Non-Reflective Cell. Eleventh Photovoltaic Specialists Conference, Scottsdale, AZ: 204-208.

5. KELDYSH-FRANZ EFFECT AND SILICON SOLAR CELLS

5.1 Introduction

The effect of high doping density on limiting the efficiency and open circuit voltage of a silicon solar cell has been recognized for many years. Experiments have shown that a low resistivity cell does not produce high open circuit voltage. This is not consistent with the simple theoretical predictions. However it is generally believed that increasing the output voltage is a key factor for obtaining a high efficiency solar cell [1,2]. Therefore, the real physical limitations of low open circuit voltage need to be identified for low resistivity solar cells.

Many hypotheses have been given to explain the inconsistancy between the predicted and the achieved voltage performance of a low resistivity silicon cell. The heavy doping effects have received much attention [3]. There are also other explanations and speculations. For example, it has been suggested that an excessive recombination current occurs in a heavily doped cell and the open circuit voltage is thereby reduced. However, the measured short circuit current and diffusion length of low resistivity cells has shown that this is not the primary factor in limiting the cell performance [3]. Recently the so-called Keldysh-Franz effect has been postulated and examined [4].

The purpose of this section is to investigate the low output voltage performance of a low resistivity silicon cell and to assess the relative influence from the Keldysh-Franz effect. The Keldysh-Franz effect is modeled by an equivalent bandgap reduction in the depletion region from a

high internal electric field. Therefore the temperature dependence of
the forward and reverse dark I-V characteristics can be calculated and
used to identify the real V_{oc} limitations by several proposed physical
effects.

5.2 Keldysh-Franz Effect

In 1958 Franz [5] and Keldysh [6] independently calculated and
predicted the so-called Keldysh-Franz effect, which is tunneling assisted
light sbsorption. The essential idea of this theory is that the elec-
trons tunnel into the forbidden band before optical absorption can occur.
This results in a broadening of absorption and can be treated like a band-
gap shift with the electric field of

$$\Delta E_g(E) = [\frac{h^2}{2\pi m*} (qE)^2]^{1/3}. \tag{5.1}$$

This shift of the fundamental absorption edge has been observed for many
semiconductors such as Ge, Si, GaAs, etc. The space charge recombination
current density will thereupon increase by a factor of $\exp(\Delta E_g(E)/2kT)$ as

$$I_R = \frac{qn_1}{\tau_{po}+\tau_{no}} W_D \frac{2\sinh(qV_J/2kT)}{(V_o-V_J)q/kT} \cdot f(b) \cdot \exp(q\Delta E_g(E)/2kT). \tag{5.2}$$

Therefore the recombination current becomes important for high bandgap
and heavily doped materials and at low temperature because of this
Keldysh-Franz effect.   These phenomena are generally consistent with
the experimental observations.

In this work an empirical value of the bandgap reduction as a
function of internal electric field has been taken from the work of

Britsyn and Smirnov [7]. Their results have confirmed the functional
dependence of the Keldysh-Franz effect on the electric field strength.

5.3 Junction Analysis and the Electric Field in the Depletion Region

At a p-n junction there exists a strong internal electric field from
the potential barrier. It is known that such an internal electric field
can alter the bandgap through the Keldysh-Franz effect. Thus the forward
or reverse dark current density will be increased by the enhanced deple-
tion region recombination current density. From Equation (5.2) it is
clear that the recombination current density is higher at low resistivity
and low temperatures. In order to predict the importance of Keldysh-
Franz effects on a silicon solar cell, the complete Poisson equation
must be numerically solved. The effective electric field is calculated
for the unperturbed or perturbed bandgap along the p-n junction. The
forward and reverse dark current densities are next determined. The
effective electric field in the depletion region is plotted in Figure
5.1 for the model cell of Table 5.1.

Table 5.1. Material and dimensional parameters.

Table 5.1 Material and Dimensional parameters

Cell Thickness	250 μm
Cell Structure	n^+p
n^+ Thickness	1 μm
n^+ Doping concentration	$4 \times 10^{20}/cm^3$, erfc
p Doping concentration	$5 \times 10^{17}/cm^3$, (0.1 Ω-cm)
Diffusion length in p region	100 μm
Diffusion length in n^+ region	$(L_D(MED) + L_D(MIN))/2$
Surface recombination velocity	10^3 cm/sec

The characteristics of the electric field in the depletion region is changed after considering the Keldysh-Franz effect. The peak electric field is reduced; while the strong field region is broadened. This is a direct consequence of the bandgap variation with the electric field in the depletion region. The peak electric field is located near the n^+p metallurgical boundary where there is the greatest bandgap reduction. Therefore the peak electric field will be decreased due to the lower forbidden barrier height.

The dark current density is presented in Figure 5.2 and 5.3 for the forward and reversed biased conditions respectively. The higher current density after considering the Keldysh-Franz effect is basically from the enhanced recombination current density in the depletion region. It is estimated from Figure 5.2 that the reduction of open circuit voltage due the Keldysh-Franz effect is approximately 6, 8 and 11 mV at temperatures of 350°K, 300°K and 250°K, respectively.
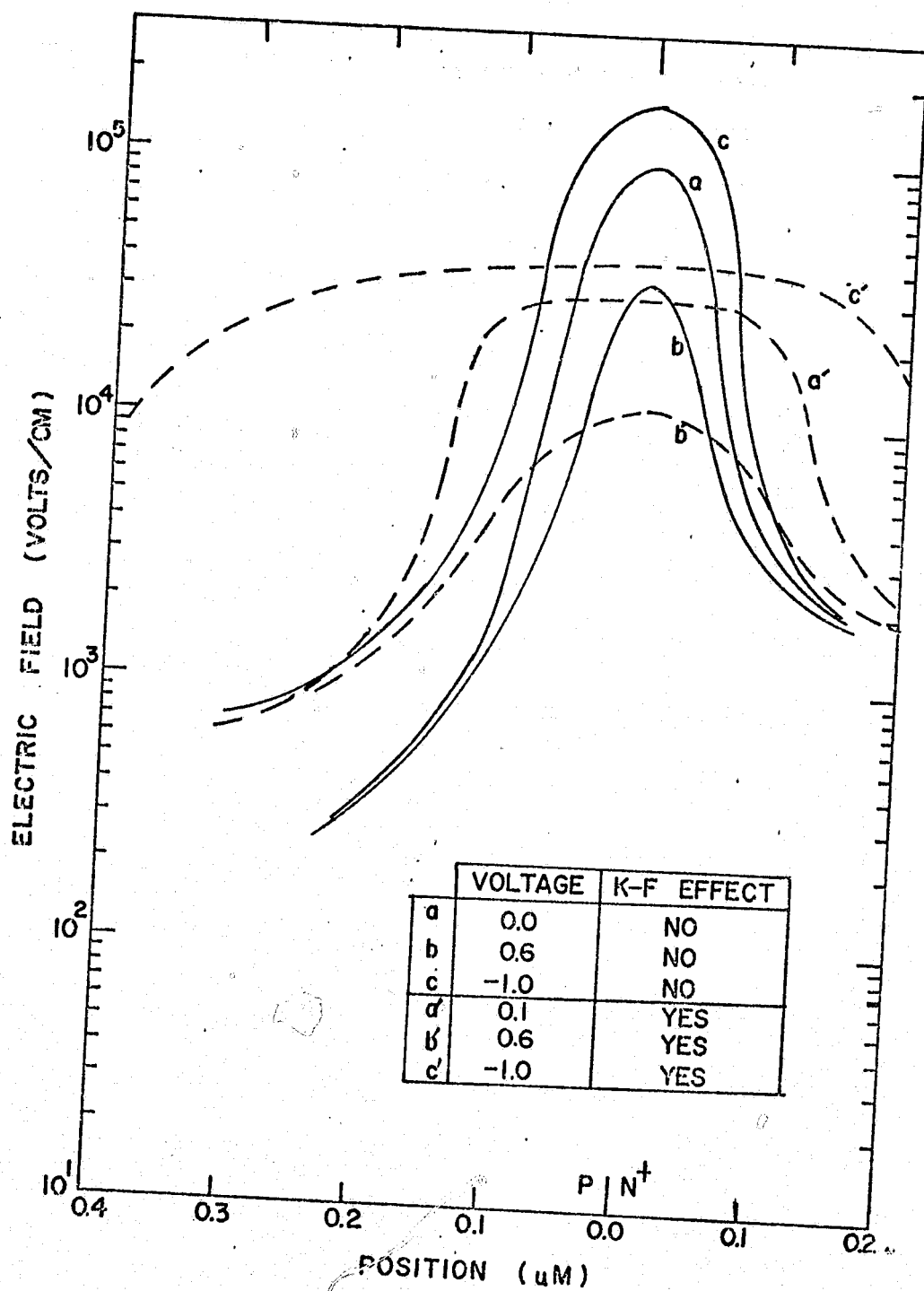
Figure 5.1. The electric field in the depletion region of a n⁺p solar cell.

	VOLTAGE	K-F EFFECT
a	0.0	NO
b	0.6	NO
c	-1.0	NO
a′	0.1	YES
b′	0.6	YES
c′	-1.0	YES

C - 2
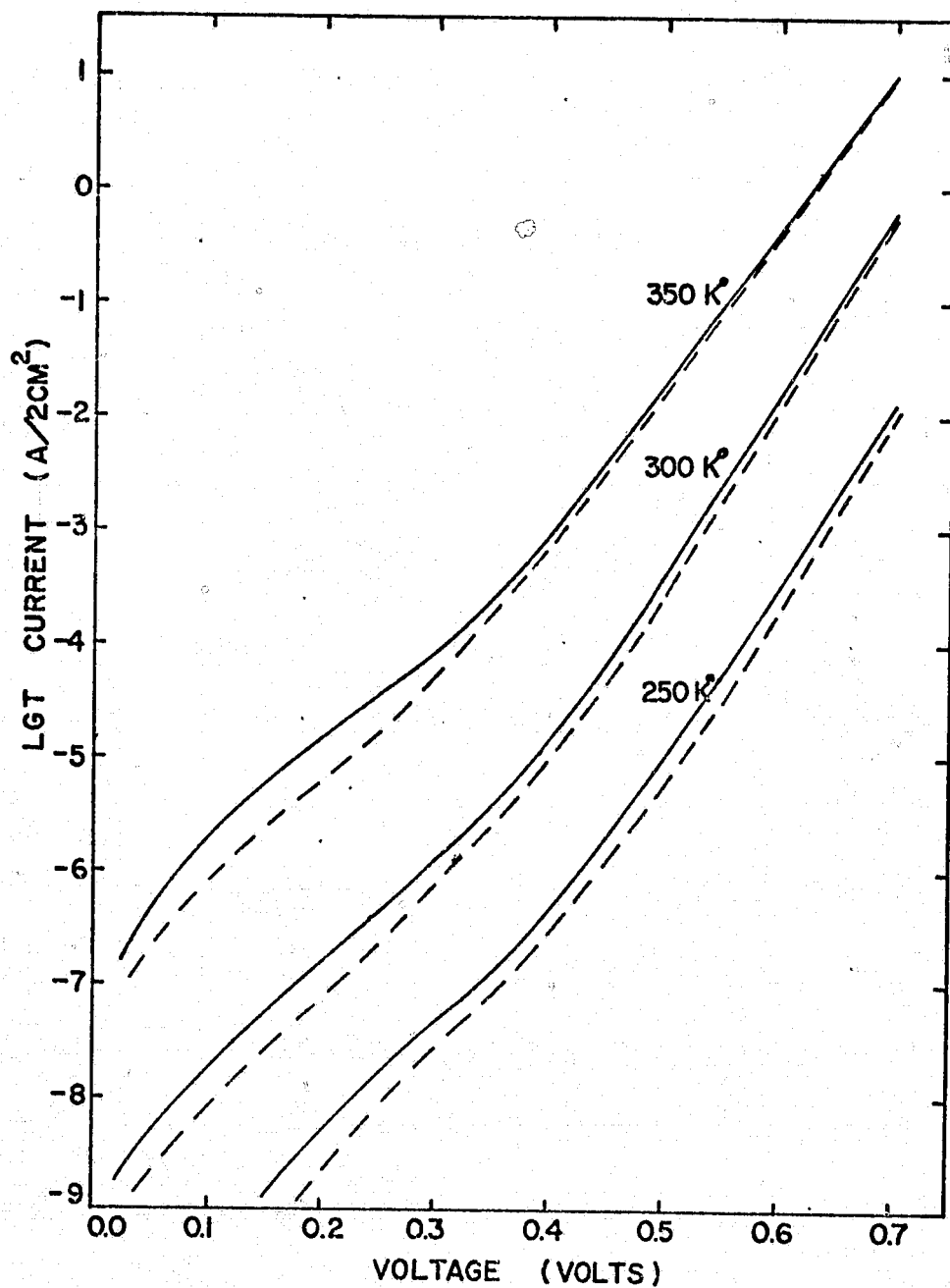
Figure 5.2. Forward dark I-V characteristics with (solid lines) or without (dashed lines) Keldysh-Franz effects.
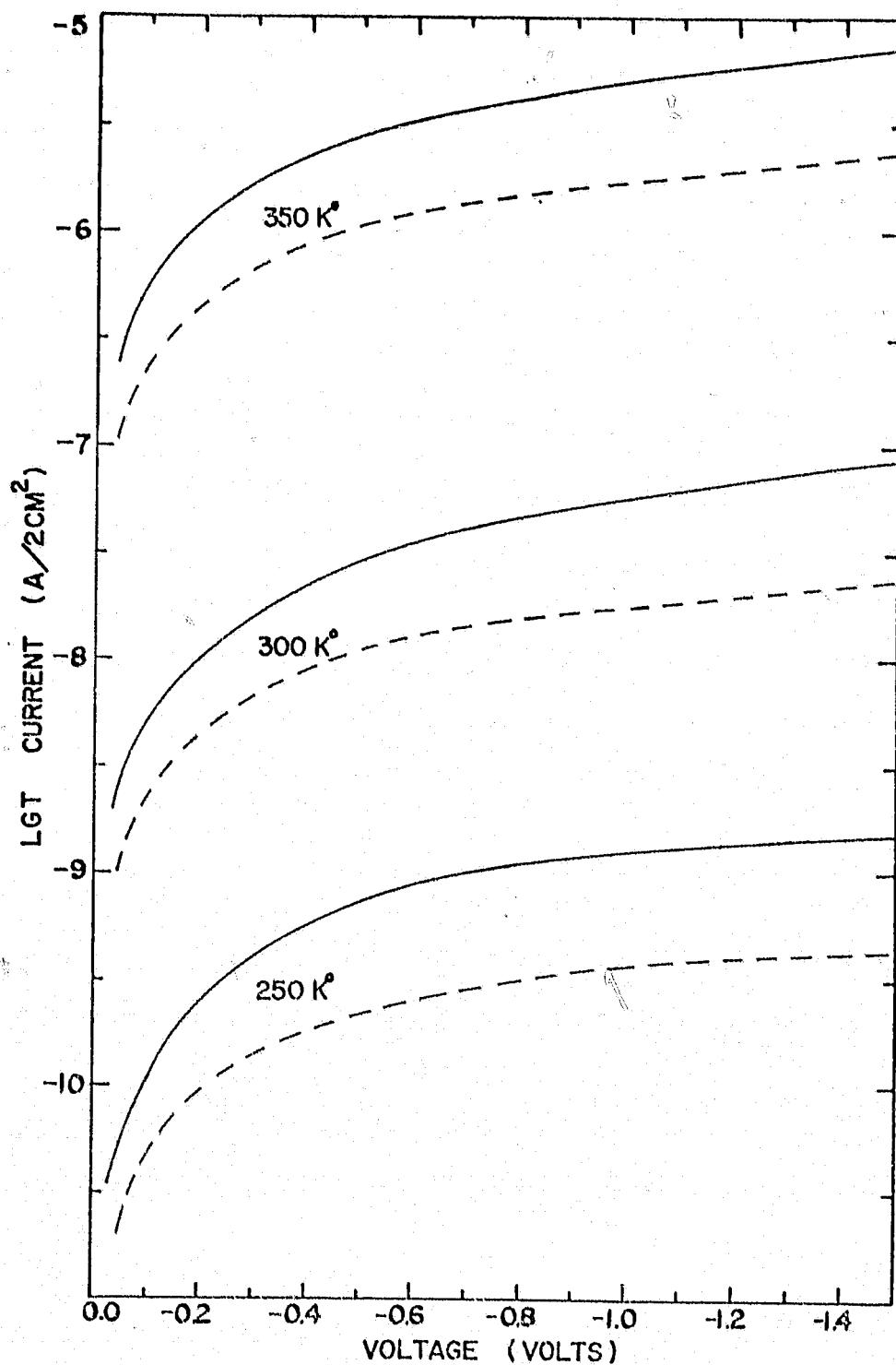
Figure 5.3. Reversed dark I-V characteristics with (solid lines) or without (dashed lines) Keldysh-Franz effects.

5.4 Heavy Doping Effect

It has been recognized that the heavy doping effects on minority carriers can be treated by either an effective intrinsic carrier concentration or by an effective doping density [2,8]. The reduced effective surface doping density of a conventional silicon solar cell is found to be responsible for the low voltage output of a low resistivity cell [1]. This also leads to the reduction of the emitter efficiency and current gain β of a transistor [9].

Figure 5.4 shows the effective surface doping profile as a function of temperature. The characteristics of the effective doping density can be used to explain the influence of emitter doping on the temperature sensitivity of the emitter efficiency of a transistor [9]. However, this point will not be discussed here. The reduction of the output voltage of a highly doped cell is a consequence of the lower effective surface doping density which greatly increases the surface back injection current density. At the same time short circuit current density is decreased by the retrograde field near the surface.

The percentage of the surface injection current density to the total current density is shown in Table 5.2 at forward voltage of 0.5, 0.6 and 0.7 volts for temperatures of 300°K and 350°K respectively. It is clear that the back injected current density has an abnormally large value for a low resistivity cell.
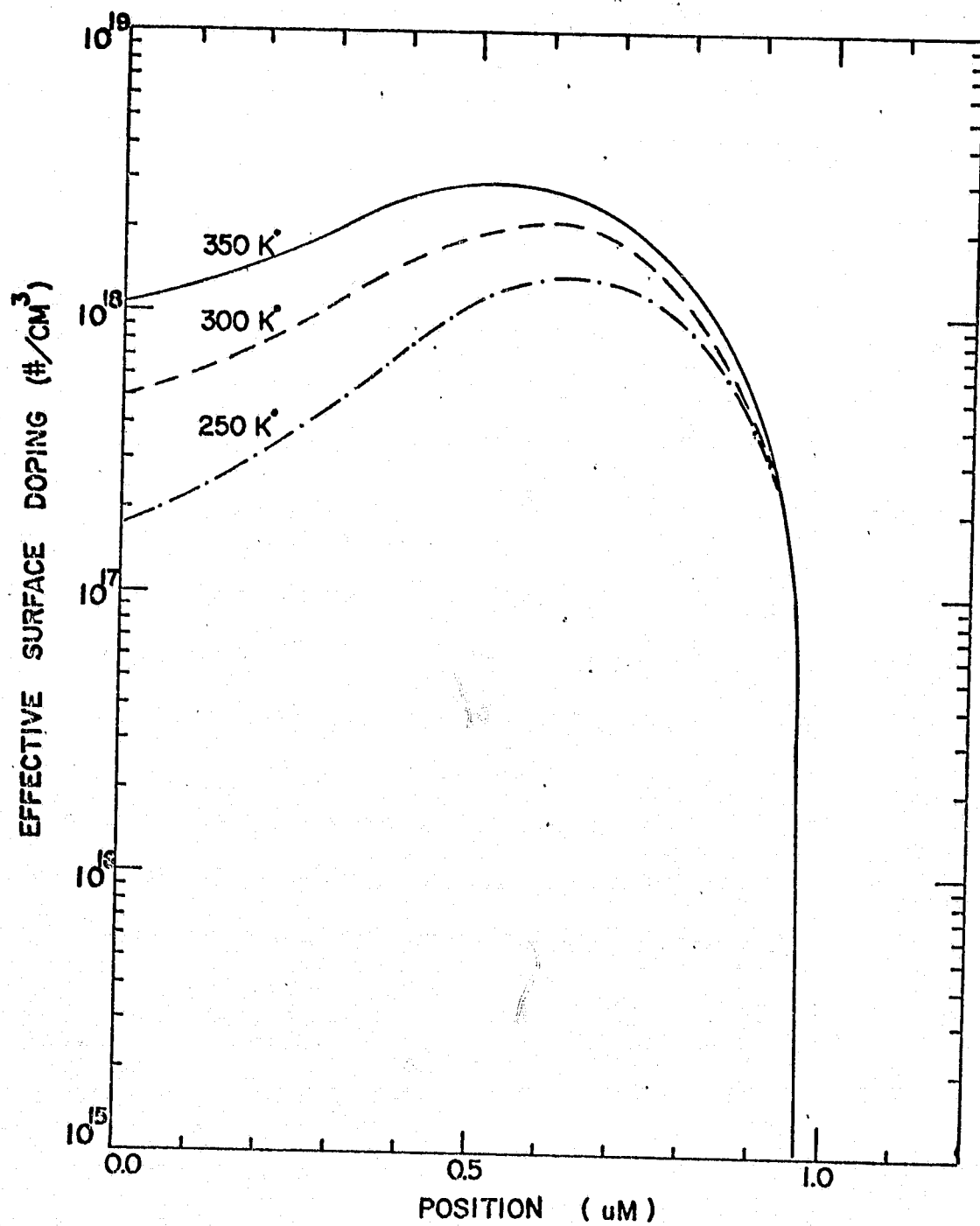
Figure 5.4. Effective surface doping density as a function of temperature and distance from the surface.

Table 5.2 Percentage of surface injection current to the total current density as a function of temperature.

T V(volts)	350°K	300°K
0.5	31.4	55.9
0.6	38.6	71.9
0.7	40.5	72.3

5.5 Discussions and Conclusions

Although the so-called Keldysh-Franz effect was originally investigated for the optical absorption properties of a semiconductor or insulator, this effect on the efficiency of a heavily doped silicon solar cell is not clear. Our calculation shows that this effect is not very important as compared to the heavy doping effect for a cell with 0.1 Ω-cm base resistivity. On the other hand, the Keldysh-Franz effect is found to be important in a first order calculation which assumes an unperturbed bandgap structure. However our model takes into account the perturbed bandgap with an effective electric field. The effective electric field is thereupon reduced because of the smaller bandgap in the depletion region. Therefore, these calculations predict a small influence due to the Keldysh-Franz effect for a silicon solar cell.

5.6. REFERENCES

1. M. P. Godlewski, H. W. Brandhorst, Jr., and C. R. Baraona. 1975. Effects of High Doping Levels on Silicon Solar Cell Performance. Eleventh Photovoltaic Specialists Conference, Scottsdale, AZ: 32-35.

2. P. M. Dunbar and J. R. Hauser. 1975. Efficiency of silicon solar cells as a function of base layer resistivity. Proc. Eleventh IEEE Photovoltaic Spec. Conf., Scottsdale, AZ: 13-18.

3. P. A. Iles and S. I. Soclof. 1973. Effect of impurity doping concentration on solar cell output. Tenth Photovoltaic Specialists Conference, Palo Alto, CA: 19-24.

4. E. S. Rittner. 1977. Improved Theory of the Silicon P-N Junction Solar Cell. Journal of Energy 1(1): 9-17.

5. W. Franz. 1958. Influence of an Electric Field on the Optical Abosrption Edge. Zeitschrift für Naturforschung 13a: 484-489.

6. L. N. Keldysh. 1958. The Effect of a Strong Electric Field on the Optical Properties of Insulating Crystals. Journal of Experimental Theoretical Physics (USSR) 34: 1138-1141.

7. K. I. Britsyn and A. A. Smirnov. 1966. Change in the width of the forbidden band of silicon in the electric field of a p-n junction. Soviet Physics Solid State 18: 126-128.

8. R. J. VAN Overstraeten, H. J. DeMAN and R. P. Mertens. 1973. Transport Equations in Heavily Doped Silicon. IEEE Trans. on Electron Devices ED-20(3): 290-298.

9. H. J. DeMAN. 1971. The Influence of Heavy Doping on the Emitter Efficiency of a Bipolar Transistor. IEEE Trans. on Electron Devices ED-18(10): 833-835.

6. THIN SILICON SOLAR CELLS

6.1 Introduction

For years there has been a great interest in experimentally producing very thin solar cells in the range of 50 μm. Such cells can be used to minimize power loss in the base region under large solar concentration. They are also required to produce lightweight space solar power systems. The interest in thin solar cells is also enhanced by the economical consideration that there is less kerf loss from the ingot cutting process. The cost from the silicon wafer can thereupon be minimized. Recently thin silicon solar cells have been fabricated using an improved low kerf loss ingot cutting process [1] and by non-preferrential etching in a NaOH solution [2].

These new technological breakthroughs are inevitably leading to new interest in a better understanding of thin cells, where there are more interactions between the incident photons and the back surface. High injection effects and the high-low junction leakage current can be studied in such structures. There are also reflections in the optical spectrum between the front and back surfaces in such a thin cell. The purpose of this section is to investigate the physical behavior of a thin solar cell. The conversion efficiency of a thin solar cell under one MeV electron irradiation is also included for cells of several base resistivities.

6.2 Some Characteristics of a Thin Solar Cell

A thin solar cell is a good structure for investigating the physical properties of the interactions between the front and back surface, due to the incident photons as well as the injected carriers.

6.2.1 Optical Interactions Between the Long Wavelength Photons and the Back Surface

A good BSF cell requires a high optical reflectance at the back surface and it should also provide a low surface recombination velocity in order to improve the long wavelength response. Unfortunately, these two requirements are experimentally found to be in conflict with each other [3]. An optically absorbing alloy interface is usually found to provide a higher electron barrier and a lower surface recombination velocity than an optically reflecting interface. The optical reflectance for alloy contacts has been measured in the range of fifty to eighty percent depending on the alloying time and temperature for wavelengths from 1.3 μm to 1.4 μm [3].

It is known that the available optical current density is a function of device thickness and the optical reflectance at the alloyed back surface. Hence it is possible to calculate an ideal collection efficiency as a function of device thickness and the back surface reflectance for a particular solar energy spectrum. Table 6.1 shows this characteristic for AMO and AM2 solar spectrums.

Table 6.1. Available current density as a function of back surface reflectance for a device thickness of 50 μm.

Reflectance			0	0.5	0.8	1.0
Solar Spectrum	Surface	Thickness (Å)	Available current density (mA/cm^2)			
AMO 135.3 (mW/cm^2)	plane	bare	28.8	29.7	30.2	30.5
	CNR	bare	37.4	38.2	38.7	39.0
	plane	Ta$_2$O$_5$,600Å	39.7	40.7	41.2	41.6
	CNR	Ta$_2$O$_5$,600Å	45.2	46.1	46.4	47.0
AM2 74 (mW/cm^2)	plane	bare	17.9	18.5	18.8	19.0
	CNR	bare	25.5	26.2	26.5	26.8
	plane	Ta$_2$O$_5$,700Å	25.8	26.5	26.8	27.1
	CNR	Ta$_2$O$_5$,700Å	28.9	29.6	29.9	30.2

Table 6.1 shows that the improvement in the available current density is only a few percent even for a perfectly reflecting back surface. On the other hand, it has been shown that the minority carrier collection depth is a strong function of the back surface recombination velocity. The collection depth is usually found to be much shorter than the device width due to recombination at a poor high-low junction. The reduction of the collection depth results in a smaller short circuit current for a thin solar cell. Also a poor high-low junction enhances the interaction between the injected carriers and the back alloyed surface and produces a low open circuit voltage and low conversion efficiency. Therefore, it can be concluded that a good high-low junction is much more important than good optical reflectance in improving the conversion efficiency of a thin solar cell with cell thickness of 50 μm or more.

6.2.2 The Interaction of the Injected Carriers and the Back Alloyed Surface

It has been shown that the high-low junction theory is an adequate model for a BSF cell [4,5]. It has also been found that the high-low junction barrier height can be lowered for high injection operation [6]. Hence the high-low junction leakage current cannot be neglected for a solar cell with long base diffusion length and short cell thickness [7]. Figure 6.1 shows the prediction of open circuit voltage as a function of the back surface recombination velcoity of a 10 Ω-cm cell with the parameters of Table 6.2. Curve (a) is calculated using an ideal SRV which is a function of the material characteristics on both sides of the high-low junction. Curve (b), (c) and (d) are calculated by increasing the SRV values by two, ten and one hundred times the ideal SRV values. Reductions in the SRV can occur in a real solar cell from low lifetime or from a high doping density at the high-low junction. It can also occur if there is local surface damage, such as dislocations, etc.

Since open circuit voltage is a direct indication of the interaction between the injected carriers and the back alloyed surface, it can be concluded from the result of Figure 6.1 that a good high-low junction barrier is important for obtaining high output voltage of a thin BSF cell.

In Figure 6.1 an exact numerical calculation of V_{oc} is also presented which shows good agreement with the predictions of first order models.
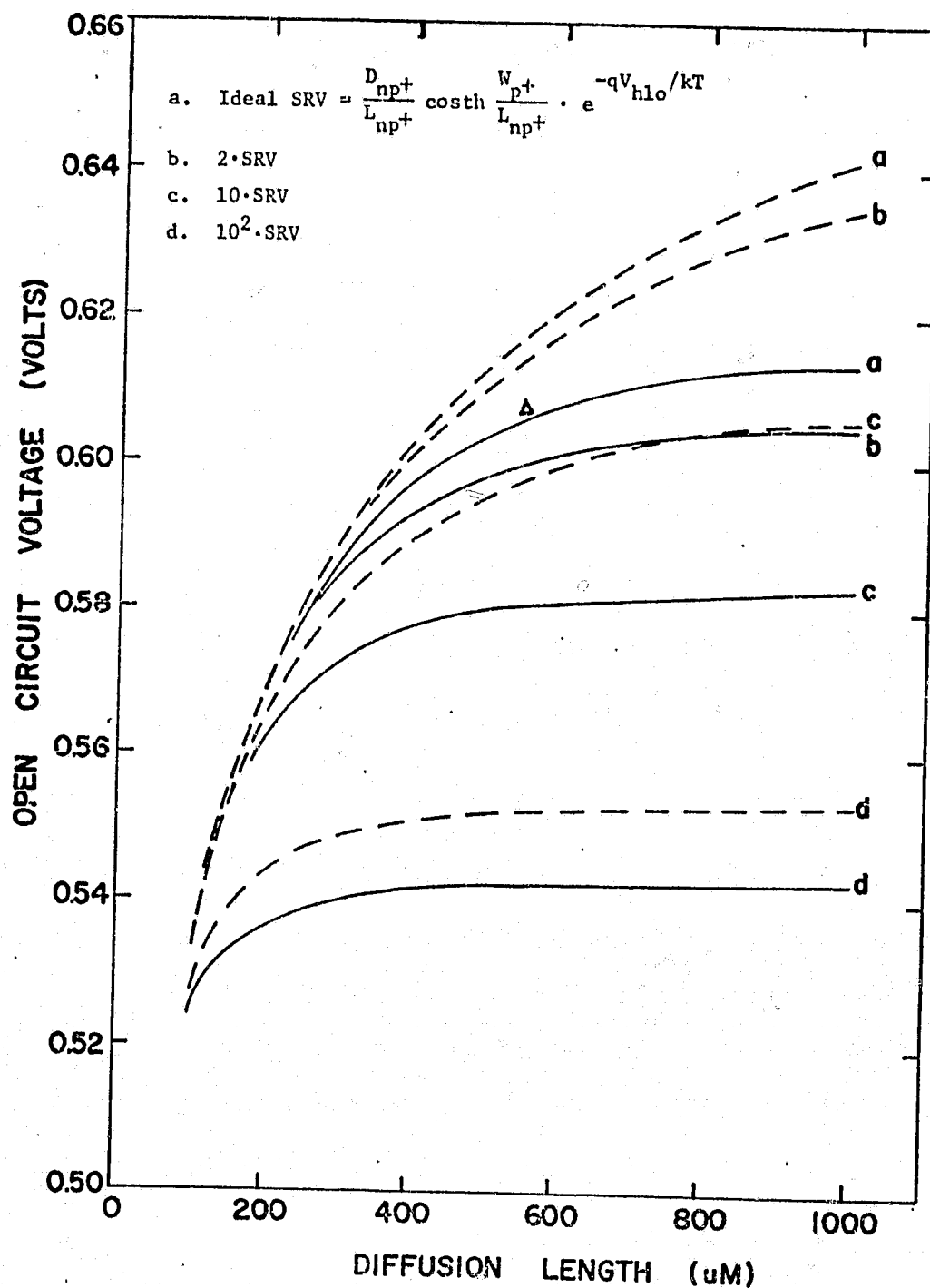
Figure 6.1. Open circuit voltage as a function of base diffusion length and high-low junction SRV for thin solar cells with a base resistivity of 10 Ω-cm. HL junction theory(---), HL junction plus leakage current theory (———), exact numerical calculation under condition a (Δ).

6.3 Numerical Calculations

Since there are several complicated physical interactions between incident photons, and minority carriers with the front and back surfaces, an exact numerical calculation is necessary to accurately predict the performance of a thin solar cell. In order to determine the best material parameters for optimum operation, a series of calculations have been performed. The model parameters are listed in Table 6.2. The radiation damage coefficient K_L is deduced from experimental measurements and shown in Figure 6.2. The results of calculation are shown in Figures 6.3 to 6.6.

Table 6.2. Material parameters of thin solar cells

Structure	$n^+ pp^+$
n^+ density (#/cm^3)	1.5×10^{20} (erfc)
n^+ thickness (μM)	0.15
p density (Ω·cm)	100, 10, 1, 0.3, 0.1
P thickness (μM)	49.35
p^+ density (#/cm^3)	10^{19} (Gaussian)
p^+ thickness (μM)	0.5
Base diffusion length	$(L_D(MAX)+L_D(MED)/2$
Surface diffusion length	$(L_D(MED)+L_D(MIN)/2$
SRV (cm/sec)	10^3
Anti-reflection oxide	Ta_2O_5, 600Å
Double reflection	YES
Radiation coefficient	Figure 6.2.

$$\frac{1}{L^2} = \frac{1}{L_o^2} + K_L \cdot \Phi$$

RESISTIVITY (Ω-CM)

DAMAGE COEFFICIENT K_L
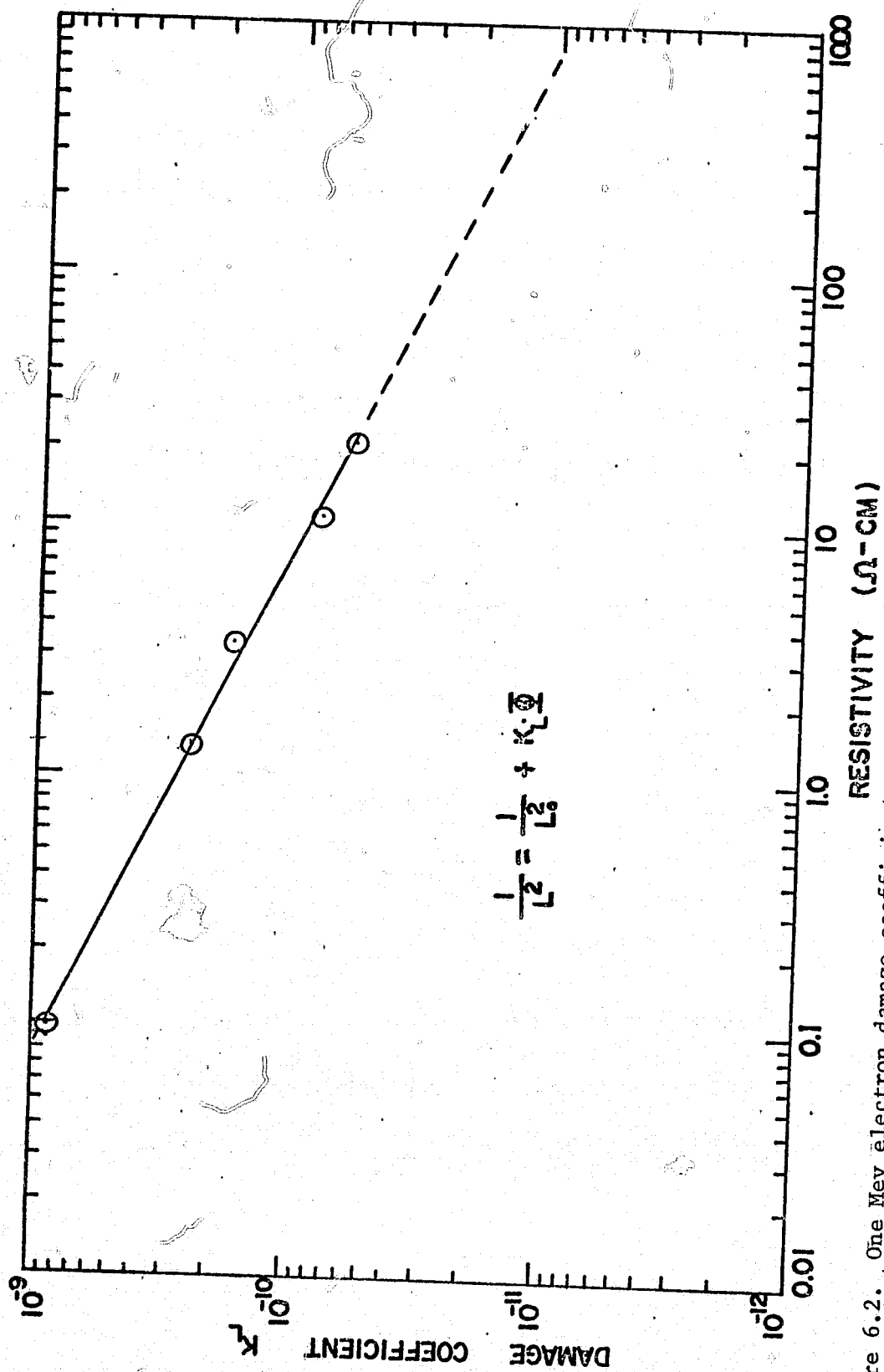
Figure 6.2. One Mev electron damage coefficients as a function of the p-type silicon resistivities.
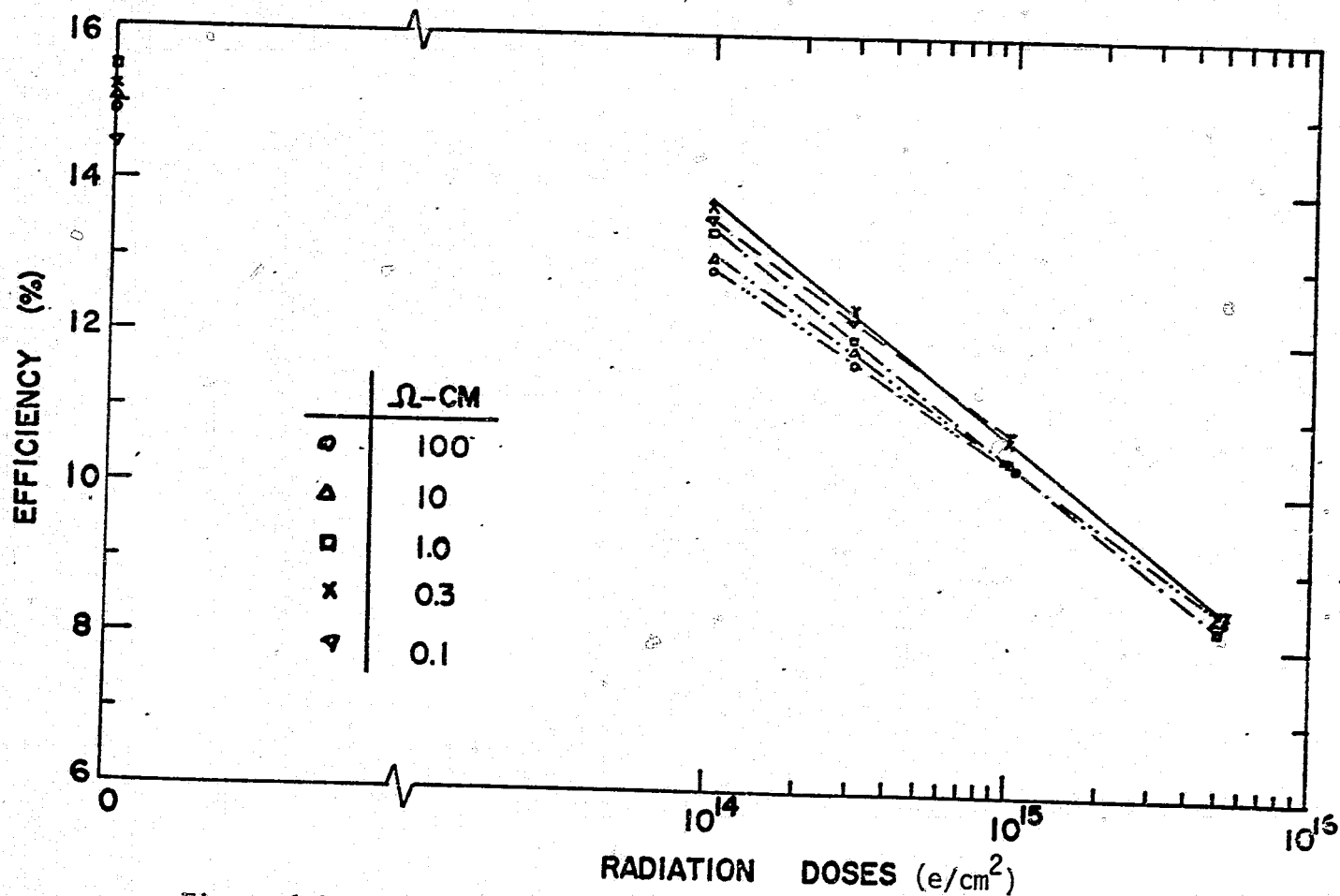
Figure 6.3. Efficiency dependence on 1 Mew electron doses and cell resistivities.
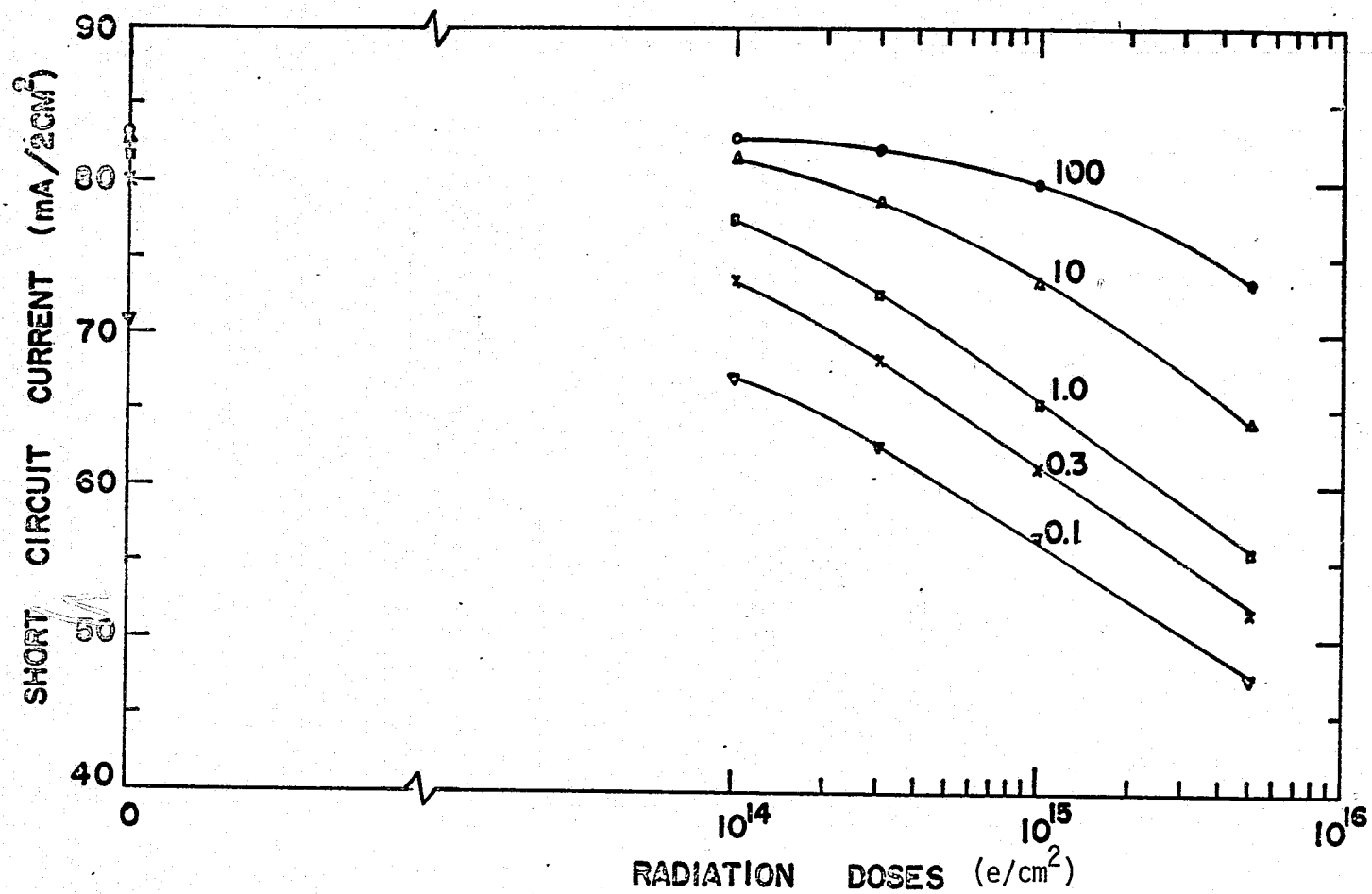
Figure 6.4.   Short circuit current dependence on 1 Mev electron radiation doses and cell resistivities.
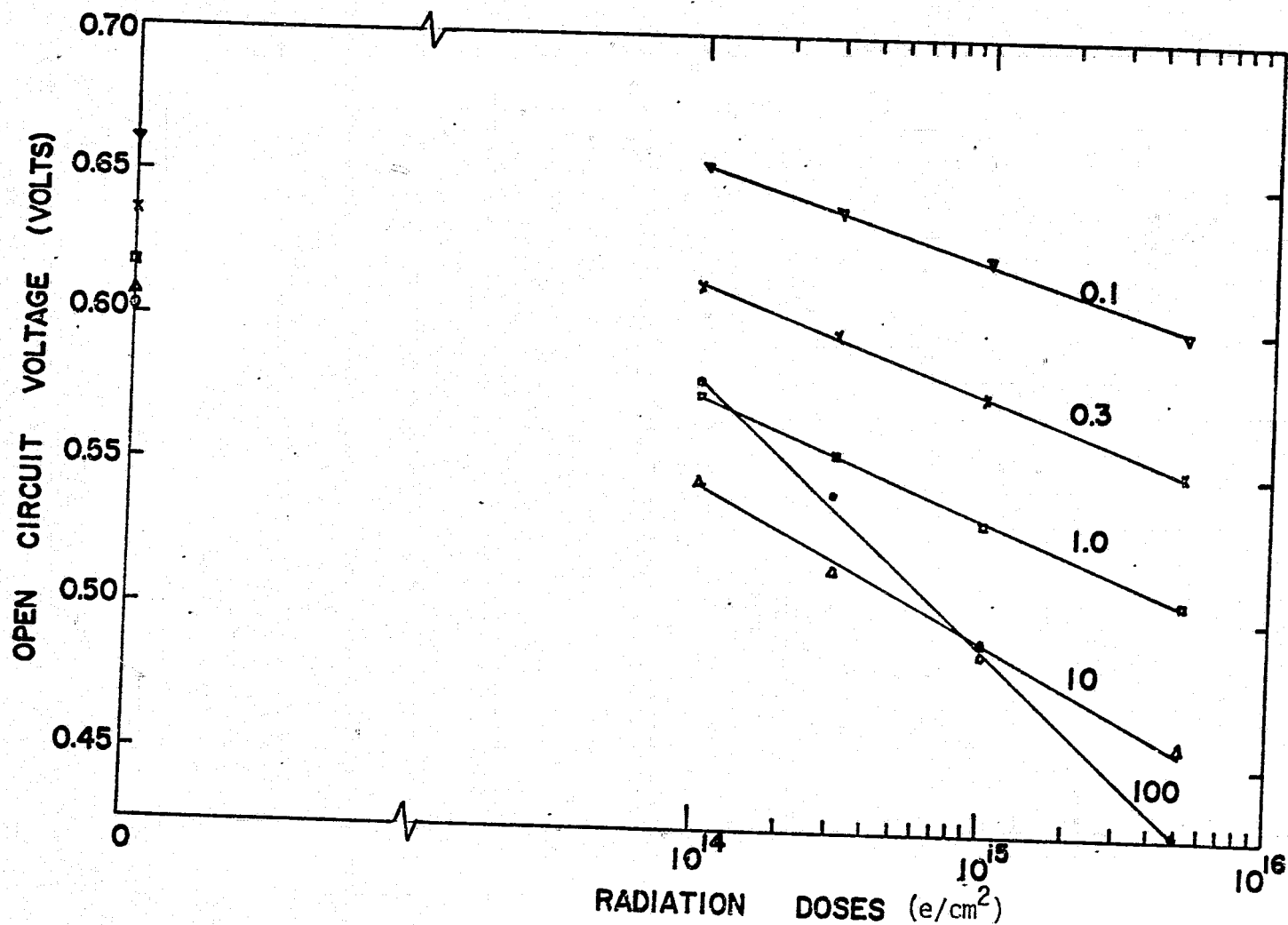
Figure 6.5. Open circuit voltage dependence on 1 Mev electron radiation doses and cell resistivities
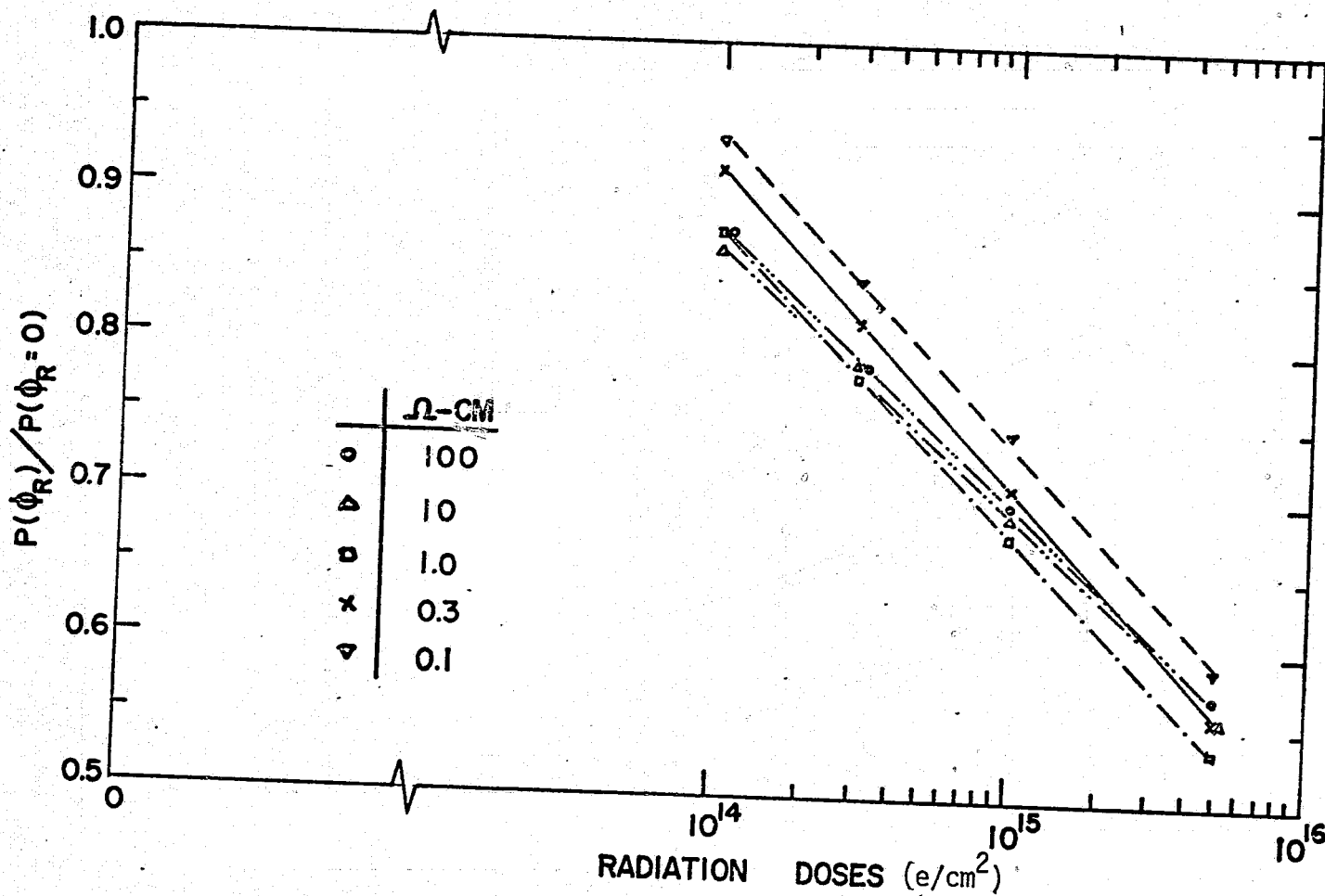
Figure 6.6. Ratio of the peak power densities as a function of 1 Mev electron radiation doses and cell resistivities.

Figure 6.3 shows the conversion efficiency as a function of radiation dose. The optimum material is found to have a base resistivity from 1 Ω·cm to 0.3 Ω·cm for a pre-irradiated cell. However, an optimum base resistivity is located between 0.3 Ω·cm to 0.1 Ω·cm after irradiation. The conversion efficiency is found to be essentially the same for different material parameters after a radiation dose of 5×10^{15} e/cm^3.

Figures 6.4 and 6.5 show the short circuit current and open circuit voltage as a function of radiation dose. It is clear from Figure 6.5 that high injection and an ineffective high-low junction are the causes of low open circuit voltage for a 100 Ω·cm cell.

Figure 6.6 shows the ratio of the peak power densities to unirradiated power density as a function of radiation dose in order to determine the radiation degradation for a thin solar cell. The results show that a low resistivity cell has the highest ratio of peak power despite its higher radiation damage coefficient. Also the degradation rate is found to be smaller for high resistivity cells as indicated by the smaller slope of the curves in Figure 6.6. However, the conversion efficiency is lower at high radiation doses for these high resistivity cells.

6.4 Conclusions

The characteristics of thin BSF silicon solar cells have been analyzed in this section. It is found that a good high-low junction is more important than an alloy junction of high optical reflectance for a thin solar cell with cell thickness of 50 μm or more. The optimum cell resistivity is identified to be from 1 Ω·cm to 0.3 Ω·cm before irradiation and from 0.3 Ω·cm to 0.1 Ω·cm after a medium dose of one MeV electron

radiation. The radiation degradation is found to be smaller for a high resistivity cell due to the smaller radiation damage coefficient. However, the conversion efficiency is lower for these high resistivity cells after heavy radiation.

6.5. REFERENCES

1. J. Michel. 1976. Black and Thin Silicon Solar Cells. Twelfth Photovoltaic Specialists Conference, Baton Rouge, LA: 603-605.

2. J. Lindmayer and C. Wrigley. 1976. A new lightweight solar cell. Twelfth Photovoltaic Specialists Conference, Baton Rouge, LA: 53-54.

3. C. Y. Wrigley. 1976. High Efficiency Solar Cells. Twelfth Photovoltaic Specialists Conference, Baton Rouge, LA: 343-346.

4. M. P. Godlewski, C. P. Baraona and H. W. Brandhorst, Jr. 1973. Low high junction theory applied to solar cells. Tenth Photovoltaic Specialists Conference, Palo Alto, CA: 13-15.

5. H. W. Brandhorst, Jr. and C. R. Baraona. 1973. Performance of epitaxial back surface field cells. Tenth Photovoltaic Specialists Conference, Palo Alto, CA: 212-217.

6. J. R. Hauser and P. M. Dunbar. 1976. Minority carrier reflection properties of semiconductor low high junctions. Solid State Electronics 18: 715-716.

7. R. C. Y. Fang and J. R. Hauser. 1977. Annual report on NASA grant NGR 34-002-195, NASA-Lewis Research Center.

7.1 Summary

A computer program has been developed to perform a two-dimensional calculation of silicon solar cell performance in order to evaluate the importance of series resistance on the conversion efficiency of concentrator solar cells. It is shown that the optimum concentrator power density for a specific grid design or the optimum grid design for a specific concentrator power density can be quantitatively predicted by this model.

7.2 Introduction

For a successful exploitation of terrestial solar energy, the cost of a photovoltaic system must be drastically reduced from today's price. Multi-sunlight concentrator systems provide a possible approach to solving this problem. Hence it is essential that an optimum cell design is achieved in order to economically utilize the solar energy.

It is known that the collection efficiency is a major factor in limiting solar cell efficiency at low solar concentrations. However series resistance becomes more important at high solar concentrations. Therefore the optimum cell design depends on the solar intensity at which a solar cell is operated. Similarly, the optimum solar concentration should be used for a specific solar cell designed to be operated under concentration.

This section describes the application of a distributed resistance and current model to the optimum design of concentrator cells and the grid pattern for multi-sunlight operation of a solar cell. A comparison between model and experiment is also attempted. In addition, the model is compared to a first order model of lumped series resistance.

7.3 Solar Cell Model

A detailed two-dimensional model has been reported elsewhere (Appendix 10.4).

7.4 Comparison Between Model and Experiment

A numerical model of a 2 cm^2 baseline silicon solar cell has been made and compared to experimental values [1]. The cell is rectangular in shape with dimensions of 1 cm by 2 cm. The front grid pattern consists of 39 fingers, 0.005 cm wide and 0.98 cm long spaced evenly across the 2 cm cell dimension. The fingers are connected at one end by a common bus bar. The front metal of silver has a resistivity of about $1.59 \times 10^{-6} \Omega \cdot cm^3$ and a thickness of 3 μm. Baseline cells with base layer resistivities of 0.3 $\Omega \cdot cm$ and 10 $\Omega \cdot cm$ have been simulated at solar intensities ranging from one to ninety AM1 power densities. The dark current density is described by a single exponential voltage dependence with a saturation current density of 5.6×10^{-12} A/cm^2 and 4.5×10^{-11} A/cm^2 and an equivalent diode factor 1.05 and 1.04 for 0.3 $\Omega \cdot cm$ and 10 $\Omega \cdot cm$ cells respectively. The surface sheet resistance is assumed to have a value of 120 $\Omega/\square$ for a junction depth of about 0.25 μm to 0.3 μm. The metal contact resistance is assumed to have a small value of 10^{-4} $\Omega \cdot cm^2$. The short circuit current densities under one AM1 solar spectrum are 28.0 mA/cm^2 and 30.5 mA/cm^2 over the active areas for 0.3 $\Omega \cdot cm$ and 10 $\Omega \cdot cm$ cells respectively.

The comparison of model and experiment is shown in Figure 7.1. It is seen that the predicted optimum concentrated solar intensities are very close to the experimental values where the peak efficiencies occur at about 20 ∿ 25 AM1 and 5 AM1 solar intensities for 0.3 $\Omega \cdot cm$ and 10 $\Omega \cdot cm$
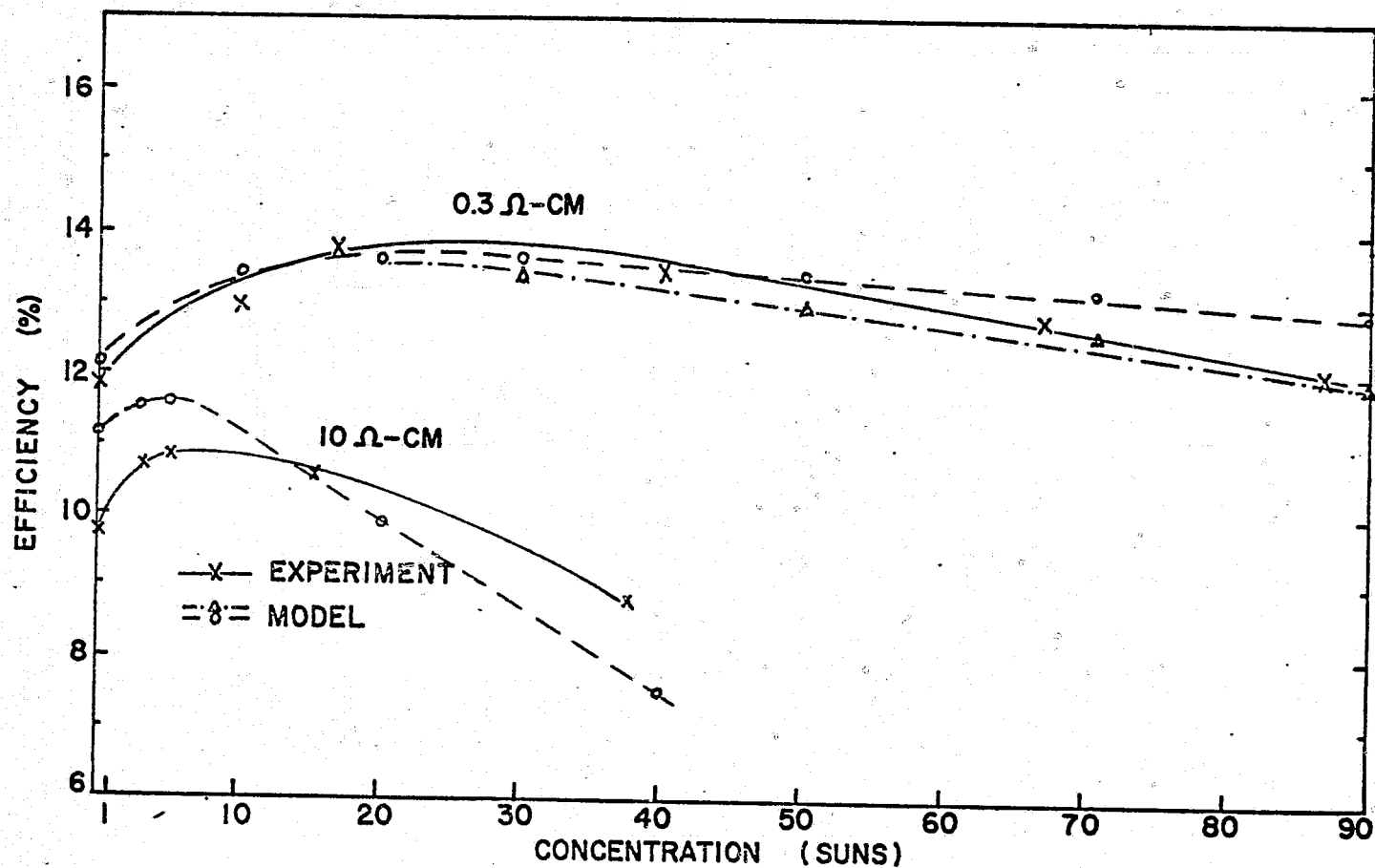
Figure 7.1 Comparison between experiment and two-dimensional model for baseline cells with base resistivities of 0.3 Ω·cm and 10 Ω·cm respectively. Surface sheet resistance is 120 Ω/□. Base contact resistance is assumed a value of 0.02 Ω·cm^2 for triangle data and 10^{-4} Ω·cm for circle data.

cells respectively. Figure 7.2 shows the absolute total power losses from metal coverage, sheet resistance, finger resistance, base resistance and contact resistance as a function of solar intensities for a 0.3 $\Omega \cdot$cm cell. Figure 7.3 shows the relative percentage of the power losses from each component of the total series resistance. It is shown in this figure that the optimum concentrated sunlight occurs at the point where a compromise occurs between the three major series resistances of sheet, finger and base resistances. Also the relative power loss from the grid coverage area is lower when the power losses from the series resistances become higher at large solar concentration.

7.5 Comparison Between the Lumped Resistor Model and the Exact Numerical Model.

The first order model usually assumes a constant lumped resistance connected in series with a solar cell. Therefore the photovoltaic current-voltage characteristic becomes

$$I = I_o \left[\exp\left(\frac{q(V-IR_s)}{A\,kT}\right) - 1 \right] - I_{sc} , \qquad (7.1)$$

where I_o is the saturation current density and I_{sc} is the short circuit current density.

It can be shown that the lumped series resistance can be represented by the following equation (Appendix A)

$$R_s = \frac{R_M \cdot SF}{WF \cdot T} \cdot \frac{LF^2}{3 \cdot A_A} + \frac{R_{ST} \cdot SF^2}{12 \cdot A_A} + \frac{R_B \cdot W_D}{A_B} + \frac{R_{SC}}{A_s} + \frac{R_{BC}}{A_B} . \qquad (7.2)$$
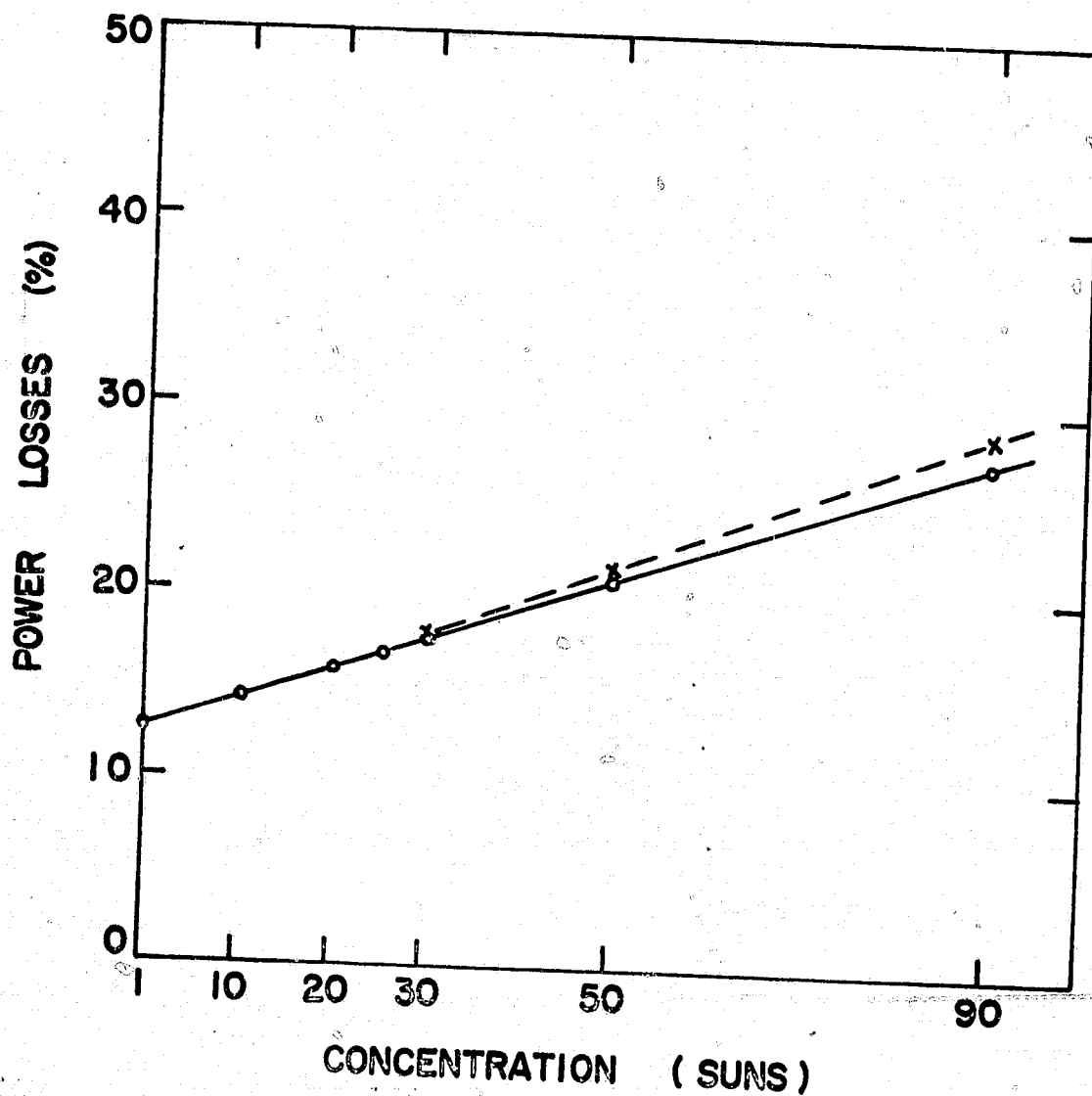
Figure 7.2 Absolute power losses of a 0.3 Ω·cm solar cell by the grid coverage, fingers, surface sheet and base bulk resistances. Two-dimensional model (solid line)/Lumped resistance model (dashed line).
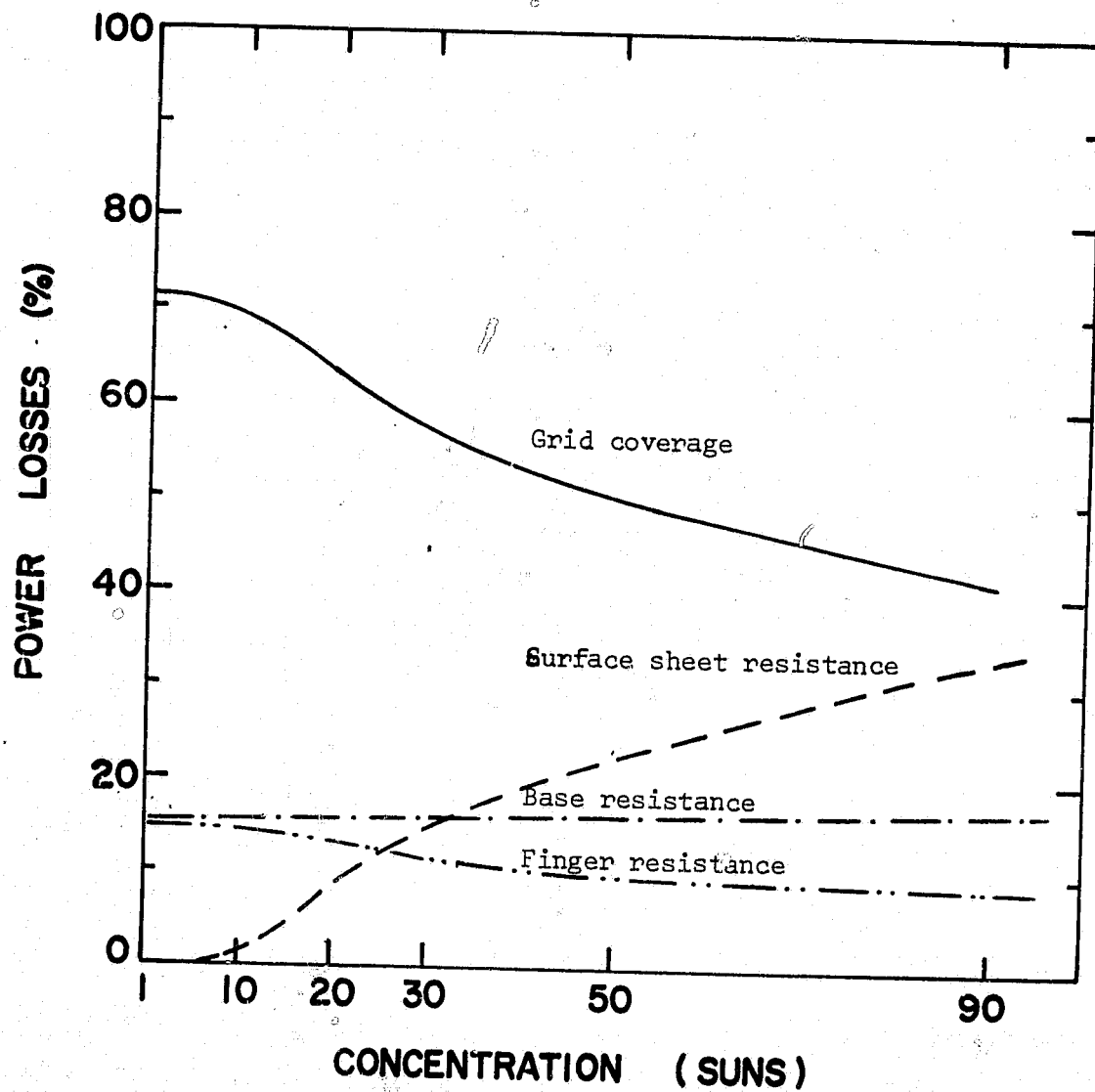
Figure 7.3. Relative power losses of the four components of the series resistance R_s.

The above five components of R_S are the finger, surface layer, base layer, surface contact and bottom contact resistances respectively. R_M and R_{ST} are metal and sheet resistivities respectively. R_{SC} and R_{BC} are the surface and bottom contact resistivities respectively. SF, WF and LF are the spacing between the fingers, the width of the fingers and the length of the fingers. R_B is the base resistivity and W_D is the cell thickness. A_S and A_B are the surface and bottom contact areas respectively. A_A is the total active area.

The comparison of the lumped resistance model to the distributive resistance and current model is shown in Figure 7.2. It is found that the lumped resistance model overestimates the power loss in a nonlinear behavior. This discrepancy is due to the fact that the total current density is assumed to flow through the total lumped resistor of a solar cell in the lumped resistance model. In fact, the resistance and current elements of a solar cell are distributive parameters and a distributed resistor and current model is a more realistic model.

In order to determine the discrepancy of the lumped resistance model, a more detailed comparison between both models is necessary. The numerical calculation of model cell D-7-1 with parameters as given in Table 7.1 is shown in Table 7.2.

Model (a) assumes that there are voltage drops across fingers, sheet surface and base bulk regions. The overestimation of the efficiency loss by using the lumped resistance model is found to be about 6 percent at fifty suns concentration level. Model (b) assumes there is only base layer bulk resistance. The overestimation of the efficiency loss is found to be about 4.4 percent. Model (c) assumes an additional base contact resistance, and the overestimation by the lumped resistance model is about 4.3 percent at fifty suns concentration level.

Table 7.1 Material parameters of cell D-7-1.

Structure	n^+p (1.0 Ω-cm)
Surface doping density	1.5×10^{20} #/cm3, erfc function
Surface junction depth	0.3 µM
Base doping density	1.6×10^{16} #/cm^3 (1.0 Ω-cm)
Base width	250 µM
Surface Diffusion Length	(L(MED)+L(MIN))/2
Base Diffusion Length	(L(MAX)+L(MED))/2
Surface Recombination Velocity	10^3 cm/sec
Sun power density	AM2 (74 mW/cm^2)
Anti-reflection film	Ta_2O_5, 60.0 Å
Baseline structure	39. fingers
Width of fingers	50 µM
Thickness of Fingers (T)	3 µM
Sheet Resistance (R_{ST})	92 Ω/□ (calculation)
Surface Contact Resistance	10^{-4} Ω-cm^2
Base Contact Resistance (R_{BC})	10^{-4} $\Omega \cdot$cm^2 or 0.05 $\Omega \cdot$cm^2
Base bulk resistance	0.025 Ω

Table 7.2. Comparison of the Lumped and Distributive Resistor Models.
Model a (T = 3 μm, R_{ST} = 92 Ω/□, R_{BC} = 10^{-4} Ω·cm^2),

Model b (T = 30,000 μm, R_{ST}=0.01 Ω/□, R_{BC}=10^{-4} Ω·cm^2),

Model c (T = 3 μm, R_{ST} = 92 Ω/□, R_{BC} = 0.05 Ω·cm^2).

	Sun Numbers	1	5	50
Models		Efficiency (%)		
Exact Model a.		15.44	16.60	17.48
Lumped R_S Model a.		15.23	16.43	16.48
Overestimation (%)		1.4	1.0	5.7
Exact Model b.		15.48	16.74	18.53
Lumped R_S Model b.		15.26	16.56	17.71
Overestimation (%)		1.4	1.1	4.4
Exact Model c.		15.41	16.42	15.49
Lumped R_S Model c.		15.20	16.26	14.83
Overestimation (%)		1.4	1.0	4.3

Therefore, it can be concluded that the overestimation of the efficiency loss by using the lumped resistance model comes from the overestimation of the voltage drop across the base bulk region, surface sheet and fingers resistances. However the lumped resistance model is still a good model at low series resistance and low solar concentration.

7.6 The Optimum Concentrator Intensity for Some Grid Designs

Since the peak efficiency of a high-intensity solar cell is a trade-off between good collection efficiency and small series resistance, there exists an optimum concentrator intensity for a specific grid design. The purpose of this section is to calculate the optimum multi-sun power density of some standard grid patterns. The results are summarized in Figures 7.1 and 7.4 to 7.7. A summary of the grid designs is shown in Table 7.3.

Figure 7.1 shows one example of the efficiency as a function of solar concentration level for the baseline cell. The other baseline structures have similar characteristics. In these calculations, the grid coverage areas are kept constant while the number of fingers are varied. Also two different sheet resistances are used in the calculations. The optimum solar concentration level is higher for cells with increasing numbers of fingers as shown in Table 7.3.

If the voltage drop across the series resistance R_s can be found at the current density of maximum efficiency under the optimum solar concentration, a design equation can be derived in a first order model. Table 7.4 shows the lumped series resistance, the voltage across R_s and the ratio of the peak-efficiency current density to the short circuit current density at the optimum solar concentration for several cell models.

The average voltage across the series resistance is about 46 milli-volts under the optimum solar concentration. The ratio of the peak-efficiency current density to the short circuit current is about 0.95. Hence the design equation can be given as

$$0.046 = 0.95 \cdot I_{SC} \cdot N_S \cdot R_S, \qquad (7.3)$$

Table 7.3. Summary of grid design for the various cell configurations.

	a	a'	b	b'	c	c'	d	d'	e	e'	f
Cell geometry (cm^2)	1x2	1x2	1x2	1x2	1x2	1x2	1x2	1x2	2x2	2x2	5 cm Dia.
No. of Fingers	39	39	30	30	20	20	10	10	60	60	240
Width of Fingers (μm)	50	50	65	65	97.5	97.5	195	195	20	20	13∿56
Thickness of Fingers (μm)	3	3	3	3	3	3	3	3	3	3	4
Space between Fingers (μm)	462.82	462,82	477.82	477.82	510.32	510.32	1805	1805	313.3	313.3	varied
Base doping density (Ω-cm)	0.3	0.3	0.3	0.3	0.3	0.3	0.3	0.3	0.3	0.3	0.3
Device Thickness (μm)	250	250	250	250	250	250	250	250	250	250	250
Sheet Resistance (Ω/□)	45	120	45	120	45	120	45	120	120	120	120
Width of Bus Bar (μm)	200	200	200	200	200	200	200	200	20→200	20→200	1800
Thickness of Bus Bar (μm)	3	3	3	3	3	3	3	3	3	15	4
No. of Bus Bars	1	1	1	1	1	1	1	1	2	2	1
Concentration Design Level	40	25	30	19	22	10	7	2	7	25	20

Table 7.4. The voltage across the lumped series resistor at the optimum solar concentration.

Cells	a	a'	b	b'	c	c'	d	d'
lumped series resistance (Ω)	0.02748	0.04087	0.03303	0.05566	0.04999	0.10090	0.14164	0.34524
voltage drop (mV)	46.8	47.4	45.9	48.8	46.3	46.5	45.8	44.7
Ratio $\dfrac{I_{MAX}}{I_{SC}}$	0.957	0.957	0.956	0.953	0.953	0.952	0.955	0.949

where I_{SC} is the short circuit current density at one sun power density, N_S is the designed solar concentration level and R_S is the lumped series resistance of Equation (7.2). A very similar equation has been reported elsewhere [2]. However the numerical interpretation is different despite the closeness of both equations.

Figure 7.4 shows efficiency as a function of illumination intensities for the violet-type cells. These cells have two tapered common bus bars and 60 fingers evenly spaced across the cell dimensions. In this case the one-sun efficiency is much higher than that of the baseline cells due to the smaller grid coverage area and the better collection efficiency of the violet cells. It also shows the peak efficiency can be greatly increased by reducing the conducting resistance of the tapered bus bar. For curve e' of Figure 7.4, the violet cell is assumed to have a conducting bus bar with a thickness of 15 μm instead of 3 μm.

If the voltage across the common bus bar is plotted against the voltage at one terminal of the bus bar, the curve looks like the illuminated I-V characteristics. In fact, the voltage difference between two terminals of the bus bar is proportional to the current density and the bus bar resistivity. Figure 7.5 shows these characteristics for the simulated violet-type cells under several solar concentrations. It is found that the optimum solar concentration level occurs when the voltage across the bus bar has a value of about kT/q. However, the cell efficiency is reduced at a higher solar concentration or a larger voltage difference across the bus bar. This value is also a good parameter for the design of optimum solar concentration for a violet cell.
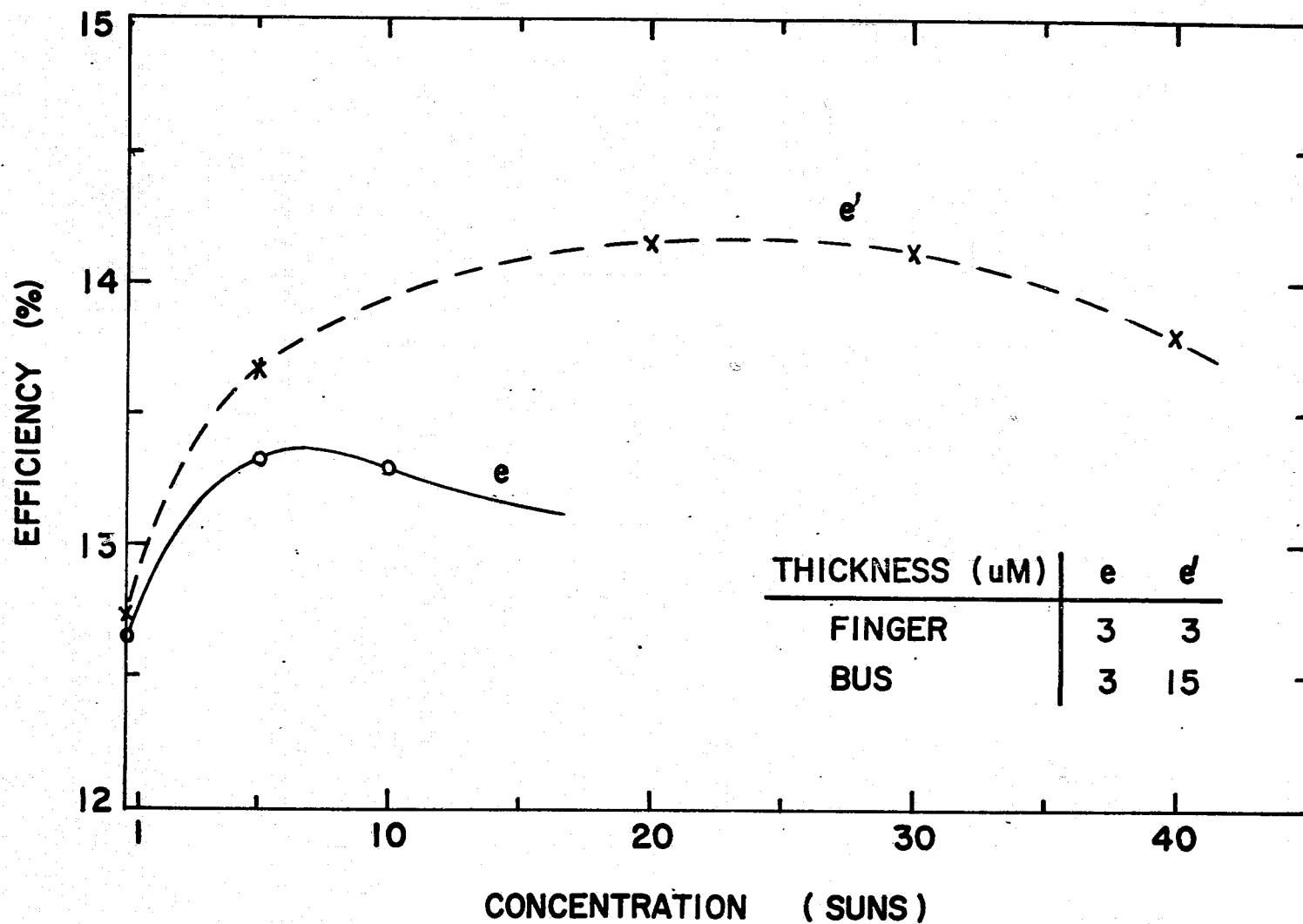
Figure 7.4.   Optimum cell efficiency as a function of the concentration level for a violet type cell.
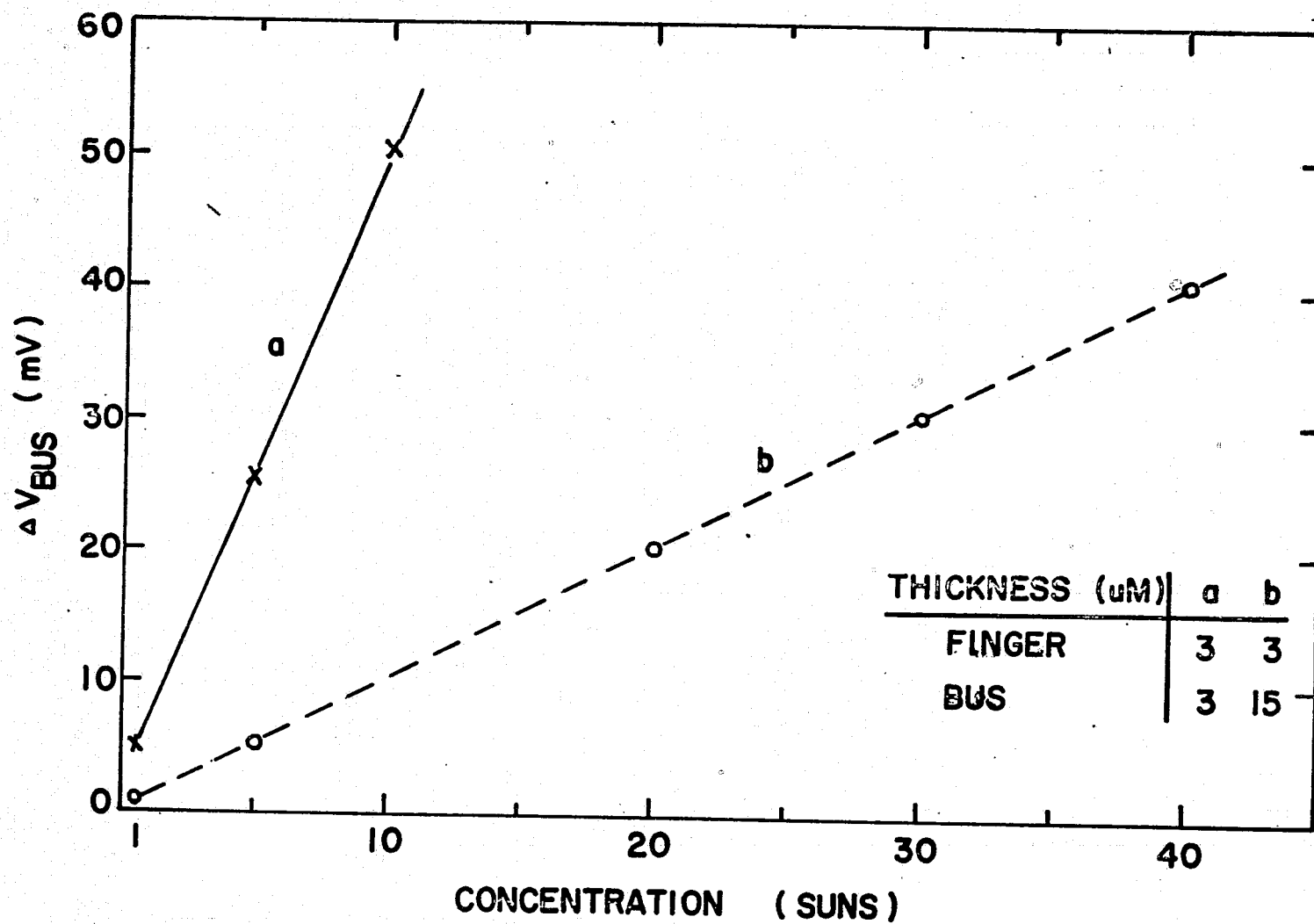
Figure 7.5.   The voltage across the tapered bus bar of a violet type cell at the short circuit condition.
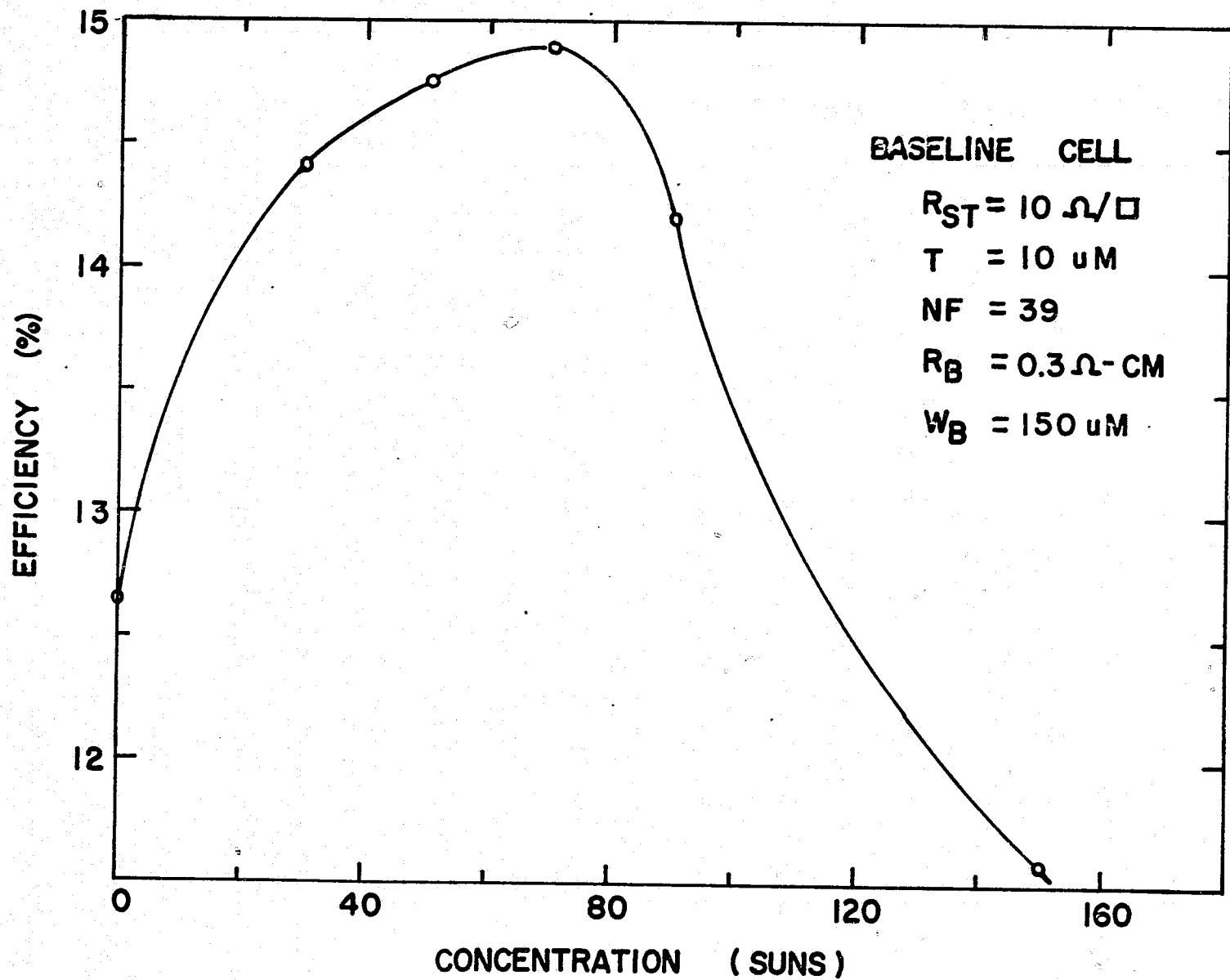
Figure 7.6. A cell design with low sheet and finger resistances.

Figure 7.6 gives an example of a solar cell with very low sheet resistance, thicker conducting metal and lower base resistance. The optimum solar concentration level is found to be close to 70 AM1 solar power density.

Figure 7.7 shows a comparison between calculations and the experimental values for the large area, high intensity silicon solar cell of Sandia Labs [1]   This cell has an effective area of 15.2 cm^2, and the active area is about 13.38 cm^2. The finger width is 56 µm at the bus bar and tapers to 13 µm near the center of the cell. The photolithographic defined metallization consists of approximately 4 µm of silver and a thin aluminum underlayer. The predicted optimum solar concentration level is about 20 $\sim$ 25 which is very close to the measured values.

7.7 Conclusions

The effects of series resistances on the multi-sunlight operation of a solar cell have been examined by a distributive resistor and current model. A number of conclusions can be made based on this work. (1) An exact numerical calculation can be made to predict the optimum illumination intensity of a specific cell design without fabricating the cell. Similarly, this technique can be used to design the optimum high intensity solar cell with respect to the specific solar concentrator. (2) High efficiency solar cell operation can be achieved with a low sheet resistance design at a high concentration level. A first-order equation is also given which can be used to design the optimum concentration level at low series resistance and/or low solar concentration levels.
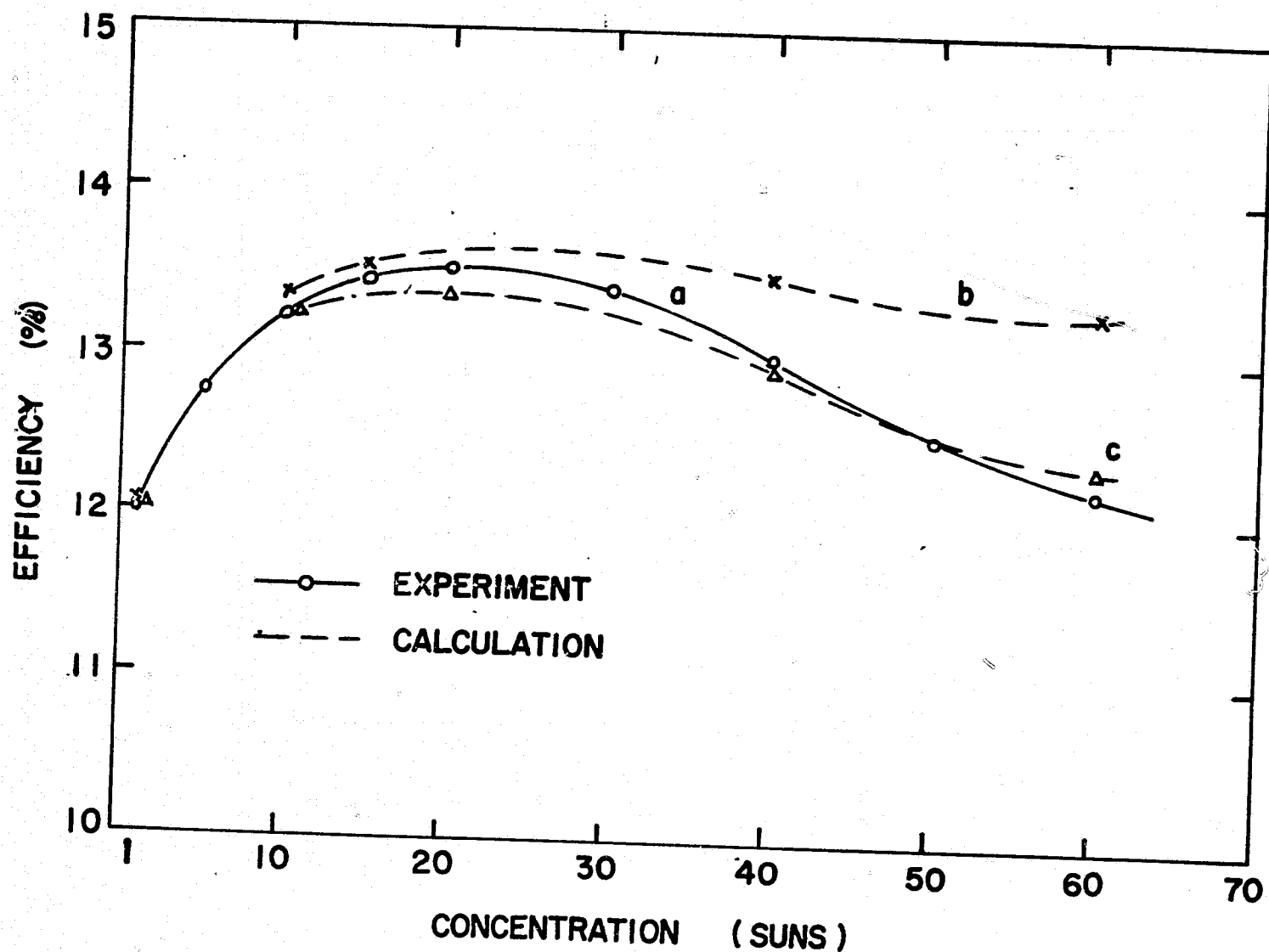
Figure 7.7. Comparison between experiments (a) and the two-dimensional calculations of the large area, high intensity silicon solar cell. Surface sheet resistance is 120 Ω/$\square$. Base contact resistances are 10^{-4} and 0.03 $\Omega \cdot cm^2$ for models b and c respectively.

(3) The lumped resistance model is found to overestimate the power losses. This discrepancy is shown to be due to the overestimation of the total series resistances of the surface sheet, finger and base bulk in the first order model.

(4) An exact solar cell model provides a valuable analysis technique for designing the optimum solar cell under multi-sunlight operation.

7.8 Appendix (B). The Lumped Series Resistance
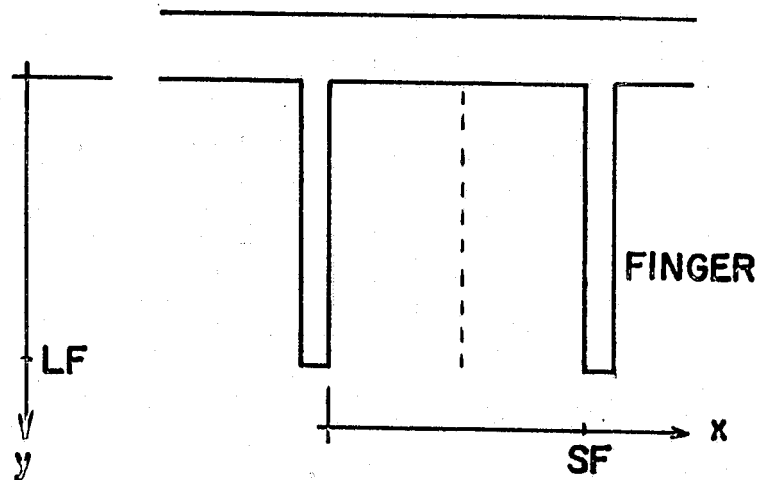
The lumped series resistance usually consists of five components which include finger, surface sheet, base, surface and bottom contact resistances. If it is assumed that the space between fingers is much less than the length of the fingers and there is negligible voltage drop across the bus bar, the lumped finger and sheet resistances can be derived as follows.

Let the voltage drop along a finger be $\Delta V(y)$ at position y. Then

$$\Delta V(y) = \int_0^y i(LF-y) \cdot \frac{SF}{2} \cdot \frac{R_M}{\frac{WF}{2} \cdot T} dy = \frac{iR_M \cdot SF}{T \cdot WF}(LF \cdot y - \frac{y^2}{2})$$

where i is the current density. The overall average voltage drop across the finger beomes

$$\overline{\Delta V(y)} = \frac{1}{L_F} \int_0^{L_F} \Delta V(y)dy = \frac{iR_M \cdot SF}{WF \cdot T} \cdot \frac{LF^2}{3} = I \cdot \frac{R_M \cdot SF}{WF \cdot T \cdot A_A} \cdot \frac{LF^2}{3}$$

Hence the effective finger resistance is equal to $\frac{R_M \cdot SF}{WF \cdot T \cdot A_A}$ $\frac{LF^2}{3}$

Similarly, the voltage drop along the sheet resistance is

$$\Delta V(x) = \int_0^x i(\frac{SF}{2} - x) \cdot R_{ST} dx = i \cdot R_{ST}(\frac{SF}{2} \cdot x - \frac{SF^2}{2})$$

The overall average voltage drop across the sheet resistance becomes

$$\overline{\Delta V_{(x)}} = \frac{1}{SF/2} \int_0^{SF/2} \Delta V_{(x)} dx = \frac{i \cdot R_{ST} \cdot SF^2}{12} = I \cdot \frac{R_{SF} \cdot SF^2}{12 \cdot A_A}$$

Hence the lumped sheet resistance is $\frac{R_{ST} \cdot SF^2}{12 A_A}$ where R_{ST} is the surface sheet resistance and A_A is the total active area.

1. E. L. Burgess and J. G. Fossum. 1977. Performance of n^+p Silicon
    Solar Cells in Concentrated Sunlight. IEEE Trans. on Electron
    Devices ED-24(4): 433-438.

2. J. A. Castle. 1976. Design Criteria for High Efficiency Silicon
    Solar Cells with Concentration. Twelfth Photovoltaic Specialists
    Conference, Baton Rouge, LA: 751-759.

8. NON-UNIFORM ILLUMINATION EFFECTS ON SOLAR CELLS

8.1 Abstract

A computer program has been developed to calculate non-uniform illumination effects on a solar cell. The non-uniformity of illumination is found to change the conversion efficiency by modifying the resistance losses of the top surface layer. It is shown that a non-uniformly illuminated solar cell can be operated near its peak power density by a suitable design of the top surface sheet resistance and grid pattern.

8.2 Introduction

Recently, solar concentrator systems have become popular as a means of economically utlizing terrestrial solar energy in the near future. However there are some problems which are not experienced in a non-concentrated solar system. For example, the input spectral intensity is usually distorted from the reflection and refraction of the different wavelengths in an optical concentrator system. At present, it is not clear how the distortion in spectral intensity affects the conversion efficiency. It is also unclear as to how intensity variations across the concentrated solar cell changes the solar cell characteristics.

In fact, there are two different kinds of non-uniform illumination in the operation of a solar cell. The space-flight cells generally have an abrupt light-dark boundary caused by the satellite body or antenna, etc. On the other hand, a concentrator cell usually has a steeply varied illumination across the solar cell. The degree of non-uniformity generally increases with the concentration level.

A computer program has been developed to calculate the characteristics of an abruptly illuminated cell with the illuminated boundary perpendicular to the finger contact. Two extreme cases of calculation are possible for the illuminated area on the near-side or far-side of the bus bar. For a concentrator cell, the computer program has been used to calculate two non-uniform illuminations in order to determine the effect of a varying intensity across the solar cell on the cell conversion efficiency. The first model assumes a cosine intensity profile with the maximum intensity farthest away from the bus bar and zero intensity at the bus bar. The second case uses a similar cosine intensity profile but with the maximum intensity at the bus bar and zero intensity at the opposite edge of the cell.

This section describes the application of a modified, distributed resistance and current model to calculate the characteristics of such non-uniformly illuminated cells. In addition, it is shown that the efficiency losses due to the non-uniform illumination can be minimized by a proper design of the concentrator cell.

8.3 Solar Cell Modeling

A detail two-dimensional model of a solar cell has been reported elsewhere (Appendix 10.4).

8.4 Comparison Between Uniform and Non-Uniform Illumination

The characteristics of a non-uniformly illuminated cell can be demonstrated for a 1x2 cm^2 baseline solar cell. This cell has a grid pattern of 39 fingers and a common bus bar at one edge of the cell.

The contact fingers are assumed to be made from silver-titanium with approximately 3 μm of silver deposited over a 500 Å titanium adhesion layer. The 50 μm wide fingers are 0.98 cm long and evenly spaced across the 2 cm cell dimension. This cell has a base resistivity of 3 Ω·cm, and the saturation current density is 5.6×10^{-12} A/cm^2 with a diode factor of 1.05. The surface sheet resistance is about 120 Ω/□ for junction depths of 0.25 μm to 0.3 μm, and the metal contact resistance is assumed to have a negligible value of 10^{-4} Ω·cm^2. The short circuit current density of an AM1 solar spectrum is 28.0 mA/cm^2 in the active area.

The cell efficiency as a function of solar concentration for the general non-uniform illumination is shown in Figure 8.1. The cosine illumination, which has a maximum intensity near the bus bar, produces the highest efficiency due to the lowest power losses in the top layer and contact grid resistance. On the contrary, the cosine illumination which has a maximum intensity farthest from the bus bar has the lowest efficiency at all illumination levels. The uniformity of the illumination influences the cell efficiency by modifying the resistance power losses in the top layer and grid resistance. Therefore, the efficiency of a solar cell depends on the current distribution on the cell surface due to a non-uniform illumination.

In Figure 8.1, a calculation is also shown for the same baseline cell which has a grid thickness of 6 μm. It is interesting to note that the uniform illumination produces a higher efficiency at high concentration than the case of maximum illumination near the grid contact. This is because the sheet resistance losses counterbalance the reduced grid resistance losses in such a favorable cosine non-uniform illumination.
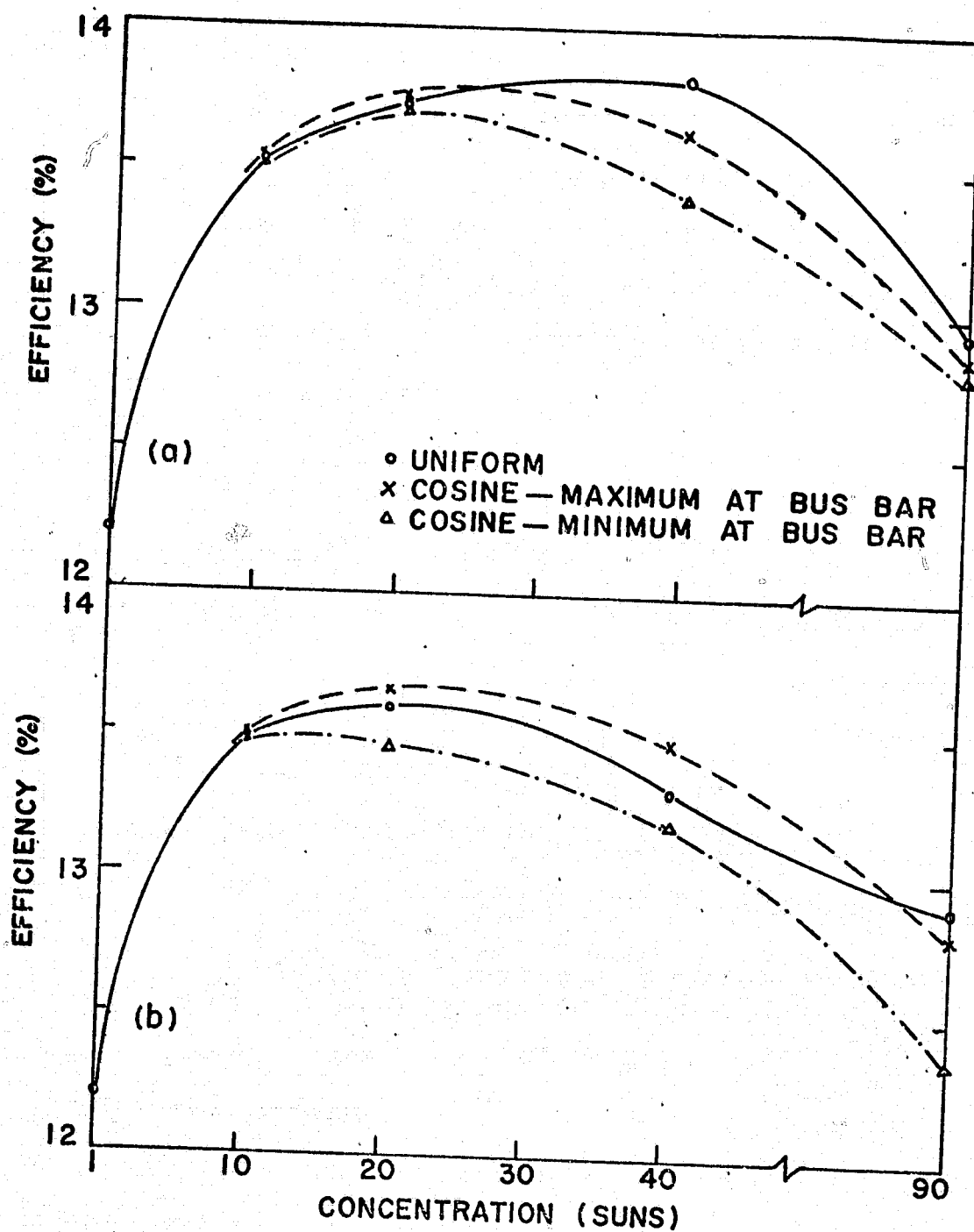
Figure 8.1 Cell efficiency as a function of the concentration level. Surface sheet resistance is 120 Ω/□ and the grid thickness is 6 μm(a) or 3 μm (b) in the calculation.

More evidence of the competition between grid resistance losses and surface sheet resistance losses can be obtained from the comparison of the two cases in Figure 8.1. The power losses in the top surface layer consist of the two components of sheet resistance and grid resistance losses. The power losses in the surface sheet resistance dominate over that in the grid resistance at high intensities of illumination. Therefore the total power loss of a non-uniformly illuminated cell is higher than that of a uniformly illuminated cell, despite the smaller grid resistance loss in this case. From Figure 8.1, it is clear that the calculation of a non-uniformly illuminated cell can be used to show the dispersion of the conversion efficiency as a function of the concentration level and the non-uniformity of illumination.

Figure 8.2 shows a solar cell design for multi-sun operation. The effect of non-uniformity of illumination is shown to be reduced to a negligible minimum with a design of low surface sheet resistance.

Figure 8.3 shows the results of the efficiency as a function of the active area for two cases of abrupt illumination. The results are plotted as a ratio of efficiency versus the ratio of the active area. where the ratios of efficiency and active area are referred to the fully illuminated solar cell. It is clear that the cell efficiency is nearly proportional to the active area and is not a strong function of the illuminating profile. This is because the cell efficiency is limited for low intensities by the collection efficiency instead of the power losses in the series resistance. The power losses in the grid resistance is small and the conversion efficiency is only a function of the active area.
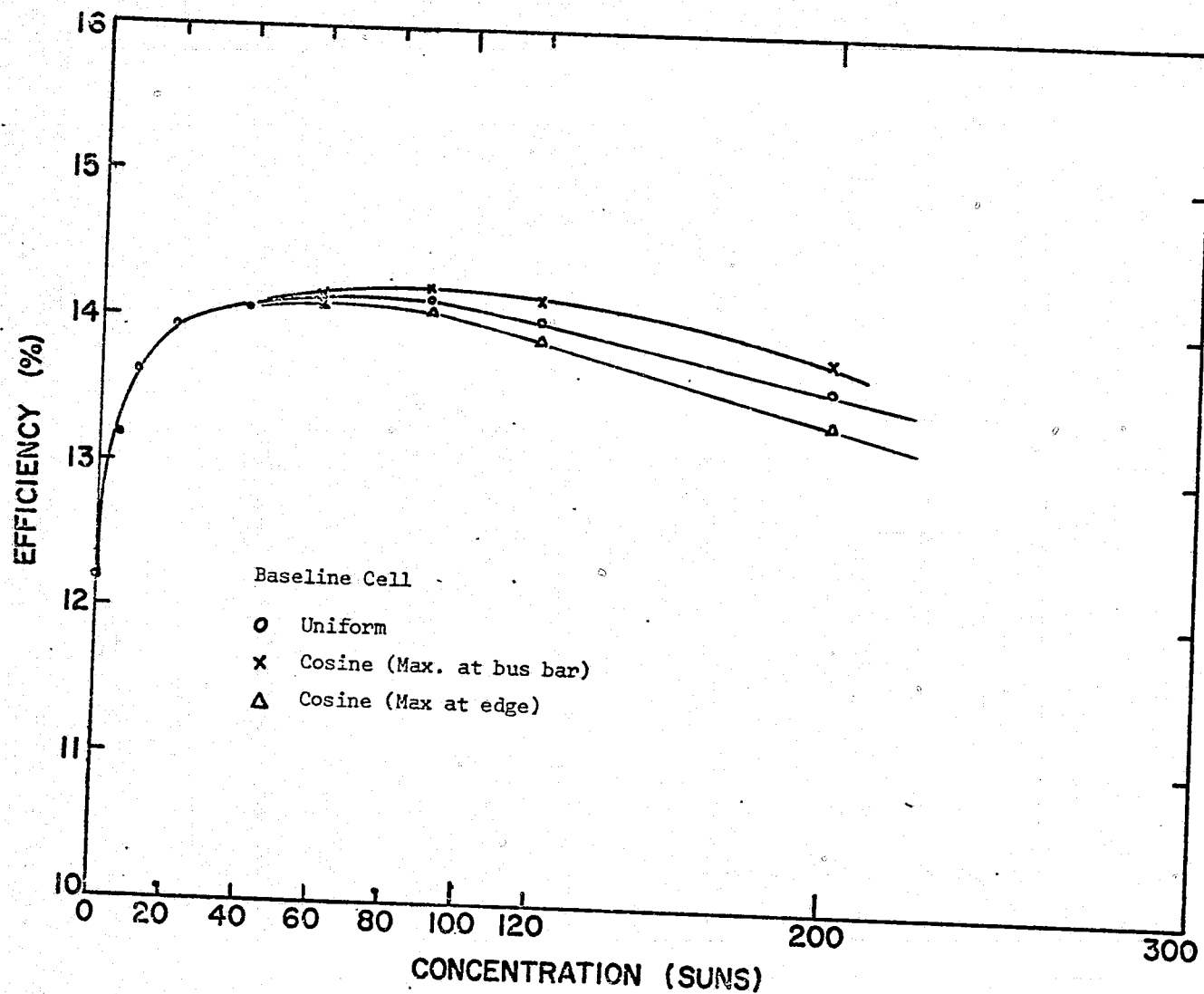
Figure 8.2. Cell efficiency as a function of the concentration level. Surface sheet resistance is 10 Ω/□ and the grid thickness is 3 μm in the calculation.
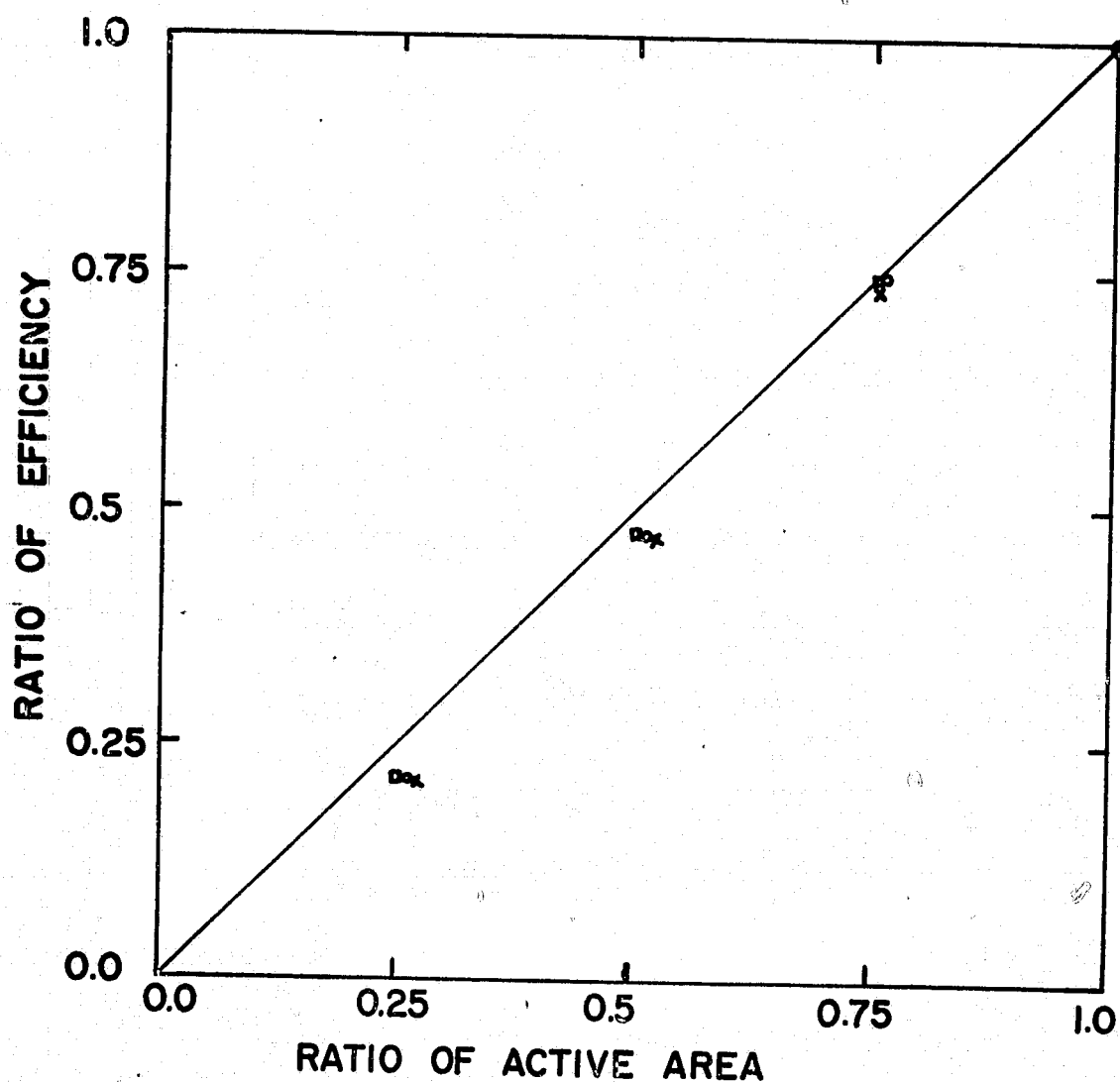
Figure 8.3 Ratio of the conversion efficiency as a function of the ratio of the illuminated area for the abrupt illuminated cell. (0) dark area near bus bar; (■), (X) light area near bus bar. The surface sheet resistance is assumed a value of 500 $\Omega/\square$ for (X) points instead of 120 $\Omega/\square$ for (0) and (■).

8.5 Conclusions

Some of the characteristics of non-uniform illumination on a solar cell have been analyzed in this chapter. Several important conclusions can be made as follows:

(1) The conversion efficiency can be analyzed as a function of the cell structure, grid pattern, illumination level and the non-uniformity of illumination by the two-dimensional solar cell model. This phase of work is important in the design of solar cells under concentration and in the design of concentration systems.

(2) The power losses in the surface sheet resistance, bulk resistance, contact resistance and grid resistance can be accurately predicted with the model developed in this work.

(3) The effects of non-uniform illumination on cell conversion efficiency have been analyzed for a few solar cell designs. It has also been shown that the effects of non-uniform illumination can be reduced to a negligible amount by an appropriate design of the surface and grid resistances.

(4) Perhaps, the most important conclusion is that the non-uniform illumination is found to decrease the cell efficiency at high concentration levels irrespective of the illumination profile, if the surface sheet resistance is the dominant loss factor.

9. HIGH-LOW JUNCTION EMITTER SOLAR CELLS

9.1 Abstract

This section discusses the physical characteristics of a recently proposed solar cell - the HLE solar cell [1] which has been predicted to give a substantial increase in the output voltage and the converstion efficiency of a highly doped junction solar cell. However, our calculation predicts the negative results. The discrepancies have also been identified as high injection effects and heavy doping effects in the emitter-high-low junction of the HLE solar cell.

9.2 Introduction

High efficiency has been predicted for solar cells with low base resistivity near about $0.1\Omega\cdot cm$ [2]. Unfortunately, the measured conversion efficiency is substantially less than the theoretical expectation for these highly doped cells. This has been found to be due to the discrepancy in the values of the output voltage and open circuit voltage. In fact, the measured value of open circuit voltage is about 150 mV less than the predicted value from the simple Shockley diffusion theory for a $0.1\ \Omega\cdot$ cm cell.

Physical studies have recently shown that the discrepancy of the V_{OC} performance of a highly doped solar cell is due to heavy doping effects in the heavily doped surface layer [3]. Therefore, there is excess surface recombination current which is usually much larger than the base layer injection current density for a highly doped solar cell.

In order to reduce the abnormally large back injection current density, a high-low junction emitter solar cell has been proposed and predicted to achieve high V_{OC} following a similar reason of a high-low junction base solar cell [1].

This section will discuss the physical operation of a high-low emitter silicon solar cell. The results of the numerical calculation will be presented for several structures of the proposed high-low emitter cells.

9.3 Numerical Calculations

A HLE cell has an additional high-low junction located in the surface region of a conventional cell. Figure 9.1 shows a schematic structure of a HLE cell with a structure of n^+np. The back injection current
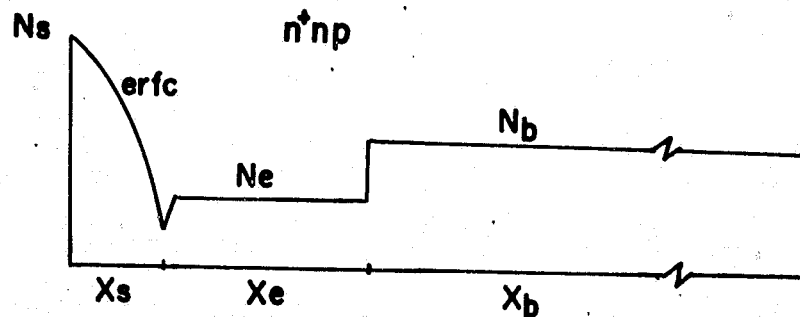
Figure 9.1. A structure of a HLE junction solar cell.

density is expected to be reduced from the minority carrier confinement in the surface n-type region due to the small SRV at the emitter high-low junction. The open circuit voltage will thereupon be increased from the resultant smaller junction saturation current density. Before discussing the physical fundamentals of the emitter high-low junction cell, the numerical calculations will be presented for several proposed models of Table 9.1.

Table 9.1. Structures of models a to j of the proposed EHL junction solar cells. N_B, X_S, and X_B are equal to 5×10^{17} /cm^3, 0.25 mm and 200 μm, respectively.

	N_S (/cm^3)	N_E (/cm^3)	X_E (μm)	Efficiency
Model a	2×10^{19}	10^{14}	0	16.59
Model b	2×10^{19}	10^{14}	1	14.77
Model c	2×10^{20}	10^{14}	10	12.23
Model d	2×10^{20}	10^{14}	0	16.25
Model e	2×10^{20}	10^{14}	1	14.58
Model f	2×10^{20}	10^{14}	10	11.60
Model g	2×10^{20}	10^{16}	1	15.40
Model h	2×10^{20}	10^{16}	5	14.94
Model i	2×10^{20}	10^{18}	5	13.70
Model j	2×10^{20}	10^{17}	10	12.78

Cells a-j are assumed to have a 595 Å thickness of Ta_2O_5 at one AMO solar intensity. The SRV of the diffused surface is assumed a value of 10^3 cm/sec. The base diffusion length is assumed to be 100 μm, which is close to L(MAX) at a base resistivity of 0.1 Ω·cm. The surface diffusion length is taken to be (L(MED) + L(MIN))/2. Therefore, the minority carriers of the surface epitaxial layer have been assumed a diffusion length of 55 μm. This value is very close to the experimental value at an n-type doping density of 10^{14}/cm^3 [4].

The results of the numerical calculations are summarized in Figures 9.2 and 9.3. It is seen in Figure 9.2 that the cell conversion efficiency is lower at a wider width of the constant doped n-layer. This is a direct consequence of the high injection effects in the lightly doped n-layer. In Figure 9.3, it is clear that the cell with a wider n-layer has a high slope in the dark I-V characteristics. Therefore, the cell curve factor is degraded and the conversion efficiency is lower. At the same time, the back injection current density is larger for cells
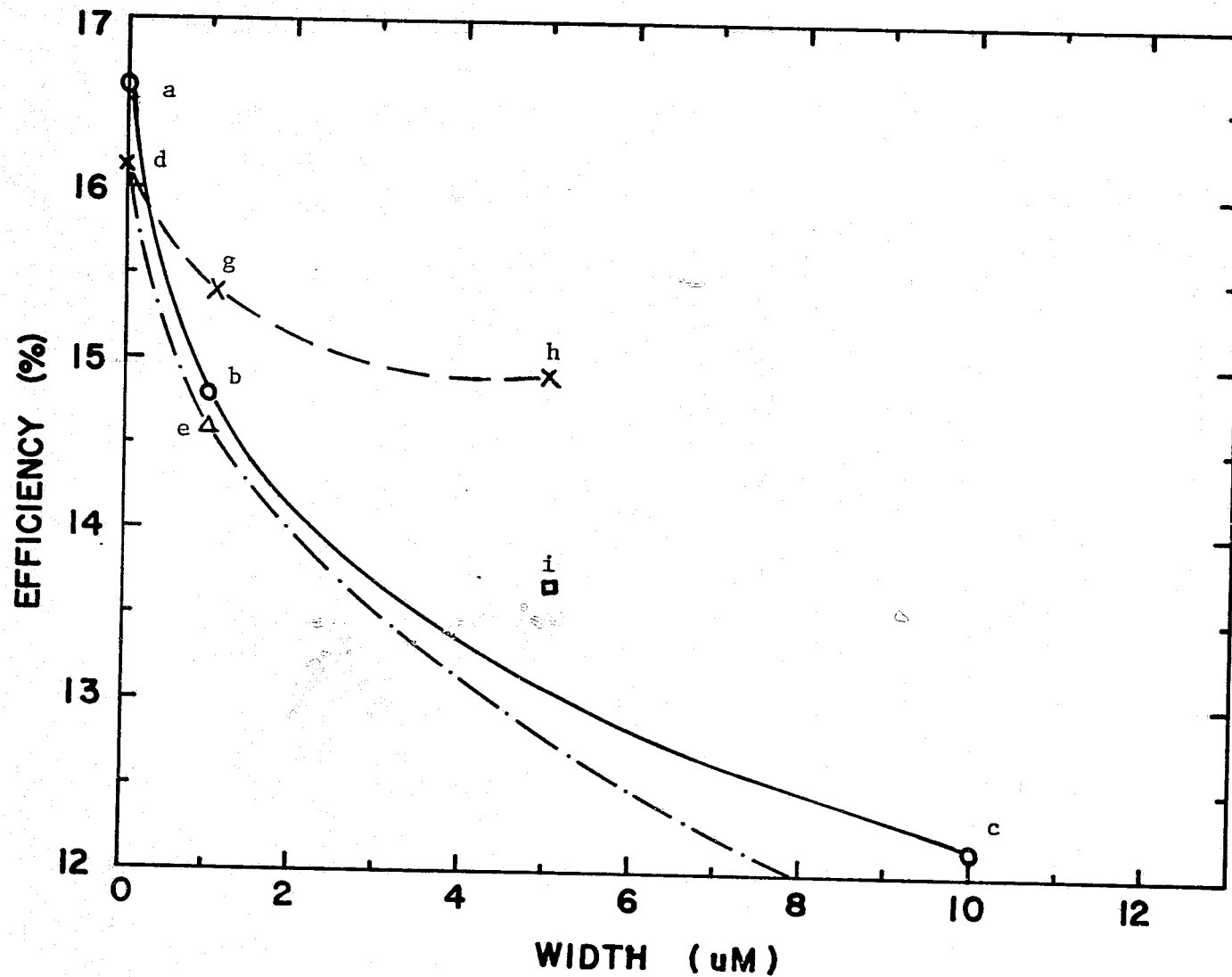
Figure 9.2. Cell efficiencies as a function of the epitaxial widths of model (a) to (i) of Table 9.1.
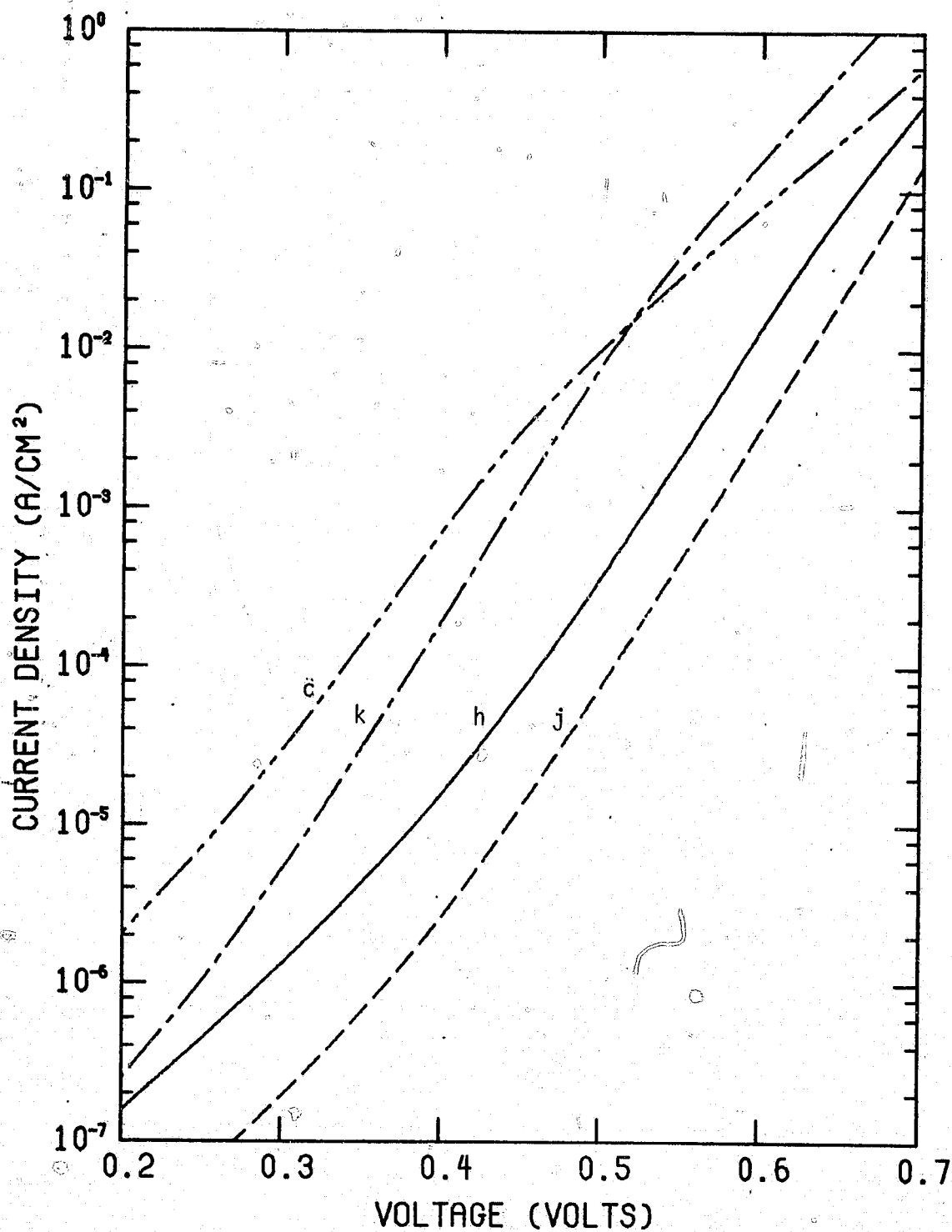
Figure 9.3. Dark I-V characteristics of n^+np cell c, h, j, and k of Table 9.1

with a wider epitaxial layer. This is due to the ineffectiveness of the SRV at the EHL junction and the low carrier lifetime or diffusion length of the n-type material. The back injection current density can be conveniently represented as

$$J = \frac{\int_0^{x_E} Aqpdx}{\tau} + AqP(X_{HL})S_{HL}, \quad (9.1)$$

where the first term is the recombination current density in the constantly doped layer. It is clear that the back injection current density is higher for a wider epitaxial layer of x_E, if the second component of Equation 9.1 can be neglected.

9.4 Physical Mechanisms of an Emitter High-Low Junction Solar Cell

It has been established that the carrier transport through a conventional p-n junction can be described by the Shockley diffusion theory or Sah's recombination current model. However, a high-low junction can be described by the HL junction theory or the HL junction theory plus the junction leakage current model [5,6]. In these models, a high-low junction has the advantage of confining the minority carriers in the lightly doped region where the carrier lifetime is supposed to be higher than that of the highly doped layer. Therefore, the junction saturation current density is lower and the corresponding V_{oc} will be higher than its conventional counterpart.

In order to determine the validity of the high-low junction model, a comparison between experiment and model is attempted and shown in Figure 9.5 for a high-low junction base solar cell of Figure 9.4 and Table 9.2 [7].
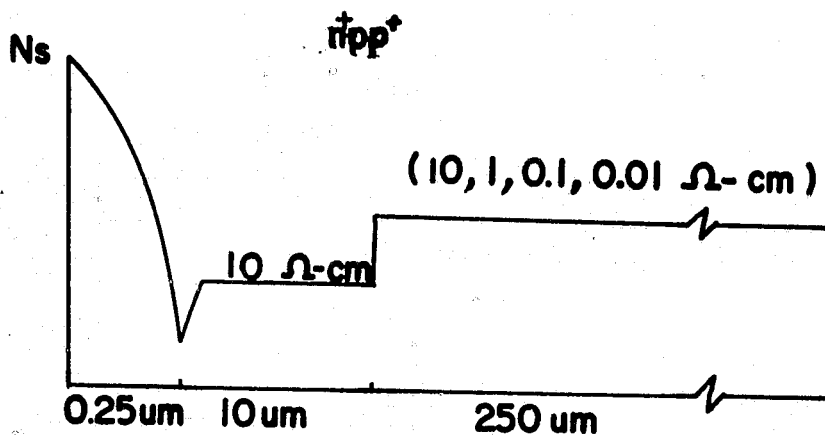
Figure 9.4. Schematic structure of the experimental cells.

Table 9.2. Parameters used in the calculation of V_{oc} variation with substrate resistivity.

Substrate

Resistivity $\Omega \cdot cm$	Diffusion Coeff.(cm^2/sec)	Diffusion Length (μm)	Width (μm)
0.01	3.2	10	250
0.1	9.3	50	250
1.0	22	125	250
10	33	150	250

Epitaxial Layer

Resistivity $\Omega \cdot cm$	Diffusion Coeff.(cm^2/sec)	Diffusion Length (m)	Thickness (μm)
10	33	80	10
10	33	80	10
10	33	80	10
10	33	80	10

The calculations of Figure 9.5 are based on the following equations for Shockley's model and HL junction model:

$$J_s = qAn_i^2 \left(\frac{D_p}{\int_0^{w_{n+}} N_D \, dx} + \frac{D_n}{\int_0^{w_p} N_A \, dx} \right),$$ (9.2)

$$J_{HL} = \frac{qAD_n}{L_n} n(x_{n+p}) \frac{S + \tanh \frac{W_n}{L_n}}{1 + S \tanh \frac{W_n}{L_n}},$$ (9.3)

$$J_{HLL} = J_{HL} + qAn(x_{HL}) \cdot S_{HL},$$ (9.4)

$$S = \frac{D_{p+}}{L_{p+}} \frac{N_p}{N_{p+}} \frac{L_p}{D_p} \coth \frac{W_{p+}}{L_{p+}} \left[1 + \frac{n_p(x_{HL})}{N_p}\right] = S_0 \left[1 + \frac{n_p(x_{HL})}{N_p}\right],$$ (9.5)

where J_x, J_{HL} and J_{HLL} are the saturation current densities for Shockley's model, HL junction model and HL junction plus leakage current model, respectively. S and S_{HL} are the normalized and unnormalized SRV at the HL junction, respectively. These values are functions of the material parameters on both sides of the HL junction, while N_p and N_{p+} are the majority carrier densities on both sides of the HL junction.

It is clear from the calculation of Figure 9.5 that the high-low junction theory is a good model for a high-low junction cell. The confinement of the minority carriers in the lightly doped layer requires a highly reflecting HL surface or a low SRV at the HL junction. This can be easily achieved in a high resistivity BHL junction solar cell. On the other hand, this may not be true for a EHL junction solar cell. Since the EHL junction is located near the illuminated surface, S_{HL} will then
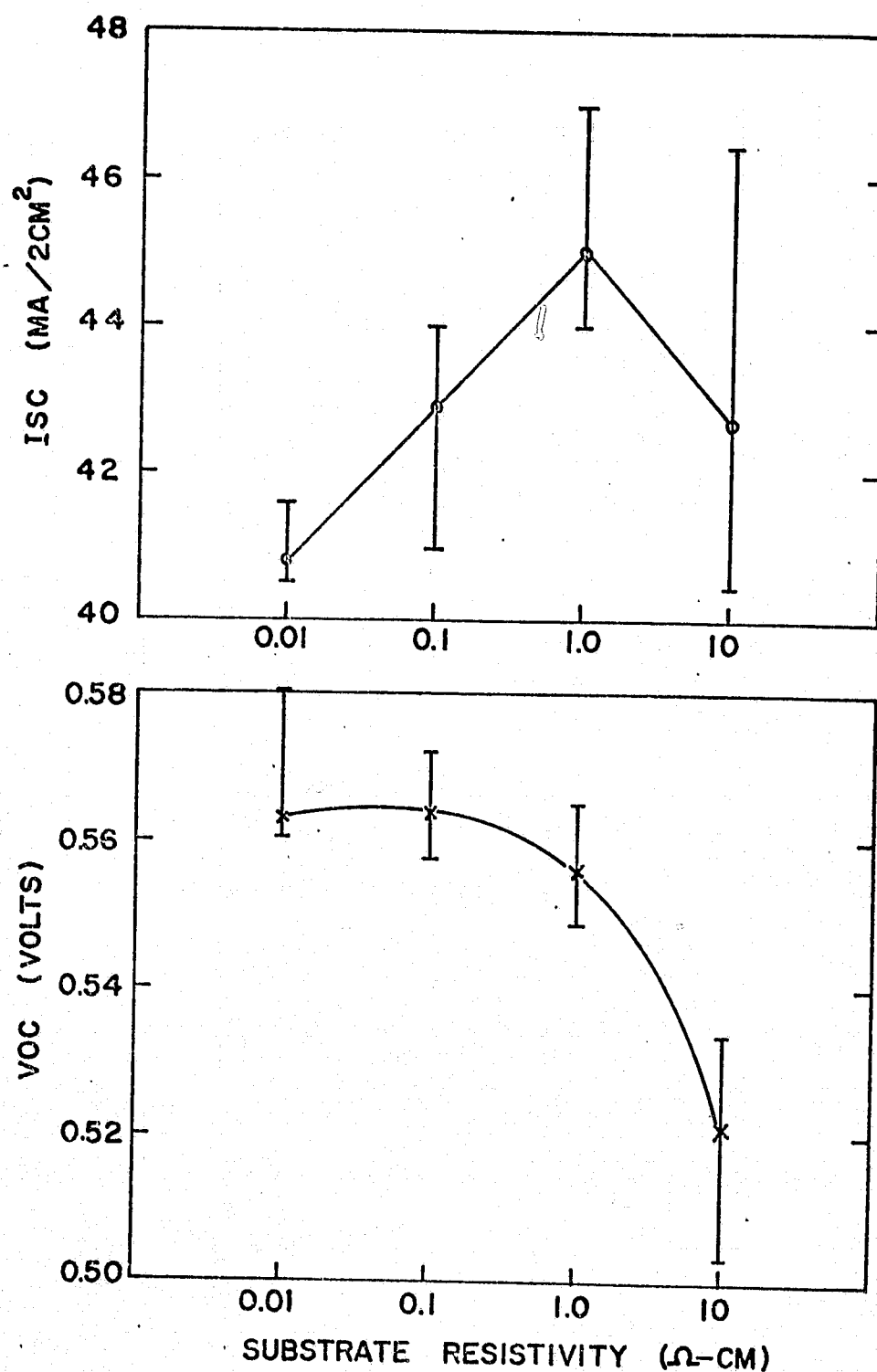
Figure 9.5. Comparison of experiments and HL junction theory for the experimental cells of Table 9.2.

be increased by the optical generated majority carrier density in the lightly doped n-type region. This is shown in Table 9.4. Therefore, the carrier confinement in the n-type region is deteriorated. On the other hand, for a BHL solar cell, the interaction between the base HL junction and the optical generated carriers is negligible due to the depth of the BHL junction from the illuminated surface. In this case, S_{HL} is primarily a function of the material parameters at both sides of the HL junction.

The predictions of V_{oc} from the first order model are shown as Tables 9.3 and 9.4 for cell (c) of Table 9.1. These are compared to the value of 0.565 volts from the exact numerical calculation.

9.5 p^+pn Emitter High-Low Junction Solar Cell

Since the previously proposed n^+np solar cell is not more efficient than the conventional junction solar cell, we now propose a similar EHL junction solar cell with a p^+pn structure. The new models are shown in Table 9.5. The structures of these cells are similar to those shown in Figure 9.1. In the numerical calculations, the solar cells are assumed to have a 595 Å thickness of Ta_2O_5 at one AM0 solar intensity. The SRV of the top surface is assumed to have a value of 10^3 cm/sec. The base diffusion lengths are assumed to be 30 μm and 60 μm, which are close to $L_D(MED)$ for the n-type base doping densities of 5×10^{17} /cm^3 and 10^{17} /cm^3 respectively. The surface p^+ and p layers are assumed to have a diffusion length of $(L_D(MAX) + L_D(MED))/2$.

The results of the numerical calculations are shown in Figure 9.6, which shows the dark I-V characteristics for cells of Table 9.5. The dark current densities are found to be nearly equal at high forward voltage irrespective of the doping density in the p-type layer. This implies

Table 9.3. Parameters used in the calculation of V_{oc} for cell (c) of Table 9.1.

EPITAXIAL LAYER

	Doping Density	Diff. Coeff.	Diff. Length (μm)	Width (μm)
Shockly's model	10^{14}	12	55	10
HL junction model	10^{14}	12	55	10
HL junction plus leakage current model	10^{14}	12	55	10

SURFACE LAYER

	Doping Density	Diff. Coeff.	Diff. Length (μm)	Thickness (μm)
Shockly's model	10^{19}	2	2.5	0.25
HL junction model	10^{19}	2	2.5	0.25
HL junction plus leakage current model	10^{19}	2	2.5	0.25

Table 9.4. Calculated V_{oc} from the first order model. Model A uses the extrinsic doping density of the n-type region in the calculation of V_{oc} while Model B takes into account the light-generated carrier density in n-type region.

	MODEL A SRV at HL junction (cm/sec)		V_{oc} (volts)	MODEL B SRV at HL junction (cm/sec)		V_{oc} (volts)
	S_o	S		S_o	S	
Shockly's Model	–	–		–	–	0.416
HL junction Model	0.80	(3.41)	0.504	8.0	1.29	0.563
HL junction plus leakage current Model	0.80	(5.7)	0.503	8.0	12.8	0.562

In Table 9.4, model B takes into account the light generated carrier density which is equal to $G\tau$. The calculated value of the light generated carrier density is about 10^{15} /cm^3 where G has a value of about 10^{21}/cm^3 in the n-type region.

Table 9.5. Structures of models a' to f' of p^+pn junction solar cell. N_S, X_S, X_b are equal to 2×10^{20} #/cm^3, 0.25mm and 200µm, respectively.

Model	a'	b'	c'	d'	e'	f'
N_B (#/cm^3)	5×10^{17}	5×10^{17}	5×10^{17}	5×10^{17}	5×10^{17}	10^{17}
N_E (#/cm^3)	-	10^{14}	10^{14}	10^{16}	5×10^{17}	10^{17}
X_E (#/cm^3)	0	10	20	10	10	10
Efficiency (%)	14.53	15.76	15.84	15.66	15.00	15.30

Table 9.6. The photovoltaic characteristics of emitter high-low junction solar cell of Table 9.1 and 9.5.

Model	c	h	j	b'	d'	e'	f'	k
Structure	n^+np	n^+np	n^+np	p^+pn	p^+pn	p^+pn	p^+pn	n^+npp^+
I_{sc} (MA/2cm^2)	79.82	77.94	62.62	75.21	74.92	71.24	77.70	85.16
V_{oc} (volts)	0.565	0.630	0.660	0.678	0.678	0.678	0.649	0.566
I_M (MA/2cm^2)	73.84	74.19	59.84	72.39	72.09	68.20	73.03	80.25
P_M (MW/2cm^2)	33.08	40.43	34.59	42.64	42.39	40.58	41.41	37.15
CFF	0.733	0.823	0.837	0.836	0.834	0.841	0.821	0.771
EFF (%)	12.22	14.94	12.78	15.76	15.66	15.00	15.30	13.73
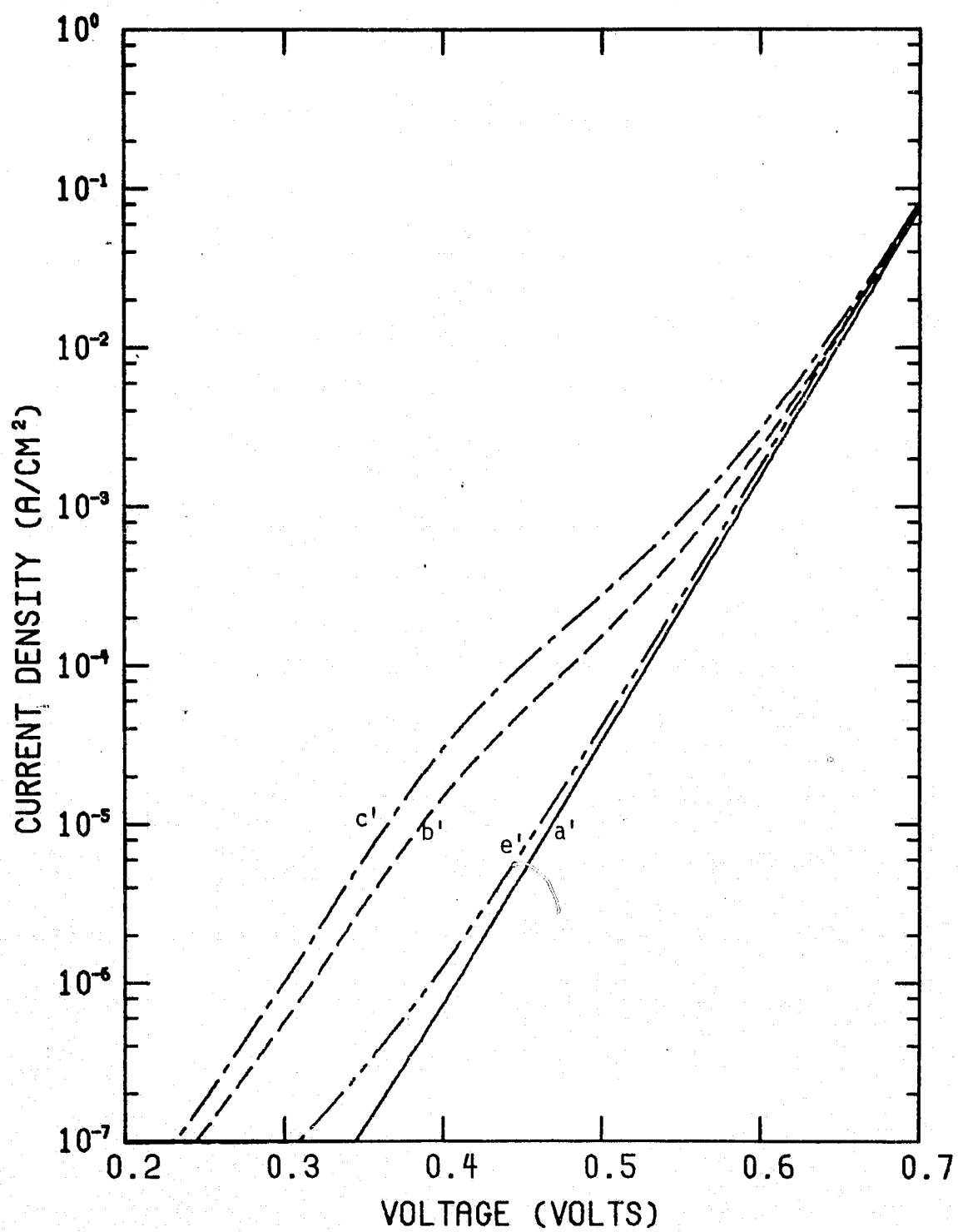
Figure 9.6. Dark I-V characteristics of p^+pn cell a', b', c', and e' of Table 9.5.

that the suppression of the dark emitter recombination current density and the total saturation current density is primarily determined by the base recombination current density in a p^+pn solar cell. Therefore, the open circuit voltage of these cells are relatively constant as shown in Table 9.6, which contains the detailed photovoltaic characteristics for some cells of Tables 9.1 and 9.5.

Finally, a novel n^+npp^+ solar cell is modelled which has both emitter and base high-low junctions. Both n-type and p-type layers are assumed to have a doping density of 1.3×10^{15} /cm^3. The p-type base layer has a diffusion length of 300mm and the n-type surface is assumed to have a diffusion length of $(L_D(MED) + L_D(MIN))/2$. The emitter and base high-low junctions have doping densities of 2×10^{20} /cm^3 and 10^{19} /cm^3 and depths of 0.25μm and 0.5μm, respectively. The calculated results are shown as Model k in Table 9.6. It is found that this cell does not show higher efficiency despite its high short circuit current density.

9.6 Discussions and Conclusions

This section will discuss the validity of the calculation of V_{oc} from the p-n junction saturation current density and the corresponding short circuit current density. In fact, V_{oc} is a series combination of the voltages across the p-n junction, surface region, base region and HL junction at the open circuit condition. Among the above components, the Dember voltages across surface and base regions are usually very small. The voltage across the HL junction is also small unless under high intensity illumination where V_{oc} reaches the junction built-in voltage [8]. Therefore, it is a good approximation to calculate V_{oc} from the junction saturation density and short circuit current density for a solar cell under one AMO solar density.

It can be concluded that the proposed n^+np junction solar cells do not yield a higher output voltage as expected from the incorporation of an additional high resistivity emitter layer in a conventional solar cell. The results show that the highest open circuit voltages are obtained for low resistivity emitter layers. On the other hand, a p^+pn junction solar cell can produce a higher open circuit voltage than an n^+np cell irrespective of the doping density in the surface layer. This is due to a more effective high-low junction and a higher diffusion length for the p^+p high-low junction.

1. C. T. Sah, F. A. Lindholm and J. G. Fossum. 1978. A high-Low Junction Emitter Structure for Improving Silicon Solar Cell Efficiency. IEEE Trans. Electron Devices ED-25(1): 66-67.

2. M. Wolf. 1972. Solar Cell - Outlook for improved efficiency. National Academy of Sciences, Washington, DC.

3. M. P. Godlewski, H. W. Brandhorst, Jr., and C. R. Baraona. 1975. Effects of high doping on silicon solar cell performance. Eleventh Photovoltaic Specialists Conference, Scottsdale, AZ: 32-35.

4. D. A. Iles and S. I. Soclof. 1973. Effect of impurity doping concentration on solar cell output. Tenth Photovoltaic Specialists Conference, Palo Alto, CA: 19-24.

5. M. P. Godlewski, C. P. Baraona and H. W. Brandhorst, Jr. 1973. Low high junction theory applied to solar cells. Tenth Photovoltaic Specialists Conference, Palo Alto, CA: 13-15.

6. R. C. Y. Fang and J. R. Hauser. 1977. Annual Report on NASA Grant. NGR 34-002-195.

7. H. W. Brandhorst, Jr., C. R. Baraona and C. K. Swartz. 1973. Performance of Epitaxial Back Surface Field Cells. Tenth Photovoltaic Specialists Conference, Palo Alto, CA: 212-217.

8. A. G. Sabnis. 1978. Junction Potentials of Strongly Illuminated n^+-p-p$^+$ Solar Cells. Solid State Electronics 21: 581-587.

10. APPENDICES

Appendix 10.1

COMPARISON OF THEORETICAL AND
EXPERIMENTAL SOLAR CELL PERFORMANCE*

C. R. Fang and J. R. Hauser

North Carolina State University
Raleigh, NC 27650

ABSTRACT

This paper presents the results of a detailed comparison between the theoretically predicted performance of silicon solar cells and the experimentally observed performance. The comparison has included the dark I-V characteristics, the spectral response characteristics and the I-V characteristics under AMO illumination. In general it has been found that the agreement between theory and experimental behavior is very good. This good agreement has been obtained for a variety of cells fabricated with junction depths ranging from 0.1 µm to more than 1 µm and for base layer resistivities from 10 Ω·cm to 0.1 Ω·cm.

INTRODUCTION

As interest has increased in solar cells in recent years, considerable progress has been made in thoroughly understanding the physics underlying solar cell operation. The discrepancies between simple theories of open circuit voltage and experimentally measured values have been of much interest and study [1]. The presence of high doping band gap reduction effects has generally become accepted as the reason for the low open circuit voltage of low resistivity base layer solar cells [2], although there is still some controversy over this effect [3].

The present study was undertaken to determine how closely present theory agrees with experiment with respect to solar cell performance. It is known that theoretical predictions are in general agreement with experimental results. However, no detailed comparison has been reported between theory and experiment for a range of specific solar cells.

ANALYTICAL APPROACH AND DEVICE PARAMETERS

The analysis has been performed using a detailed numerical solution of the semiconductor transport equations as applied to solar cells. Details of the approach and analysis have been presented elsewhere [4]. In general the analysis used is quite free from the normal simplifying approximations made in semiconductor device

analysis. A summary of the major features of the analysis include the following:

(a) Optical generation is calculated directly from available empirical measurements of a specific irradiance spectrum, including the effects of antireflection films and wavelength dependent absorption and index of refraction coefficients.

(b) The optically generated current is calculated directly from the interplay of the above generation rate and the device operation i.e. there are no assumptions pertaining to collection efficiency.

(c) Recombination is included within the analysis, not only for the bulk regions, but also for surface and depletion regions.

(d) Both drift and diffusion components of current flow are included. This allows the appearance of high injection effects, resistive loading, and the effects of any Dember type potentials.

(e) A diffused impurity profile is included in the surface region through an empirical or erfc impurity distribution.

(f) Band gap shrinkage due to heavy doping effects is included in the diffused surface region.

(g) A non-ohmic contact is included at the irradiated surface through a finite surface recombination velocity.

Several device parameters are of major importance in the modeling of solar cells. The most important of these are reviewed here to discuss the values and models used in the analysis. The lifetime or diffusion length is perhaps the single most important device parameter. The diffusion length is known to decrease in general with increasing impurity concentration. However, widely varying values as shown in Figure 1 have been reported for the diffusion length at any given doping density [3,5-8]. At low doping densities (below $10^{17}/cm^3$) measured diffusion lengths cover a range of values as large as two orders of magnitude. At large doping densities ($10^{19}/cm^3$ or above) the scatter in the experimental values appears to be much less as seen in Figure 1. This is likely due to the dominance of Auger recombination at large doping densities.

For solar cells which have good efficiency values, the base layer diffusion length must be above the center curve labeled L_n(MED) in Figure 1. Diffusion length values about midway between the L_n(MAX) and L_n(MED) curves of Figure 1 are typical of the values for the cells studied in this work.

For the base layer of the cells studied here, measured diffusion lengths were available. In most cases it was found that the calculated solar cell properties agreed well with the experimental data when the measured diffusion length or a value close to the measured value was used in the analysis. The BSF cells studied were found to be an exception to this rule. For these cells good agreement between theory and experiment could only be obtained using diffusing length values considerably larger than those measured by the X-ray technique. This is discussed in more detail in a later section.

For the diffused surface layer experimental data was not available for the diffusion length so the data of Figure 1 was used as a starting point in the analysis. The surface layer diffusion length was adjusted to obtain the best agreement between theory and experiment in the short wavelength region of the spectral response. Specific values used in the analysis are discussed in connection with the results. In general, the best agreement between theory and experiment was obtained when the surface diffusion length was taken somewhere between the L_n(MED) and L_n(MIN) curves of Figure 1. Since the surface layer is heavily doped, the region of Figure 1 of importance for the surface is around 10^{19}/cm^3 or above. In this region the difference between the solid curves is not nearly as great as at lower doping densities.

The properties of the surface layer of any silicon solar cell plays an important part in the performance of the cell. In this work, the analysis has been found to be sensitive to the doping profile used in the surface layer. As an approximation a Gaussian or erfc profile is frequently used for a diffused layer. Experimentally it is known that a phosphorous diffused layer has an impurity profile which differs significantly from the simple Gaussian or erfc profile [9]. Near the surface a region of nearly constant doping appears. This is followed by a rapid drop in carrier concentration to a region deeper into the diffused layer which follows fairly closely an erfc profile. Tsai [9] has given curves from which the surface doping density C_s, the width of the constantly doped layer X_c and the doping density C_E at the boundary of the constantly doped and erfc doped region can be estimated using the diffusion time and temperature.

In the early stages of this work simple erfc or Gaussian doping profiles were used in the theoretical calculations. With such profiles it was found to be very difficult to obtain good agreement between theory and experiment in the spectral response data. In most cases good agreement was never obtained with the simple doping profiles. After an impurity profile such as that found by Tsai [9] was used in the calculations, it became much easier to obtain good agreement between theory and experiment.

Not only the doping profile, but also heavy doping bandgap reduction effects appear to be important in the diffused surface layer. It has now been pointed out by several workers that the bandgap reduction effect appears to be the physical origin of the low open circuit voltage of low resistivity base layer cells [2,10]. As discussed previously, bandgap reduction effects were included in the analysis performed here and appears to be essential for obtaining good agreement between theory and experiment unless one uses very small diffusion lengths within the surface layer. The combination of the correct doping profile and bandgap reduction effects leads to a thin surface layer which behaves almost identically for carrier collection as the "dead layer" model of Lindmayer [11].

The Keldysh-Franz effect has recently been proposed as an important effect in solar cells [3]. This effect was included in some of the theoretical calculations using experimental data for the bandgap reduction due to an electric field [12]. The major effect has been to increase the calculated dark current from a cell at low voltages by a factor of 2 to 5. The effect has typically been very small for voltages above about 0.5 volts forward bias. The Keldysh-Franz effect can only be of major importance in solar cells dominated by depletion region current and the cells studied in this work did not show this characteristic.

An accurate modeling of the optical processes is important to obtaining good agreement between theory and experiment in spectral response data. In general the optical processes associated with surface reflection and bulk absorption are well known and characterized for silicon. One region where some uncertainty still exists is the long wavelength absorption coefficient around 1.0 µm. This is difficult to experimentally measure because of long wavelength free carrier absorption in silicon. At the beginning of this work the data of Dash and Newman [13] was used for α in the long wavelength region. However, it was soon found that good agreement between theory and experiment could not be obtained at 0.95 µm and 1.0 µm using this data. The reported range of absorption coefficient values in this wavelength range is shown in Table 1. As can be seen there are very significant reported differences with Dash and Newman's values being near the largest reported. After using several potential values, good agreement between theory and experiment was obtained using the values in the last row of Table 1. These values can be seen to be well within the range of reported values and we believe these values are more accurate than most of the reported experimental values since they give good agreement between theory and experiment for a wide variety of solar cells.

In addition to absorption coefficient an accurate modeling of surface reflection is needed.

Some of the cells studied had bare silicon surfaces while others had a Ta_2O_5 coating of about 595Å in thickness. At the beginning of this work a comparison was made between theory and experimental data for the transmission coefficient of a bare surface and a Ta_2O_5 coated surface. The agreement was within about 1% except in the 0.9 to 1.1 μm region where larger differences occurred. The origin of the discrepancy here is not known. However, the excellent agreement elsewhere, give confidence in the accurate modeling of surface reflection and transmission properties.

A complete characterization of solar cells requires that account be taken of the two-dimensional effects associated with the contact grids. Spectral response measurements made at low light levels are not greatly affected by the contact grid except for the area reduction factor. However, the dark and light I-V characteristics are influenced by the sheet resistance, contact resistance and two-dimensional properties. Values of efficiency and curve factor are especially influenced by two-dimensional effects. In this work a two-dimensional grid model was used to accurately model these effects. Details of the analysis and model are discussed elsewhere [19]. A two-dimensional modeling of the contact effects is necessary if good agreement is to be obtained between theory and experiment for efficiency, open circuit voltage, and curve factor.

RESULTS OF COMPARISON

A few general comments are needed to explain the manner in which the comparison between theoretical and experimental results has been made. The experimental data which was used consists of three different types of measurements. These are 1) dark current I-V characteristics, 2) short circuit spectral response data and 3) light I-V characteristics under simulated AM0, 1 sun illumination. In addition to this general breakdown, two types of dark current data was available. The first technique simply measures the terminal I-V characteristics of a solar cell in the dark. The second technique measures open circuit voltage V_{oc} and short circuit current I_{sc} at various intensities of illumination and plots the resulting pairs of numbers. These two techniques will be referred to as the dark I-V technique and the $I_{sc}-V_{oc}$ technique. For an ideal one-dimensional solar cell with no series resistance both techniques should give the same curve, since at the open circuit voltage condition the internal dark current exactly equals the short circuit solar generated current. The two curves differ when series resistance and two-dimensional effects are considered. At high current densities the $I_{sc}-V_{oc}$ technique tends to be much closer to the ideal one-dimensional theory since the voltage is measured under conditions of zero net current flow in the solar cell. The differences between the two measurement techniques will become clearer after the discussion of the specific examples.

In comparing the theory and experimental data not all device parameters are of major importance

in each set of measurements. For example the spectral response depends very little on sheet resistance, contact resistance and other two-dimensional properties of the cell. Also as just discussed the $I_{sc}-V_{oc}$ measurement is relatively insensitive to two-dimensional effects. The device parameters of most importance in these characteristics are the device diffusion lengths, doping profile, surface recombination velocity, and heavy doping models. Thus the $I_{sc}-V_{oc}$ data and the spectral response data has been compared with the results of the one-dimensional calculations. The parameters of sheet resistance, contact resistance and grid structure were then included along with the one-dimensional results in the two-dimensional computer program and compared with the dark I-V characteristics and the light I-V characteristics. For almost all of the devices a combination of sheet resistance and contact resistance was required to accurately describe the two-dimensional nature of the cells.

The solar cells studied can be broadly divided into three categories of cells based upon the resistivity of the base layer and the type of cell design. The first category consists of n^+-p cells with 0.1 Ω·cm base layers and a finished thickness of either 6 mils or 10.2 mils. The second category consists of n^+-p cells with 10 Ω·cm base layers and a thickness of about 10.5 mils. The third type of cell is a back surface field (BSF) cell with a 16 Ω·cm base layer and a thickness of about 6.5 mils.

The first two categories of cells were 1 cm by 2 cm and used a ten finger grid pattern while the third category of cells were 1 cm by 2 cm and used a nine finger grid pattern. Table 2 gives parameters for the two different gird patterns used on the cells. The first two categories had a bare silicon surface while the third category cells were coated with 595 Å of Ta_2O_5 and a 5 mil Teflon FEP cover.

The solar cells were fabricated and measured at the NASA-Lewis Research Center, Cleveland, Ohio. The n-type surface layers were phosphorous diffused, using $POCl_3$. The temperature and duration of the diffusion process are described for each type of cell in the following sections. The top and bottom contacts were made using a metal mask with evaporated aluminum (200 ~ 500 Å) followed by evaporated silver of a few μm. The contacts were sintered at temperatures of 550 to 650°C in H_2. For each cell the base layer diffusion length was measured at NASA Lewis by the X-ray method.

Within each class of cells the measured characteristics were consistent and certain cells considered to be typical of each type were selected for detailed study. The major differences in any given category of cells were in the dark current values at low voltages. These differences do not greatly influence solar cell performance since operation is at larger voltages where the differences between cells is reduced.

CELLS WITH 0.1 Ω·CM BASE LAYERS

Results for two different cells within this general category are presented. These cells were

fabricated on 0.1 Ω·cm ($5 \times 10^{17}/cm^3$) Boron doped wafers. Various device parameters for the two cells which are D-1 and D-2 are listed in Table 3. The major differences between the two cells are the cell thickness, 6 mils and 10.2 mils, and junction depth, 1.0 μm and 0.72 μm. The base layer diffusion lengths of 60 μm and 105 μm are the experimental values which were also used in the computer calculations.

A comparison of the calculated and experimental dark I-V characteristics is shown in Figure 2. The comparison between theory and experiment is very good for voltage values of 0.45 volts or larger. There is a large difference between theory and experiment at low voltages and this is typical of all the solar cells studied. It might first be suggested that this difference is due to the Franz-Keldish effect which was neglected in the calculations. However the current is much larger than that calculated including the Franz-Keldish effect. Also the voltage dependence of this excess current is not consistent with the Franz-Keldish effect.

The triangle points in Figure 2 show the current which would result from a pure resistor of 2.57 KΩ in parallel with the solar cell. As can be seen from the figure this voltage dependence fits the excess current almost exactly. The presence of such a shunting resistance has been seen in all cells studied. The magnitude of this resistance has been observed to vary greatly from cell to cell within a particular category. This shunting resistance has not been studied in any detail in this work, but it has also been observed by previous workers [20]. The physical origin of this resistance remains somewhat of a mystery. It may be due to shunting precipitates for example within the junction depletion region.

The dotted curve in Figure 2 illustrate the sensitivity of the calculated dark I-V characteristic to the diffusion length (or lifetime) in the diffused surface layer. Values calculated using the L_D(MED) curve of Figure 1 are definitely below the experimental curve. The best fit was obtained using values midway between L_D(MED) and L_D(MIN) of Figure 1. The final selection of base layer and surface layer diffusion lengths must be made from comparing not only the dark current data but also the spectral response data. A small surface layer lifetime cannot be distinguished from a small base layer lifetime using dark current data alone since both lead to large dark currents. However, differences can be seen between these two cases in the spectral response calculations.

A comparison between the theoretical and experimental spectral response calculations is shown in Figure 3. The parameters which give good dark current calculations are also seen to provide good spectral response calculations. Curves are also shown of the relative contributions to the spectral response from the base layer, depletion layer and surface layer. The spectral response calculations prove to be a sensitive test for accurate device parameters.

The spectral response at 0.9 - 1.0 μm is determined almost entirely by the base layer properties. Values at this point are very sensitive to the base layer diffusion length and long wavelength absorption coefficient. The corrections to the long wavelength absorption coefficient discussed earlier were identified studying the long wavelength spectral response. Before the absorption coefficient values of the last line in Table 1 were used, it was not possible to accurately match the dark current data and long wavelength spectral response, not only of this cell, but of all the cells studied.

The spectral response at 0.4 - 0.45 μm is determined almost entirely by the surface layer properties, which include not only surface layer lifetime, but also surface recombination velocity, doping profile and bandgap reduction effects. Because of the interaction of all these effects it is difficult to attribute a given spectral response value to any one of these effects alone. Initial calculations were made for the cells using an erfc doping profile in the surface layer. With this type of doping profile it proved difficult to obtain a good match of spectral response at all wavelengths. In general the spectral response would be too large at 0.4 - 0.45 μm if a good fit was obtained at larger wavelenths. Reasonable combinations of diffusion length, surface recombination, surface doping etc. could not be found to match the data. However, when an impurity profile modeled after the experimental work of Tsai was used, good agreement such as shown in Figure 3 became relatively easy to obtain. The parameters describing the surface doping profile are listed in Table 4 for this device and the other devices studied.

In the final analysis the only device parameters which were adjusted somewhat to obtain the good agreement between theory and experiment seen in Figures 2 and 3 were the surface recombination velocity and the surface layer diffusion length. The final values used and reported in Table 3 are quite consistent with the diffusion length data of Figure 1 and other reported values of surface recombination velocity [7].

In calculating the light I-V characteristics and the overall efficiency at AM0, additional parameters describing the contact grid (Table 2) and values of surface layer sheet resistance and contact resistance must be introduced into the two-dimensional model. The D-1 solar cell and other devices with the 1.0 μm junction depth were found to have very low values of sheet resistance and contact resistance. Values used in the analysis are given in Table 5 for this and the other cells studied. Figure 4 shows a comparison between the solar cell power quadrant I-V characteristics and the theoretical calculations. Again the agreement between theory and experiment is very good.

The second cell in this category for which data is reported (D-2) is similar to that just discussed except for the shallower junction depth and increased base layer thickness as shown in

Table 3. Tables 3 and 4 also show that essentially the same parameters were used in the theoretical calculations as for cell D-1. A larger diffusion length of 105 µm was measured in this cell and this value was used in the calculations.

Figures 5, 6 and 7 show a comparison between theory and experiment for this cell. In Figure 5, a significant difference is seen in the experimental dark I-V and I_{sc}-V_{oc} measurements at voltages of 0.6 and 0.7 volts. The I_{sc}-V_{oc} data agrees well with the one-dimensional calculations while the two-dimensional calculations including sheet resistance and contact resistance is required to describe the dark I-V data.

Several curves are shown in Figure 5 to illustrate several different theoretical models. The solid curve gives a good fit at large voltages using the parameters of Tables 3 and 4. A dashed curve shows the effect of including the Keldish-Franz effect in the device. Above about 0.5 volts the Keldish-Franz effect is seen to have little influence on the curves. The curve including the Keldish-Franz effect combined with a shunting resistance of 5 kΩ does appear to give the best fit to the low current data for this particular cell.

The dotted curve shows a calculation using the same parameters as the solid curve but neglecting heavy doping bandgap reduction effects. The current can be seen to be much too small at high voltages. Without the heavy doping effects a very low surface layer lifetime would be required to get agreement between theory and experiment.

The parameters which give a good fit to the dark current, also give good spectral response calculations as seen in Figure 6. Without heavy doping effects the spectral response is also seen to be much too large at short wavelengths.

A comparison between theory and experiment for the light I-V characteristics is given in Figure 7. In this case it is seen that the inclusion of the shunting resistance and the Keldish-Franz effect gives the best fit to the experimental data. For both of the two-dimensional calculations sheet resistance and contact resistances of 21 Ω/□ and 0.12 Ω respectively were used in the calculations.

CELLS WITH 10 Ω·CM BASE LAYERS

The second general class of cell studied were fabricated on 10 Ω·cm material of 10.5 mils thickness. Additional data on the cells is contained in Tables 3 and 4. The junction was diffused at 850°C for 30 mins, resulting in a junction depth of about 0.57 µm. Parameters used in the calculations to describe the doping profile are given in Table 4.

Basically the same models and device parameters were used for these cells as for the 0.1 Ω·cm cells. A detailed comparison between theory and experiment is shown in Figures 8, 9 and 10. In Figure 8 a large difference is seen at large

currents between the I_{sc}-V_{oc} characteristic and the standard dark I-V characteristic. This indicates a very large sheet resistance and/or contact resistance. The difference between the curves is accurately described by a sheet resistance of 1500 Ω/□ and a contact resistance of 1.12 Ω. These values are both very large and much larger than can be tolerated in high efficiency solar cells. No attempt was made on this cell to describe the low current region by either the Keldish-Franz effect or a shunting resistance since this has little effect on the characteristic above about 0.4 volts.

The comparison between theory and experiment for the spectral response is shown in Figure 9. Good agreement is again seen over the entire wavelength range. Included for comparison are calculations for an erfc doping profile at various surface recombination velocity (SRV) values. A good fit to the short wavelength values could not be obtained for the erfc profile even with very small values of SRV.

A reasonably good overall fit to the light I-V characteristic is shown in Figure 10. The agreement in this case is not quite as good as for the 0.1 Ω·cm devices. The largest error between theory and experiment occurs in V_{oc} which has about a 2% error. This is probably due to a theoretical dark current which is slightly too large. This in turn could be due to a diffusion length used in the base or surface layers which was slightly too small. In general, however, the agreement between theory and experiment is good considering the large values of sheet resistance and contact resistance for these cells.

CELL WITH 16 Ω·CM BASE LAYERS

The final general class of cells studied were BSF cells on 16 Ω·cm base layers. Relevant device data is given in Tables 3 and 4. The devices had a very shallow junction depth of about 0.2 µm. Because of the very shallow junction depth, the diffusion profile was modeled by a single erfc profile. The back surface field region was made by alloying Al. This p^+ layer was modeled as a Gaussian doped region of $10^{19}/cm^3$ doping density and 0.5 µm in width. A Ta_2O_5 antireflecting layer of 595Å was present on the cells and this was included in the computer calculations.

The terminal I-V characteristics are shown in Figure 11. Two theoretical curves are shown. The dotted curve was calculated using the experimental diffusion length value of 160 µm. This is seen to give a current much larger than the experimental values. The dark current could not be made to agree with experiment until the base layer diffusion length was increased to about 460 µm. The resulting curve is the solid one in Figure 11. For the non BSF cells studied the measured diffusion length was found to give a good theoretical calculation. However, the failure of the X-ray measurement technique to give a reliable diffusion length value is not too surprising in the present case. The cell thickness of 6.5 mils corresponds to 165 µm which almost exactly equals the measured

diffusion length. The X-ray technique is known to become unreliable when the diffusion length becomes larger than the cell thickness [21]. The 460 μm diffusion length value is also consistent with the expectation that 16 Ω·cm material should have a larger diffusion length than 10 Ω·cm material. This inconsistency between the measured diffusion length and the calculated performance was observed for all thin BSF cells studied in this group.

Comparisons of spectral response and light I-V data are shown in Figures 12 and 13. The agreement is again very good. For this cell a sheet resistance value of 380 Ω/□ and a negligible contact resistance were found to give a good match to both the efficiency and the dark current I-V data.

SUMMARY AND CONCLUSIONS

This work has involved a detailed comparison of the experimental performance of three types of solar cell designs with the theoretical results calculated with a detailed numerical analysis of solar cell performance. The analysis included a two-dimensional analysis of sheet resistance and contact resistance effects.

In general it has been found that an accurate modeling of all the physical effects present and of the device doping profile leads to theoretical calculations which are in very good agreement with experimental results. The most important physical effects which were found to be necessary in order to obtain good agreement between theory and experiment are:

1. The base layer and surface layer lifetimes or diffusion lengths.

2. The doping profile within the diffused surface layer.

3. The presence of heavy doping bandgap reduction effects.

4. An accurate modeling of the absorption coefficient and surface reflection.

5. An accurate modeling of the two-dimensional nature of the surface sheet resistance and metal contact resistance.

The good correlation of theory and experiment obtained here give confidence that the theoretical calculations can be extended to other device structures and device designs and accurate results obtained.

ACKNOWLEDGMENT

REFERENCES

1. Brandhorst, H. W., Jr., Record of Ninth Photovoltaic Spec. Conf., 37 (1972).

2. Godlewski, M.P., Brandhorst, H.W., Jr., and Baraona, C.R., Eleventh Photovoltaic Spec. Conf., Scottsdale, AZ, 32 (1975).

3. Rittner, E.S., Jour. of Energy, 1, no.1,9(1977).

4. Dunbar, P.M. and Hauser, J.R., Proc. Eleventh IEEE Photovoltaic Spec. Conf., IEEE Press(1975).

5. Iles, P.A. and Soclof, S.I., Tenth Photovoltaic Spec. Conf., Palo Alto, CA, 19 (1973).

6. Fisher, H. and Pschunder, W., Tenth Photovoltaic Spec. Conf., Palo Alto, CA, 404 (1973).

7. Wolf, M., Energy Conversion, 11, 63 (1971).

8. Kendall, D., Conf. Physics and Application of Lithium Diffused Silicon, NASA-Goddard Space Flight Center, 1969.

9. Tsai, J.C.C., Proc. IEEE, 57, No.9, 1499 (1969).

10. Lindholm, F.A., Neugroschel, A., Sah, C.T., Godlewski, M.P. and Brandhorst, H.W.,Jr., IEEE Trans. on Electron Dev., ED-24, No. 4, (April 1977).

11. Lindmayer, J. and Allison, J.F., COMSAT Tech. Rev. 3, No.1, 1 (Spring 1973).

12. Britsyn, K.I. and Smirnov, A.A., Sov. Phys. Sol. St., 18, 126 (1966).

13. Dash, W.C. and Newman, R., Phys. Rev. 99 4, 1151 (1955).

14. Vedam, K., JPL Cont. No. 952385, 1969 (Unpub.).

15. Runyan, W.R., Final Rept., NASA-Grant No. NGR-44-007-016, 1968 (Unpub.).

16. Vol'fson, A.A. and Subashiev, V.K., Sov. Phys. Semicond. 1, 327 (1967).

17. MacFarlon, G.G., McLean, T.P., Quarrington, J.E. and Roberts, V., Phys. Rev. 111, 1245 (1958).

18. Reynolds, J.H. and Meulenberg, A., Jr., Jour. of Appl. Phys., 45, 2582 (1974).

19. Fang, C.R. and Hauser, J.R., Paper presented at Thirteenth Photovoltaic Conf., (1978).

20. Stirn, R. J., Ninth Photovoltaic Spec. Conf., Silver Spring, 72 (1972).

21. Zimmerman, W., Phy.Stat.Sol.(a), 12, 671 (1972).

Table 1. Comparison of reported absorption coefficient values at long wavelengths [18].

	Absorption Coefficient (cm⁻¹)		
	1.1 μm	1.0 μm	0.95 μm
[13] Dash & Newman	7	100	220
[14] Vedam	–	–	270
[15] Runyan	–	67	170
[16] Vol'fson & Subashiev	–	64	150
[17] Macfarlon	3.9	74	204
This work	3.9	74	204

Table 2. Parameters for the two grid patterns.

Parameter	1 cm by 2 cm 10 finger cell	1 cm by 2 cm 9 finger cell
Length of fingers (cm)	0.9736	1.949
Width of fingers (cm)	0.02	0.0055
Thickness of metal (cm)	0.00019	0.00019
Spacing between fingers (cm)	0.18	0.1056
Bus bar width (cm)	0.0264	0.051
Resistivity of metal ($\Omega \cdot cm$)	1.56×10^{-6}	1.56×10^{-6}

Table 5. Resistance parameters for two-dimensional analysis.

Parameter	Cell number			
	D-1	D-2	D-3	D-4
Sheet resistance $\Omega/\square$	9	21	1500	380
Contact resistance	10^{-4}	0.12	1.12	10^{-4}

Table 3. Device parameters.

Parameter	Cell number			
	D-1	D-2	D-3	D-4
Base layer resistivity	$0.1 \ \Omega \cdot cm$	$0.1 \ \Omega \cdot cm$	$10 \ \Omega \cdot cm$	$16 \ \Omega \cdot cm$
Thickness (mils)	6.0	10.2	10.5	6.5
BSF Cell	NO	NO	NO	YES
Surface profile	empirical	empirical	empirical	$2 \times 10^{20} erfc$
$L_{surface}$	$L^{*}_{min} \sim L_{med}$	L_{min}	$\frac{1}{2}(L_{min}+L_{med})$	$\frac{1}{2}(L_{min}+L_{med})$
L_{base} (μm)	60	105	230	160(460*)
Junction depth (μm)	1.0	0.72	0.57	0.2
SRV (cm/sec)	10^{5}	10^{5}	2×10^{4}	5×10^{3}
Anti-reflection layer	absent	absent	absent	$595 \overset{\circ}{A} \ Ta_2O_5$

*Value actually used in calculations.

Table 4. Parameters of surface diffused layer.

Parameter	Cell Number			
	D-1	D-2	D-3	D-4
X_j (μm)	1.0	0.72	0.57	0.2
C_s (cm^{-3})	4×10^{20}	4×10^{20}	2×10^{20}	2×10^{20}
C_E (cm^{-3})	8×10^{19}	8×10^{19}	2×10^{19}	2×10^{20}
X_c (μm)	0.4	0.20	0.07	0.0
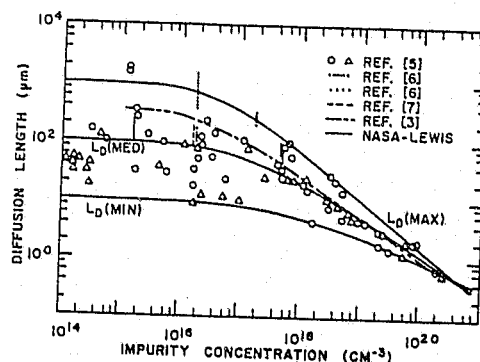
Figure 1. Model of the diffusion length and comparison to experimental data. All experimental data are for p-type material except those marked by triangles.
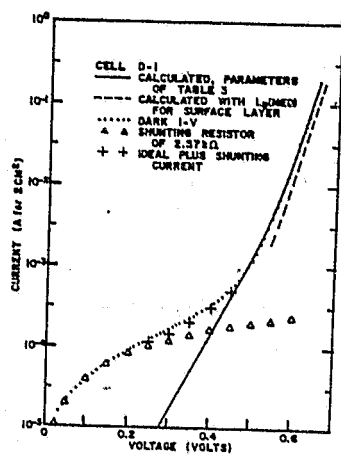
Figure 2. Dark I-V characteristics of Cell D-1.

Figure 5. Dark I-V characteristics of Cell D-2.

Figure 3. Spectral response of Cell D-1.
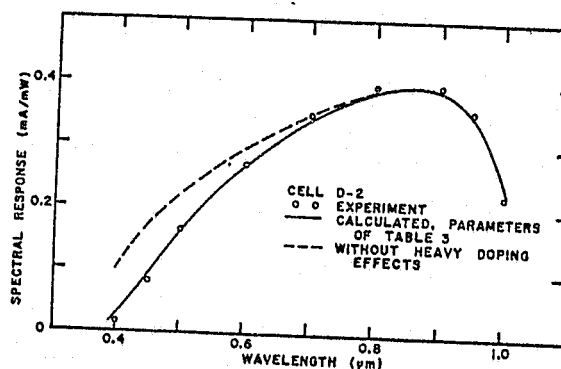
Figure 6. Spectral response of Cell D-2.
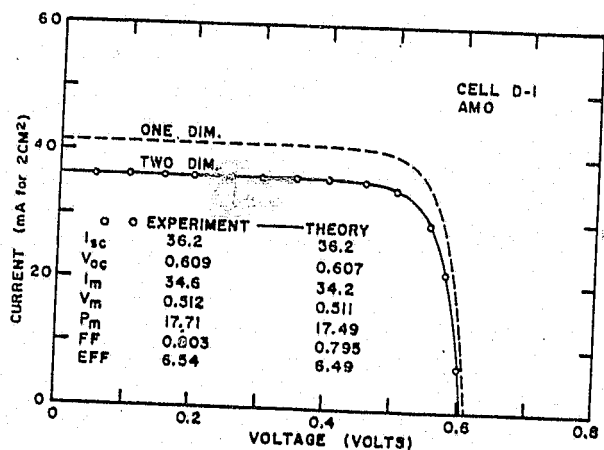
Figure 4. Comparison of theory and experiment for the photovoltaic I-V characteristics of Cell D-1.
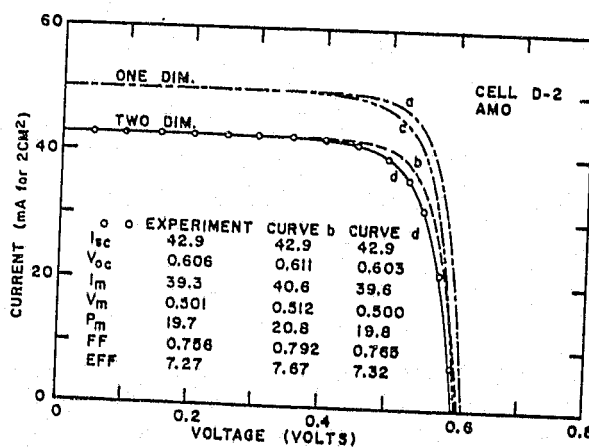
Figure 7. Comparison of theory and experiment for the photovoltaic I-V characteristics of Cell D-2. Curves a and b are for the parameters of Table 1. Curves c and d include a shunting current and Franz-Keldysh effect.
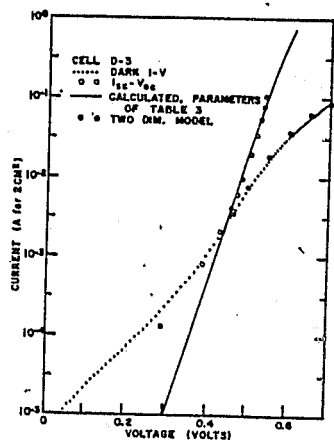
Figure 8. Dark I-V characteristics of Cell D-3.
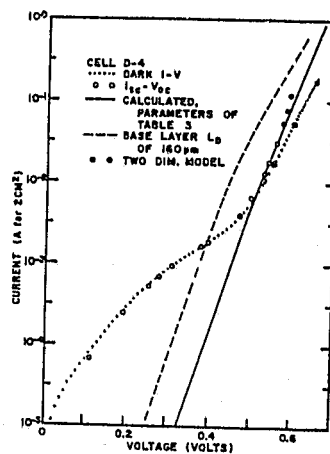
Figure 11. Dark I-V characteristics of Cell D-4.
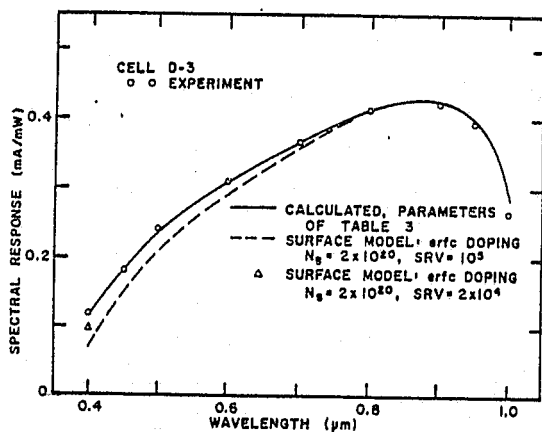
Figure 9. Spectral response of Device D-3.
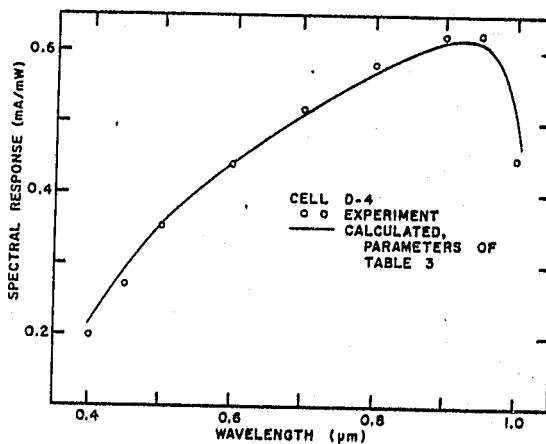
Figure 12. Spectral response of Cell D-4.
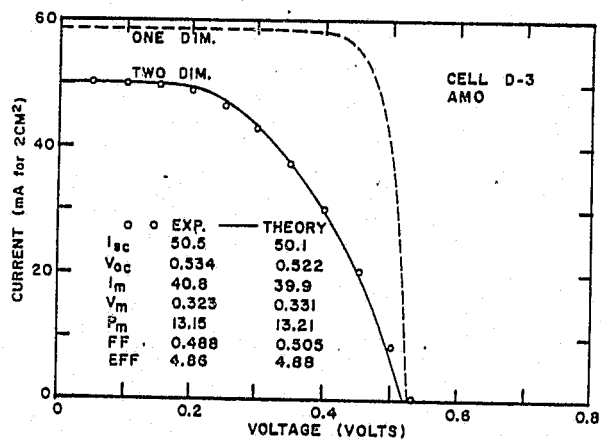
Figure 10. Comparison of theory and experiment for the photovoltaic I-V characteristics of Cell D-3.
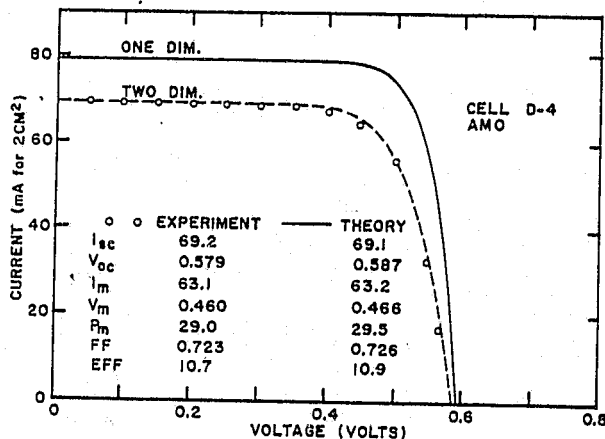
Figure 13. Comparison of theory and experiment for the photovoltaic I-V characteristics of Cell D-4.

Appendix 10.2   A TWO DIMENSIONAL ANALYSIS OF SHEET RESISTANCE AND

CONTACT RESISTANCE EFFECTS IN SOLAR CELLS*

C. R. Fang and J. R. Hauser

North Carolina State University
Raleigh, NC 27650

ABSTRACT

Most studies of contact resistance and sheet resistance effects in solar cells have modeled these effects in terms of a lumped resistance in series with an ideal solar cell. The two-dimensional nature of the distributed sheet resistance from the surface layer, however, makes the accurate modeling of a solar cell more involved than a simple series resistance. If an ideal one-dimensional solar cell has a dark current which varies as exp(qV/kT), the terminal current of a cell including sheet resistance will have a voltage dependence which approaches exp(qV/2kT) at large currents due to the sheet resistance ohmic voltage drops. This effect cannot be accurately modeled by a lumped resistance. In this work an analytical model and detailed numerical calculations have been studied for describing the sheet resistance and contact resistance effects in solar cells.

INTRODUCTION

The important effects of contact resistance and the sheet resistance of the surface layer have been recognized for some time. Series resistance effects are especially important in determining peak efficiency and curve factor of a cell and are of lesser importance in determining short circuit current, open circuit voltage and spectral response. Analytical studies have been conducted by several workers [1,2] developing expression for the series resistance to be used in modeling solar cells. As discussed later these approaches all have limited application because the two-dimensional nature of the sheet resistance cannot be accurately modeled by a lumped resistance unless one is considering only small changes in voltage about some operating point.

Figure 1 shows a typical solar cell structure with a conventional contact finger geometry. The front surface metal consists of a main bus bar to which metal fingers which collect the current are attached. Such a structure has the following major sources of resistance:

1. Bus bar metal resistance,

2. Finger metal resistance,

3. Front surface contact resistance between metal grid and semiconductor,

4. Sheet resistance of the semiconductor layer at the surface,

5. Base layer bulk resistance,

6. Back surface contact resistance between metal and semiconductor.

In particular solar cells any or all of these could provide the major source of series resistance, but for solar cells operating at 1 sun, the two major sources of resistance are usually contact resistance and surface layer sheet resistance. This assumes that the contact metal grid structure has been designed with sufficient thickness of metal that voltage drops along the contact fingers are small. This is readily done at 1 sun intensity.

For multi-sun operation it becomes more and more difficult as the intensity is increased to achieve a good contact grid design. The spacing between the grids must be decreased as well as decreasing the width of the contact stripes. Ohmic drops along the contact fingers tend to become more important under multi-sun conditions. The base layer resistance can also become more important. However for BSF (back surface field) cells in which the base layer is less than a diffusion length, conductivity modulation effects in the base tend to minimize base layer resistivity effects, even under multi-sun conditions.

The major emphasis of this work has been on the contact resistance and sheet resistance as they dominated the solar cells studied. The two-dimensional computer analysis, however, was designed to include all of the effects discussed above except for any bus bar resistance, i.e., the bus bar was assumed to be at a constant potential.

SOLAR CELL MEASUREMENTS

There are three fundamental sets of terminal I-V measurements which are influenced in different ways by the series resistance and two-dimensional effects. In the first method the terminal I-V characteristic is measured under a steady illumination. These measurements may be made for AM0, AM2 or some other spectrum and under 1 sun or multi-sun conditions. In any case by varying the

load resistance the power quadrant of active solar cell operation is obtained. The important parameters determined from this are short circuit current, open circuit voltage, efficiency, fill factor, etc. This is of course the most important final test of solar cell performance. For the first order model of an ideal solar cell in series with a cell resistance, this curve is described by the equation

$$I=I_{sc}-I_o\{exp[q(V-IR_s)/kT]-1\}, \qquad (1)$$

where I_{sc}, I_o and R_s are constants for the cell and illumination conditions.

In the second technique the dark forward I-V characteristics are measured by applying a terminal voltage and observing the current. If a solar cell can be described as an ideal diode in series with some resistance, the current in this measurement can be expressed as

$$I=I_o\{exp[q(V-IR_s)/kT]-1\}, \qquad (2)$$

where I_o and R_s are constants.

The third method referred to here as the I_{sc}-V_{oc} method uses a varying illumination level and measures open circuit voltage and short circuit current. A plot of the corresponding points then gives an I-V curve, which according to the model of an ideal cell in series with a series resistance can be expressed as

$$I_{sc}=I_o\{exp(qV_{oc}/kT)-1\}. \qquad (3)$$

This method has been used independetly by Heeger [3], Wolf [1] and Queisser [4]. The advantage of this technique is that the effects of series resistance are eliminated, according to first order theories.

Figure 2 shows experimental data measured on one particular solar cell by the two techniques discussed above. Attention should be directed to the regions of the curves for which voltage >0.5 volts. Below about 0.5 volts the curves are dominated by depletion region currents and shunting resistance currents and the ideal diode theory does not apply. The I_{sc}-V_{oc} data is seen to follow almost exactly the expected (See Equation (3)) exp(qV/kT) dependence as indicated by the solid curve. The standard dark current curve, however, is seen to follow almost exactly an exp(qV/2kT) dependence. This cannot be described by Equation (2) for any constant value of series resistance.

The type of behavior seen in Figure 2 has been observed on a wide range of solar cells. The I_{sc}-V_{oc} data at large currents follows almost the ideal diode behavior. Deviation from the ideal exp(qV/kT) behavior are always observed at low currents and are again observed at high currents where high injection effects begin to occur. In the region where the standard dark current data begins to deviate from the I_{sc}-V_{oc} data the slope of the curve on a semilog graph tends to be almost exactly one-half that of the I_{sc}-V_{oc} data. This type of behavior can only be explained by the model of an ideal diode in series with a resistor,

as for example Equation (2), if one assumes that R_s is a function of current level. A series resistance which varies with current level has indeed been found and reported by several workers [1,5]. However, the almost exact factor of 2 in the slope of the two curves leads to the suspicion that there is some fundamental physical process responsible for this and that the effect is not simply a current dependent resistance. This is indeed the fact as shown in the next section where the two-dimensional nature of the sheet resistance is shown to account exactly for this factor of 2 in slope.

DISTRIBUTED SHEET RESISTANCE

The sheet resistance of the surface layer of a solar cell is one of the most important, if not the most important, contribution to the resistance effect in solar cells. Figure 3 shows a cross sectional view of a solar cell illustrating the distributed nature of the surface layer sheet resistance. Consider the dark I-V characteristics of the cell generated by applying a voltage to the terminals as in Figure 3. The current which crosses the p-n junction must flow in a direction transverse to the p-n junction to reach parts of the junction away from the contact. This causes a potential drop along the surface layer V(x). This in turn causes regions of the junction away from the contact be be less heavily forward biased. For large voltages and high terminal currents, the current density is crowded into an area near the contacts and uniform current density no longer occurs.

The current crowding problem described above for solar cells is almost identical to that which occurs in bipolar transistors due to base current flow transvers to the p-n junction. In fact for analysis purposes the solar cell looks like a transistor with zero current gain. The current crowding problem has been extensively studied for transistors and the results can be readily applied to solar cells [6].

The current crowding problem can be thought of as giving rise to some effective width, L_{eff} in Figure 3, over which one can consider uniform injection at the junction to occur. The current on each side of a finger can then be expressed as

$$I_r=J_o L_r L_{eff} exp(qV/kT), \qquad (4)$$

where L_r is the length of the finger and L_{eff} is the effective distance over which current flow occurs. Of course at low voltages $L_{eff} \rightarrow S_r/2$, where S_r is the spacing between the fingers. Equation (4) neglects the current due to the area under the fingers and bus bar. This is usually small due to the small metal coverage factor.

As the current density increases, the effective width decreases. When severe current crowding occurs, it has been shown that [6]

$$L_{eff} \rightarrow \frac{2kTL_F}{q\rho_{ST}} \frac{1}{I_F}, \qquad (5)$$

where ρ_{ST} is the sheet resistance of the surface layer. This shows that the effective width decreases inversely with total current. Combining Equations (4) and (5) and solving for the total terminal current gives

$$I = \sqrt{AJ_o I_T} \; \exp(qV/2kT), \qquad (6)$$

where

$$I_T = \frac{2kT}{q} \frac{h^2}{\rho_{ST}} \frac{1}{A}, \qquad (7)$$

with h equal to the perimeter of the contact grid pattern. Since current crowding can occur around the entire metal surface, it is clear that h should be the total perimeter of the contact grid which includes both the contact fingers and the bus bar.

Equation (6) has the correct voltage dependence to describe the high current experimental results as shown in Figure 2. The difference between the I_{sc}-V_{oc} data and the conventional dark current data is seen in this model to be due to the sheet resistance, but the effect cannot be simply expressed as a constant resistance in series with an ideal solar cell. The current I_T has a simple physical interpretation in terms of the measured I-V characteristics. If one solves the ideal current equation

$$I = AJ_o \exp(qV/kT), \qquad (8)$$

and Equation (6) simultaneously, one finds that I_T is the intersection current of the two curves. This provides a simple means of determining sheet resistance from experimental I-V data. Two curves are drawn as shown in Figure 4. One curve fitting the I_{sc}-V_{oc} data and a second curve with 1/2 the slope of the I_{sc}-V_{oc} data to describe the conventional dark I-V data. The intersection of the two curves then determines I_T and from this the sheet resistance is calculated as

$$\rho_{ST} = \frac{2kT}{q} \frac{h^2}{I_T} \frac{1}{A}, \qquad (9)$$

where h is again the total perimeter of the metal area and A is the total solar cell area. This technique has been used to estimate the sheet resistance of a number of solar cells with very good results. The values obtained in this manner have been used in a detailed two-dimensional numerical calculation with good results as discussed in detail in the next section.

A large metal sheet resistance can lead to a second type of current crowding along the length of the metal fingers instead of perpendicular to the metal fingers as occurs when the semiconductor surface layer is the limiting factor. This could occur for an improperly designed contact structure or perhaps in cells operating under multi-sun conditions. This distributed cutoff effect along the fingers will also lead to a dark current which varies as $\exp(qV/2kT)$. The presence of this effect can be predicted quite readily by calculating the expected voltage drop along the contact fingers at any given current level. If the expected voltage drop assuming a uniform current

collection along the fingers exceeds kT/q volts, then one can expect a distributed resistance effect due to finger resistance.

In principle, a solar cell could have distributed resistance effects due to both the semiconductor surface and the grid fingers acting simultaneously. In such a case the dark I-V characteristic would be expected to have a slope of 1/4 that of the I_{sc}-V_{oc} data. This would lead to a current dependence of $\exp(qV/4kT)$. This type of behavior was not observed in any of the cells studied in this work. Typically one or the other distributed resistance effect will dominate, and for the cells studied in this work, the semiconductor sheet resistance was found to be the dominant effect.

After accounting for the distributed sheet resistance effect, the experimental data of Figure 4 shows a deviation at large currents from the predicted $\exp(qV/2kT)$ voltage dependence. This excess voltage is identified as $R_s' \cdot I$ in Figure 4. For all the cells studied in this work, it has been found that this excess voltage can be accurately described by a constant resistance in series with the terminal current. There are several potential sources for this resistance such as bus bar resistance, metal finger resistance, and front and back surface contact resistance. For the solar cells studied in this work, the metal-semiconductor contact resistance has been identified as the most likely source of this resistance. Detailed evaluations of this resistance are discussed in a later section.

An analytical model describing both the low current and high current distributed resistance behavior of a solar cell can be constructed from the two limiting cases of Equations (6) and (8). Solution of the equation

$$I^2 + II_T = I_o I_T \exp[q(V-R_s'I)/kT], \qquad (10)$$

where $I_o = AJ_o$ provides an approximation to the current at all voltages. Also included in Equation (10) is a lumped series resistance R_s' to describe the non-distributed resistance such as contact resistance.

It should be pointed out that although a simple analytical model can be used to describe the terminal dark I-V characteristic, no such simple model is available for describing the distributed sheet resistance effects on illuminated cells. The model of a diode in parallel with a current source cannot be employed for the complete cell when distributed resistance effects are dominant. The only known technique for accurate calculations under these conditions is a two-dimensional numerical technique.

COMPUTER CALCULATIONS

A detailed two-dimensional computer model has been used to also study distributed resistance effects in solar cells. The model which has been used consists of a two-dimensional array of ideal one-dimensional solar cells interconnected by series resistance. An array of NX and NY points

between two grid fingers are used to locate an element of the two-dimensional array. The number of grid points in the X-direction is NX and the corresponding number in the Y-direction is NY. Figure 5 shows the equivalent circuit of the incremental two-dimensional model where the current source and diode is that of a one-dimensional model including both optically generated current and forward bias current. For the present work this current was calculated from the tabulated current vs. voltage values obtained from a one-dimensional computer analysis. R_{ST} is the sheet resistance of the semiconductor surface layer and R_C is the contact resistance between the metal-semiconductor interface. The collecting metal is also assumed to have a finite resistance R_M which is included between array elements located on the edges of the grid fingers.

The distributive resistance elements can be calculated from the following equations:

a. Sheet resistance: $R_{M-1} = R_{M+1} = R_{ST} \dfrac{\Delta X}{\Delta Y}$, (10)

b. Sheet resistance: $R_{M-NX} = R_{M+NX} = R_{ST} \dfrac{\Delta Y}{\Delta X}$, (11)

c. Contact resistance: $R_C' = R_C/A_C$, (12)

d. Metal resistance: $R_M' = R_M \dfrac{T}{A_C}$, (13)

where ΔX and ΔY are the spacings between grid points in the X- and Y-direction respectively, R_{ST} is the sheet resistance in Ω/square, R_C is the contact resistivity in $\Omega \cdot cm^2$, and R_M is the metal resistivity in $\Omega \cdot cm$. A_C is the incremental area of the metal contact and T is the thickness of the metal contact grid.

Any bulk resistance R_{B1} in Figure 5 which arises from the bulk resistivity of the base layer need not be included here, since it is already included in calculating the one-dimensional I-V characteristics. Also the distributive base resistance R_{B2} in Figure 5 can be usually neglected, since most solar cells are covered with an ohmic contact over the entire back surface.

The bus bar is assumed to be at a constant potential which equals the terminal solar cell voltage. The voltage of all other grid points can then be calculated from the simultaneous solution of the node voltage equations at each grid point. Details of the solution method are discussed elsewhere [7]. The input data to the two-dimensional computer program consists of the one-dimensional I-V data plus structural data on the contact finger arrangement. An iterative solution technique based on a modified Newton-Raphson technique has been used to solve the nonlinear coupled node equations. Calculations have typically been made until the voltage is accurate at each array point to less than 10^{-4} volts.

The two-dimensional program provides calculated values of voltage and current density at each node point between the grid fingers as well as providing terminal I-V calculations including the distributed resistance effects of the solar cell.

COMPARISON OF THEORY AND EXPERIMENT

The results of the two-dimensional calculations have been compared with experimental data for a number of different solar cells. Results are reported here for three specific solar cells with widely varying sheet resistance values.

The first requirement for modeling the distributed resistance effects is to have an accurate model or representation for the intrinsic properties of a one-dimensional solar cell neglecting these effects. In this work this was obtained from a computer modeling of the one-dimensional solar cell. Details of this work are reported elsewhere [8]. For the purpose of this work it can be stated that the one-dimensional calculations were found to agree very well with the experimental I_{sc}-V_{oc} data such as shown in Figure 2. Thus for the purposes of this present work, the I_{sc}-V_{oc} data can be taken as the one-dimensional solar cell I-V characteristics used in the two-dimensional computer calculations.

Figure 6 shows measured I-V data for a good solar cell in which there is little difference in the measured I_{sc}-V_{oc} data and the conventional dark current I-V data. This cell had a junction depth of 0.7 μm and a base layer of 0.1 $\Omega \cdot cm$ resistivity. The sheet resistance and contact resistance values which give the best agreement between theory and experiment are 21 Ω/$\square$ and 0.12 Ω, respectively. The calculated points in Figure 6 show very good agreement between theory and experiment.

Figure 7 shows the corresponding agreement between theory and experiment for the same cell under AM0, 1 sun illumination. The agreement is again very good. Because of the small resistance values, good agreement can also be obtained for this cell using a lumped series resistance model. Data for a solar cell with a larger value of sheet resistance has been previously shown in Figure 2. This particular cell had a junction depth of about 0.3 μm, resulting in a sheet resistance of about 940 Ω/$\square$. When this was used along with a contact resistance of 0.2 Ω good agreement between theory and experiment was obtained from the two-dimensional calculations. Figure 8 shows the good agreement between theory and experiment in this case.

Finally data for a solar cell with a very large sheet resistance and contact resistance are shown in Figure 9. This data can only be explained by severe current crowding. This cell had a junction depth of 0.07 μm and the value of sheet resistance which best describes the experimental data is 8200 Ω/$\square$. The sheet resistance is somewhat larger than would be expected from a junction depth of 0.07 μm. However, with such a shallow junction, the junction depletion region may occupy a large part of the layer accounting for the large sheet resistance. The contact resistance at the front and/or back surface was also found to be large at a value of about 2.84 Ω. Some of this large value may arise from the back surface contact to the 10 $\Omega \cdot cm$ base layer of this particular cell.

Although not shown, even with such large values of sheet resistance and contact resistance,

the agreement between theory and experiment for the illuminated characteristics are very good. For such large resistances it is not possible to obtain good agreement between theory and experiment without the use of the detailed two-dimensional computer analysis of the distributed resistance effects.

SUMMARY AND CONCLUSIONS

In this work the two-dimensional nature of the sheet resistance and contact resistance effects in solar cells has been discussed. One of the major results of this work is the demonstration, both theoretically and experimentally, that the distributed nature of the semiconductor sheet resistance causes the terminal dark I-V characteristics to exhibit an $\exp(qV/2kT)$ type dependence even when the one-dimensional characteristics of the cell exhibit an $\exp(qV/kT)$ type voltage dependence. The analytical model developed also provides an easy method for estimating the sheet resistance of a solar cell from the terminal I-V data.

When the distributed nature of the sheet resistance is important in the terminal I-V characteristics it is not possible to accurately model a solar cell by an ideal diode and current source in series with a fixed resistance. A two-dimensional computer analysis using an array of grid points can be used to accurately model the solar cell. The results of such an analysis are in agreement with the analytical model developed here for the dark I-V characteristics of a cell. The computer analysis has been found to be in very good agreement with experimental results of sheet resistance and contact resistance effects for a wide variety of solar cells. By comparing theory and experimental results it has been possible to determine semiconductor sheet resistance and metal-semiconductor contact resistance for a number of silicon solar cells.

ACKNOWLEDGMENT

REFERENCES

1. Wolf, M. and Rauschenbach, H., Advanced Energy Conversion, 3, 455 (1963).

2. Handy, R. J., Sol. St. Elec., 10, 765 (1967).

3. Heeger, A. J. and Nisbet, T. R., Rept. LMSD No. 310003, Lockheed Missile Systems Div., Cal. (1958).

4. Queisser, H. J., Sol. St. Elec., 5, 1 (1962).

5. Imamura, M. S. and Portscheller, J. I., Eighth Photovoltaic Conf., 102 (1970).

6. Hauser, J. R., IEEE Trans. On ED, ED-11, 238 (1964).

7. Fang, C. R. and Hauser, J. R., Annual Rept. on NASA Grant NGR 34-002-195, Sept. 1977.

8. Fang, C. R. and Hauser, J. R., Paper presented at Thirteenth Photovoltaic Conf. (1978).
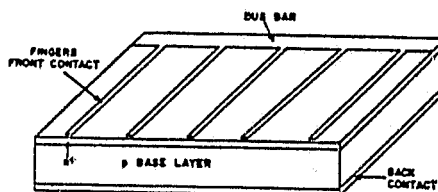
Figure 1. Solar cell with conventional contact finger arrangement.
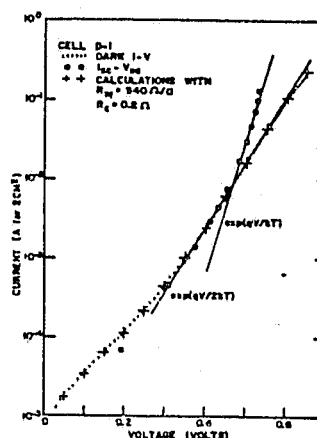
Figure 2. Terminal I-V characteristics of cell D-1.
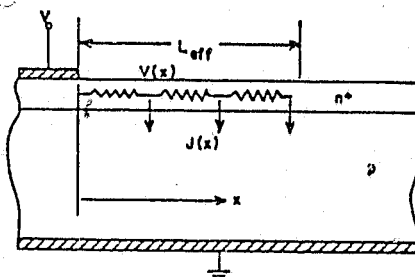
Figure 3. Distributed nature of the surface layer sheet resistance.
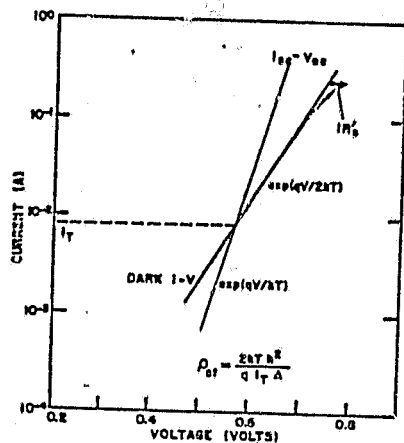
Figure 4. Experimental method for determining sheet resistance.

Figure 5. Incremental model of two-dimensional solar cell.

Figure 6. Terminal I-V characteristics of cell D-2.
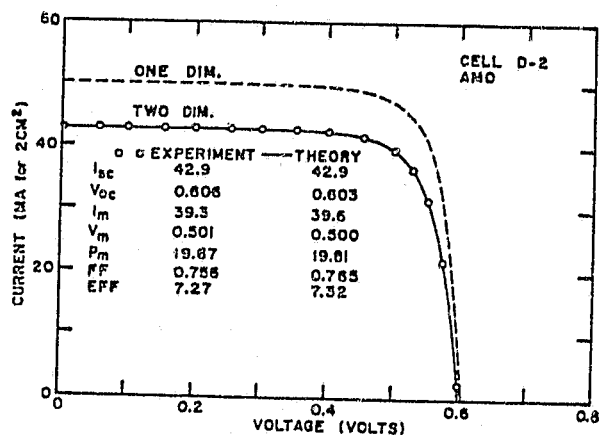
Figure 7. Comparison of the photovoltaic I-V characteristics of cell D-2. One-dimensional calculations are with total area (dashed curve). Two-dimensional calculations include series resistance.

Figure 8. Comparison of the photovoltaic characteristics of cell D-1. Various curves are: (a) one-dimensional with total area; (b) one-dimensional with active area; (c) two-dimensional with no series resistance and; (d) two-dimensional with series resistance.
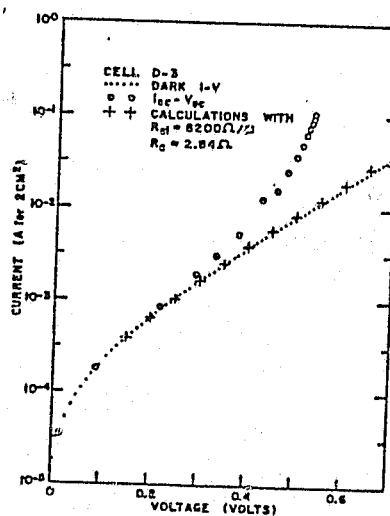
Figure 9. Terminal I-V characteristics of cell D-3 with very large sheet resistance.

Appendix 10.3

Impurity Gradients and High Efficiency Solar Cells[*]

C. R. Fang and J. R. Hauser
North Carolina State University
Raleigh, NC 27607

ABSTRACT

One potential means of improving the efficiency of solar cells especially after space irradiation is to incorporate built-in fields into the device through the use of impurity doping gradients. Previously published papers have indicated an improved minority carrier collection efficiency and improved efficiency when doping gradients are present. In this work a detailed numerical calculation of solar cell performance has been used to study various types of doping gradients. In general the predicted improvements in performance have been less than previously reported due to various device effects such as high injection and the dependence of lifetime on doping density.

I. INTRODUCTION

There have been a number of theoretical investigations into the efficiency of drift field solar cells in recent years [1-4]. In these earlier investigations the emphasis has been on the calculation of collection efficiency as a result of including drift fields, with somewhat different approximations in lifetime, mobility and other important parameters. Wolf [1] was the first to demonstrate that a surface drift field helps the short wavelength response and to show that a base field can considerably reduce the effects of radiation damage and increase the useful life of solar cells. In 1967 Bullis and Runyan [3] found that there exists an optimum field width which is approximately twice the diffusion length or about 25 μ whichever is shorter in n^+-p cells for maximum collection efficiency. Van Overstraeten, _et al_. [4] have shown that the advantage of the drift field is mainly determined by the layer close to the collection junction. To obtain higher collection efficiency, the magnitude of the drift field should be high, at its optimum width and the doping density should be as low as possible.

In considering impurity doping gradients, it is useful to distinguish two somewhat different types of doping gradients. First, if the doping change is very rapid, space charge regions form. On the other hand if the change in doping density is very gradual, a state of quasi-neutrality exists at every point and a built-in electric field is produced throughout the bulk of a solar cell. A gradient sufficient to give rise to a space charge region will be referred to here as a high-low junction while a gradual change in doping will be referred to as a drift field region.

Despite the theoretical predictions of the drift field enhancing the collection efficiency, the advantages of drift fields are still unconfirmed experimentally, especially with regard to total conversion efficiency [5]. The purpose of this paper is to explain the physical mechanism governing the operation of drift field cells and the discrepancies of those earlier results. The emphasis is on maximizing the total conversion efficiency as a result of including the base field. In this paper the major mechanisms which tend to limit the conversion efficiency due to the incorporation of drift field in Si solar cells are discussed.

The use of a high-low junction in solar cells is a more recent innovation than the drift field concept. However, the advantages of such abrupt doping gradients have been experimentally demonstrated and incorporated into the design of high efficiency solar cells. Basically the high-low junction near the back surface prevents minority carriers from reaching the back ohmic contact and thus acts as a minority carrier reflecting boundary [6].

II. FIRST ORDER THEORY

The structure of the basic solar cell to be considered here is shown in Figure 1. The n^+ surface layer is a thin (0.1-0.5 μm typically) heavily doped layer which may have a doping gradient. The p-type base layer is shown with a high-low junction near the back ohmic contact and a wide, drift field region. Because of the major role of the base layer properties in determining solar cell performance, the discussion here concentrates on the base layer.

Within the drift field region of the base, excess minority carrier electrons ($\bar{n}$) are controlled by the basic drift-diffusion and continuity equations which when combined into a single equation for steady state gives

$$D_n \frac{d^2\bar{n}}{dx^2} + [\frac{dD_n}{dx} + \mu_n E] \frac{d\bar{n}}{dx} + [\frac{d}{dx} (\mu_n E) - \frac{1}{\tau_n}]\bar{n} + G = 0, \tag{1}$$

where G is the optical pair generation rate. For a general doping profile Equation (1) must be solved by numerical techniques. Also the dependence of mobility μ_n and lifetime τ_n on doping density complicates the solution.

The special case of a constant electric field (exponential doping profile) with constant τ_n and μ_n has been frequently used for drift cells and provides certain insight into drift cell operation. If the simpler equation for these conditions

$$D_n \frac{d^2\bar{n}}{dx^2} + \mu_n E \frac{d\bar{n}}{dx} - \frac{\bar{n}}{\tau_n} + G = 0, \tag{2}$$

is considered, an exact solution can be obtained of

$$\bar{n} = A_1 \exp(x/L^+) + A_2 \exp(-x/L^-) + \tau_n G, \tag{3}$$

where $$1/L^{\pm} = \sqrt{(1/L_n)^2 + (qE/2kT)^2} \quad (qE/2kT). \tag{4}$$

The basic theory behind the drift field solar cell is that the electric field increases the collection depth for optically generated minority carriers within the base layer since $L^+ > L_n$.

The value of a constant drift field can be written as

$$E = \frac{kT}{q} \frac{1}{N_A} \frac{dN_A}{dx} = \frac{kT}{qW} \ln (\frac{N_2}{N_1}), \tag{5}$$

where W is the width of the drift field region and N_2, N_1 are the doping densities at the ends of the drift field region. The ratio N_2/N_1 is limited in value to around 10^5 in practical cases and this sets an upper limit to the field which can exist. From Equation (5) it is seen that the

largest field occurs when W is as small as possible. However, if W becomes less than L^+, Equation (4) begins to lose meaning since the field doesn't exist over the assumed dimensions. Thus by setting W larger than or equal to L^+ and combining Equations (4) and (5) a limit on L^+ can be established as

$$L^+ < L_n \sqrt{1 + \ell n(N_2/N_1)}. \tag{6}$$

With a ratio of 10^5 for N_2/N_1 this gives $L^+ < 3.54 L_n$. Thus an enhancement in collection depth by a factor of about 3 for the conditions stated above is the most that can be realized due to doping density limitations.

Previous studies of drift field cells have concentrated on the improved collection efficiency. Equally important in determining solar cell efficiency is dark forward current and open circuit voltage which, according to first order device models, are related as

$$J_{dark} = J_o \exp(qV/kT) \tag{7}$$

$$V_{oc} = \frac{kT}{q} \ell n(J_{sc}/J_o), \tag{8}$$

where J_{sc} is short circuit current density and J_o is a function of device geometry, and material parameters. For a drift field cell with constant mobility

$$J_o = \frac{qD_n}{L^+} \frac{n_i^2}{N_1} > \frac{qD_n}{L_n \sqrt{1 + \ell n(N_2/N_1)}} \frac{n_i^2}{N_1}. \tag{9}$$

For a large open circuit voltage, J_o should be minimized. A large drift field requires that N_2 be large and N_1 be small, while Equation (9) shows that this is far from the condition for minimum dark current where N_1 should be as large as possible. Thus large drift fields and minimum dark current

are incompatible objectives. For many potential drift field designs, it appears that increases in dark current almost completely eliminate any increased collection efficiency due to the drift field.

The previous considerations have been for cells with a base layer thickness large compared with a diffusion length. These considerations must be modified considerably if the cell thickness is comparable or less than the diffusion length. For such thin cells, the diffusion length is not the major factor determining collection efficiency and a back surface high-low junction has been found to be effective in increasing the efficiency of such cells.

The purpose of a high-low junction such as shown in Figure 1 is to prevent minority carriers created either by light or forward injection from recombining at the back surface. The high-low junction interface can be characterized as a low surface recombination boundary to the base layer. The high-low junction is most effective for solar cells in which the base width is less than a diffusion length. As discussed elsewhere [6-8], the high-low junction can be very effective in reducing back surface losses, giving a collection depth approximately equal to the total cell thickness. An ideal high-low junction minimizes dark current and maximizes short circuit current and open-circuit voltage simultaneously.

III. NUMERICAL CALCULATIONS

In order to investigate in detail the ideas discussed above, a series of calculations have been made of solar cell performance with various types of drift fields and high-low junctions. The analysis consists of a detailed numerical solution of the semiconductor device equations. Details of the
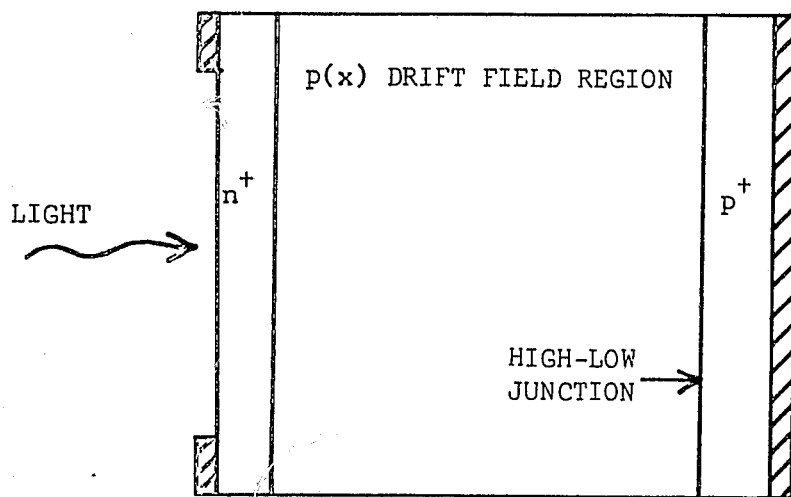
Figure 1. Structure of the solar cell with base drift field.

modeling and solution techniques have been discussed elsewhere [9].

The solutions include all types of nonlinear device effects such as

high level injection as well as doping and field dependences of device

parameters.

In any comparison of solar cell performance with and without drift

fields, the type of cell and the parameters which are held constant in

the analysis are very important. In this work the approach has been

as follows. Since a uniformly doped base layer solar cell with a back

surface high-low junction has so far demonstrated the highest experimental

efficiencies, the approach has been to take this cell as a reference cell

and to see if other types of doping gradients improve the efficiency.

The analysis has been performed for a cell with the device parameters

listed in Table I. The density of $2 \times 10^{19}/cm^3$ is chosen as a constant

surface density, since this is approximately the highest doping density

obtainable after considering heavy doping effect which doesn't produce

any retrograde surface field [9,10].

SiO is used as the antireflection layer in its optimum thickness of

800 $\overset{o}{A}$ where it allows 45.4 mA/cm^2 current density to be available for

collection. Despite the short wavelength absorption in SiO, it makes

little difference in the collection efficiency of the base layer since

most of the short wavelength photons are absorbed in the surface layers.

To avoid problems in interpreting the results, heavy doping effects were

not considered throughout this work. However, such effects as bandgap

reduction would not significantly change the results because of the low doping

density used for the surface layer in the calculations. The irradiance condition

used is AMO and total optical reflection at the back ohmic contact was assumed.

TABLE I. DEVICE STRUCTURE PARAMETERS

Overall cell thickness	150 μm
n^+ surface thickness	0.2 μm
p base thickness	144.8 μm
p^+ thickness	5 μm
n^+ surface doping	2×10^{19}/cm^3
p base doping	Optimized
p^+ doping	10^{19}/cm^3
Lifetime model	Iles [10]
Surface recombination velocity	10^3 cm/sec
Antireflection layer	SiO, 800 Å
Irradiance	AMO

TABLE II. RESULTS OF SOLAR CELL CALCULATIONS FOR DIFFERENT
DIFFUSION LENGTHS AND DIFFERENT DRIFT FIELDS

E_B (V/cm)	L_D	N_1(cm^{-3})	N_2(cm^{-3})	J_{sc} (mA/cm^2)	V_{oc} (Volts)	η (%)	CF	J_o (mA/cm^2)	J_R (A/cm^2)
0	Max	5.6×10^{16}	5.6×10^{16}	42.40	0.690	18.19	0.841	4.44×10^{-13}	2.87×10^{-10}
10	Max	3.24×10^{17}	9.9×10^{14}	42.79	0.693	17.79	0.812	1.45×10^{-12}	3.73×10^{-10}
20	Max	6.49×10^{17}	6.04×10^{12}	42.82	0.698	17.60	0.798	6.24×10^{-11}	1.11×10^{-9}
0	Med	9×10^{16}	9×10^{16}	35.82	0.623	13.70	0.830	7.43×10^{-13}	2.96×10^{-9}
10	Med	3.6×10^{17}	1.1×10^{15}	40.83	0.561	13.71	0.810	7.19×10^{-11}	1.92×10^{-8}
20	Med	7.2×10^{17}	6.7×10^{12}	42.09	0.524	11.79	0.724	4.29×10^{-9}	7.7×10^{-8}
0	Min	5×10^{17}	5×10^{17}	22.63	0.613	8.39	0.818	4.69×10^{-12}	2.77×10^{-8}
10	Min	2.9×10^{18}	8.8×10^{15}	27.13	0.501	7.91	0.787	4.12×10^{-10}	3.39×10^{-7}
20	Min	5.8×10^{18}	5.4×10^{13}	31.29	0.385	6.35	0.713	7.53×10^{-8}	1.83×10^{-6}

Another very important factor in any solar cell study is the assumed relationship between diffusion length, or lifetime, and doping density. Three different relationships as shown in Figure 2 have been used in this work. These curves are based upon experimental data by Iles, et al. [11] with the top and bottom curves representing limits near the top and bottom of measured diffusion length data, while the middle curve represents values near the center of the measured range. These curves are convenient for the 150 μm cell thickness since the three curves represent, at light doping densities, cases where the diffusion length is much larger, approximately equal and much less than the total cell thickness. The behavior of the cell and the importance of drift fields depends on which of these three cases is considered.

For a given cell thickness and given diffusion length curve, there is an optimum uniform base layer doping density which results in maximum efficiency, and this condition was first determined. Table II (E_B= 0 case) lists the optimum uniform doping density for maximum efficiency and the corresponding device parameters for the three diffusion length cases. Also shown in Table II are performance parameters for cells with drift fields (E_B) of 10 and 20 V/cm. For each different L_D case the average doping density remains constant as the field increases.

N_1 and N_2 are the doping density near the high-low junction and p-n junction respectively. It is clear that the collection efficiency as measured by I_{sc} indeed increases after building in the drift field with the larger increase for the lower base layer diffusion length. For the minimum L_D case I_{sc} increases from 22.6 mA to 31.3 mA as the drift field increases.
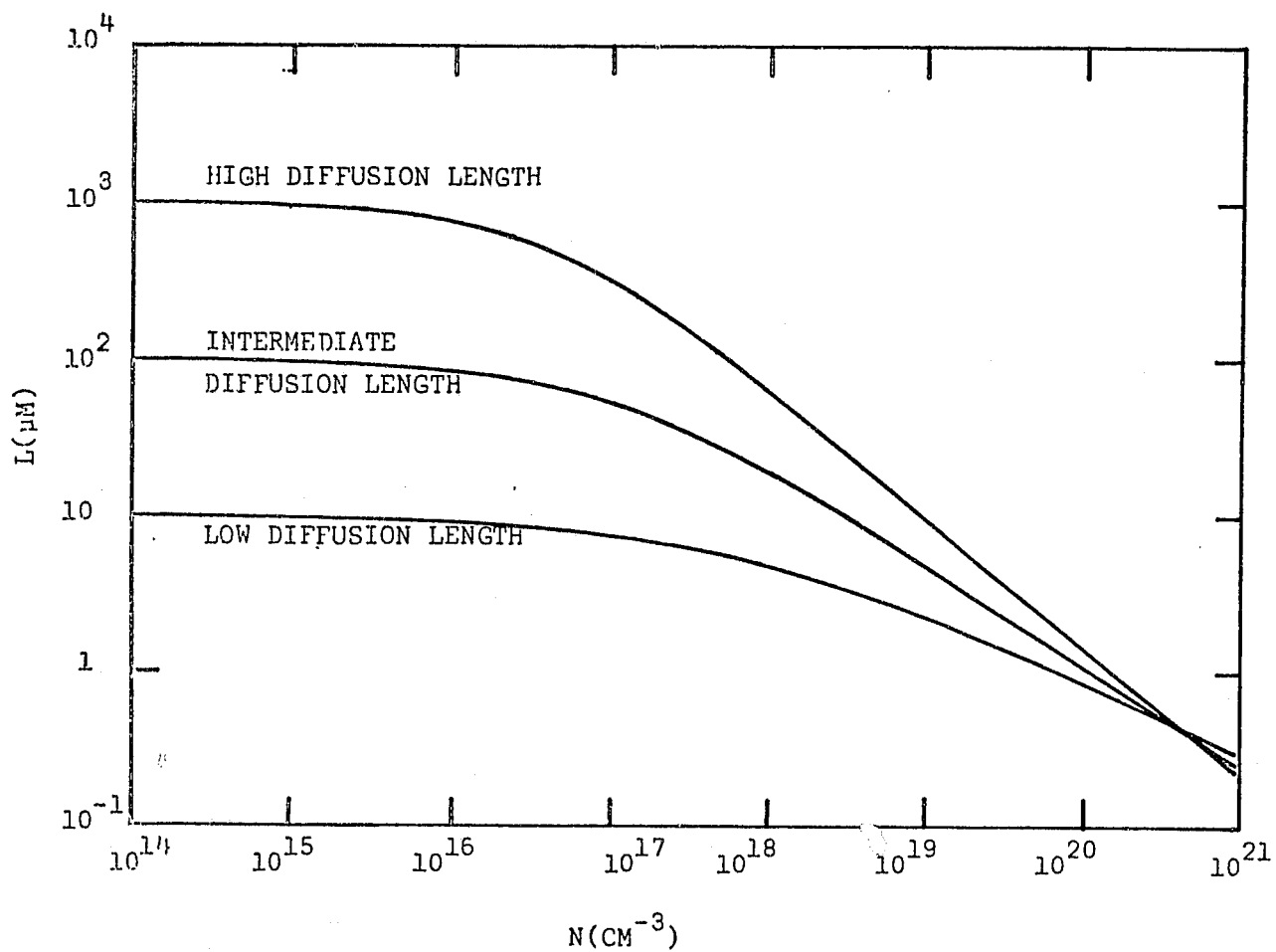
Figure 2. Model of the diffusion length as a function of the doping density.

Figure 3 shows the minority carrier current density as a function of position in the base region for the calculations of Table II. It can be seen in the table that the increase in collection efficiency is very limited for the maximum diffusion length used here which is already larger than the base width. Figure 3 shows that the collection distance can be effectively expanded all across the base layer with the appropriate drift field for the case of the medium diffusion length. The curves for the minimum diffusion length indicate a much smaller increase in collection depth. Since collection occurs only over part of the base, this suggests that an improved cell can be obtained by grading only over part of the base layer near the p-n junction. This has been verified and is discussed later.

With the inclusion of the base field, the doping density near the p-n junction (N_2 of Table 3) is inevitably reduced assuming that the average doping density remains constant. This reduction in doping density has profound effects on the cell operations. In analyzing the calculated results the dark current was approximated by an equation of the form

$$J = J_o \ \exp(qV/kT) + J_R \ \exp(qV/2kT). \tag{10}$$

The J_o and J_R values which give the best fit to the calculated dark current curves are listed in Table II. The forward injection current density as evidenced by the J_o term increases as a result of lowering the injecting barrier, and this typically results in a reduced open circuit voltage as also seen in Table II. The depletion layer expands which leads to a larger space charge recombination current density as evidenced by the increased J_R term. Third, and perhaps most importantly is the fact that high injection may easily occur at a voltage well below the operating voltage of the maximum power point.
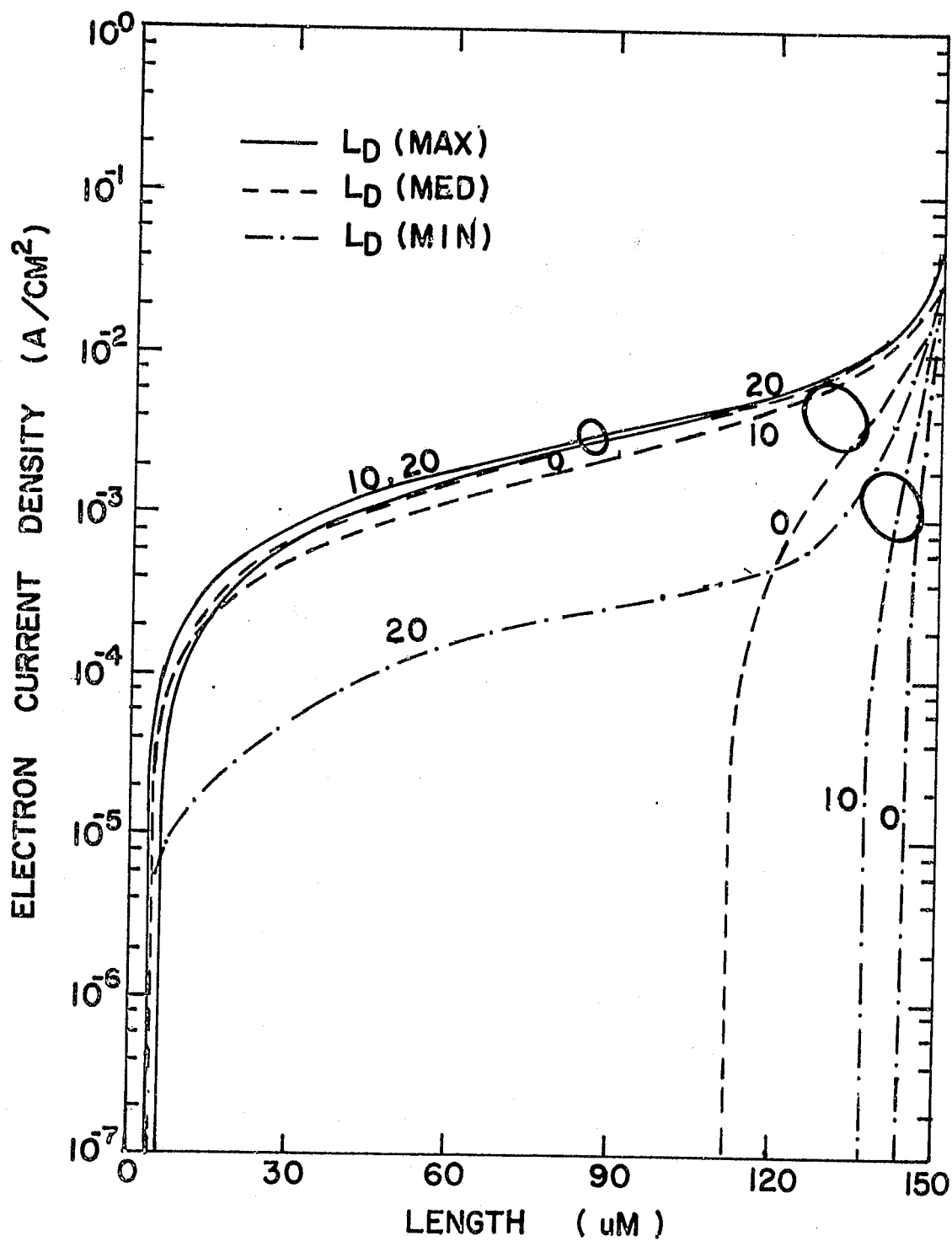
Figure 3. Minority carrier densities in the base region for models of different built-in drift field and base diffusion length.

In Table III the transition voltage V_H^* between the low and high injection regions is calculated from the equation

$$V_H^* = 2 \frac{kT}{q} \ell n(N_2/n_i).$$

The table also shows the transition voltage V_R^* where the depletion region current equals the ideal injection current density. It's clear that the cell is operating at a voltage well above the high injection limit for the case of 20 V/cm for both the maximum and medium diffusion length cases. The high injection effect is the major reason for the reduction of the curve factor CF in Table II and the overall drop in conversion efficiency.

Although there is a small reduction in CF due to the increased depletion region recombination current density, the major reduction is due to the deterioration of the open circuit voltage as a result of a much higher forward injection current density. The increased dark current which is predicted by the approximate model of Equation (9) due to a decreased N_1 is definitely verified by the computer calculations.

From the results of Table II several conclusions can be drawn with regard to solar cells with the same average base doping levels. First, a drift field enhances the collection efficiency with the largest changes occurring when the diffusion length is much less than the base layer thickness. Second, almost all of the increased collection efficiency is offset by increases in dark current and a reduced open circuit voltage. Third, for large drift fields, operation near the p-n junction tends to be in the high injection region which further tends to reduce efficiency due to a reduced curve factor.

Table IV shows calculations for cells with the same electric field but with different average base layer doping densities. In comparing this data with that of Table III, it is seen that the highest efficiency results from a compromise between retaining a large open circuit voltage and achieving an enhanced collection efficiency due to the drift field. The calculations have shown that for highest efficiency the doping density near the p-n junction should be kept near the value which gives highest efficiency for a uniformly doped base layer.

A series of calculations have been made to determine the optimum drift field conditions for highest effieicny for the three different lifetime cases. The general impurity profile considered is shown in Figure 4. The n^+ surface layer is taken as uniformly doped at $2x10^{19}/cm^3$. The back surface p^+ layer is also uniformly doped at $10^{19}/cm^3$. The base region was assumed to have a constantly doped region near the back p^+ region of varying doping density N_W. The graded doping region was varied in width and type of doping profile to study the effects on overall efficiency. The types of doping profiles studied were 1) constant, 2) exponential and 3) erfc. The erfc profile gives the largest electric field at the p-n junction while the exponential profile gives a uniform electric field.

C-2
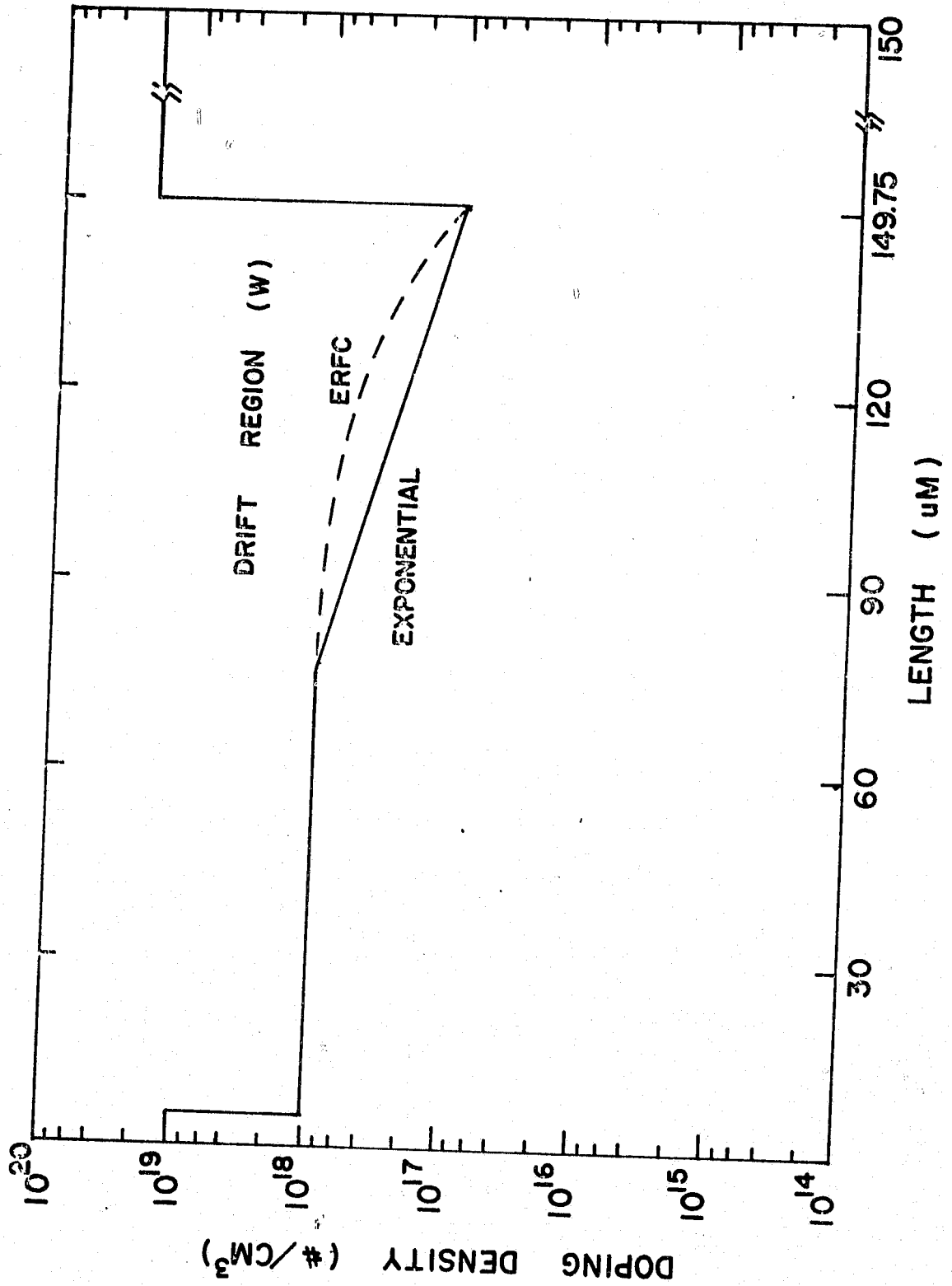
Figure 4. Models of the base doping profile.

TABLE III. COMPARISON OF TRANSITION VOLTAGES V_R^* AND V_H^* WITH THE
OPEN CIRCUIT VOLTAGE V_{oc} AND THE MAXIMUM POWER VOLTAGE V_m

E_B (V/cm)	L_D	V_R^* (volts)	V_H^* (volts)	V_M (volts)	V_{oc} (volts)
0	Max	0.334	0.780	0.600	0.690
10	Max	0.286	0.572	0.597	0.693
20	Max	0.148	0.309	0.594	0.698
0	Med	0.428	0.805	0.450	0.623
10	Med	0.288	0.577	0.444	0.561
20	Med	0.149	0.315	0.413	0.524
0	Min	0.448	0.893	0.309	0.613
10	Min	0.346	0.685	0.427	0.501
20	Min	0.165	0.422	0.301	0.385

TABLE IV. CALCULATED PARAMETERS FOR CELLS WITH
DIFFERENT AVERAGE DOPING DENSITIES

	N_1 (cm^{-3})	N_2 (cm^{-3})	J_{sc} (mA/cm^2)	V_{oc} (volts)	CF	η (%)
Max L_D						
$E_B=3$	3.14×10^{17}	1.15×10^{15}	42.63	0.689	0.839	18.21
$E_B=3$	3.02×10^{17}	5.6×10^{16}	42.28	0.694	0.844	18.29
Min L_D						
$E_B=10$	1.37×10^{20}	5×10^{17}	23.28	0.617	0.818	8.69
$E_B=10$	6.87×10^{18}	2.5×10^{16}	26.61	0.530	0.790	8.23
$E_B=10$	1.37×10^{21}	5×10^{18}	18.53	0.674	0.824	7.60

Table V shows calculated results for cells with the maximum L_D values for different doping profiles. For these large values of L_D the diffusion length is larger than the cell thickness and therefore the drift field width was taken as equal to the cell thickness. The field is seen to have little effect on cell efficiency giving an increase from 18.19% for a BSF cell to only 18.29%. Larger fields than those shown in the table were found to give lower efficiencies because of reductions in open circuit voltage.

Calculated results using the medium diffusion length case are shown in Figure 5. In this series of calculations the doping density was varied exponentially between $9 \times 10^{16}/cm^3$ at the p-n junction to $10^{18}/cm^3$ at the edge of the drift region (W). The width of the drift region was varied from 20 μm to 100 μm with the results shown in Figure 5. The peak efficiency is seen to occur when the drift field exists over about 40 μm. This peak value of 14.64% is slightly better than the 13.70% obtained without the drift field.

Similar calculations to those shown in Figure 5 have been made with the graded region doping varying between $9 \times 10^{16}/cm^3$ and $10^{19}/cm^3$. The results as a function of width of graded region are similar to those of Figure 5. The major differences are a peak efficiency of 14.70% for a graded region width of about 80 μm.
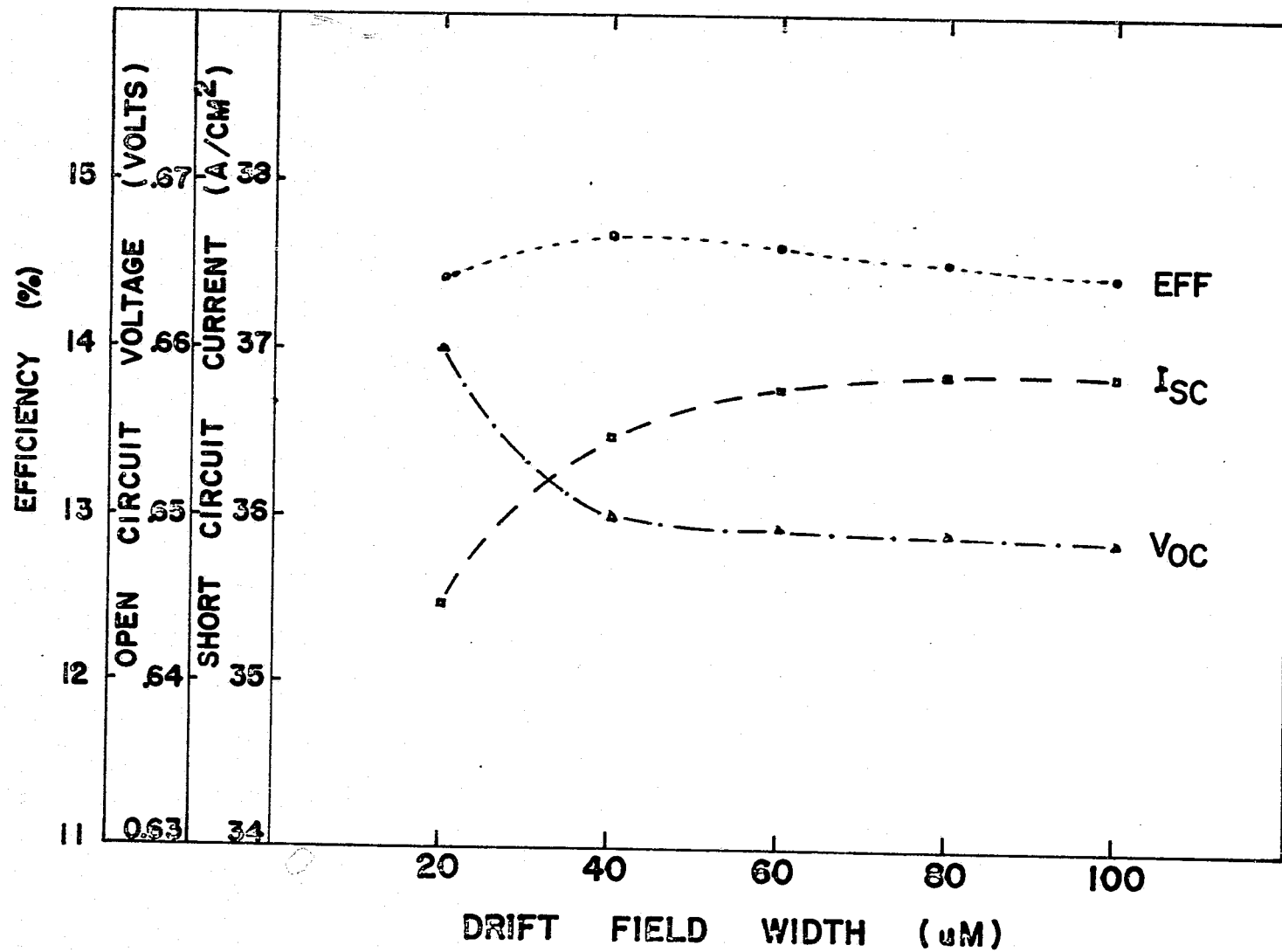
Figure 5. Output characteristics for different drift field width.

TABLE V. COMPARISON OF CELLS WITH DIFFERENT DOPING PROFILES (W=144.8 μm, MAX L_D')

Doping Profile	N_1 (cm^{-3})	N_2 (cm^{-3})	J_{sc} (mA/cm^2)	V_{oc} (volts)	CF	η (%)
Constant	5.6×10^{16}	5.6×10^{16}	42.40	0.690	0.841	18.19
Exponential	3.02×10^{17}	5.6×10^{16}	42.28	0.694	0.844	18.29
Exponential	1.15×10^{18}	5.6×10^{16}	42.20	0.695	0.844	18.29
Erfc	10^{17}	5.6×10^{16}	42.73	0.692	0.835	18.24
Erfc	10^{18}	5.6×10^{16}	41.72	0.699	0.845	18.20

TABLE VI. MAXIMUM CALCULATED EFFICIENCIES

L_D	W (μm)	E (V/cm)	J_{sc} (mA/cm^2)	V_{oc} (volts)	CF	η (%)
Max	144.8	3 (0)	42.28 (42.40)	0.694 (0.690)	0.844 (0.841)	18.29 (18.19)
Med	80	15.3 (0)	36.61 (35.82)	0.650 (0.623)	0.836 (0.830)	14.70 (13.70)
Min	10	77.9 (0)	24.70 (22.63)	0.635 (0.613)	0.820 (0.818)	9.50 (8.39)

Calculations for the medium diffusion length case using an erfc doping profile between the same doping limits as used for the exponential doping have also been made. The results are very similar to those shown in Figure 5. For an erfc doping profile between 9×10^{16}/cm^3 and 10^{18}/cm^3 the peak efficiency was calculated as 14.62% which is slightly less than the 14.64% value obtained with the exponential doping. For the erfc doping profile between 9×10^{16}/cm^3 and 10^{19}/cm^3 the peak efficiency was found to be 14.76% at a graded region width of about 100 μm. This efficiency is slightly larger than the corresponding value for the exponential profile.

Calculations made with the minimum diffusion length curve of Figure 2 have given results similar to those discussed above. The largest calculated efficiencies were found to occur when the doping density was graded between 5×10^{17}/cm^3 at the p-n junction to 10^{19}/cm^3 at some distance W from the junction. Optimum values of W were found to be about 10 μm for the exponential grading and about 5 μm for the erfc grading with peak calculated efficiencies of 9.50% and 9.45% respectively.

In all of the calculations, the maximum efficiency has been observed to occur when the width of the drift region is approximately twice the diffusion length. This appears to be the best compromise between enhanced collection efficiency and increased dark current.

The maximum efficiencies in various drift field type cells calculated in the present study are shown in Table VI. Shown for comparison purposes (in parenthesis) are the maximum efficiencies for cells with uniformly doped base layers. These values may not represent absolute maximum values since optimization studies were not done on all possible parameters. However they should be close to the efficiency enhancement to be expected in drift

field cells. The largest improvements are observed in cells with low diffusion lengths which is to be expected. However the improvement which can be achieved is fairly limited. This is consistent with the first order models of Section II which show that the collection depth can only be improved by about a factor of three. The major limitation, however, is the increased dark current and lowered open circuit voltage which tends to accompany any attempt to build in a large drift field through the use of doping gradients.

IV. RADIATION RESISTANCE

One of the major reasons for considering cells with built-in fields is the potential for improved radiation resistance. This is consistent with the results of the previous section where it was shown that the drift field had the largest improvement in cells with low diffusion lengths.

The degradation in lifetime with radiation fluence ϕ is normally modeled by an equation of the form

$$\frac{1}{\tau} = \frac{1}{\tau_o} + K\phi \qquad (12)$$

where τ_o is the initial lifetime and K is a damage coefficient, which may change with doping density and radiation dose. In the present calculations for electron irradiation, K has been taken as a constant and of value 3.2×10^{-9} cm^2/sec.

To investigate the expected degradation in efficiency, calculations have been made on three different cells with the basic device parameters of Table I. In the first cell the base region was uniformly doped at $5.6 \times 10^{16}/cm^3$. In the second cell an exponentially graded region from

$5.6 \times 10^{16}/cm^3$ to $10^{19}/cm$ was taken over a distance of 54 μm, while in the third cell the graded region width was taken over a distance of 18 μm. The calculated changes in maximum efficiency with electron fluence are shown in Figure 6. It is seen that the drift fields do improve the efficiency for large radiation doses. The graded width of 54 μm and 18 μm were selected as approximately twice the diffusion length after total doses of 10^{15} and $10^{16}/cm^2$ respectively. The cell with a 54 μm graded region is seen to be best at $10^{15}/cm^2$ and the 18 μm cell is best at $10^{16}/cm^2$ as expected from the selection of graded region widths. Other potential devices have also been studied and in all cases an enhanced radiation resistance could only be achieved at the expense of the initial cell efficiency.

V. CONCLUSIONS AND SUMMARY

In this work a detailed numerical computer analysis program has been used to study the efficiency of silicon solar cells with various internal drift fields achieved by use of doping gradients. In agreement with earlier works, it has been found that a drift field can be used to significantly enhance the short circuit current of solar cells with short diffusion lengths. However, these improvements are to a large extent offset in terms of peak efficiency by increases in dark current and by reductions in curve factor when a drift field is present.

For a given ratio of doping density across the drift field region, there is an optimum width for the drift field region. The optimum width was found to be on the order of twice the diffusion length when the diffusion length is less than the cell thickness. When the diffusion length is larger than the cell thickness, very little improvement was found in efficiency due to the drift field. This conclusion holds only
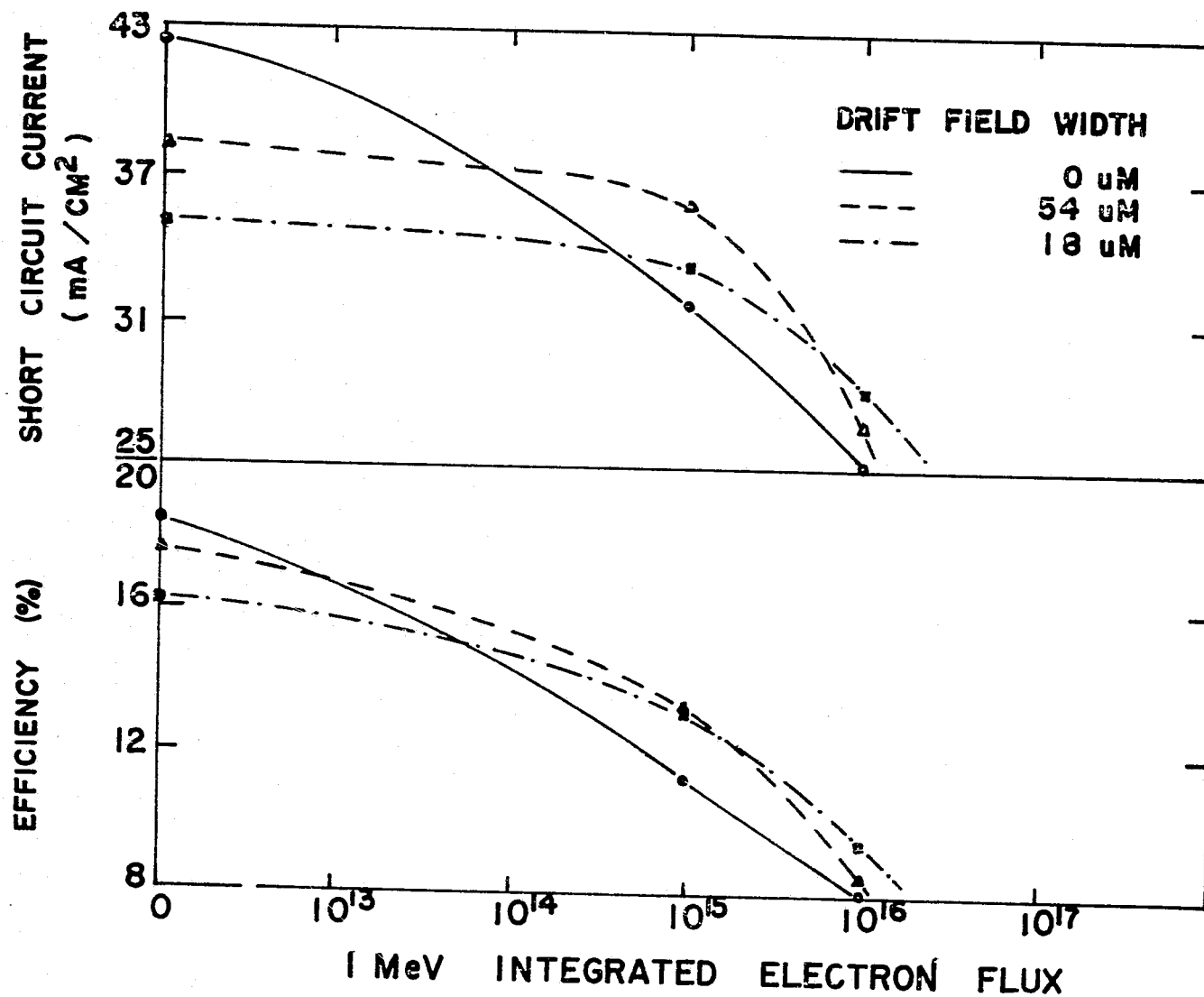
Figure 6. Radiation effects of the drift field solar cells.

for cells with a high-low junction at the back surface and larger improvements are observed for n^+-p cells with a back surface ohmic contact.

The calculations indicate that drift field cells can have somewhat higher efficiencies after electron irradiation than similar cells without the drift field. However, this is obtained only at the expense of lower initial efficiencies.

REFERENCES

1. M. Wolf, "Drift fields in photovoltaic solar energy converter cells," Proc. IEEE, vol. 51, May 1963, pp. 674-693.

2. S. Kaye and G. P. Polik, "Optimum bulk drift-field thicknesses in solar cells," IEEE Trans. on ED, vol. ED-13, July 1966, pp. 563-570.

3. W. Murray Bullis and W. R. Runyan, "Influence of mobility and lifetime variations on drift field effects in silicon junction devices," IEEE Trans. on ED, ED-14, Feb. 1967, pp. 75-81.

4. R. Van Overstraeten and W. Nuyts," Theoretical Investigation of the efficiency of drift-field solar cells," IEEE Trans. on ED, vol. ED-16, July 1969, pp. 632-641.

5. W. R. Runyan and E. G. Alexander, "An experimental study of drift-field silicon solar cells," IEEE Trans. on ED, vol. ED-14, Jan. 1967, pp. 3-9.

6. M. P. Godlewski and C. R. Baraona, "Low-high junction theory applied to solar cells," Tenth Photovoltaic Specialists Conference, Palo Alto, CA, Nov. 13-15, 1973.

7. J. R. Hauser and P. M. Dunbar, "Minority carrier reflecting properties of semiconductor high-low junctions," Solid-State Elec., vol. 18, pp. 715-716.

8. J. G. Fossum, "Physical Operation of Back-Surface-Field Silicon Solar Cells," IEEE Trans. on ED, vol. ED-24, April 1977, pp. 322-325.

9. P. M. Dunbar and J. R. Hauser, "A Study of efficiency in low resistivity silicon solar cells," Solid-State Elec., vol. 19, 1976, pp. 95-102.

10. M. P. Godlewski, H. W. Brandhorst, Jr. and C. R. Baraona, "Effects of high doping levels on silicon solar cell performance," Eleventh IEEE Photovoltaic Specialists Conference, Scottsdale, AZ, May 1975.

11. P. A. Iles and S. I. Soclof, "Effect of impurity doping concentration on solar cell output," Proceedings of Eleventh Photovoltaic Specialists Conference, Scottsdale, AZ, May 1975.

Appendix 10.4   Two-Dimensional Model of a Solar Cell

10.4.1   Introduction

A solar cell is in general at least a two-dimensional device. One
dimensional is parallel to the p-n junction where the light-generated cur-
rent flows,while the other dimension is perpendicular to the p-n junction.
Although the optical current may be uniformly generated over the junction
area, the surface current density is non-uniformly distributed over the
active area. The sheet resistance and contact resistance which are tra-
versed by the surface current density are thus functions of the relative
location of a given area to the finger contact. All these considerations
add to the complexity of a solar cell and require the use of a two-dimen-
sional model for an accurate analysis of the terminal properties of a
solar cell.

The equations of the two-dimensional carrier flow and its associated
photovoltaic potential have been previously developed in analytical form
[1-3]. Since the equations are non-linear functions of the current density
and series resistance, they can only be solved in closed form under very
stringent assumptions such as low light levels or specimens with special
contact shapes. Hence the use of closed form equations is very limited.
In this chapter a general two-dimensional model for solar cell analysis
is proposed and developed. A comparison of the calculated results to
experimental data is also presented.

10.4.2   Distributed Resistance and Current Density Model of a Solar Cell

The distributed resistance and current density model considered here
is actually a two-dimensional array of ideal one-dimensional solar cells

interconnected by series resistance. Shown in Figure 10.1 is an array of NX and NY points between two grid fingers which are used to locate an element of the two-dimensional array. The number of grid points in the X-direction is NX and the corresponding number in the Y-direction is NY. Figure 10.2 shows the equivalent circuit of the two-dimensional model. Figure 10.3 shows the distributive resistance and current model at each grid point where the current source is that of an ideal one-dimensional model including both optically generated current and forward bias current. For the present work, this current is calculated from the tabulated current vs. voltage values obtained from the one-dimensional computer analysis. R_{ST} is the sheet resistance on the surface and R_c is the contact resistance between the metal-semiconductor interface. The collecting metal is also assumed to have a finite resistance R_M which is included between array elements located on the edges of the grid fingers.

The distributive resistance elements can be calculated from the following equations.

a. Sheet resistance - $R_{N-1} = R_{N+1} = R_{ST} \frac{\Delta X}{\Delta Y}$, (10.1)

b. Sheet resistance $R_{N-NX} = R_{N+NX} = R_{ST} \frac{\Delta Y}{\Delta X}$, (10.2)

c. Contact resistance $R'_c = R_c/A_c$, (10.3)

d. Metal resistance $R'_M = R_M \frac{T}{A_c}$, (10.4)

where ΔX and ΔY are the spacings between grid points in the X- and Y-direction respectively, R_{ST} is the sheet resistance in $\Omega/\square$, R_c is the contact resistivity in $\Omega \cdot cm^2$, and R_M is the metal resistivity in $\Omega \cdot cm$. A_c is the incremental area of the metal contact and T is the thickness of the metal contact grid.
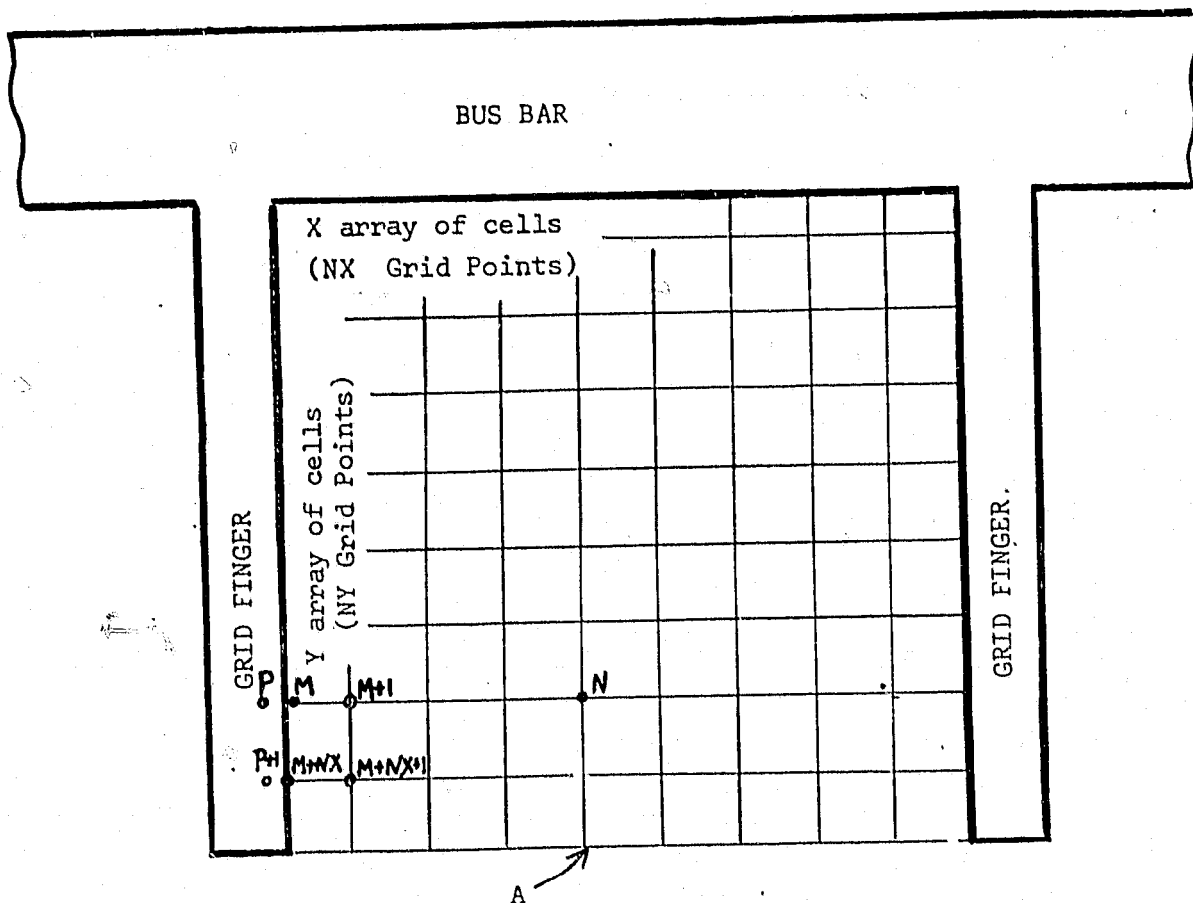
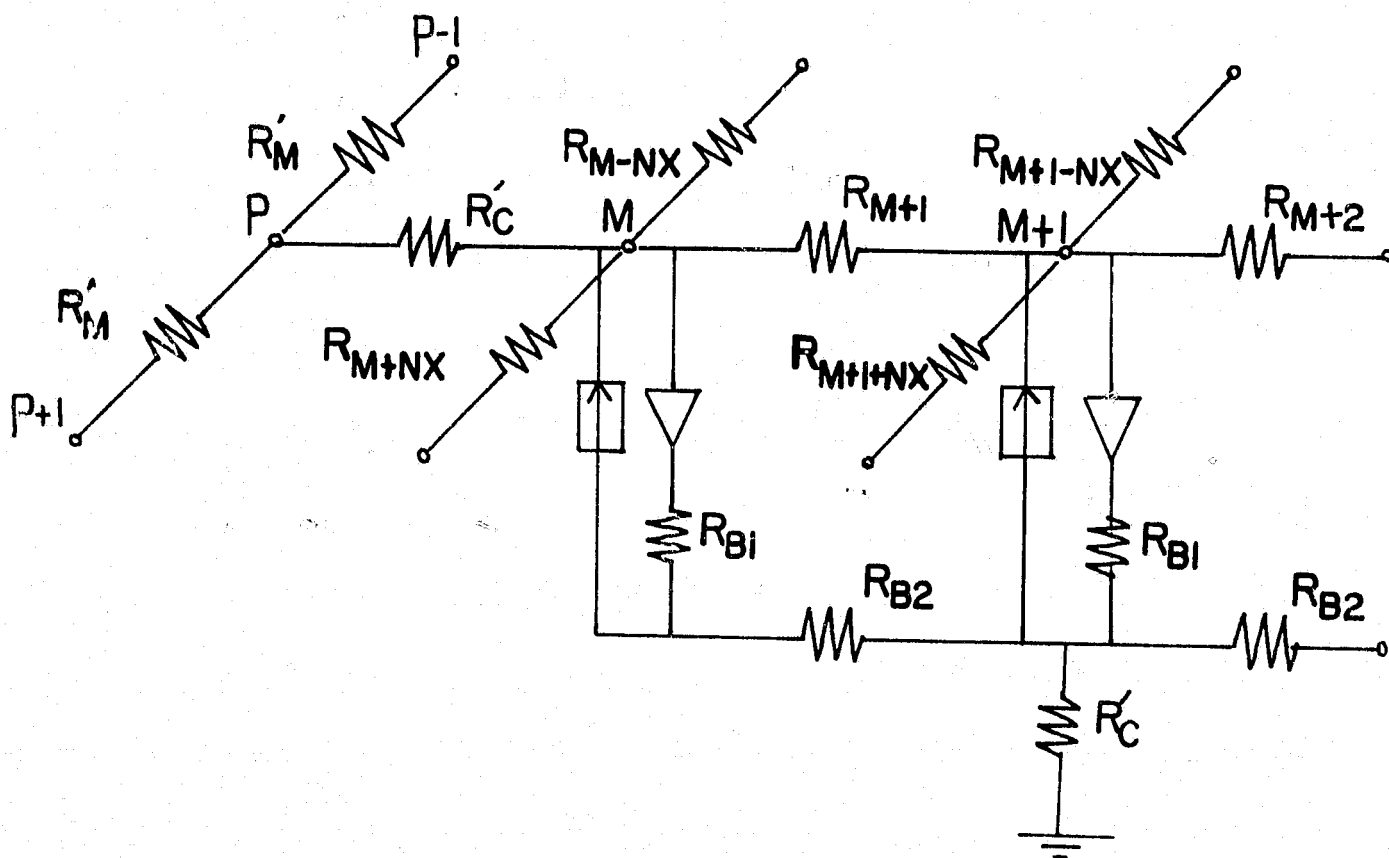Figure 10.1. Array of Grid Points used for Two-Dimensional Solar Cell Calculation.

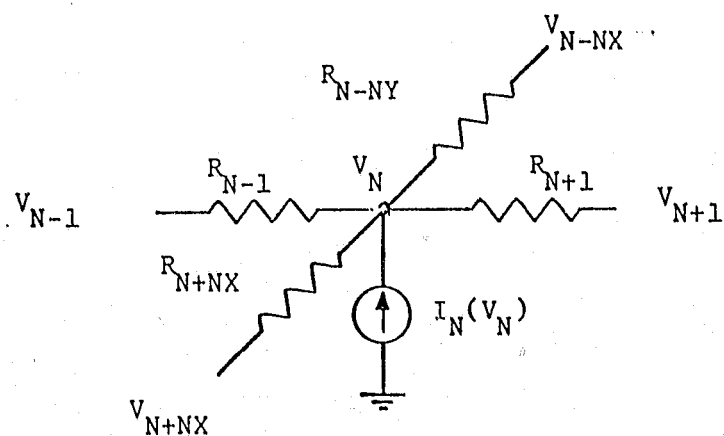Figure 10.2. Equivalent circuit of a two-dimensional solar cell.

Figure 10.3. Two-dimensional array of one-dimensional cells interconnected by series resistances.

Any bulk resistance R_{B1} in Figure 10.2 which arises from the bulk resistivity of the base layer need not be included here, since it is already included in calculating the one-dimensional I-V characteristics. Also the distributive base resistance R_{B2} in Figure 10.2 can be usually neglected, since most solar cells are covered with an ohmic contact over the entire back surface.

The bus bar is assumed to be at a constant potential which equals the terminal solar cell voltage. The voltage of all other grid points then can be calculated from the simultaneous solution of the node voltage equations at each grid point.

The node voltage equation can be written for each point of the array in the active area (Equation (10.5)), for points under the grid contact (Equation (10.6)) and for the points on the grid pattern (Equation (10.7))

$$F[V(N)]=V(N)[G(N-1)+G(N+1)+G(N+NX)+G(N-NX)]-V(N-1)\cdot G(N-1)$$
$$-V(N+1)\cdot G(N+1)-V(N-NX)\cdot G(N-NX)-V(N+NX)G(N+NX)-I_N[V(N)]=0 \qquad (10.5)$$

$$F[V(M)]=V(M)[G(M-1)+G(M-NX)/2+G(M+NX)/2+GC(M)]-V(M-1)\cdot G(M-1)$$
$$-V(M-NX)\cdot G(M-NX)/2-V(M+NX)\cdot G(M+NX)/2-GC(M)\cdot V(P)-I_M[V(M)]=0, \qquad (10.6)$$

$$F[V(P)]=V(P)\cdot[GC(M)+GF\cdot V(P-1)+GF\cdot V(P+1)]-V(P-1)\cdot GF-V(P+1)\cdot$$
$$GF-GC(M)\cdot V(M)=0. \qquad (10.7)$$

The task now becomes a problem of solving a system of (NX+2)(NY+1) simultaneous equations in the same number of unknowns.

10.4.3 Numerical Algorithm

The computer algorithm which has been used to solve this system of simultaneous equations is an iterative solution technique based on the modified Newton-Raphson method. A brief discussion of this technique follows.

The Newton-Raphson method can be derived from a Taylor series expansion. For a single function $f(x) = 0$, the algorithm used is $x_{i+1} = x_i - f(x_i)/f'(x_i)$ where x_{i+1} is the approximate value at the $(i+1)$th iteration. For two coupled equations with two unknowns $f_1(x,y)=0$ and $f_2(x,y)=0$, the algorithm can be written as

$$x_{i+1} = x_i - \frac{1}{J} \begin{vmatrix} f_1(x_i,y_i), & \dfrac{\partial f_1(x_i,y_i)}{\partial y} \\[2em] f_2(x_i,y_i), & \dfrac{\partial f_2(x_i,y_i)}{\partial y} \end{vmatrix}, \qquad (10.8)$$

$$y_{i+1} = y_i - \frac{1}{J} \begin{vmatrix} \dfrac{\partial f_1(x_i,y_i)}{\partial x}, & f_1(x_i y_i) \\[2em] \dfrac{\partial f_1(x_i,y_i)}{\partial x}, & f_2(x_i,y_i) \end{vmatrix}, \qquad (10.9)$$

where J is the Jacobian

$$J = \begin{vmatrix} \dfrac{\partial f_1(x_i,y_i)}{\partial x}, & \dfrac{\partial f_1(x_i,y_i)}{\partial y} \\[2em] \dfrac{\partial f_2(x_i,y_i)}{\partial x}, & \dfrac{\partial f_2(x_i,y_i)}{\partial y} \end{vmatrix}. \qquad (10.10)$$

For a solution to occur, J must not be zero.

The requirement of a non-zero Jacobian is difficult to check before running the program and the computation of the matrix operations is time consuming, hence a simpler modifier Newton-Raphson method is generally used. This consists of applying the single-variable Newton-Raphson method n times, once for each variable in a system of n simultaneous equations. Each time we do this, we assume that the other variables are kept constant.

Consider as an example two equations with two unknowns such as

$$f_1(x,y) = 0, \qquad\qquad (10.11)$$

$$f_2(x,y) = 0. \qquad\qquad (10.12)$$

Taking x_o and y_o as the initial guesses new values are obtained as

$$x_1 = x_o - \frac{f_1(x_o,y_o)}{\frac{\partial f_1(x_o,y_o)}{\partial x}}, \qquad\qquad (10.13)$$

$$y_1 = y_o - \frac{f_2(x_o,y_o)}{\frac{\partial f_2(x_o,y_o)}{\partial y}}. \qquad\qquad (10.14)$$

The algorithm is then repeated until the desired degree of accuracy is achieved. An important question is which variables should be used to calculate the next approximate solution and in what order.

One simple example given below will illustrate this point.

$$f_1(x,y) = 0.2X + 0.1\,Y - 0.01, \qquad\qquad (10.15)$$

$$f_2(x,y) = 0.1X + 0.2Y - 0.01. \qquad\qquad (10.16)$$

When we use $f_1(x,y)$ to calculate x and $f_2(x,y)$ for y, convergence to an error of 10^{-4} is achieved in 14 iterations. While the choice of $f_2(x,y)$ to calculate x and $f_1(x,y)$ to calculate y gives a fast divergence. In general, it can be easily shown that the function with the steeper slope at the solution point with respect to variable x should be chosen to calculate the next approximate x, and similarly for y.

The question of convergence for the modified Newton-Raphson method is a touchy one, since one cannot always guarantee a solution. For n simultaneous equations with n unknowns, there are n! ways of picking the variables and order of execution and sometimes only one of these choices will converge [4].

Sometimes the modified Newton-Raphson method does not converge but instead oscillates back and forth around the solution. This raises the question of when to stop the iterations. In this work the iteration has typically been continued until the maximum changes of the variables is below some selected small value, but what this may mean with respect to the answer is another question. In fact, it is possible that the difference between two successive calculations may be very small even though the values are nowhere near the right answer in the case of very slow convergence. To overcome this difficulty, the so-called under-and-over relaxation method has been used as a weighting parameter in the variable correction equation.

In this work, the unknown variables are always chosen from the equation which shows the steepest slope with respect to that particular variable at the solution point. The order of evaluations are arranged to assure fast convergence with an appropriate relaxation weight.

Suppose $V(N)_j$ is the j'th iteration value of $V(N)$. The next corrected value by using the one-variable Newton-Raphson method is then

$$V(N)_{j+1} = V(N)_j - \frac{F[V(N)_j]}{F'[V(N)_j]}, \qquad (10.17)$$

where $F'[V(N)_j]$ is the partial derivative with respect to $V(N)_j$. The explicit form of $F'[V(N)_j]$ is

$$F'[V(N)_j] = G(N+L)+G(N-1)+G(N-NX)+G(N+NX) - \frac{\partial I_N[V(N)_j]}{\partial V(N)_j} \qquad (10.18)$$

for the grid points on the active area. $I_N[V(N)]$ is the current density of the dark current density superimposed on the optically-generated current density. The current derivative can be accurately calculated, if the injected dark current density is assumed to be an exponential function of the potential at each particular grid point.

A flow chart of the two-dimensional analysis program is shown in Figure 10.4. The input data consists of the one-dimensional I-V data plus structural data on the contact finger arrangement. The complete two-dimensional I-V characteristic of the solar cell is then calculated at specified terminal voltage points using the modified Newton Raphson method. Calculations have typically been made until the voltage is accurate at each array point to less than 10^{-4} volts. With the voltage known at each array point the total solar cell current can then be evaluated by summing the current contributions from each node in the array.
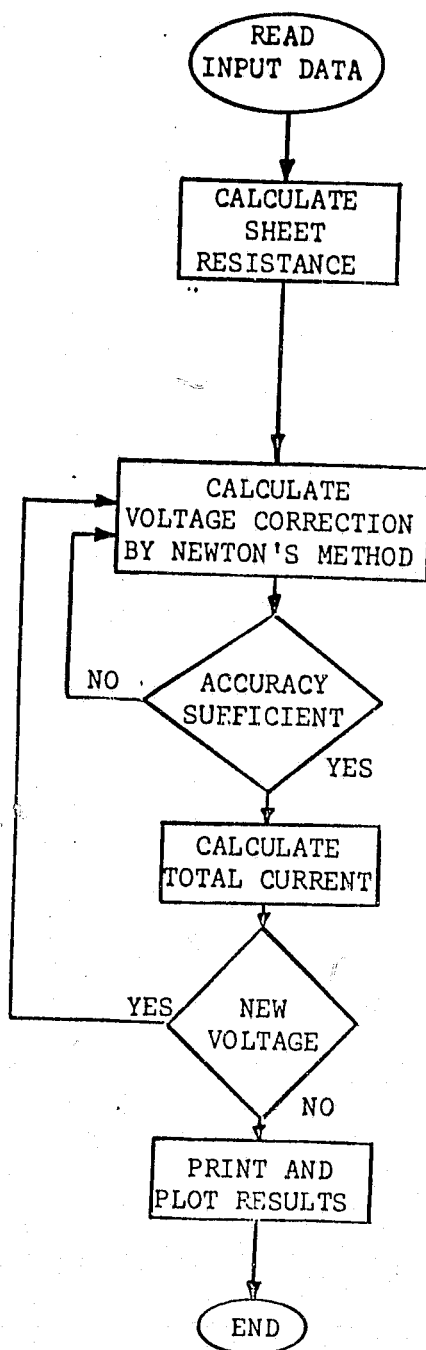
Figure 10.4. Flow Chart of Two-Dimensional Analysis Program

10.4.4 Discussions

Several questions may arise concerning the accuracy of this model. The first question concerns the number of grid points used in the calculation. Theoretically we can use as many points as we want to improve the precision in calculating. In this work, an array of 20x20 grid points has generally been used unless mentioned otherwise. This results in errors of only a few percent even in very severe conditions such as high sheet and contact resistance.

The second question concerns the validity of the one dimensional I-V characteristics used in the two-dimensional analysis. Since the typical built-in field in the diffused surface is in the range of 10^3-10^4 volts/cm, which is several orders of magnitude larger than the transverse field, the development of a transverse field in the two-dimensional analysis has a negligible influence upon the minority current density obtained from the one-dimensional model.

The third question is the assumption that the optically generated carriers in the base region will only be collected at the junction under the illuminated area. It is possible for the generated carrier in the base region to diffuse to the junction under the grid pattern, especially for the case of a thin collecting metal grid and a long diffusion length of the base minority carrier. For "good" cells with low sheet and contact resistance, this effect is found to be relatively unimportant, since the total collected optical current is the same in both cases.

The fourth assumption concerns modeling of contact resistance through a distributed surface contact resistor. In good solar cells, the surface contact resistance is usually very small because of the high

surface doping density. The base contact resistance is limited by the substrate doping density for non BSF cells and may not be negligible. The base contact resistance can however be transformed into an effective surface contact resistance. The calculated photovoltaic potential is the potential difference across the p-n junction irrespective of the combination of contact resistance from the surface or base. The relative voltage drop across the surface or base contact resistance can be determined experimentally.

10.4.5 Conclusions

(A) A general two-dimensional program has been developed which can simulate a practical solar cell with any arbitrary grid pattern and series resistance.

(B) A general two-dimensional program is a good tool for the optimum design of grid patterns and the prediction of the non-linear series resistance effects at the maximum power output.

10.4.6 REFERENCES

1. G. Lucovsky. 1960. Photoeffects in non-uniformly irradiated p-n junctions. Journal of Applied Physics 31(6).

2. T. Y. Gorbach, Z. S. Bribnikov and K. M. Krolevets. 1962. The photovoltage of a non-uniformly illuminated p-n junction. Radio Eng. Elect. (USA): 956-964.

3. P. X. D. Souza, etc. 1971. Development of a two-dimensional model of a solar cell. IEEE Fall Electronics Conference, Chicago, IL: 175.

4. P. A. Stark. 1970. Introduction to Numerical Method. The Macmillan Company, New York, New York.

Appendix 10.5 Fill Factor and Diode Factor of Solar Cells.

10.5.1 Abstract

The interrelation between fill factor, diode factor, series resistance, saturation current and space charge current densities for solar cells has not been definitely identified before. In the literature, a simplified dark I-V characteristic is usually assumed as follows:

$$I_{DK} = I_0 e^{\frac{qV}{AkT}},$$

where I_0 and A are taken as two independent parameters. However, this assumption cannot be physically justified, and the extensive adoption of this equation may sometimes lead to erroneous conclusions. In this paper, a better physical model of the cell current-voltage characteristics is used and the fill factor dependence on the diode factor, series resistance, saturation current and space charge current densities can therefore be more accurately predicted.

10.5.2 Introduction

In recent years, considerable effort has been made to raise the conversion efficiency of photovoltaic devices. The efficiency of a solar cell can be conveniently represented by

$$\eta = \frac{V_M I_M}{P_{IN}} = \frac{CFF \cdot V_{OC} \cdot I_{SC}}{P_{IN}}, \tag{1}$$

where the fill factor CFF is a measure of the sharpness of the photovoltaic I-V characteristics of a solar cell. It is clear that high cell efficiency can be achieved by raising the values of CFF, V_{OC} and I_{SC}.

However, it is also clearly recognized that increasing one component of the above parameters will adversely affect other components. The interelationships between fill factor V_{OC}, I_{SC} and other cell characteristics have not always been definitely identified.

In previous analyses, there are some discrepancies about the dependence of CFF on the above cell characteristics. Lindmayer [1] suggests that the reduced fill factor of a practical solar cell is due to space charge recombination current. However the effects of series resistance and saturation current density are not considered in this analysis. Pulfrey [2], on the other hand, shows that the fill factor of a solar cell is principally determined at a given series resistance by the saturation dark current density instead of the diode A factor. The fill factor is also found to improve with an increasing value of diode A factor for a constant series resistance.

On the contrary, Hovel [3] and Green [4] point out that, at a given series resistance, the fill factor is reduced with a higher value of diode A factor. However, it is very doubtful that a complete independence between the saturation current density or open circuit voltage and the diode A factor exists in a practical solar cell as was arbitrarily assumed in the previous analyses [1-4].

This paper will calculate the fill factor of a solar cell in a more general analysis without the constraints and assumptions of the previous references [1-4]. The dependence of fill factor on the cell characteristics, namely the saturation current density, the space charge current density, the diode A factor, and the series resistance is presented and examined.

10.5.3 Calculation of Fill Factor and Diode Factor

It has long been recognized that silicon p-n junction behavior does not follow ideal diffusion theory. In addition to injection into the neutral region of a p-n junction, electrons and holes can recombine via the localized recombination centers in the space charge region without surmounting the potential barrier. In the quantitative treatment of reference [5], which assumes a Shockley-Read recombination center, it is shown that

$$I_{DK} = I_{01} \cdot (\exp[q(V-RS \cdot I_{DK})/kT]-1) + I_{02} \cdot (\exp[q(V-RS \cdot I_{DK})/nkT]-1) \qquad (2)$$

where the first term represents normal injection; and the second term is the space charge current. The series resistance R_S can be represented by the following equation in the first order model:

$$R_S = \frac{R_{ST} \cdot SF^2}{12 \cdot AA} + \frac{LF^2 \cdot SF \cdot RM}{3 \cdot T \cdot WF \cdot AA} + \frac{R_B}{AR} + \frac{R_{CS}}{(AR-AA)} + \frac{R_{CB}}{AR}, \qquad (3)$$

where the meanings of the above parameters are explained in Table 1. It is also shown that the n value of Equation (2) varies between 1 and 2, where the value of n is 2 if the recombination peaks in the vicinity of the center of the space charge region [6].

If the superposition of the light and dark currents of an illuminated solar cell is assumed to be valid, then the photovoltaic I-V characteristic becomes

$$I_{LT} = I_{DK} - I_{SC} , \qquad (4)$$

or

$$I_{LT} = I_{01} \cdot (\exp[q(V-R_S \cdot I_{LT})/kT]-1) + I_{02} \cdot (\exp[q(V-R_S \cdot I_{LT})/2kT]-1) -I_{sc}, \quad (5)$$

where n=2 has been assumed in the space charge region current. The short circuit current I_{SC} and the open circuit voltage can be inter-related by setting $I_{LT}=0$ in Equation (5), i.e.

$$I_{SC} = I_{01} \cdot (\exp[qV_{OC}/kT]-1) + I_{02} \cdot (\exp[qV_{OC}/2kT]-1). \tag{6}$$

The maximum power can be calculated by setting $d(I_{LT} \cdot V)/dV$ to zero and calculating the corresponding V_M and I_M. The following equation is found:

$$I_{SC}-I_{01}(1+2x) \cdot e^{2x}-I_{02}(1+x) \cdot e^{x}=0, \tag{7}$$

where $x = q(V_M-R_S \cdot I_{LT})/2kT$. The fill factor CFF can be calculated as

$$CFF = \frac{V_M I_M}{V_{OC} I_{SC}}. \tag{8}$$

Instead of using Equation (2) to describe the dark I-V characteristics of a solar cell, the following simple equation is frequently used in the solar cell literature [1-4]

$$I_{DK} = I_0(\exp[qV/AkT]-1), \tag{9}$$

where A is a dimensionless number which is usually found equal to or greater than 1 in a practical silicon solar cell. Also A is not a constant value, but changes with the terminal voltage or current level of the device. In addition to the uncertain value of A, I_0 has no physical meaning except as a parameter fitting to Equation (9). This value of I_0 does not correspond to the actual reverse saturation current density, and it is also different from the prediction of simple diffusion theory.

From Equation (2) and (9), the empirical A factor can be calculated at the maximum power point as:

$$A = \frac{V_1 - V_2}{\frac{kT}{q} \log \frac{I_{DK}(V_1)}{I_{DK}(V_2)}},$$

(10)

where V_1 and V_2 are two voltages in the vicinity of V_M.

10.5.4 Relationships Between Fill Factor, Saturation Current Density, Series Resistance and A Factor

Numerical calculations of Equations (1) to (10) have been performed for cells of Tables 1 and 2. The results are shown as Figures 1 to 3.

Figure 1-a shows that the fill factor decreases with the series resistance and the space charge current density. The diode A factor can be calculated from Equation (10) for a specific value of the series resistance and the space charge current density. The interrelation between fill factor and the corresponding diode A factor is thereupon shown as Figure 1-b. This figure clearly shows that the fill factor is a monotonically decreasing function of the diode A factor for a constant series resistance. Moreover, the dashed line shows that the fill factor will decrease with the series resistance at a given value of the space charge current density. At a zero series resistance, the fill factor is about 0.80 or 0.75 at a current ratio I_{01}/I_{02} of 10^3 or 10^4. The A factor is about 1.08 or 1.58 in this case. However, with the series resistance of model c in Table 2, the fill factor has a value of 0.77 or 0.72 and the corresponding A factor is 1.2 or 1.92 at a current ratio I_{01}/I_{02} of 10^3 and 10^4 respectively.

Table 1

			Baseline Cells	$10\Omega\cdot cm$	$1\Omega\cdot cm$	$0.1\Omega\cdot cm$
Area	AR	(cm^2)		2	2	2
Active Area	AA	(cm^2)		1.734	1.734	1.734
Sheet Resistance	R_{ST}	$(\Omega/\square)$		120	120	120
No. of Fingers	NF			10	10	10
Width of Fingers	WF	(cm)		0.015	0.015	0.015
Space of Fingers	SF	(cm)		0.00019	0.00019	0.00019
Length of Fingers	LF	(cm)		0.9375	0.9375	0.9375
Thickness of Fingers	T	(cm)		0.0635	0.0635	0.0635
Length of Bus	LB	(cm)		2	2	2
Width of Bus	WB	(cm)		0.0625	0.0625	0.0625
Base Bulk Resistance	RB	$(\Omega\cdot cm^2)$		0.25	0.025	0.0025
Surface Contact Resistance	R_{CS}	$(\Omega\cdot cm^2)$		10^{-4}	10^{-4}	10^{-4}
Base Contact Resistance	R_{CB}	$(\Omega\cdot cm^2)$		Varied	Varied	Varied
Saturation Current Density	I_{01}	(A/cm^2)		6.94×10^{-11}	6.83×10^{-12}	1.76×10^{-13}
Space Charge Current Density	I_{02}	(A/cm^2)		Varied	Varied	Varied
Short Circuit Current	I_{SC}	(mA/cm^2)		43.0	40.0	35.0

Table 2. Models of the Series Resistance R_S in the calculation of Fill Factor of a solar cell

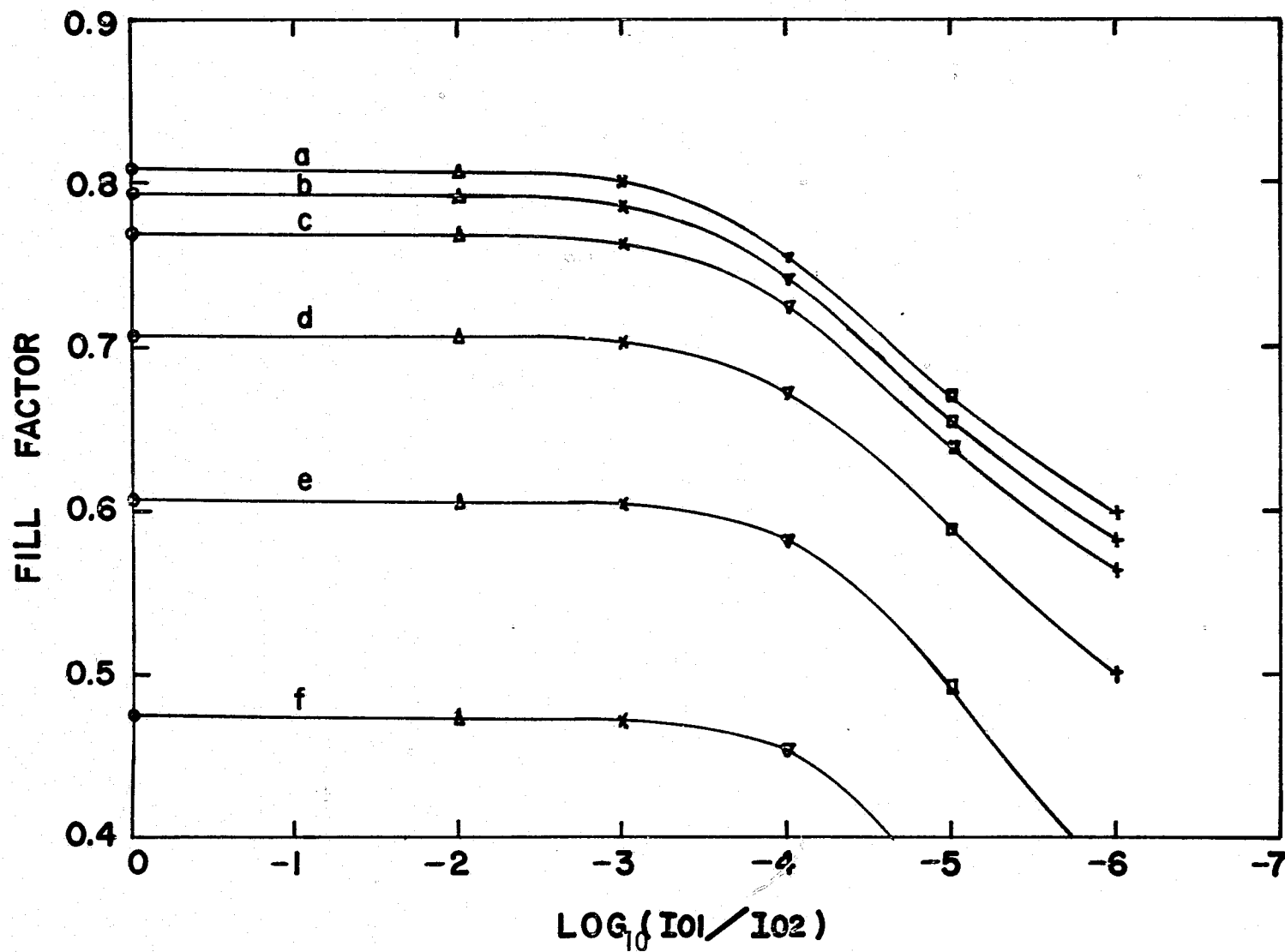| Models	$R_{CB}(\Omega\cdot cm^2)$	$10\ \Omega\cdot cm$ $R_S(\Omega)$	$1\ \Omega\cdot cm$ $R_S(\Omega)$	$0.1\ \Omega\cdot cm$ $R_S(\Omega)$
a	0	0	0	0
b	10^{-4}	0.32	0.21	0.20
c	0.5	0.57	0.46	0.45
d	1.5	1.07	0.96	0.95
e	3.0	1.82	1.71	1.70
f	5.0	2.82	2.71	2.70

Figure 1-a. Fill factor dependence on the space charge current density and series resistance a to f for 10 Ω-cm cell.

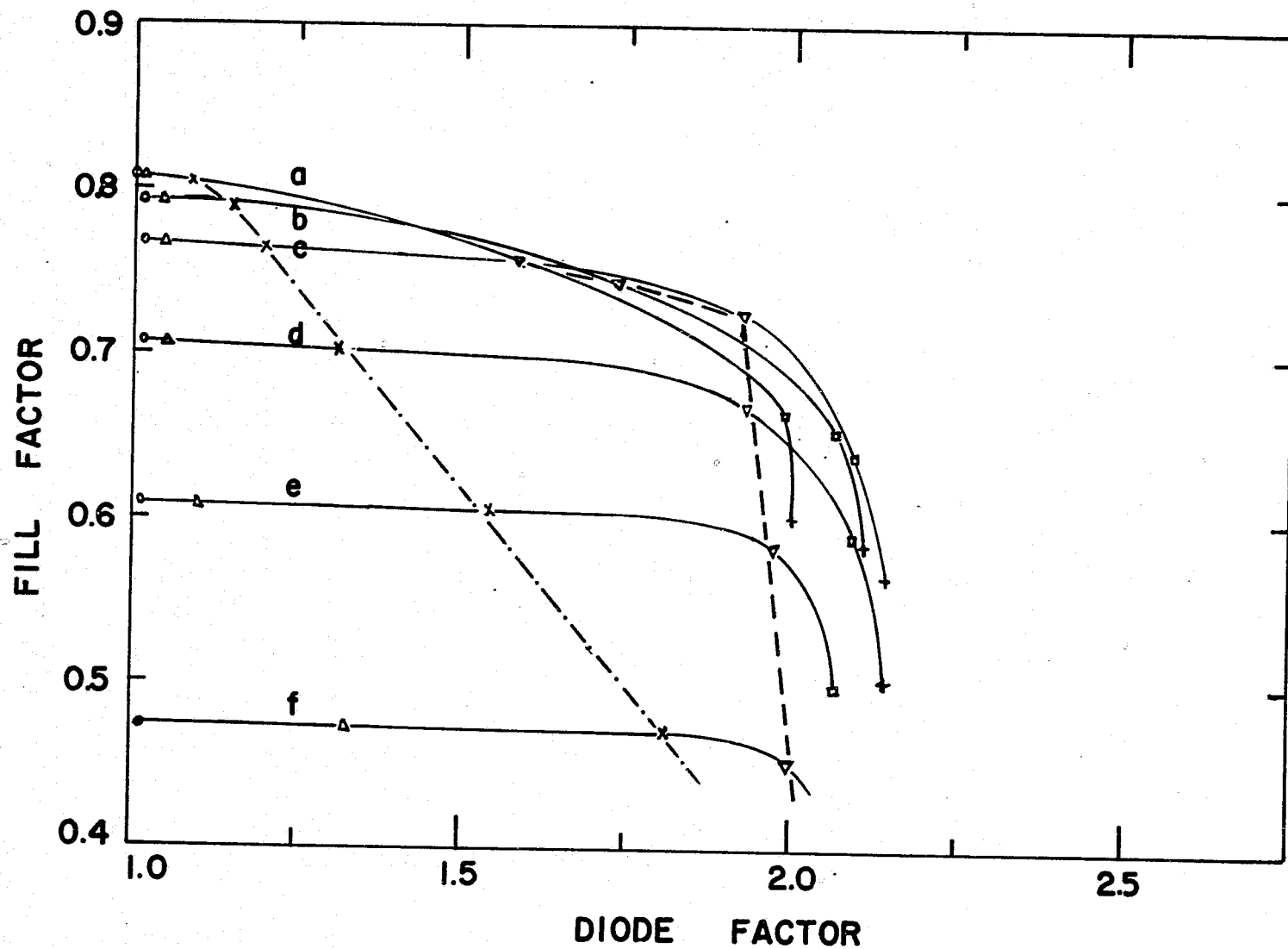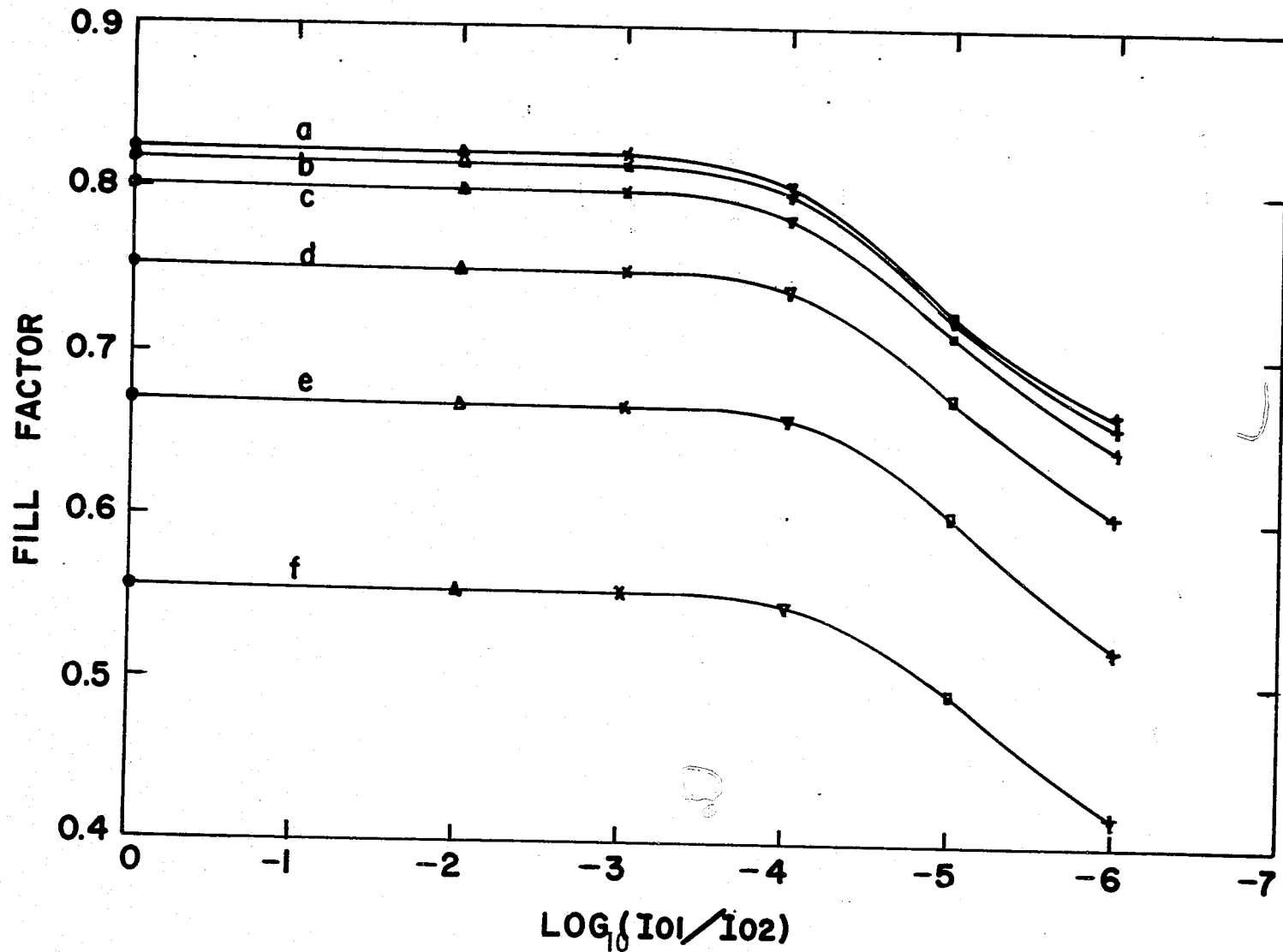Figure 1-b. Fill factor dependence on the diode A factor and series resistance a to f for 10 Ω-cm cell. $\log_{10}(I_{01}/I_{02}) = -3 (-\cdot-\cdot-)$, $\log_{10}(I_{01}/I_{02}) = -4 (---)$.

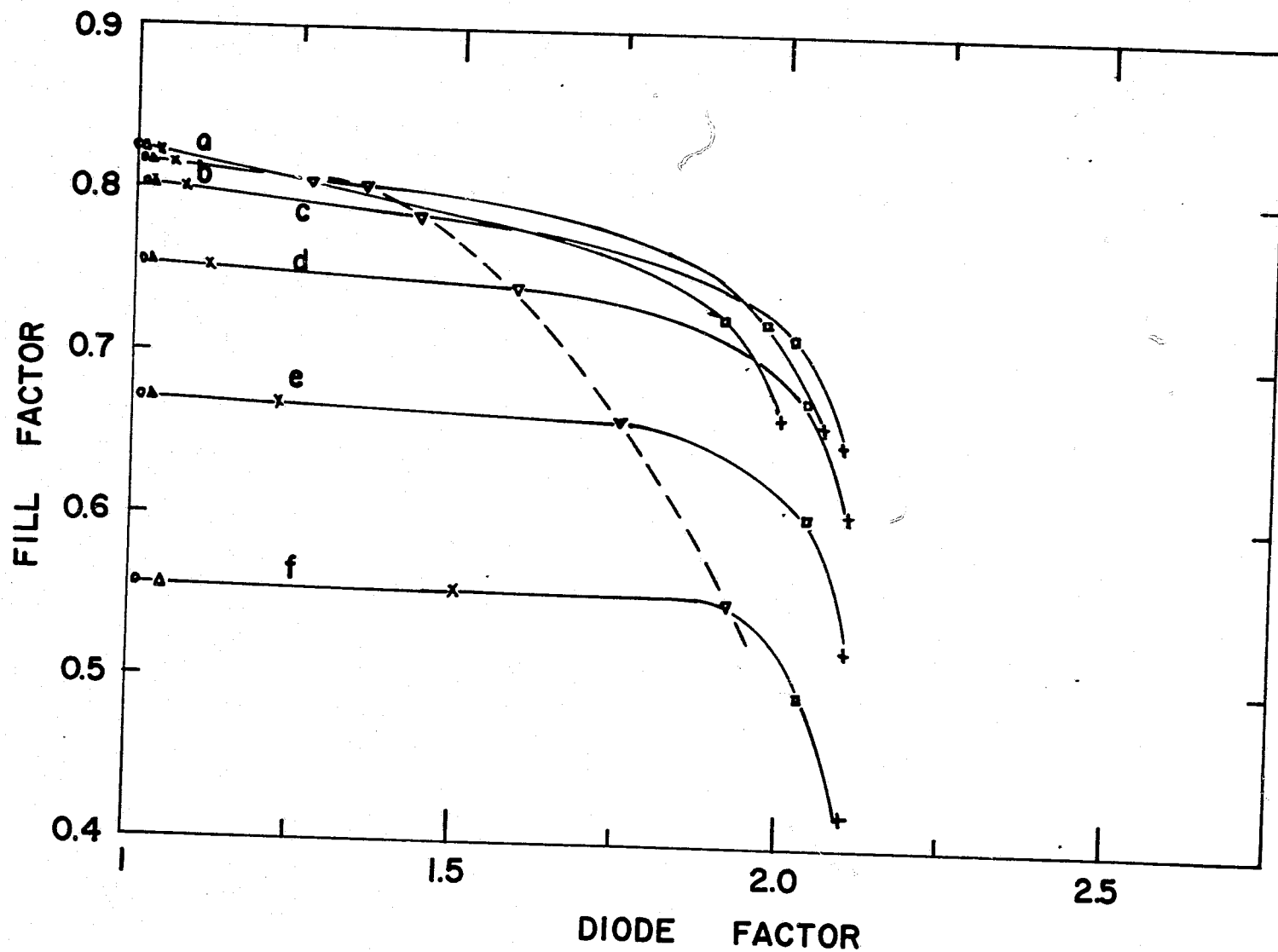Figure 2-a. Fill factor dependence on the space charge current density and series resistance a to f for 1 Ω-cm cell.

Figure 2-b.   Fill factor dependence on the diode A factor and series resistance a to f for 1 Ω-cm cell. $\log_{10}(I_{01}/I_{02}) = -4 (---)$.
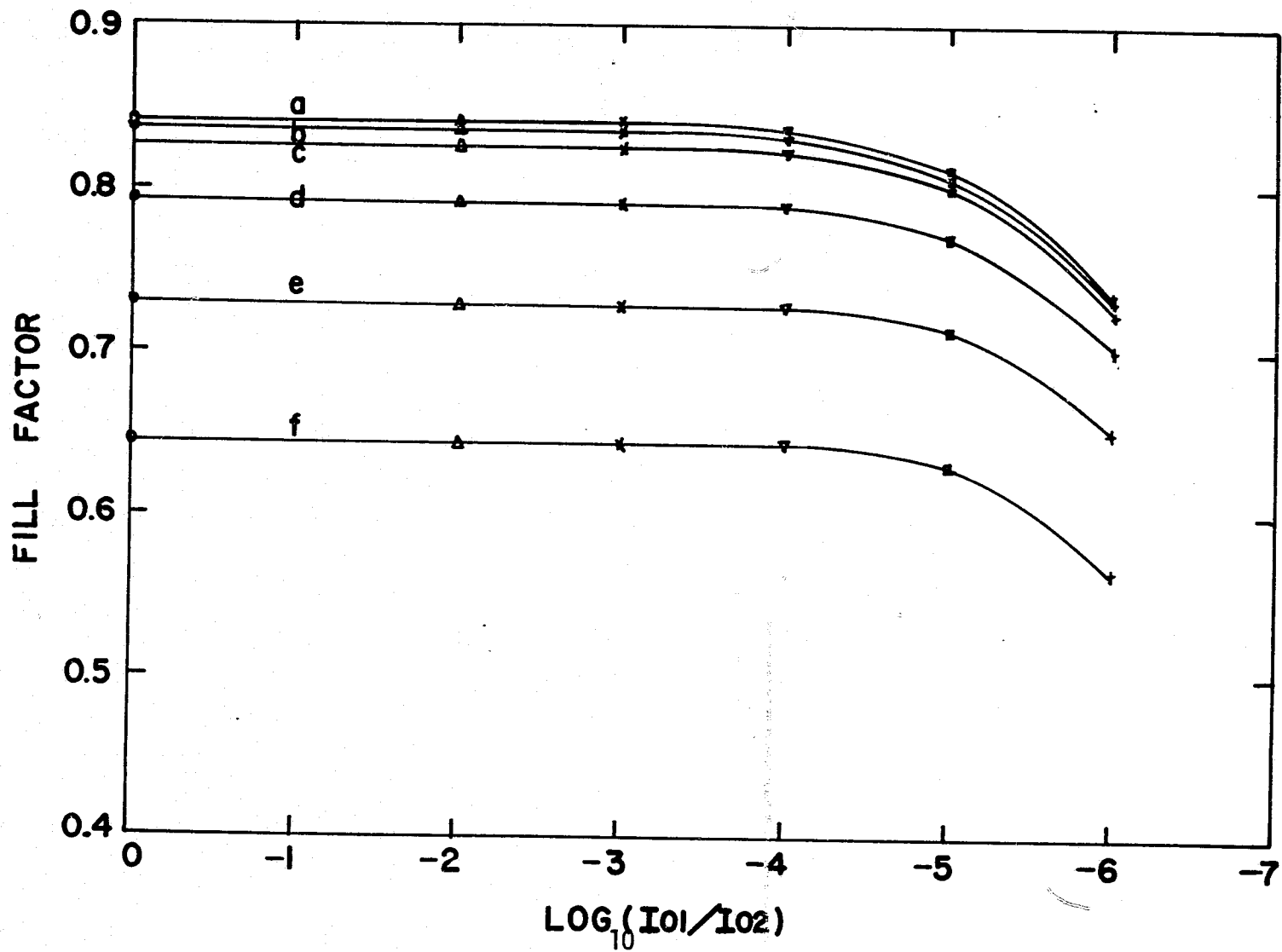
Figure 3-a. Fill factor dependence on the space charge current density and series resistance a to f for 0.1 Ω-cm cell.
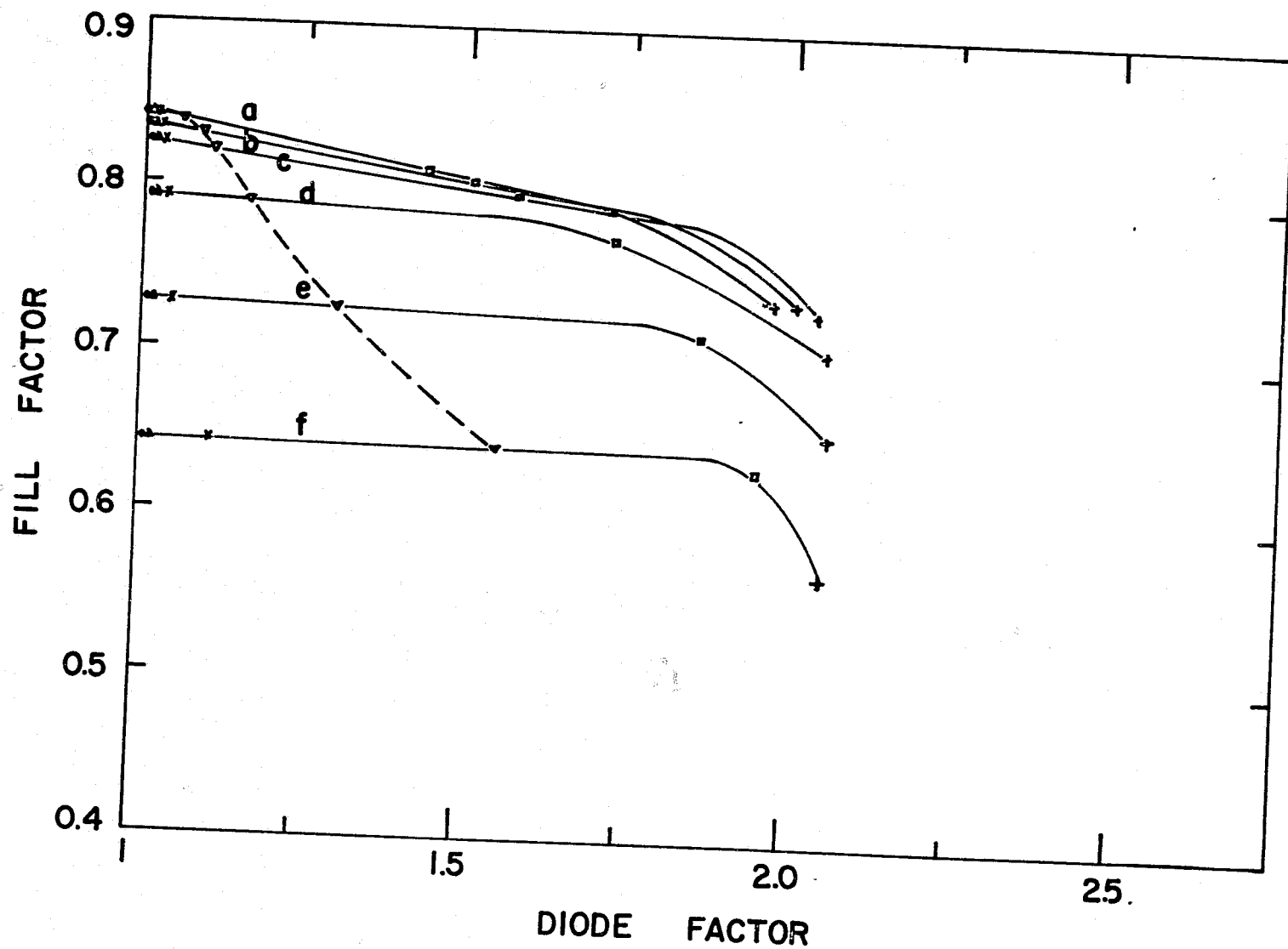
Figure 3-b. Fill factor dependence on the diode A factor and series resistance a to f for
0.1 Ω-cm cell. $\log_{10} (I_{01}/I_{02}) = -4 (---)$

It is known that a conventional n^+p silicon cell has a fill factor of about 0.72. On the other hand, the theoretically predicted fill factor is about 0.81. This discrepancy has been identified above as a result of a high space charge current density and a high series resistance in a practical silicon solar cell. Similar results are shown in Figures 2-a, 2-b, 3-a and 3-b for a 1 $\Omega \cdot cm$ or 0.1 $\Omega \cdot cm$ solar cell. From the comparison of parts a and b of Figures 1, 2 and 3, it is clearly seen that the fill factor is higher for a low resistivity solar cell at a specific series resistance and space charge current density. Therefore a low resistivity cell has the advantage of a higher fill factor than a high resistivity cell.

10.5.5 Discussions and Conclusions

This section discusses the discrepancies in previous theoretical analyses [1-4]. As has been shown, the previous analyses of fill factor began with the simple Equation (9). In this representation, the values of the two empirical parameters of A and I_0 need to be varied along with the voltage and current levels in order to fit the dark I-V characteristics of a practical solar cell. Therefore, it is doubtful that one can arbitrarily assume independent values of A and I_0. However, it is still a good representation if it is used to calculate the cell characteristics at or around only one particular point such as the maximum power density. Moreover the values of A, I_0 and R_S are closely interrelated and they can not be treated as independent parameters.

In this paper, Equation (2) instead of Equation (9) has been used in the analysis. There is a definite physical meaning for each parameter of Equation (2). In our calculation of the fill factor, the space charge current density I_{02} is allowed to vary due to the physical condition in the space charge region. The diode A factor is calculated at the maximum power point; therefore, the fill factor and diode factor can be correlated without the limitation of the assumptions of the previous analyses.

It can therefore be concluded that the fill factor of a solar cell is a monotonically decreasing function of the series resistance, the space charge current density and the diode A factor. In order to obtain a high value of fill factor, it is important to design a solar cell with a low series resistance and space charge current density A low resistivity cell is also found to give a higher fill factor than a high resistivity solar cell.

10.5.6 References

1. J. Lindmayer, Comsat. Tech. Rev. 2, 105 (1972).

2. D. L. Pulfrey, Solid-St. Electron. 21, 519 (1978).

3. H. J. Hovel, "Solar Cells" Semiconductors and Semimetals, Vol. II, pp. 58-61, (1975).

4. M. A. Green, Solid-St. Electron. 20, 265, (1977).

5. C. T. Sah, R. N. Noyce and W. Shockley, Proceedings of the IRE, Vol. 45, No. 9, 1228, (1957).

6. M. Wolf, G. T. Noel and R. J. Stirn, IEEE Trans. Electr. Dev., ED-24, 419, (1977).